



**This electronic thesis or dissertation has been  
downloaded from Explore Bristol Research,  
<http://research-information.bristol.ac.uk>**

*Author:*

**Yip, Stanley T H**

*Title:*

**Volcanic deformation and degassing**

*the role of volatile exsolution and magma compressibility*

**General rights**

Access to the thesis is subject to the Creative Commons Attribution - NonCommercial-No Derivatives 4.0 International Public License. A copy of this may be found at <https://creativecommons.org/licenses/by-nc-nd/4.0/legalcode>. This license sets out your rights and the restrictions that apply to your access to the thesis so it is important you read this before proceeding.

**Take down policy**

Some pages of this thesis may have been removed for copyright restrictions prior to having it been deposited in Explore Bristol Research. However, if you have discovered material within the thesis that you consider to be unlawful e.g. breaches of copyright (either yours or that of a third party) or any other law, including but not limited to those relating to patent, trademark, confidentiality, data protection, obscenity, defamation, libel, then please contact [collections-metadata@bristol.ac.uk](mailto:collections-metadata@bristol.ac.uk) and include the following information in your message:

- Your contact details
- Bibliographic details for the item, including a URL
- An outline nature of the complaint

Your claim will be investigated and, where appropriate, the item in question will be removed from public view as soon as possible.

# Volcanic deformation and degassing: the role of volatile exsolution and magma compressibility

By

Stanley Yip Tze Hou



School of Earth Sciences  
UNIVERSITY OF BRISTOL

A PhD dissertation submitted to the  
University of Bristol in accordance with the  
requirements for award of the degree of  
Doctor of Philosophy in the Faculty of Science

1 January 2024  
Supervised by Juliet Biggs & Marie Edmonds

Word count:  
38598



# Abstract

Integrating multi-parameter observations of volcanic processes is crucial for volcano monitoring. Qualitative models demonstrate that combining observations of volcanic deformation, gas emissions, and other parameters enhances the detection of volcanic unrest and provide insights into the magma plumbing system. Despite the progress made in this field, quantitative models that link these observations are still lacking.

Thermodynamic models have been used to constrain the characteristics of magma properties and its plumbing system. In this thesis, I develop models based on melt inclusion data and thermodynamics to reconstruct magma properties such as compressibility, and investigate how magmatic volatile content and magma storage conditions influence observations of volcanic deformation and SO<sub>2</sub> degassing.

By comparing mafic systems in arc and ocean island settings, I provide evidence for the lack of deformation observed during water-rich arc eruptions. In contrast, despite having low magmatic volatile content, ocean island eruptions have high SO<sub>2</sub> emissions due to their high diffusivity, which results in co-eruptive degassing. By comparing model predictions and observations, I show that all magmatic systems experience a certain degree of outgassing prior to an eruption, consistent with current conceptual models of transcrustal magmatic systems. Additionally, integrating time series of deformation, degassing, and extrusion flux can reveal the evolution of magma properties. Using this framework, I provide evidence for the increase in bulk magma compressibility following the removal of the degassed magma during the 2004 eruption of Mount St. Helens.

This study contributes to the better understanding of the effects of magmatic volatile content and pre-eruptive gas segregation on the physicochemical properties of magma, and provides a framework for modelling magma properties that can be applied to global volcano monitoring.





# Author's Declaration

I hereby confirm that the research presented in this dissertation complies with the University's Regulations and Code of Practice for Research Degree Programmes. This work has not been previously submitted for any other academic qualification. Unless explicitly referenced, the content of this dissertation is the original work of the author. Collaborative efforts or contributions from others are appropriately acknowledged. The views expressed in this dissertation solely reflect those of the author.

.....

Stanley Yip

1 January 2024



# Acknowledgements

The past few years have been an enriching and transformative journey, filled with challenges and rewards. I am sincerely grateful to the many individuals who have provided me with unwavering support and encouragement throughout my PhD journey.

First and foremost, I am immensely grateful to Juliet Biggs for her patient guidance, tireless support, and invaluable feedback that have shaped my research and helped me overcome obstacles along the way. Your passion and expertise in the field and dedication to mentoring have inspired me to strive for excellence. I am forever grateful for the time and effort you have invested in my growth, and they will stay with me forever.

I am thankful to my colleagues and fellow researchers who have contributed to my development. Their valuable insights, feedback and camaraderie have enriched my PhD experience and fostered a supportive research environment. I would like to extend special thanks to Marie Edmonds, Philippa Liggins, and Oliver Shorttle for their expertise and constructive criticism that have significantly influenced the quality of my work. I would also like to acknowledge Matthew Watson, Joachim Gottsmann, Katherine Cashman, and Alison Rust for their engaging discussions and pastoral support throughout the challenging times, especially during the COVID-19 pandemic. I am also thankful to the Volcanology and Geophysics groups in Bristol and COMET for providing the stimulating environment and valuable opportunities to share my research.

I am also grateful of my friends and colleagues who have shown faith in my abilities, which have been instrumental in keeping me motivated. I want to extend a special mention to Fabien, Mark, James, Robbie, Alex, Cristina, Tesfaye, Ben, Julia, Simon and Edna for their friendship, laughter, and banter that have added joy to my journey.

Lastly, I would like to express my gratitude to the Leverhulme Trust, COMET, and the Bristol Alumni Grant for their financial support. Their investment in my academic pursuits has allowed me to pursue my passion and contribute to the advancement of knowledge in my field.

My final heartfelt thanks goes to my family. Your unwavering support, encouragement, and belief in me have been instrumental in my success. This thesis is for you.



# Table of Contents

<b>Abstract</b>	<b>i</b>
<b>Author's Declaration</b>	<b>iii</b>
<b>Acknowledgements</b>	<b>v</b>
<b>Table of Contents</b>	<b>vii</b>
<b>List of Figures</b>	<b>xi</b>
<b>List of Tables</b>	<b>xiii</b>
<b>1 Introduction</b>	<b>1</b>
1.1 Motivation . . . . .	1
1.2 Volcano remote sensing . . . . .	2
1.2.1 SO <sub>2</sub> emissions . . . . .	2
1.2.2 Ground deformation . . . . .	5
1.2.3 Erupted volume . . . . .	6
1.3 Thermodynamic modelling . . . . .	7
1.4 Thesis structure . . . . .	10
<b>2 Contrasting volcanic deformation in arc and ocean island settings due to exsolution of magmatic water</b>	<b>15</b>
2.1 Introduction . . . . .	17
2.2 Background . . . . .	19
2.3 Methodology . . . . .	21
2.3.1 Thermodynamic modelling . . . . .	21
2.3.2 Linking magma properties to observable parameters . . . . .	23
2.4 One-at-a-time Sensitivity Tests . . . . .	25

## TABLE OF CONTENTS

---

2.4.1	Effects of H <sub>2</sub> O content on magma properties . . . . .	28
2.4.2	Effects of CO <sub>2</sub> content on magma properties . . . . .	30
2.4.3	Effects of sulfur content on magma properties . . . . .	31
2.4.4	Effects of oxygen fugacity on magma properties . . . . .	33
2.4.5	Effects of chamber compressibility . . . . .	36
2.4.6	Summary of sensitivity analyses . . . . .	37
2.5	Comparison Between Arc Basalts and Ocean Island Basalts . . . . .	38
2.5.1	Thermodynamic modelling of magma properties . . . . .	38
2.5.2	Comparison to Satellite Observations . . . . .	41
2.6	Limitations . . . . .	46
2.7	Conclusion . . . . .	47
<b>3</b>	<b>The role of pre-eruptive exsolved volatile segregation on observations of volcanic deformation and degassing</b>	<b>49</b>
3.1	Introduction . . . . .	51
3.2	Model Setup . . . . .	52
3.2.1	Thermodynamic framework . . . . .	52
3.2.2	Effect of Magma Composition . . . . .	54
3.2.3	Effect of chamber compressibility . . . . .	57
3.3	Pre-eruptive gas segregation . . . . .	57
3.3.1	Conceptual Model . . . . .	57
3.3.2	Modelling Gas Segregation . . . . .	61
3.3.3	Model Results . . . . .	63
3.4	Comparison to Observations . . . . .	63
3.4.1	Data compilation . . . . .	64
3.4.2	Sulfur Dioxide, $\tilde{S}$ . . . . .	67
3.4.3	Volume Change, $\tilde{V}$ . . . . .	67
3.4.4	Combining $\tilde{V}_{obs}$ and $\tilde{S}_{obs}$ . . . . .	70
3.5	Discussion . . . . .	71
3.6	Conclusions . . . . .	73
<b>4</b>	<b>Temporal evolution of magma gas content and compressibility using volcanic deformation and degassing</b>	<b>77</b>
4.1	Introduction . . . . .	79
4.2	Two-layer Model . . . . .	80
4.2.1	Model Setup . . . . .	82

4.2.2	Model Results . . . . .	83
4.3	Case study . . . . .	86
4.3.1	Case Study 1: Degassed Plug . . . . .	86
4.3.2	Case Study 2: Gas-rich cap . . . . .	96
4.4	Discussion . . . . .	100
4.5	Conclusion . . . . .	101
<b>5</b>	<b>Discussion</b>	<b>103</b>
5.1	Effects of temperature on volatile solubility . . . . .	103
5.2	Additional case studies . . . . .	105
5.2.1	Applicability of thermodynamic framework . . . . .	105
5.2.2	Time series analysis . . . . .	110
5.3	Limitations of data and model assumptions . . . . .	113
5.3.1	Limitations of thermodynamic model . . . . .	113
5.3.2	Limitations of monitoring data . . . . .	113
5.3.3	Limitations of crustal data . . . . .	115
5.4	Outlook . . . . .	115
<b>6</b>	<b>Concluding remarks</b>	<b>119</b>
<b>A</b>	<b>Supplementary Material for Chapter 2</b>	<b>123</b>
A.1	Supplementary Tables . . . . .	125
A.2	Supplementary References . . . . .	131
<b>B</b>	<b>Supplementary Material for Chapter 3</b>	<b>139</b>
B.1	Fractional Crystallisation . . . . .	140
B.2	Magma Density . . . . .	141
B.3	Supplementary Tables . . . . .	143
B.4	Supplementary References . . . . .	169
<b>C</b>	<b>Supplementary Material for Chapter 4</b>	<b>179</b>
C.1	Supplementary References . . . . .	189
	<b>References</b>	<b>191</b>





# List of Figures

1.1	Data types available for volcano monitoring . . . . .	4
1.2	Examples of inputs and outputs of a thermodynamic model . . . . .	8
2.1	Conceptual model of magma degassing during eruptions of different styles . .	20
2.2	Physicochemical properties of basalts when varying the initial magmatic H <sub>2</sub> O from 1.0-3.0 wt% . . . . .	29
2.3	Physicochemical properties of basalts when varying the initial magmatic CO <sub>2</sub> from 500 to 1500 ppm . . . . .	30
2.4	Physicochemical properties of basalts when varying the initial magmatic S from 1000 to 3000 ppm . . . . .	32
2.5	Physicochemical properties of basalts when varying $f_{O_2}$ of magma storage from NNO-1 to NNO+2 . . . . .	34
2.6	Physical properties of basalts when varying the crustal shear modulus ( $\mu$ ) from 0.1 to 30 GPa and chamber geometry . . . . .	35
2.7	Comparison of magma properties between arc basalts and ocean island basalts	39
2.8	Satellite detectability of volcanic deformation and degassing . . . . .	42
3.1	Sensitivity tests showing the physicochemical properties of rhyolite when varying magmatic volatile content and oxygen fugacity. . . . .	55
3.2	Comparison of model predictions for basaltic and rhyolitic eruptions, and water-poor and water-rich compositions. . . . .	56
3.3	Sensitivity tests showing the effects of chamber compressibility on deformation.	58
3.4	Conceptual model of gas segregation within magmatic system. . . . .	59
3.5	Model predictions considering pre-eruptive gas segregation processes . . . . .	62
3.6	Observations of deformation and SO <sub>2</sub> degassing from 20 eruptions between 2005-2021 . . . . .	66
3.7	Comparison between model predictions and observations of SO <sub>2</sub> degassing and co-eruptive volume change . . . . .	69

## LIST OF FIGURES

---

3.8	Conceptual model comparing the magmatic systems feeding silica-rich and silica-poor eruptions. . . . .	72
3.9	Illustration of the three best currently-available catalogues for volcano monitoring . . . . .	74
4.1	Temporal variations in magma properties during an eruption involving a two-layered plumbing system . . . . .	81
4.2	Temporal variation of SO <sub>2</sub> emissions and volume changes for a two-layered magma reservoir with a degassed plug or a gas-rich cap . . . . .	85
4.3	Conceptual model of the 2004 eruption of Mount St. Helens . . . . .	87
4.4	Temporal evolution of eruption data for the 2004 eruption of Mount St. Helens	89
4.5	Misfit plot between observed and modelled volume change . . . . .	95
4.6	Temporal evolution of eruption data for the 2011 eruption of Cordón Caulle .	97
5.1	Physicochemical properties of basalts when varying the initial temperature from 1000-1400 °C . . . . .	104
5.2	Magma and crustal properties of the 2011 eruption of Grímsvötn versus pressure/depth . . . . .	106
5.3	Temporal evolution of magma properties during the eruptions of Grímsvötn 2011, Eyjafjallajökull 2010, and Augustine 2006 . . . . .	111
5.4	Flowchart of the thermodynamic framework webtool . . . . .	116

# List of Tables

2.1	Volatile composition of the parameters explored . . . . .	26
2.2	Summary table showing the maximum percentage change of each observation	27
3.1	Compilation of observations for 20 recent eruptions. . . . .	64
4.1	Symbols and the initial parameters for the simulated eruption . . . . .	84
4.2	Input parameters and the parameter space explored in the forward models for Mount St. Helens, 2004 . . . . .	92
4.3	Input parameters and the parameter space explored in the forward models for Cordon Caulle, 2011 . . . . .	99
5.1	Model parameters for the 2011 eruption of Grimsvötn . . . . .	107
A.1	Volcanic eruptions and satellite detection of deformation and SO <sub>2</sub> emissions between 2005-2022. . . . .	125
A.2	Satellite detectability of deformation and SO <sub>2</sub> degassing. . . . .	129
B.1	Initial volatile contents and oxygen fugacity used in EVo models. . . . .	143
B.2	Summary of the maximum percentage change of rhyolitic magma for each observation across the depth range. . . . .	143
B.3	General characteristics of eruptions and volcanoes, and satellite detection of deformation and SO <sub>2</sub> degassing during corresponding eruption. . . . .	144
B.4	Co-eruptive volume change of eruptions. . . . .	148
B.5	SO <sub>2</sub> emissions of eruptions. . . . .	152
B.6	Volume erupted of eruptions. . . . .	156
B.7	Reservoir depth of volcanic eruption. . . . .	160
B.8	Normalised volume change and normalised SO <sub>2</sub> of eruptions. . . . .	164
B.9	Reservoir depth of volcanic eruption. . . . .	166

## LIST OF TABLES

---

C.1	GPS measurements for the 2004 eruption of St. Helens spanning 2004-2005 (Anderson and Segall, 2013). . . . .	181
C.2	Volume erupted for the 2004 eruption of St. Helens spanning 2004-2005 (Gerlach et al., 2008). . . . .	187
C.3	SO <sub>2</sub> measurements for the 2004 eruption of St. Helens spanning 2004-2005 (Gerlach et al., 2008). . . . .	188

# Chapter 1

## Introduction

### 1.1 Motivation

Monitoring volcanic activity and eruption processes heavily rely on observational sciences. Geophysical techniques involve making measurements near the surface of a volcano to understand magmatic processes occurring at depth, and geochemical analyses use magma and volatile compositions to provide insights into subsurface magmatic conditions. Volcanic processes are fundamentally linked, yet these observations are often treated as independent measurements due to the lack of multiparameter sensors that is not available in the majority of the world's 1400 subaerial volcanoes (Loughlin et al., 2015).

Magmatic volatile content (dissolved and exsolved) modulates magma properties, which in addition to crustal properties, affect ground deformation. While it is known that gas content in a reservoir suppresses volume change of a reservoir, and thus ground deformation, the extent in which the gas content in the reservoir suppresses ground deformation is unclear. Moreover, the gas content in the reservoir changes before and during an eruption - what does this inform us about the pre-eruptive magma storage conditions, and how does this affect eruption styles?

The eruption style of a volcano is modulated by magma properties (Cassidy et al., 2018), which evolves continuously during an eruption. The transition between explosive and effusive eruption can pose a significant hazard to life and surrounding infrastructures. Understanding magma properties is therefore key to reducing the associated risks and improving the preparedness of communities living in close proximity to volcanoes.

In this thesis, I use thermodynamic models to reconstruct the process of volatile exsolution and simulate the resulting changes in magma properties, such as compressibility. The magma properties predicted by the model are compared with observations of  $\text{SO}_2$  and deformation, normalised by the volume erupted, to characterise the challenges in volcano monitoring, particularly volcanic deformation in different tectonic settings (Chapter 2), magma composition (Chapter 3), and eruptive transitions (Chapter 4).

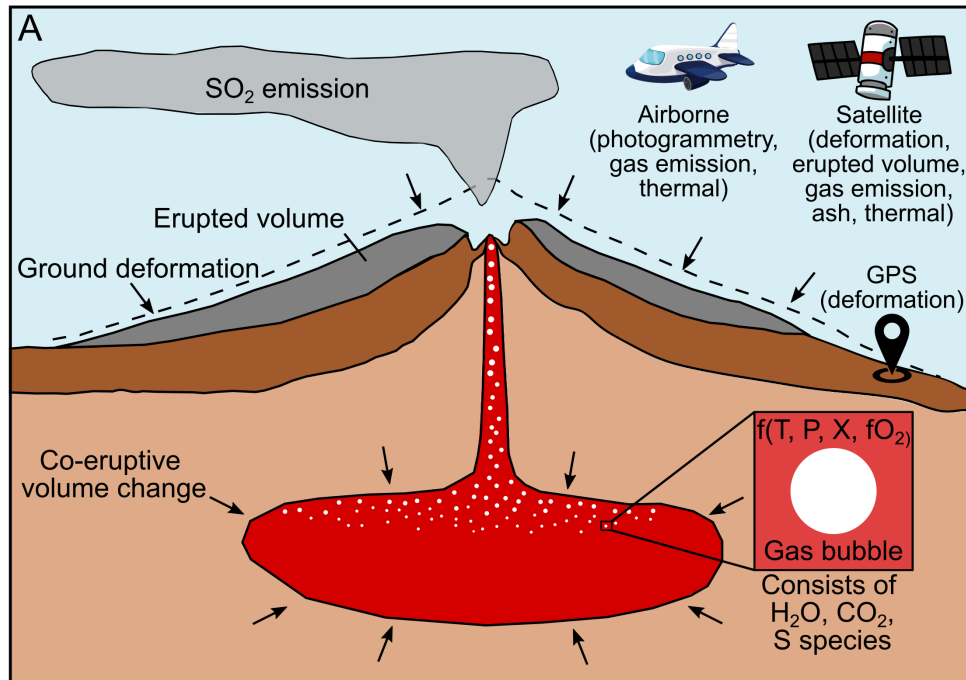
## **1.2 Volcano remote sensing**

Many types of volcano remote sensing data are available, such as thermal anomalies, gas emissions, surface deformation, topographic change, and ash clouds (e.g., Yamaguchi et al., 1998; Biggs and Pritchard, 2017; Carn et al., 2017; Lechner et al., 2018; Dualeh et al., 2023) (Figure 1.1a). Multidisciplinary measurements have provided crucial information for tracking volcanic unrest leading to an eruption (e.g., 2020-2021 eruption of La Soufrière volcano, St. Vincent Joseph et al., 2022). In fact, integrating multiparameter dataset does not only provide insights into magmatic processes, it also improves eruption forecasting and detecting signals of volcanic unrest that may not be readily observable in all sensors (Cameron et al., 2018; Furtney et al., 2018; Reath et al., 2020).

In this section, I present an overview of various data types used in my study (Figure 1.1).  $\text{SO}_2$  emissions can be utilised to reflect the gas content in the reservoir and the permeability of the reservoir (Section 1.2.1). Ground deformation data can provide estimates of volume change of the reservoir, which can be used to identify magma properties such as compressibility (Section 1.2.2). The volume of erupted materials that alters the morphology of a volcano can be used to estimate the extrusion rate of lava (Section 1.2.3). Notably, the erupted volume in this study serves as a normalisation factor for  $\text{SO}_2$  emissions and ground deformation data.

### **1.2.1 $\text{SO}_2$ emissions**

Volcanic gas emissions is crucial to volcano monitoring as it provides insights into volcanic activity and forecasting potential eruptions. Volcanic gases are dominated by  $\text{CO}_2$  at pressures of over 50-100 MPa, which can become enriched with  $\text{H}_2\text{O}$  at lower pressures (e.g., Papale, 2005; Burgisser et al., 2015; Liggins et al., 2020). However,



**Sierra Negra**

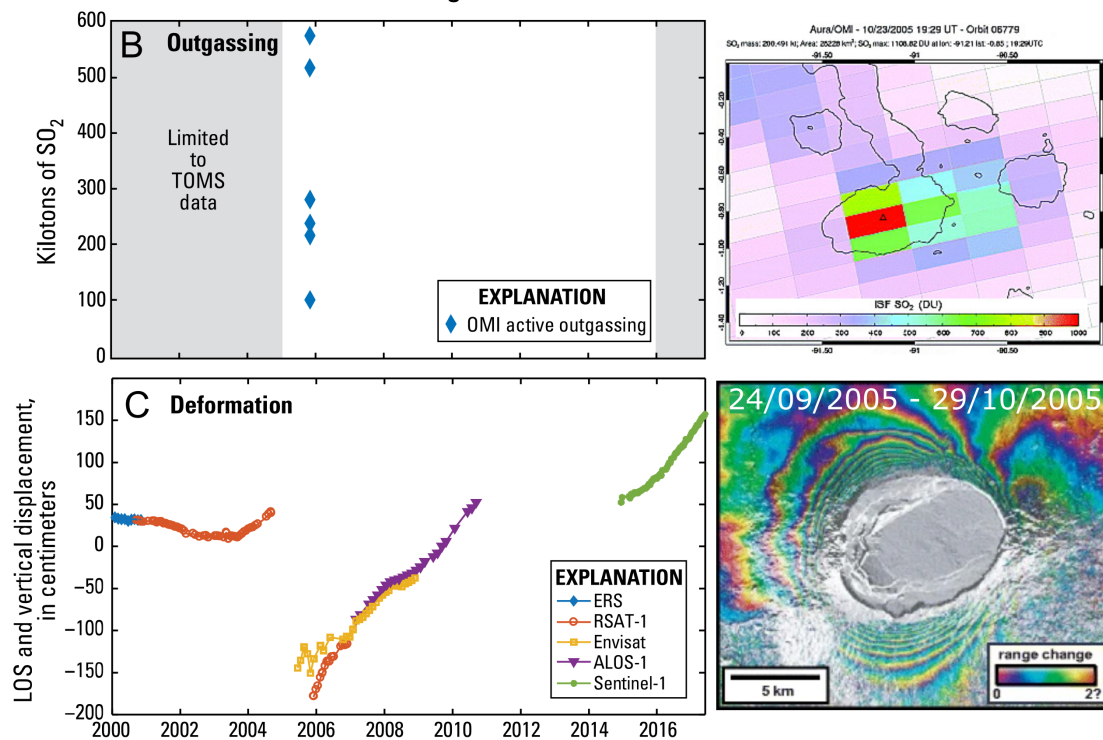




FIGURE 1.1. (page 3): (a) Schematic diagram illustrating the various data types available for monitoring volcanoes, which can provide valuable insights into the underlying volcanic processes. The exsolution of volatiles into the gas phase can lead to increased  $\text{SO}_2$  emissions and cause the magma to become more compressible, resulting in muted ground deformation. (b-c) The left panels show the time series spanning 17 years at Sierra Negra Volcano, Ecuador (Reath et al., 2020) and the right panels show co-eruptive  $\text{SO}_2$  emissions and ground deformation of the 2005 eruption (Geist et al., 2008; Yang et al., 2009). (b) Time series of  $\text{SO}_2$  emissions from the Ozone Monitoring Instrument (OMI) (Carn, 2016; Carn et al., 2017). OMI data is available from 2005 and is only analysed until 2016 (from Reath et al., 2020). OMI detected  $\text{SO}_2$  emissions associated with the 2005 eruption on 23 October (from Yang et al., 2009). (c) Time series of ground deformation acquired from different satellite sensors (from Reath et al., 2020). The time series and the interferogram generated using synthetic aperture radar images between 24 September and 29 October recorded co-eruptive deflation associated with the 2005 eruption (from Geist et al., 2008).

$\text{SO}_2$  gas is the most frequently monitored volcanic gas due to its detectability against background concentrations (e.g., Shinohara et al., 2003; Mori and Burton, 2006).

Volcanic  $\text{SO}_2$  gas can be measured using ground-based, airborne, and satellite-based techniques (Figure 1.1a). Ground-based methods incorporate the use of spectrometers to measure  $\text{SO}_2$  concentrations in the plume discharged from the volcano (e.g., Mori and Burton, 2006; Wilkes et al., 2017), while airborne methods involve traversing the volcano with specialised instruments that measure the concentration of  $\text{SO}_2$  in the plume (e.g., Gerlach et al., 1997; Shinohara et al., 2003; Liu et al., 2020). Satellite-based methods detect and quantify  $\text{SO}_2$  emissions from space using a range of ultraviolet and infrared sensors such as the Ozone Monitoring Instrument (OMI) or the TROPospheric Monitoring Instrument (TROPOMI) (e.g., Carn et al., 2016; Taylor et al., 2018; Theys et al., 2019). In fact, OMI has recorded  $\text{SO}_2$  emissions from at least 100 volcanoes based on a decade of measurements between 2005 and 2015 (Carn et al., 2016). Figure 1.1b shows detection of  $\text{SO}_2$  emissions at Sierra Negra during the 2005 eruption. While typically measured during explosive and effusive eruptions,  $\text{SO}_2$  emissions can also be detected in non-eruptive phases through passive degassing (Carn et al., 2017), and thus, passive  $\text{SO}_2$  measurements are included in this study where available.

Monitoring changes in  $\text{SO}_2$  emissions can not only detect volcanic unrest, it also provides

insight into the composition and content of volcanic gases in the reservoir (Shinohara et al., 2003; Aiuppa et al., 2009). Notably, volcanic SO<sub>2</sub> emissions observed through remote sensing techniques can differ by several orders of magnitude from those predicted based on the initial amount dissolved in pre-eruptive silicate melts, due to various pre- and co-eruptive processes described in Section 3.3.1 (e.g., Gerlach et al., 1994; Wallace, 2005; Yip et al., 2022).

### 1.2.2 Ground deformation

Volcanic deformation is a critical component of volcano surveillance that provides valuable insights into the behaviour of volcanic systems. Volcanic deformation occur for various reasons, including magma intrusion or withdrawal from a region in the crust (e.g., Bato et al., 2021; Bemelmans et al., 2021), exsolved volatiles migrating to shallow reaches of magma chambers (e.g., Anderson, 1995; Boudreau, 2016), and pressurisation of a hydrothermal system (e.g., Hutchison et al., 2016; Albino et al., 2019), cooling and crystallisation of magma (e.g., Tait et al., 1989; Townsend, 2022).

Volcanic deformation can be measured using satellite and ground-based techniques (Figure 1.1a). While ground-based Global Positioning Systems (GPS) measurements offer high temporal resolution of horizontal and vertical movements of the volcano, they are not available at all volcanoes. In cases where ground-based measurements are not available, I use space-borne Interferometric Synthetic Aperture Radar (InSAR) measurements that provide consistent acquisitions for volcanoes over a wide area globally. InSAR measures changes in the surface elevation using phase changes between two satellite radar images based on the look angle of the sensor, which is also known as the line-of-sight (LOS). Figure 1.1c shows the time series of ground deformation at Sierra Negra and illustrates the co-eruptive deflation associated to the 2005 eruption. The term LOS displacement is used to refer to these measurements, while the radial component is used for GPS measurements.

Deformation signals are usually derived from the upper parts of the crust since changes in pressure in shallow magma reservoirs result in a higher magnitude of ground deformation (Ebmeier et al., 2018). When combined with source models, deformation signals can be used to determine the location and size of magma chambers, as well as the volume change of a reservoir during an eruption (Bagnardi and Hooper, 2018; Jiang and González, 2020).

Unfortunately, not all eruptions are accompanied by deformation (e.g., Ebmeier et al., 2013b; Delgado et al., 2017; Lesage et al., 2018). Several factors can contribute to the absence of volcanic ground deformation, including the depth of magmatic sources and interference from atmospheric noise for InSAR measurements (Moran et al., 2006; Fournier et al., 2010; Ebmeier et al., 2013b; Remy et al., 2015; Yip et al., 2019). In this study, I focus on the effects of magmatic volatile content, such as water, and the presence of an exsolved volatile phase (gas bubbles) on the physicochemical properties of magma (e.g., Wallace, 2005; Edmonds and Woods, 2018). The presence of gas bubbles within the magma introduces a significant layer of complexity when measuring volcanic deformation. Gas bubbles, due to their higher compressibility compared to the surrounding magma, enhances magma compressibility and may thus suppress volume changes of the reservoir despite changes in the reservoir pressure (Rivalta and Segall, 2008; Kilbride et al., 2016; Yip et al., 2022). The lack of volume changes of the reservoir results in muted volcano deformation, and thereby introduces discrepancies and uncertainties when assessing the size and geometry of magma reservoirs. This, in turn, amplifies the challenges associated with assessing risks and hazards during volcanic crises.

### **1.2.3 Erupted volume**

Monitoring volcano extrusion flux is crucial to assessing the rate of magma ascent and understanding the dynamics of volcanic eruptions (Cashman et al., 2013; Ryan et al., 2010). Extrusion flux refers to the rate at which magma is extruded from the volcano's vent during an eruption, which can be used to estimate the volume of erupted materials.

The erupted volume can be estimated from direct measurements, or extrusion flux from ground-based monitoring or satellite-based remote sensing. Direct measurements, such as field mapping, use the thickness and area of tephra deposits to provide estimates erupted volume (e.g., Pyle, 1989; Alfano et al., 2011; Pistolesi et al., 2015). Ground-based monitoring techniques, such as the use of video cameras or thermal imaging, can provide real-time estimates of extrusion flux during an eruption (e.g., Coppola et al., 2015; Coltelli et al., 2017). Satellite-based techniques include the use of Synthetic Aperture Radar (SAR) or comparison between digital elevation models (DEM), which estimates extrusion flux by measuring changes in the shape of the volcano's surface (e.g., Wadge et al., 2012; Delgado et al., 2019; Dualeh et al., 2023). Considering the uncertainties associated

with measuring erupted volume, such as uncertainties in field data and erosion, the estimations are likely to be underestimated.

Variations in extrusion rate can provide insights into changes in magma properties such as rheology (Melnik and Sparks, 1999; Melnik et al., 2005; Rutherford, 2008), and pre-eruptive storage conditions (Popa et al., 2021). Additionally, changes in extrusion rate can provide critical information about the transitions between eruption styles, which is essential for accurately assessing potential hazards associated with an eruption, including the risk of lava flows, pyroclastic flows, and ash fall (e.g., Sparks, 1978; Calder et al., 1999; Cassidy et al., 2018). For example, prior to the 2010 eruption of Merapi volcano, monitoring of extrusion flux from the lava dome was used to assess the magnitude of the eruption and determine the extent of necessary evacuations (Pallister et al., 2013).

While monitoring the volume of erupted material is crucial, measurements are often limited due to the risks of field mapping near an erupting volcano, especially during explosive eruptions. Post-eruption mapping can underestimate the total erupted volume due to uncertainties such as erosion or rainfall. Additionally, it is often challenging to determine the exact volume of material that was erupted on the date of interest, particularly during the beginning of an explosive eruption. While satellite techniques have been useful in quantifying the erupted volume, data availability is limited.

## 1.3 Thermodynamic modelling

Determining the magmatic volatile content at various pressures (and therefore depths) is critical for understanding the physicochemical properties of magma and the behaviour of magmatic systems. The solubility of volatiles in magmas is dependent on various conditions such as pressure, temperature, melt composition and oxygen fugacity (Scaillet and Pichavant, 2005; Duan, 2014). The primary volatile content in the exsolved phase is  $\text{CO}_2$  as it has a low solubility compared to  $\text{H}_2\text{O}$ , but the exsolved phase can become enriched with  $\text{H}_2\text{O}$  at shallow pressures (e.g., Holloway and Blank, 1994; Dixon et al., 1995; Papale, 2005). At equilibrium, a fraction of the volatiles are dissolved in the magma, while the remaining fraction are in the exsolved phase (Scaillet and Pichavant, 2005).

Exsolved volatiles plays a critical role in the physicochemical properties and the eventual eruption of magma. In particular, exsolved  $\text{H}_2\text{O}$  gas bubbles have high compressibility

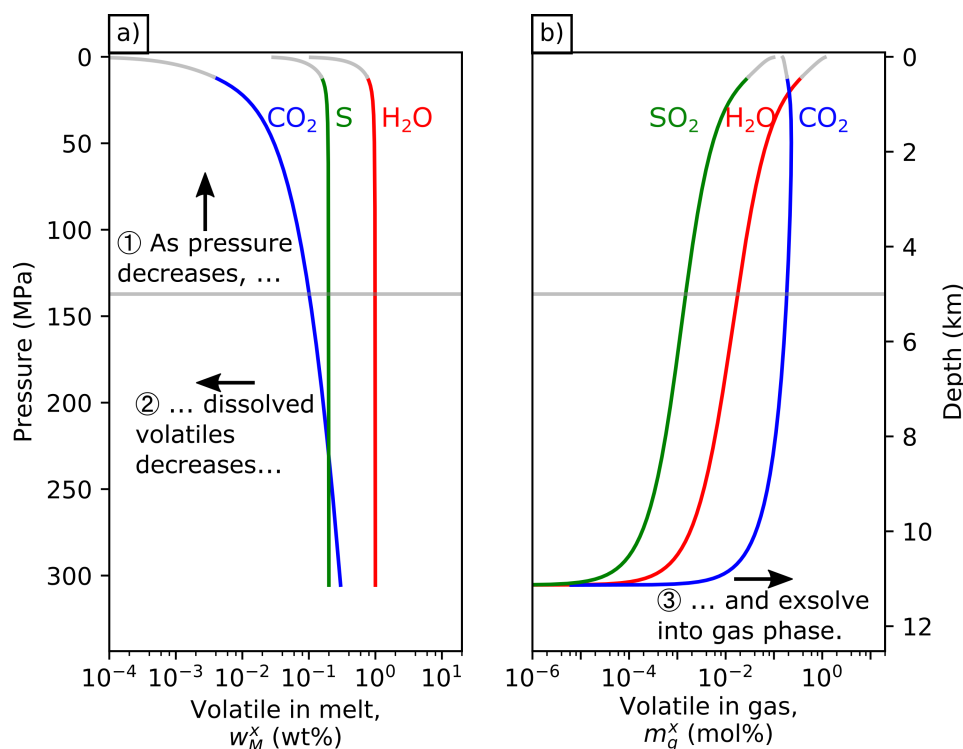


FIGURE 1.2. Examples of inputs and outputs of a thermodynamic model. A thermodynamic model can be initialised using magmatic volatile content, such as  $\text{H}_2\text{O}$ ,  $\text{CO}_2$  and  $\text{S}$ , at a specified pressure/ depth. The thermodynamic model uses solubility constants of volatiles at various pressures to calculate for the (a) weight fraction of dissolved volatile remaining in the melt and the (b) mole fraction of exsolved volatile in gas phase. The annotations are used to guide the reader on the process of volatile exsolution.

that can accommodate changes in pressure with little volume changes of a reservoir (Agee, 2008; Kilbride et al., 2016; Yip et al., 2022). Compressible magma can expand or contract like a ‘magma sponge’ (Rivalta and Segall, 2008) in response to the injection or withdrawal of magma, which may impede effective volcano monitoring (Biggs and Pritchard, 2017).

While numerous models are available to constrain magma properties (e.g., Papale et al., 2006; Duan, 2014; Burgisser et al., 2015; Wieser et al., 2022; Allison et al., 2022), it is important to select an appropriate model for a specific purpose. Thermodynamic models utilise mass balance and equilibrium constants to determine the mass and composition of the exsolved volatile phase (e.g., Ohmoto and Kerrick, 1977; Gaillard and Scaillet, 2014). The models use solubility laws of each volatile species to determine concentration of each

corresponding volatile species that is exsolved at a particular temperature and pressure (Burgisser et al., 2015). For example, the decrease in reservoir pressure decreases the solubility of volatiles such as  $\text{H}_2\text{O}$  and  $\text{CO}_2$ , and as a result, the dissolved volatiles are exsolved into gas phase (Figure 1.2).

Similarly, it is important to consider sulfur speciation when modelling sulfur degassing. Sulfur in the melt phase ( $\text{S}^{2-}$  and  $\text{S}^{6+}$ ) behaves differently during degassing, and thus influence  $\text{SO}_2$  and  $\text{H}_2\text{S}$  content in high-temperature gas phase (e.g., Zajacz et al., 2012; Zajacz, 2015; Fiege et al., 2015). Recent experiments that have provided insights into sulfur partition coefficients in magmas (e.g., Zajacz et al., 2012; Fiege et al., 2015; Nash et al., 2019; Gennaro et al., 2020) should be taken into account when selecting an appropriate thermodynamic model, as they are not included into many existing model calibration.

In this study, I employ the Python degassing model EVo (Liggins et al., 2020, 2022). EVo utilises recently released thermodynamic models including the  $\text{CO}_2$  solubility model of Eguchi and Dasgupta (2018), the sulfide capacity law from O'Neill (2021) and the sulfate capacity law from Nash et al. (2019), which is applicable at pressures of 300 MPa or less, to predict the physicochemical properties of magmas as a function of various input parameters such as melt composition, magmatic volatile content, temperature, pressure, and oxygen fugacity. The model can also be initialised by calculating the saturation pressure for a given composition (e.g., initial gas content = 0%). Every model has limitations, and this model is no exception. This model uses the sulfide capacity law of O'Neill (2021), which is most suitable for more reduced melts than those considered in our study. However, a recent study by Ding et al. (2023), which compared the different sulfide and sulfate capacity laws of Nash et al. (2019) and O'Neill and Mavrogenes (2022), shows that for a given temperature and composition the sulfur degassing pathways are similar regardless of the different laws used. Similarly, the recently published degassing model by Hughes et al. (2023b) shows very similar sulfur degassing behaviour to Sulfur\_X (Hughes et al., 2023a).

Outputs from thermodynamic models, such as melt composition, can be used to understand the physical properties of magma, such as magma density (Spera, 2000) and compressibility (Kilbride et al., 2016; Yip et al., 2022). The magma density calculated by EVo operates on the assumption of the ideal gas law (Liggins et al., 2020, 2022),

which correlates positively with gas density, molar mass, and pressure while inversely correlating with temperature. This assumption is valid for gases such as  $\text{H}_2\text{O}$  and  $\text{CO}_2$  under atmospheric conditions. However, fluids approach or enter the supercritical state at high pressure, which is typical in volcanic systems. In non-ideal states, fluids nearing its critical point experiences a gradual decrease in density and transition from a liquid to a supercritical phase. Supercritical fluids have densities closer to liquids and therefore is less compressible compared to gases. Consequently, this implies that volume changes in supercritical fluids are larger than those observed in gases that obeys the ideal gas law.

By modelling changes in magma properties over time, thermodynamic models can offer valuable insights into the evolution of magmatic systems and transitions in eruptive styles, as well as provide accurate assessments of hazards (Woods, 1995; Degruyter et al., 2012; Cassidy et al., 2018; Joseph et al., 2022). This is crucial for effective hazard mitigation. Additionally, modelling changes in magma composition is essential for understanding the potential hazards associated with volcanic eruptions, such as the risk of explosive eruptions, and predicting the potential for gas emissions, which can pose significant hazards to human health and the environment (Williams-Jones and Rymer, 2015; Edmonds, 2021).

To summarise, thermodynamic modelling of magma properties is critical for understanding the behaviour of magmatic systems and predicting volcanic activity. By utilising empirical data and theoretical calculations to determine magma properties, thermodynamic models can provide valuable insights into the dynamics of volcanic eruptions and the potential hazards associated with them.

## 1.4 Thesis structure

This thesis investigates the magma properties and the corresponding observations of volcanic  $\text{SO}_2$  emissions and deformation using a thermodynamic framework developed over the course of my PhD.

In **Chapter 2**, I develop a Python-based thermodynamic framework for estimating the deformation and gas emissions associated with magmas with different magmatic volatile and gas contents. The framework was integrated with the EVo thermodynamic model and presented as a means to model magma properties such as compressibility,

providing a quantitative link between observations of volcanic deformation and degassing. I explore the parameter space that are known to influence observations of volcanic SO<sub>2</sub> emissions and ground deformation, namely H<sub>2</sub>O, CO<sub>2</sub>, S,  $f_{O_2}$  and crustal shear modulus ( $\mu$ ). The magma properties are modelled using a generic basaltic composition (48 wt% SiO<sub>2</sub>) at a temperature of 1200 °C, and the parameters including magmatic volatile content (H<sub>2</sub>O, CO<sub>2</sub> and S) and oxygen fugacity  $f_{O_2}$  are listed in Table 2.1. I find that magmas with high magmatic H<sub>2</sub>O content exhibit high volumes of exsolved gas in the chamber, leading to high magma compressibility, which results in muted surface deformation during eruptions. The results obtained from exploring the parameter space were extended to natural eruptions. Since volatile content of magmas varies between tectonic settings, the magnitude of ground deformation and the extent of degassing during eruptions. Due to the water-rich nature of arc eruptions, many ground deformation at arc volcanoes are not detected by satellite observations despite being highly explosive. Overall, the thermodynamic framework helped to improve the understanding of the effects of magmatic volatile content and degassing on the physicochemical properties of magma. This chapter is published in *Geochemistry, Geophysics, Geosystems* and has been selected as the Editors' Highlights in *Eos*.

**Chapter 3** further extend the thermodynamic framework developed in the previous chapter to account for pre-eruptive gas segregation, specifically gas accumulation or loss, and its impact on observations of volcanic SO<sub>2</sub> emissions and deformation. The parameters used to model the properties of generic basalts and rhyolites, including the temperature, SiO<sub>2</sub> content, magmatic volatile content (H<sub>2</sub>O, CO<sub>2</sub>, and S), and the oxygen fugacity ( $f_{O_2}$ ), can be found in Table B.1. While reservoir depth and magmatic volatile content influence volume changes of a reservoir, the variation in eruption data suggests that other factors, such as pre-eruptive gas segregation, also have an impact. Using the extended framework, I find that pre-eruptive gas accumulation results in increased SO<sub>2</sub> emissions and reduced co-eruptive deformation, while pre-eruptive outgassing has the opposite effect. Extending my findings to natural systems show that mafic systems exhibit higher co-eruptive volume changes and a wider range of SO<sub>2</sub> emissions than intermediate-silicic systems due to their high volatile diffusivity and tendency for effusive eruptions (co-eruptive degassing). Model predictions indicate that all magmatic systems undergo some degree of outgassing prior to an eruption – the gas content of the reservoir from an eruption is gas-rich when compared to predictions based on melt-inclusion data but partially depleted in gas content when compared to predictions based on fractional



crystallisation. These findings are consistent with models of transcrustal magmatic systems. This chapter is published in *Earth and Planetary Science Letters*.

**Chapter 4** introduces the time component into the thermodynamic framework to investigate the role of evolving magma properties during an eruption and eruptive transitions. I model for a two-layered magma reservoir that has a degassed plug or a gas-rich cap on the upper layer and a magma that had undergone closed-system degassing at the bottom layer. The simulated eruption is that of a generic basaltic composition (48 wt% SiO<sub>2</sub>), and the parameters such as magmatic volatile content, oxygen fugacity, temperature, and pre-eruptive gas segregation constant  $k$  value are listed in Table 4.1. The temporal evolution of the properties of the two-layered magma are determined through a weighted average of the magma on the upper layer and the underlying magma. The model shows that the removal of a degassed plug increases the bulk magma compressibility and suppresses volume change of the reservoir, while the collapse of a gas-rich cap reduces the bulk magma compressibility. I analyse the 2004 eruption of Mount St. Helens and the 2011 eruption of Cordón Caulle, which were determined to have a degassed magma and a gas-rich magma, respectively. The input parameters for the forward models are outlined in Table 4.2-4.3. I used 189 forward models based on the thermodynamic framework to quantify the evolving magma properties of the 2004 eruption of Mount St. Helens. I find that the erupted volume of the extensively degassed magma is  $5.2 \times 10^7 \text{ m}^3$ , which accounts for 0.55 of the total erupted volume. The underlying magma had undergone a certain degree of pre-eruptive degassing, but remains relatively gas-rich compared to the degassed magma. This is consistent with the differences between the total erupted volume and the estimated volume change of the reservoir, which can be explained by magma compressibility.

**Chapter 5** presents preliminary studies conducted on several eruptions using the thermodynamic framework and the time-dependent model. The focus is on demonstrating the capability of the thermodynamic framework to estimate the total SO<sub>2</sub> budget and ground deformation by using melt inclusion data, with the 2011 eruption of Grímsvötn serving as an illustrative example. Next, three eruptions were selected as case studies to demonstrate the application of the time-dependent model in monitoring the temporal changes in magma properties. These case studies showcase the potential benefits and limitations of the time-dependent model. I will also discuss limitations in volcano monitoring data and provide an outlook to the future, offering perspectives to improve the

thermodynamic framework. Lastly, I present a flowchart of a webtool for the thermodynamic framework, which can facilitate volcanologists in utilising the thermodynamic framework to understand magma compressibility and encourage collaboration between volcanologists.

Finally, **Chapter 6** summarises the main results of the thermodynamic framework and the time-dependent model, highlighting their implications for volcano monitoring. The chapter concludes by emphasising the potential of utilising satellite data for near-real-time monitoring of magma properties, which can significantly enhance our understanding of volcanic processes and contribute to the improvement of early warning systems for volcanic activity.



## Chapter 2

# Contrasting volcanic deformation in arc and ocean island settings due to exsolution of magmatic water

Published in *Geochemistry, Geophysics, Geosystems*:

**Yip, S. T. H.**, Biggs, J., Edmonds, M., Liggins, P., & Shorttle, O. (2022). Contrasting volcanic deformation in arc and ocean island settings due to exsolution of magmatic water. <https://doi.org/10.1029/2022GC010387>

Featured in EOS:

<https://eos.org/editor-highlights/why-do-arc-volcanoes-deform-less-than-ocean-island-volcanoes>

**Author contribution and declaration:** This chapter is supervised by J. Biggs and M. Edmonds. J. Biggs and M. Edmonds assisted with the development of the thermodynamic framework. P. Liggins developed the thermodynamic model EVo, supervised by O. Shorttle, and provided training and support for using EVo. P. Wallace, M. Pritchard, K. Cashman, J. Gottsmann, A. Rust, and M. Watson also provided useful discussions that improved the quality of this chapter.

### **Abstract**

Two of the most widely observed co-eruptive volcanic phenomena - ground deformation and volcanic outgassing - are fundamentally linked via the mechanism of magma degassing and the development of compressibility, which controls how the volume of magma changes in response to a change in pressure. Here we use thermodynamic models - constrained by petrological data - to reconstruct volatile exsolution and the consequent changes in magma properties. We use the fraction of  $\text{SO}_2$  exsolved during decompression to predict co-eruptive  $\text{SO}_2$  flux and magma compressibility to predict co-eruptive surface deformation (both normalised by erupted volume). We conduct sensitivity tests using properties of typical basalts to assess how varying magma volatile content, crustal properties, and chamber geometry affect co-eruptive deformation and degassing. We find that magmatic  $\text{H}_2\text{O}$  content has the most impact on both  $\text{SO}_2$  flux and volume change. Our findings have general implications for typical basaltic systems in arc and ocean island settings. The higher water content of arc magmas makes them more compressible than ocean island magmas and leads to muted or non-existent deformation being observed during arc eruptions. Our models are consistent with observation: deformation has been detected during 48% of basaltic eruptions in ocean island settings (16/33) during the satellite era (2005-2020), but only 11% of basaltic eruptions in arc settings (7/61).

## 2.1 Introduction

The increasing number of satellite missions launched in the past decade has driven an explosion in data for studying the Earth’s dynamic processes (Chaussard et al., 2013; Morales Rivera et al., 2016; Carn et al., 2017; Furtney et al., 2018; Biggs and Wright, 2020). The array of sensors onboard satellites routinely provide near real-time observations of volcanic eruptions such as SO<sub>2</sub> plumes and clouds (e.g., Carn et al., 2016; Carboni et al., 2016; Ge et al., 2016) and ground deformation (e.g., Biggs and Pritchard, 2017; Ebmeier et al., 2018; Pritchard et al., 2018), both of which are key indicators of eruption progress and may be used to track eruptive activity and understand pre-eruptive magma storage conditions. However, observations reveal that not all volcanoes exhibit pre- or co-eruptive deformation (Rivalta and Segall, 2008; Biggs et al., 2014; Reath et al., 2020); the causes of the wide variation in deformation systematics between volcanoes and between tectonic settings are not well understood (Piochi et al., 2005; Ebmeier et al., 2013b; Chaussard and Amelung, 2014).

Reconciling observations of volcanic deformation and degassing can help identify the conditions that lead to the lack of observations of ground deformation (Kilbride et al., 2016; Reath et al., 2020). The magmatic processes that drive volcanic deformation and degassing are fundamentally linked: exsolution of volatiles from silicate melt in crustal magma reservoirs (during isobaric cooling and crystallisation, also termed as ‘second boiling’, or due to decompression) causes magma to become compressible, thereby allowing it to change its volume in response to pressure perturbations experienced by the magma during eruption and recharge (Woods and Huppert, 2003; Kilbride et al., 2016; Wong et al., 2017; Wong and Segall, 2020). While it is becoming increasingly common to compile multisensor data (e.g., Furtney et al., 2018; Reath et al., 2019, 2020), until recently there has not been a quantitative framework to jointly interpret observations of volcanic deformation and degassing, including CO<sub>2</sub> and SO<sub>2</sub> gas fluxes (Girona et al., 2014; Kilbride et al., 2016; Wong and Segall, 2020).

Thermodynamic models, constrained by petrological data, may be used to calculate the varying proportions of melt, crystals and exsolved volatiles in shallow magmatic reservoirs under a range of pressure, temperature and magma composition conditions (e.g., Papale et al., 2006; Gualda et al., 2012; Burgisser et al., 2015; Liggins et al., 2020, 2022). The total volume of gas emitted during an eruption is a combination of gas stored

in the chamber (generated by decompression prior to reaching the chamber and second boiling), and additional gas exsolved during decompression and ascent from the chamber to the surface. For explosive intermediate and silicic eruptions, it has been proposed that much of the sulfur outgassed is derived from a pre-existing exsolved volatile phase (Wallace, 2001, 2005). For effusive eruptions however, where magma ascends more slowly to the surface, the outgassed sulfur is derived from both second boiling and shallow decompressional degassing. Since the physicochemical properties of magmas are inter-dependent, magma properties such as density and compressibility can be calculated using the law of conservation of mass (Spera, 2000; Huppert and Woods, 2002). The compressibility of magma and the properties of the chamber, including geometry and host rheology, control the co-eruptive volume change, which consequently affects co-eruptive ground deformation at the surface (Dieterich and Decker, 1975; Huppert and Woods, 2002; Edmonds et al., 2019; Head et al., 2019; Zhan and Gregg, 2019; Sigmundsson et al., 2020).

Previous work by Kilbride et al. (2016) introduced a thermodynamic framework for reconciling satellite observations of atmospheric sulfur yield and volcanic deformation during discrete explosive eruptions (where there is assumed to be little volatile exsolution during magma ascent; i.e. all of the outgassed sulfur is derived from a pre-existing volatile phase; (Wallace, 2003)). The framework uses thermodynamic models to illustrate the effect of initial magmatic volatile content ( $\text{H}_2\text{O}$ ,  $\text{CO}_2$ ) and oxygen fugacity on  $\text{SO}_2$  degassing and volcanic deformation. Sensitivity analyses were performed for magma of rhyolitic composition to provide model predictions of magma properties as a function of depth (Kilbride et al., 2016). Kilbride et al. (2016) then compared their model predictions to observations from 11 discrete explosive eruptions to illustrate the factors controlling volcanic deformation and degassing.

In this study, we use a thermodynamic framework to evaluate observations of volcanic deformation between eruptions of arc and ocean island basalts (which have more and less magmatic water respectively, see later for ranges). We extend the thermodynamic framework developed by Kilbride et al. (2016) to enable large-scale analyses, such as sensitivity tests and Monte-Carlo simulations, for basaltic eruptions (see Table 2.1). The sensitivity tests use properties typical for basaltic magmas (i.e., 45-52%  $\text{SiO}_2$ ) to explore how varying initial magmatic volatile contents ( $\text{H}_2\text{O}$ ,  $\text{CO}_2$ , S) and oxygen fugacity affect magma properties such as density and compressibility, and consequently volcanic

deformation and degassing. We also consider the effects of variable crustal shear modulus  $\mu$  and chamber geometry on co-eruptive volcanic deformation. Finally, we compare the properties of basaltic magmas from arc and ocean island settings arising from their different volatile contents using Monte-Carlo simulations and discuss the implications for satellite observations of deformation during eruptions in different tectonic settings.

## **2.2 Background: Observations Of Volcanic Deformation and Degassing**

Satellites with short repeat time and high spatial resolution provide consistent spatio-temporal coverage for monitoring volcanoes on regional to global scales (e.g., TerraSAR-X, Sentinel-1), which is particularly valuable for monitoring volcanoes with few or no ground-based stations (e.g., Telling et al., 2015; Carboni et al., 2016; Ebmeier et al., 2016; Delgado et al., 2017; Pritchard et al., 2018; Coppola et al., 2020). Interferometric Synthetic Aperture Radar (InSAR) is a satellite technique that measures the phase change between pairs of satellite radar images to generate maps of surface displacement, which may be used to monitor volcanoes exhibiting deformation in response to changes in magma activity. However, while many volcanoes exhibit pre-eruptive inflation associated with magma intrusion and/or co-eruptive deflation during magma withdrawal, some do not (Moran et al., 2006; Rivalta and Segall, 2008; Biggs and Pritchard, 2017; Ebmeier et al., 2018). One possible cause of the lack of deformation is the presence of an exsolved gas phase in the magma at chamber depths that is more compressible than the surrounding crust and silicate melt (Huppert and Woods, 2002; Woods and Huppert, 2003; Kilbride et al., 2016).

The most volumetrically significant volcanic volatile species produced during an eruption are  $\text{H}_2\text{O}$  and  $\text{CO}_2$ , yet it is difficult to distinguish these volatiles from atmospheric background in satellite measurements. In contrast, volcanic  $\text{SO}_2$  has a strong absorption signal in the near-ultraviolet and infrared spectrum, and thus can be measured using satellite-based spectrometers (e.g., Carn et al., 2016; Carboni et al., 2016). The total mass of  $\text{SO}_2$  emitted from a volcano is the integrated sum of degassing in the chamber and during ascent of magma to the surface.

Conceptual models of magmatic systems may be used to understand different degassing configurations and their impact on monitoring signals (Figure 2.1). Volatiles including



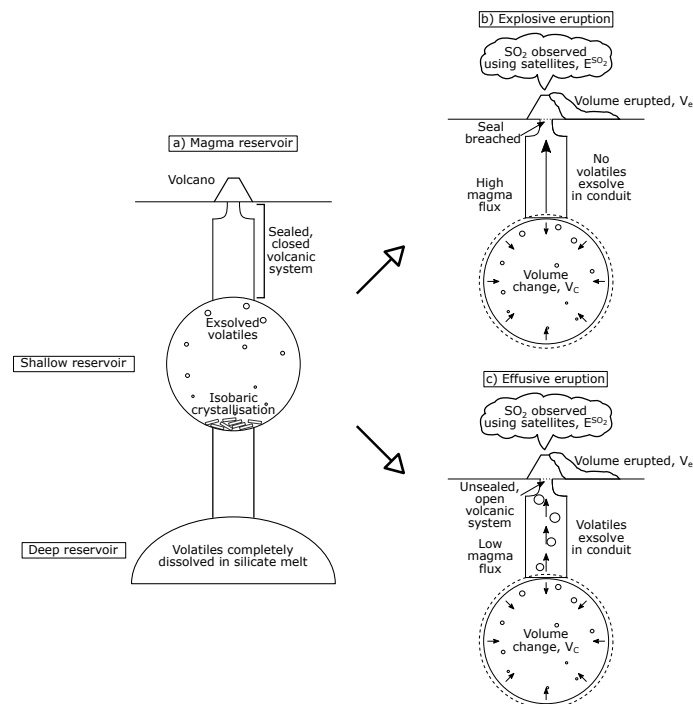


FIGURE 2.1. Conceptual model of magma degassing during eruptions of different styles. (a) Volcano with chambers at different depths, prior to an eruption. Magmatic volatiles are more soluble in deep magmatic chambers and thus a higher proportion of the total volatile load will be dissolved in the silicate melt. In the shallow chamber (at a lower pressure) there is a higher proportion of exsolved volatiles, with degassing being driven both by decompression as magma moves up from the lower chamber, and by isobaric cooling and crystallisation. (b) During explosive eruptions of silicic magmas, magma is removed from the chamber and decompressed rapidly, with little volatile exsolution during magma ascent. Much of the volatiles emitted as gases during the eruption represents a pre-eruptive exsolved volatile phase that was present in the chamber prior to decompression (and which made the magma compressible). In this ‘explosive’ case we expect the volume change inferred from ground deformation at the surface to be related to the amount of volatiles emitted during eruption (both normalised by erupted volume). (c) Effusive eruptions, on the other hand, are characterised by a low magma ascent rate between the chamber and the surface, allowing extensive volatile exsolution in the conduit, i.e., co-eruptive degassing. The volcanic gases observed at the surface are mostly derived from decompressional degassing and do not constrain the compressibility of the chamber. In this ‘effusive’ case, we do not expect a relationship between the amount of gases released during the eruption and the volume change inferred for the ‘source’ chamber during eruption.

H<sub>2</sub>O, CO<sub>2</sub> and SO<sub>2</sub>, are more soluble at higher pressures and hence they are largely dissolved in silicate melt in deep magmatic systems (Figure 2.1a). Volatiles exsolve during magma decompression, but if magma stalls in a chamber and cools, volatiles also exsolve during isobaric cooling and crystallisation, a process termed ‘second boiling’ (Candela and Piccoli, 1998).

For an explosive eruption, the high magma ascent rate limits volatile exsolution between the chamber and the surface (Figure 2.1b) and we make the simplifying assumption here that the gas emitted during the eruption is sourced entirely from the pre-eruptive exsolved volatile phase. In this case the amount of gases released (per unit of magma erupted) may be used to constrain the compressibility of the magma in the chamber prior to eruption, which will be related to the amount of deformation observed. In contrast, effusive eruptions involve a low magma ascent rate, such that volatiles exsolve extensively in the conduit (Figure 2.1c). In this case, the gases released during eruptions are mostly produced during magma ascent and cannot simply be related to the properties of the magma in the chamber prior to eruption without careful reconstruction of the degassing process using a thermodynamic model. Owing to the high diffusivity of volatiles in basaltic melts at high temperature, basaltic magma is likely to undergo extensive degassing during shallow magma ascent and eruption (e.g., Zhang and Stolper, 1991; Sigmarsson et al., 2013; Hurwitz and Anderson, 2019).

## **2.3 Methodology**

### **2.3.1 Thermodynamic modelling**

Volatile solubility can be defined as the concentration of a volatile species that may be dissolved in magma at a particular set of pressure, temperature, melt composition and oxygen fugacity conditions (e.g., Scaillet and Pichavant, 2005; Duan, 2014; Burgisser et al., 2015). At equilibrium, the fugacity of each volatile species in the melt is equal to its fugacity in the fluid (Scaillet and Pichavant, 2005), such that a fraction of volatiles are dissolved in magma and the remainder are exsolved in the gas phase. Since magmatic volatiles are less soluble at low pressure, magma decompression is a principal driver for volatile exsolution (e.g., Papale, 1999; Duan, 2014; Burgisser et al., 2015).

Thermodynamic models based on mass balance and equilibrium constants may be used

to calculate the mass and composition of the exsolved volatile phase in the chamber and this may be then used to estimate bulk magma properties such as density and compressibility (Ohmoto and Kerrick, 1977; Gaillard and Scaillet, 2014). The concentration of each volatile species exsolved at any given pressure and temperature can be calculated using its corresponding solubility laws (e.g., Burgisser et al., 2015). Here, we use the Python degassing model EVo, as implemented in EVolve (Liggins et al., 2020, 2022), which uses the H<sub>2</sub>O and CO<sub>2</sub> solubility constants from Burgisser et al. (2015), along with the sulfide capacity law of O'Neill (2021) and the sulfate solubility model of Nash et al. (2019), to predict the physicochemical properties of basaltic magma, such as the composition of the gas phase and magma density, as a function of melt composition, magmatic volatile content, oxygen fugacity of magma, temperature and pressure. We note there are limitations in this model for predicting sulfur behaviour, in that it uses the sulfide capacity law of O'Neill (2021) that is more appropriate for sulfur in more reduced melts than those considered here, and the lack of sulfate capacity law that limits the accuracy of the model at high  $f_{\text{O}_2}$  conditions (Liggins et al., 2020, 2022).

We use EVo to calculate magma and fluid compositions in the C-O-H-S-Fe system during magma decompression (Liggins et al., 2020, 2022). We initialise the model using the weight fraction of the volatile species H<sub>2</sub>O, CO<sub>2</sub> and S as input parameters. The oxygen fugacity ( $f_{\text{O}_2}$ ) is adjusted relative to the Ni-NiO buffer (NNO). EVo can be initialised by either 1) specifying starting pressure ( $p$ ), and gas weight fraction ( $w_g$ ), or 2) calculating the saturation pressure for the given composition (i.e.,  $w_g \approx 0$  wt%). Here we use the saturation point based on melt composition to find an appropriate starting pressure/depth (Liggins et al., 2022). We do not consider the processes of crystallisation or magma recharge implicitly in our model, for simplicity.

At a specified depth, the gas volume fraction ( $V_g$ ) is controlled by the total gas weight fraction ( $w_g$ ) and gas density ( $\rho_g$ ):

$$V_g = \left(1 + \frac{MP(1 - w_g)}{RT\rho_M w_g}\right)^{-1}, \quad (2.1)$$

where  $M$  is the average molar mass of the gas phase,  $R$  is the universal gas constant (8.31 J mol<sup>-1</sup> K<sup>-1</sup>) and  $\rho_M$  is the volatile-free magma density (e.g., Burgisser et al., 2015). Magma density ( $\rho_m$ ) is a function of the density and volume fraction of both melt and gas (Spera, 2000):

$$\rho_m = \rho_g V_g + \rho_M (1 - V_g). \quad (2.2)$$

$V_g$  increases during magma decompression and hence decreases  $\rho_m$ . Since  $\rho_m$  changes with  $p$ , magma compressibility ( $\beta_m$ ) can be linked to the density and density gradient of magma with respect to pressure (Huppert and Woods, 2002):

$$\beta_m = \frac{1}{\rho_m} \frac{\delta \rho_m}{\delta p}. \quad (2.3)$$

Given how  $\rho_m$  changes with  $V_g$ , magma compressibility is dominated by the weight fraction of exsolved gas phase and hence magmatic volatile content (Kilbride et al., 2016; Edmonds et al., 2018).

Permeability develops when gas bubbles coalesce to form porous networks, thereby allowing exsolved volatiles to percolate through magma efficiently (Lowenstern, 1994; Candela, 1997; Bachmann and Bergantz, 2006; Collins et al., 2009; Lindoo et al., 2017). Magma becomes permeable when it reaches critical porosity, which is also defined as the percolation threshold ( $\phi_c$ ). In this study, we use gas volume fraction ( $V_g$ ) to represent magma porosity and assume that magma becomes permeable and degasses as it reaches the percolation threshold. The value of  $\phi_c$  is widely variable, ranging from  $\sim 17$ -78 vol%, due to the complex interplay between magma properties and physical processes such as melt viscosity and decompression rate (Rust and Cashman, 2011; Burgisser et al., 2017; Colombier et al., 2020). For melts with low viscosity and overpressure, such as the basaltic melts considered here, bubbles can grow and rise buoyantly, which reduce the likelihood of the bubbles coalescing to form a porous network. Colombier et al. (2020) suggest that low viscosity melts would become permeable at  $\phi_c > 37$  vol% and we use that threshold here.

## 2.3.2 Linking magma properties to observable parameters

### 2.3.2.1 Deformation

Observations of subsurface volume change (derived from inverting measurements of surface deformation) may be compared to the model of magma properties during degassing. We define the normalised volume change,  $\bar{V}$ , as the ratio between the subsurface volume change ( $\Delta V_c$ ) and the volume erupted ( $V_e$ ; assuming dense-rock equivalent, DRE):

$$\bar{V} = \frac{\Delta V_c}{V_e} = (1 + \frac{\beta_m}{\beta_c})^{-1}, \quad (2.4)$$

where  $\beta_m$  is magma compressibility and  $\beta_c$  is chamber compressibility (Rivalta and Segall, 2008; Kilbride et al., 2016). Note that the definition of  $\bar{V}$  is the inverse of that from Kilbride et al. (2016), i.e.,  $r = \bar{V}^{-1}$ . In an elastic half-space, chamber compressibility is affected by host rock properties and chamber geometry, which can be defined as

$$\begin{aligned} \text{Spherical point source: } \beta_c &= \frac{3}{4\mu} \\ \text{Prolate chamber: } \beta_c &= \frac{1}{\mu} \\ \text{Horizontal oblate ellipsoid (sill): } \beta_c &= \frac{1}{\mu} \left( \frac{a}{c} \frac{3}{2\pi} - \frac{3}{5} \right) \end{aligned} \quad (2.5)$$

where  $\mu$  is the shear modulus of the crust and  $\frac{a}{c}$  is the ratio of major to minor semi-axes of an oblate ellipsoid (Amoruso and Crescentini, 2009; Anderson and Segall, 2011).

For compressible magmas,  $\Delta V_c$  would be less than  $V_e$  (i.e.,  $\bar{V} < 1$ ), such that compressible magmas with low  $\beta_c/\beta_m$  have low volume change per unit erupted (Voight et al., 2010), while  $\Delta V_c$  would be approximately equal to  $V_e$  (i.e.,  $\bar{V} \approx 1$ ) for incompressible magmas and high  $\beta_c/\beta_m$ . Since chamber geometry and host rock properties also affect  $\beta_c$  and hence the magnitude of  $\bar{V}$ , volcanoes with compressible magmas and rigid surrounding crust (i.e., high  $\mu$  and low  $\beta_c$ ) cause small volume changes during an eruption (Rivalta and Segall, 2008; Kilbride et al., 2016).

A directly observable parameter is surface deformation. Here we define normalised displacement  $\bar{z}$  as the maximum vertical displacement per unit volume erupted (i.e. located directly above the source). For simplicity, we only calculate the normalised displacement for a spherical point source in a uniform and elastic half-space (Mogi, 1958),  $\bar{z} = \bar{V} \frac{1-v}{\pi} \frac{1}{d^2}$ , where  $v$  is Poisson's ratio and  $d$  is the depth of magma chamber, although other models are also available (e.g., Okada, 1985; Yang et al., 1988; Fialko et al., 2001; Masterlark, 2003; Albino et al., 2019; Zhan et al., 2019).

### 2.3.2.2 Degassing

Observations of  $\text{SO}_2$  degassing are made by satellite-based sensors (e.g., Prata and Kerkmann, 2007; Carn et al., 2016; Theys et al., 2019). We define normalised  $\text{SO}_2$  ( $\bar{S}$ ) as

the observed  $\text{SO}_2$  emitted ( $E^{\text{SO}_2}$ ), normalised by the volume of magma erupted ( $V_e$ ).  $\bar{S}$  estimates the mass of  $\text{SO}_2$  per unit volume of magma:

$$\bar{S} = \frac{E^{\text{SO}_2}}{V_e} = \frac{m^{\text{SO}_2} M^{\text{SO}_2} \rho_e w_g}{M_g}, \quad (2.6)$$

where  $m^{\text{SO}_2}$  is the mole fraction of  $\text{SO}_2$  in gaseous phase,  $M^{\text{SO}_2}$  is the molecular mass of  $\text{SO}_2$ ,  $\rho_e = 2800 \text{ kg m}^{-3}$  is the erupted rock density typical for basalts (Stolper and Walker, 1980; Wu et al., 2020), and  $M_g$  is the mean molecular mass of the gas phase. We consider all sulfur species in the degassing model, but we extract the  $\text{SO}_2$  flux to compare to observations. For explosive eruptions, we assume that the mass of  $\text{SO}_2$  emissions at the surface ( $E^{\text{SO}_2}$ ) is the same as the mass of  $\text{SO}_2$  in equilibrium with magma at chamber depth, meaning that there is no additional degassing as magma rises from the chamber to the surface (Figure 2.1b). For effusive eruptions, volatiles exsolve in the conduit as magma ascends slowly such that  $\text{SO}_2$  degassing is dominated by co-eruptive degassing (Figure 2.1c). For simplicity, we assume all exsolved  $\text{SO}_2$  is emitted as  $\text{SO}_2$  in the plume (i.e., there are no other sulfur-bearing species present) and that all  $\text{SO}_2$  can be detected by satellites. We ignore sulfur loss due to leaching, sulfur scrubbing by hydrothermal systems, and the formation of sulfide globules during sulfide saturation. We note that these assumptions may break down during some eruptions, which has been demonstrated for the 2011 eruption of Grimsvötn (Sigmarsson et al., 2013) and the 2018 eruption of Kilauea (Wieser et al., 2020).

## 2.4 One-at-a-time Sensitivity Tests

In this section, we explore the sensitivity of the calculated magma properties to initial magmatic  $\text{H}_2\text{O}$  content ( $w^{\text{H}_2\text{O}}$ ), magmatic  $\text{CO}_2$  content ( $w^{\text{CO}_2}$ ), oxygen fugacity ( $f_{\text{O}_2}$ ), magmatic S content ( $w^{\text{S}}$ ), crustal shear modulus ( $\mu$ ) and chamber geometry. We conduct one-at-a-time sensitivity tests by holding other parameters constant and varying the chosen parameter. The ranges in each parameter were chosen to represent the natural variation within typical basalts (45-52%  $\text{SiO}_2$ ). For each example, we first consider the general sensitivity of the model to changing magma properties by looking at the greatest percentage changes over a range of depths, and then provide an illustrative example for a chamber at a depth of 5 km (i.e., pressure of 137 MPa). While this provides a clear understanding of the role of each parameter, it does not consider the co-dependence of input variables, which may result in parameter combinations that are not physically

## CHAPTER 2. CONTRASTING VOLCANIC DEFORMATION IN ARC AND OCEAN ISLAND SETTINGS DUE TO EXSOLUTION OF MAGMATIC WATER

TABLE 2.1. Parameter space used for sensitivity tests (Section 2.4) and Monte Carlo simulations of arc and ocean island basalts (Section 2.5.1): initial  $\text{H}_2\text{O}$ ,  $\text{CO}_2$  and S contents, and oxygen fugacity ( $f_{\text{O}_2}$ ). The sensitivity tests vary the chosen parameter (bracketed) while holding all other parameters constant (unbracketed).

Parameters	$\text{H}_2\text{O}$ (wt%)	$\text{CO}_2$ (ppm)	$f_{\text{O}_2}$	S (ppm)
Sensitivity test	2.0 (1.0-3.0)	3000 (1000-5000)	NNO (NNO – 1-NNO + 2)	2000 (1000-3000)
Arc basalts	$3.9 \pm 0.4$	$4000 \pm 1000$	$3000 \pm 1000$	$\text{NNO} + 1.4 \pm 1$
Ocean island basalts	$1.0 \pm 0.2$	$6500 \pm 3500$	$1600 \pm 1000$	$\text{NNO} + 0.7 \pm 0.9$

realistic.

Bulk magma volatile contents are informed by observations of dissolved volatile content from melt inclusions of basalts. For simplicity, we assume an isothermal magma at 1200 °C. We use values of  $w^{\text{H}_2\text{O}}$ ,  $w^{\text{CO}_2}$  and  $w^{\text{S}}$  that are typical for basaltic magmas (e.g., Wallace, 2005; Ruscitto et al., 2012; Plank et al., 2013), in the ranges of 1.0 to 3.0 wt%  $\text{H}_2\text{O}$ , 1000 to 5000 ppm  $\text{CO}_2$ , and 1000 to 3000 ppm S, respectively (Table 2.1). We use  $f_{\text{O}_2}$  from NNO–1 to NNO+2, which are calibrated for basaltic systems (Konecke et al., 2019), to explore the effects of oxygen fugacity on the solubility of volatile species. Since  $f_{\text{O}_2}$  has a minimal effect on both  $\text{H}_2\text{O}$  and  $\text{CO}_2$  concentrations over the range we consider, we expect that varying  $f_{\text{O}_2}$  will primarily affect the proportions of  $\text{H}_2\text{S}$  and  $\text{SO}_2$  in the vapour phase.

To test how chamber compressibility ( $\beta_c$ ) affects volcanic deformation, we use  $\mu$  from 0.1 to 30 GPa (Heap et al., 2020), and consider three chamber geometries: a spherical point source, a vertical prolate ellipsoid (pipe-like chamber) and a horizontal oblate ellipsoid (sill) (Gudmundsson, 2008; Amoroso and Crescentini, 2009; Anderson and Segall, 2011). Although we do not expect the gas to remain in contact with the magma when  $V_g$  exceeds the percolation threshold at which magma becomes permeable, i.e.,  $\phi_c > 37$  vol% (Colombier et al., 2020), we run our sensitivity tests all the way to the surface. This is because basaltic magmas have high volatile diffusivities due to high temperature and the sulfur left dissolved in the melt may continue to exsolve during ascent such that the actual amount of  $\text{SO}_2$  emitted is in equilibrium with surface pressure. Table 2.2 summarises the greatest percentage change over the depth range of each parameter for the estimated values of  $\bar{S}$ ,  $\bar{V}$  and  $\bar{z}$ .

TABLE 2.2. Summary of sensitivity tests showing the greatest percentage change of each observation and the depth at which it occurred. To conduct the sensitivity tests, we increase the value of each parameter (shown in brackets) while holding other parameters constant. For example, when increasing  $\text{H}_2\text{O}$  wt% from 1.0 to 3.0, initial  $\text{CO}_2$ ,  $S$ ,  $f_{\text{O}_2}$  and  $\mu$  are kept constant. Please refer to Table 1 for details of the parameter space

Parameters	% Change in normalised $\text{SO}_2$ , $\bar{S}$	Depth (km)	% Change in normalised volume change, $\bar{V}$	Depth (km)	% Change in normalised displacement, $\bar{z}$	Depth (km)
Magmatic $\text{H}_2\text{O}$ , $w^{\text{H}_2\text{O}}$ (1.0-3.0 wt%)	+170%	0.51 km	-68%	3.5 km	-83%	1.8 km
Magmatic $\text{CO}_2$ , $w^{\text{CO}_2}$ (1000-5000 ppm)	+180%	1.5 km	-53%	3.3 km	-58%	2.8 km
Oxygen fugacity, $f_{\text{O}_2}$ (NNO-1-NNO+2)	+183%	surface	+4.3%	3.7 km	+4.8% 4.2 km	
Magmatic $S$ , $w^S$ (1000-3000 ppm)	+109%	surface	< -1.0%	surface	< -1.0%	surface
Crustal shear modulus, $\mu$ (0.1-30 GPa)	n/a	n/a	-94%	4 km	-100%	surface



### 2.4.1 Effects of H<sub>2</sub>O content on magma properties

First, we vary the initial dissolved H<sub>2</sub>O content ( $w^{\text{H}_2\text{O}}$ ) in the melt and investigate how it affects magma properties  $\rho_m$  and  $\beta_m$ , and observables  $\bar{S}$ ,  $\bar{V}$  and  $\bar{z}$  (Figure 2.2). In this sensitivity test,  $w^{\text{H}_2\text{O}}$  ranges from 1.0-3.0 wt% and the constant parameters are  $w^{\text{CO}_2} = 3000$  ppm,  $f_{\text{O}_2} = \text{NNO}$ ,  $w^{\text{S}} = 2000$  ppm. We assume a fixed chamber compressibility for a spherical cavity (Equation 5) where  $\mu = 2.1$  GPa (i.e.,  $\beta_c = 3.6 \times 10^{-10} \text{ Pa}^{-1}$ ).

Solubility decreases with decreasing pressure for each volatile component, so as pressure decreases, the mass fraction dissolved in the melt ( $w_M^x$ ) decreases and the mole fraction that has exsolved to the gaseous phase ( $m_g^x$ ) increases (Figure 2.2a-b). Higher  $w^{\text{H}_2\text{O}}$  reduces the solubility of CO<sub>2</sub> and S (Figure 2.2a), thus increasing the mole fraction of  $m_g^{\text{H}_2\text{O}}$ ,  $m_g^{\text{CO}_2}$  and  $m_g^{\text{S}}$  (Figure 2.2b). Normalised SO<sub>2</sub> ( $\bar{S}$ ) represents the mass of exsolved SO<sub>2</sub> per unit volume of magma, assuming that the exsolved SO<sub>2</sub> remains in the bulk magma and does not segregate. By increasing  $w^{\text{H}_2\text{O}}$  by a factor of 3,  $\bar{S}$  increases up to a maximum of  $\sim 170\%$  at 0.51 km depth (Figure 2.2c). Gas volume fraction ( $V_g$ ) increases as volatiles exsolve and gas bubbles expand at lower pressures. Since  $V_g$  is dominated by  $w^{\text{H}_2\text{O}}$ ,  $V_g$  increases up to a maximum of  $\sim 210\%$  at 0.65 km depth when increasing  $w^{\text{H}_2\text{O}}$  from 1.0 to 3.0 wt% (Figure 2.2d).

The increase in  $w^{\text{H}_2\text{O}}$  increases  $V_g$ , which decreases magma density ( $\rho_m$ ; Equation 2.2; Figure 2.2e) and increases magma compressibility ( $\beta_m$ ; Equation 2.3; Figure 2.2f). Therefore, with the increase of  $w^{\text{H}_2\text{O}}$  from 1-3 wt%,  $\beta_m$  increases up to a maximum of  $\sim 650\%$  at 2.1 km depth (Figure 2.2f), and normalised volume change ( $\bar{V}$ ) decreases up to a maximum of  $\sim 68\%$  at 3.5 km depth (Figure 2.2g). Based on the simple Mogi model, there is a trade-off between volume change and depth, such that the same volume change will cause a larger displacement at a shallow depth. However, when  $V_g$  and  $\beta_m$  are considered, the maximum vertical displacement per unit volume ( $\bar{z}$ ) does not vary in a simple way; the increase in  $V_g$  towards the surface causes a local minimum in  $\bar{z}$  at 0.5 km depth. Given that  $\bar{z}$  is controlled by chamber depth and  $\bar{V}$ , increasing  $w^{\text{H}_2\text{O}}$  thus causes a relative decrease in the normalised displacement ( $\bar{z}$ ) up to a maximum of  $\sim 83\%$  at 1.8 km depth (Figure 2.2h).

To illustrate these results, we give specific values for a chamber depth of 5 km. Varying  $w^{\text{H}_2\text{O}}$  from 1.0 to 3.0 wt% increases  $\bar{S}$  from  $0.064 \text{ kgm}^{-3}$  to  $0.16 \text{ kgm}^{-3}$  (Figure 2.2c).  $V_g$  increases from 1.2 vol% to 2.8 vol%, which corresponds to the increase in  $\beta_m$  from

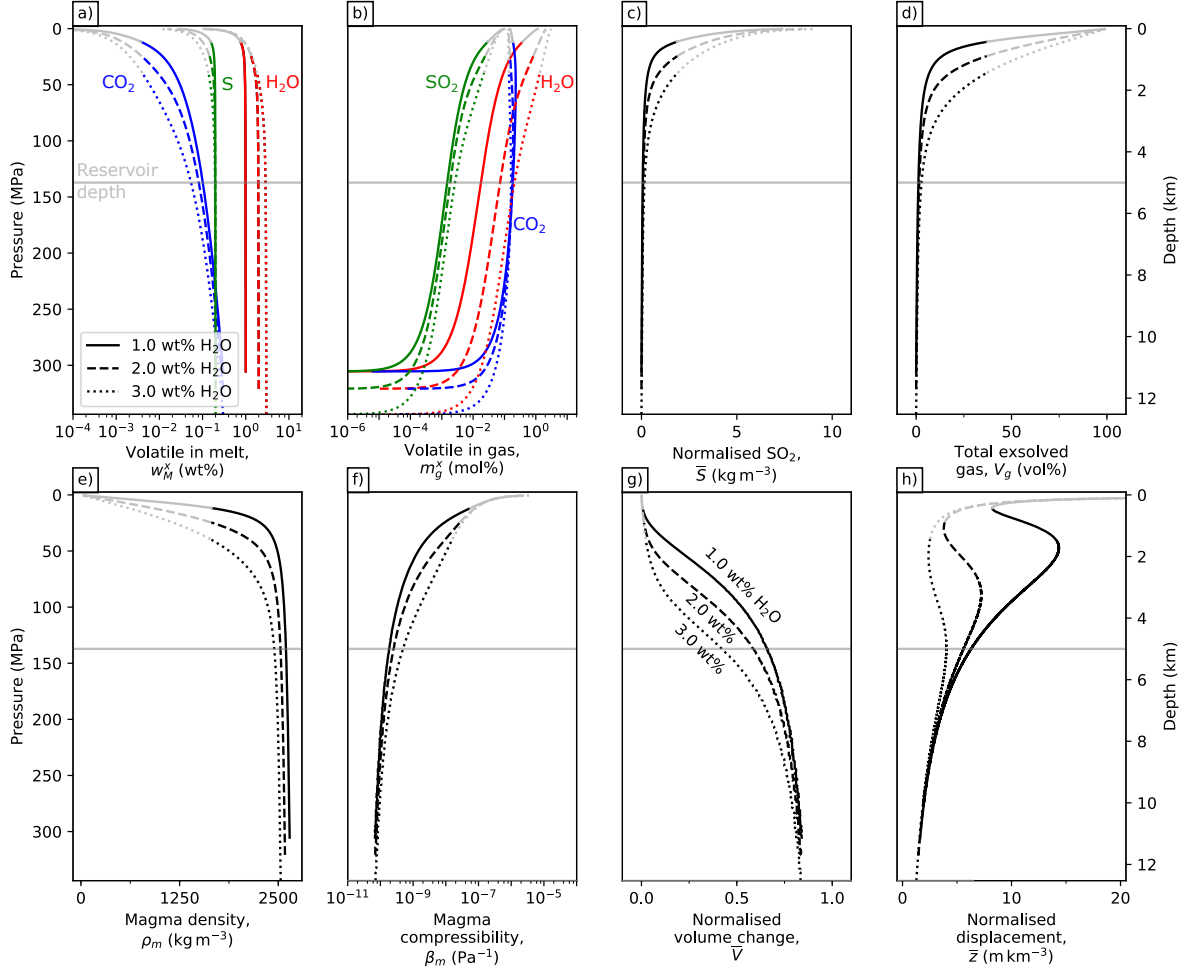


FIGURE 2.2. Physicochemical properties of basalts when varying the initial magmatic  $\text{H}_2\text{O}$  from 1.0-3.0 wt%. (a) Weight fraction of dissolved  $\text{H}_2\text{O}$ ,  $\text{CO}_2$  and S in melt ( $w_M^x$ ). (b) Mole fraction of exsolved  $\text{H}_2\text{O}$ ,  $\text{CO}_2$  and  $\text{SO}_2$  in gas ( $m_g^x$ ). (c) Mass of  $\text{SO}_2$  gas per unit volume of magma, also defined as normalised  $\text{SO}_2$  ( $\bar{S}$ ). (d) Volume fraction of exsolved gases in magma ( $V_g$ ). (e) Magma density ( $\rho_m$ ). (f) Magma compressibility ( $\beta_m$ ). (g) Model predicted volume change normalised by unit volume of magma ( $\bar{V}$ ). (h) Maximum vertical displacement normalised by unit volume of magma ( $\bar{z}$ ). Panels a, b, d and e show magma properties as a function of depth and panels c, g and h represent the model value for a unit volume of magma that instantaneously erupted from a particular depth. The grey lines represent magma properties after exceeding percolation threshold  $\phi_c = 37$  vol%. Fixed parameters:  $w^{\text{CO}_2} = 3000$  ppm,  $f_{\text{O}_2} = \text{NNO}$ ,  $w^{\text{S}} = 2000$  ppm and  $\mu = 2.1$  GPa.

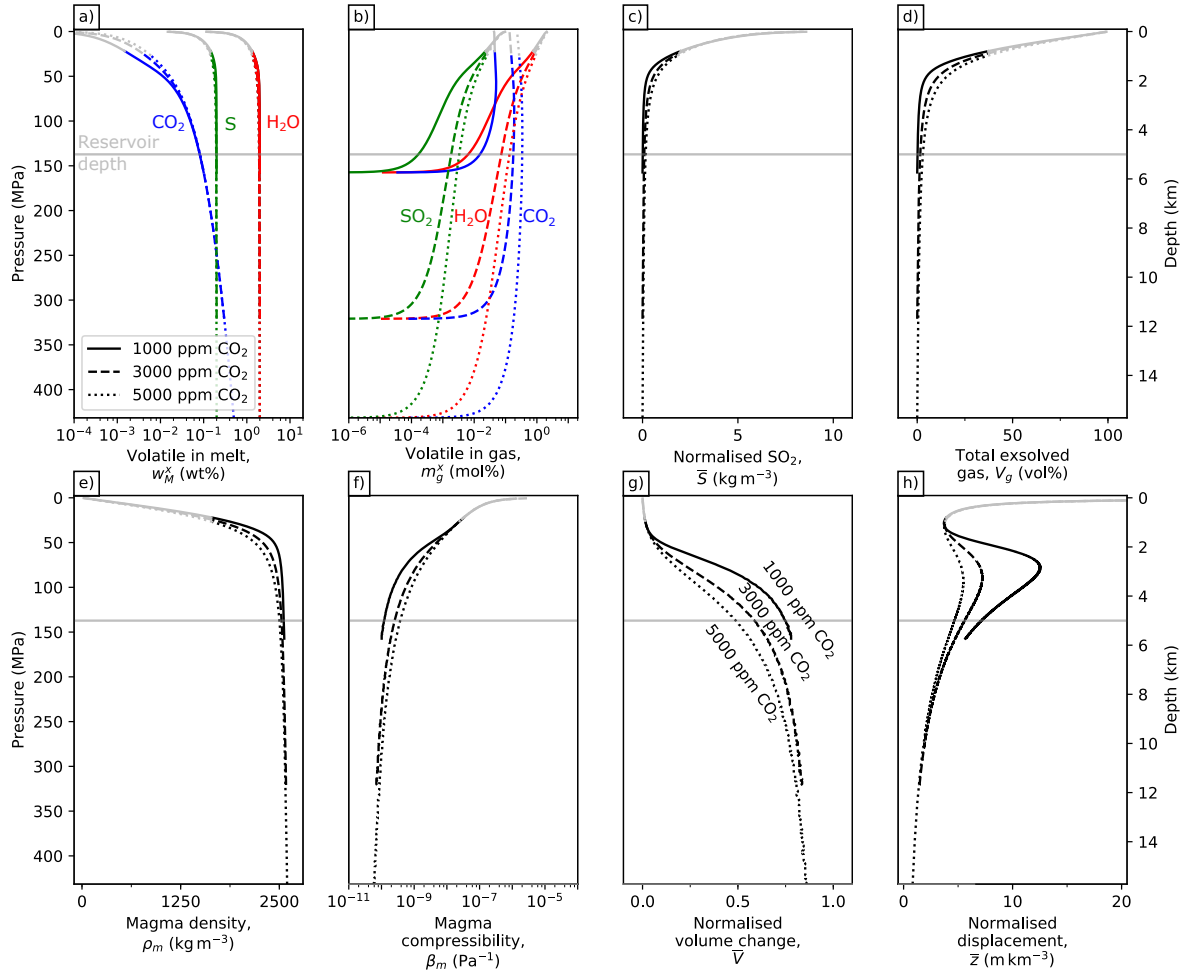


FIGURE 2.3. Physicochemical properties of basalts when varying the initial weight fraction of dissolved CO<sub>2</sub> ( $w^{\text{CO}_2}$ ) from 1000 to 5000 ppm. Same general format as for Figure 2.2. Fixed parameters:  $w^{\text{H}_2\text{O}} = 2.0$  wt%,  $f_{\text{O}_2} = \text{NNO}$ ,  $w^{\text{S}} = 2000$  ppm and  $\mu = 2.1$  GPa.

$1.9 \times 10^{-10} \text{ Pa}^{-1}$  to  $4.9 \times 10^{-10} \text{ Pa}^{-1}$  (Figure 2.2f). As a result,  $\bar{V}$  decreases from 0.65 to 0.42 (Figure 2.2g) and  $\bar{z}$  is reduced from  $6.3 \text{ m km}^{-3}$  to  $4.0 \text{ m km}^{-3}$  (Figure 2.2h). The model thus predicts that basalts with high initial H<sub>2</sub>O content have high  $\bar{S}$  and  $\beta_m$ , and as a result, low  $\bar{V}$  and  $\bar{z}$  (Figure 2.2).

## 2.4.2 Effects of CO<sub>2</sub> content on magma properties

Here, we vary the initial dissolved CO<sub>2</sub> content in the magma to understand how it affects magma properties and observables  $\bar{S}$ ,  $\bar{V}$  and  $\bar{z}$  (Figure 2.3). We use  $w^{\text{CO}_2}$  in the

range of 1000 to 5000 ppm and fixed  $w^{\text{H}_2\text{O}} = 2.0$  wt%,  $f_{\text{O}_2} = \text{NNO}$ ,  $w^{\text{S}} = 2000$  ppm and  $\mu = 2.1$  GPa for this model.

Figure 2.3a shows that increasing  $w^{\text{CO}_2}$  from 1000 to 5000 ppm increases the amount of dissolved  $w_M^{\text{CO}_2}$  up to a maximum of 73% at 1.5 km depth, but decreases  $w_M^{\text{H}_2\text{O}}$  and  $w_M^{\text{S}}$  by <12% and <11%, respectively. This results in a relative increase in the amount of exsolved  $\text{SO}_2$  ( $m_g^{\text{SO}_2}$ ) and  $\bar{S}$  up to a maximum of ~120% and ~180%, respectively, at 1.5 km depth (Figure 2.3b-c). Similarly, varying initial  $\text{CO}_2$  content increases  $V_g$  up to a maximum of ~110% at 1.5 km depth (Figure 2.3d). Increasing  $w^{\text{CO}_2}$  corresponds to an increase in  $\beta_m$  up to a maximum of <250% and a decrease in  $\bar{V}$  up to a maximum of 53% at 3.3 km depth (Figure 2.3f-g), which correlates to the decrease in  $\bar{z}$  up to a maximum of 58% at 2.8 km depth (Figure 2.3h).

Here, we quantify these results for a depth of 5 km to illustrate the sensitivity to  $w^{\text{CO}_2}$ . Increasing initial  $\text{CO}_2$  from 1000 to 5000 ppm increases  $\bar{S}$  from  $0.0082 \text{ kg m}^{-3}$  to  $0.163 \text{ kg m}^{-3}$  and  $V_g$  from 0.14 vol% to 3.0 vol% (Figure 2.3c-d). This corresponds to an increase in  $\beta_m$  from  $1.2 \times 10^{-10} \text{ Pa}^{-1}$  to  $3.8 \times 10^{-10} \text{ Pa}^{-1}$  (Figure 2.3f). As a result,  $\bar{V}$  decreases from 0.75 to 0.49 (Figure 2.3g) and  $\bar{z}$  is reduced from  $7.2 \text{ m km}^{-3}$  to  $4.7 \text{ m km}^{-3}$  (Figure 2.3h). The model shows that increasing initial  $\text{CO}_2$  content from 1000 to 5000 ppm causes significant changes to both  $\bar{V}$  and  $\bar{z}$ , similar to that of varying initial  $\text{H}_2\text{O}$  content from 1.0 wt% to 3.0 wt%.

### 2.4.3 Effects of sulfur content on magma properties

Here, we vary initial dissolved sulfur (S) content to understand how it affects magma properties and observables  $\bar{S}$ ,  $\bar{V}$  and  $\bar{z}$  (Figure 2.4). We use  $w^{\text{S}}$  in the range of 1000 ppm to 3000 ppm and fixed  $w^{\text{H}_2\text{O}} = 2.0$  wt%,  $w^{\text{CO}_2} = 3000$  ppm,  $f_{\text{O}_2} = \text{NNO}$  and  $\mu = 2.1$  GPa for this model.

Figure 2.4a shows that  $w_M^{\text{S}}$  increases by <200% at ~12 km depth with increasing  $w^{\text{S}}$  from 1000 ppm to 3000 ppm, which corresponds to the increase in  $m_g^{\text{SO}_2}$  and  $\bar{S}$  up to a maximum of ~122% and ~109% at the surface, respectively (Figure 2.4b-c). The total gas volume fraction, however, increases by only <3.7% at 1 km depth (Figure 2.4d). Since varying initial S content has minimal impact on  $V_g$ ,  $\beta_m$  only increases by <0.24% at surface depth (Figure 2.4f), which results in <1% decrease in both  $\bar{V}$  and  $\bar{z}$  (Figure 2.4g-h).

## CHAPTER 2. CONTRASTING VOLCANIC DEFORMATION IN ARC AND OCEAN ISLAND SETTINGS DUE TO EXSOLUTION OF MAGMATIC WATER

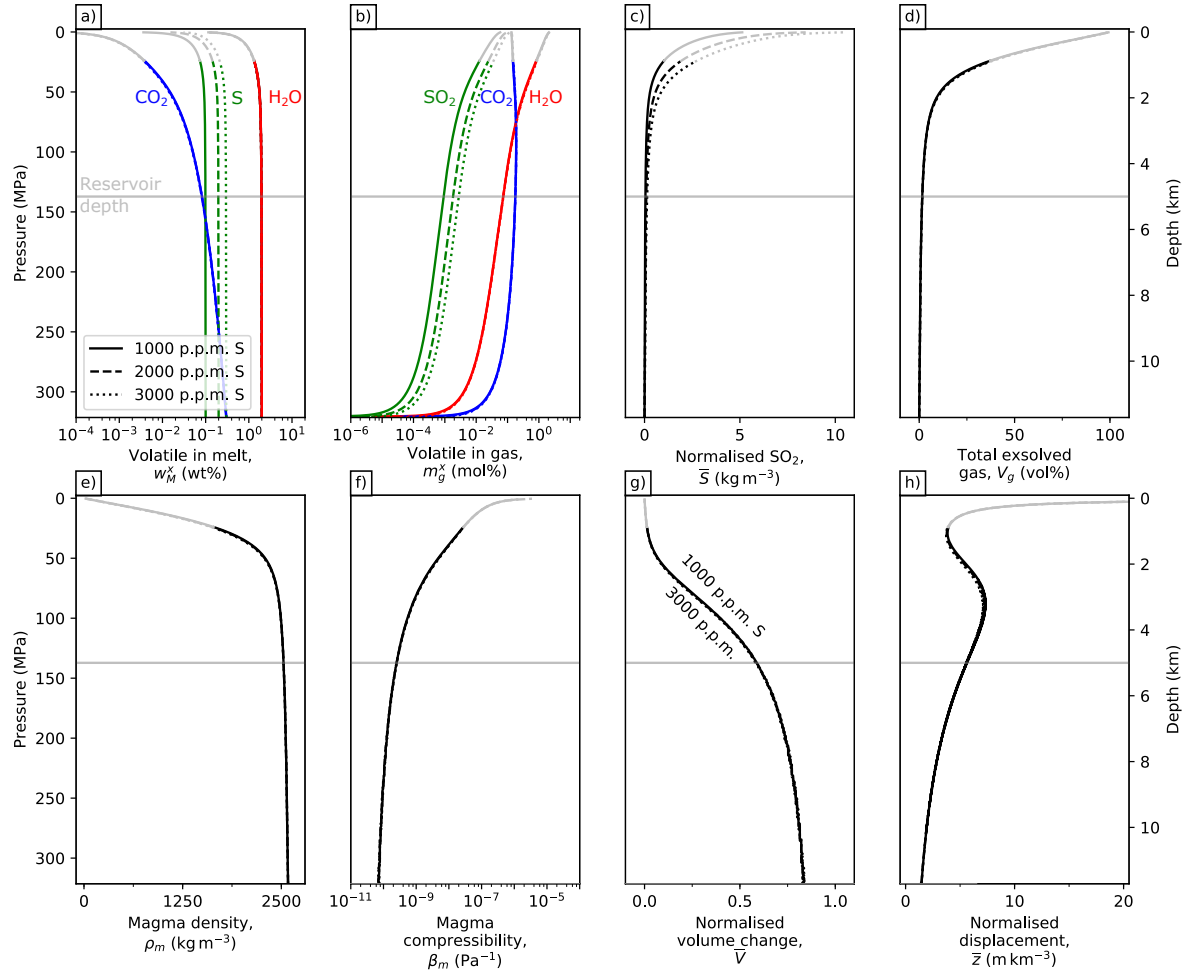


FIGURE 2.4. Physicochemical properties of basalts when varying the initial weight fraction of dissolved S ( $w^S$ ) from 1000 to 3000 ppm. Same general format as for Figure 2.2. Fixed parameters:  $w^{\text{H}_2\text{O}} = 2.0$  wt%,  $w^{\text{CO}_2} = 3000$  ppm,  $f_{\text{O}_2} = \text{NNO}$  and  $\mu = 2.1$  GPa.

We quantify these results for a depth of 5 km to illustrate the effect of varying  $w^S$  from 1000 ppm to 3000 ppm. This range of sulfur is less than the sulfur content at sulfide saturation. Increasing magmatic  $w^S$  increases  $\bar{S}$  from  $0.045 \text{ kgm}^{-3}$  to  $0.14 \text{ kgm}^{-3}$  (Figure 2.4c), which is so minimal that  $V_g$  remains constant 1.6 vol% despite increasing  $w^S$  from 1000 ppm to 3000 ppm (Figure 2.4d). This corresponds to indistinguishable changes in  $\beta_m$  at  $2.5 \times 10^{-9} \text{ Pa}^{-1}$  (Figure 2.4f). As such, both  $\bar{V}$  and  $\bar{z}$  are 0.59 and  $5.6 \text{ m km}^{-3}$ , respectively (Figure 2.4g-h). The model shows that basalts with high initial  $w^S$  release high  $\bar{S}$  but  $\beta_m$  and hence co-eruptive deformation is only minimally affected.

#### 2.4.4 Effects of oxygen fugacity on magma properties

Figure 2.5 shows how varying oxygen fugacity ( $f_{\text{O}_2}$ ) affects magma properties, and consequently observables  $\bar{S}$ ,  $\bar{V}$  and  $\bar{z}$ . We vary  $f_{\text{O}_2}$  from NNO-1 to NNO+2 and fix  $w^{\text{H}_2\text{O}} = 2.0 \text{ wt\%}$ ,  $w^{\text{CO}_2} = 3000 \text{ ppm}$ ,  $w^S = 2000 \text{ ppm}$  and  $\mu = 2.1 \text{ GPa}$  for this model.

The model predicts that varying  $f_{\text{O}_2}$  from NNO-1 to NNO+2 increases  $w_M^{\text{CO}_2}$ ,  $w_M^{\text{H}_2\text{O}}$  and  $w_M^S$  up to a maximum of 2.2%, 6.6% and 21%, respectively, at 1 km depth, because  $f_{\text{O}_2}$  is primarily affecting the fugacities of  $\text{H}_2\text{S}$  and  $\text{SO}_2$  in the gas phase and only indirectly affects  $\text{H}_2\text{O}$  and  $\text{CO}_2$  as a result. (Figure 2.5a). The significant increase in  $w_M^S$  causes a relative increase  $m_g^{\text{SO}_2}$  and  $\bar{S}$  up to a maximum of 176% and 183%, respectively, at surface depth (Figure 2.5b-c).

However,  $V_g$  is reduced by only <7% at 2.8 km depth so varying  $f_{\text{O}_2}$  has minimal impact on  $\rho_m$  and  $\beta_m$  (Figure 2.5e). In fact, increasing  $f_{\text{O}_2}$  from NNO-1 to NNO+2 decreases  $\beta_m$  by 6.9% at 3.6 km depth (Figure 2.5f) and hence  $\bar{V}$  of oxidised basalts is <4.3% greater than its reduced counterpart at 3.7 km depth (Figure 2.5g). While  $\bar{z}$  is controlled by chamber depth and  $\bar{V}$ , the maximum increase in  $\bar{z}$  of less than 4.8% also occur at 4.2 km depth due to insignificant difference in  $\bar{V}$  when varying  $f_{\text{O}_2}$  (Figure 2.5h).

Next, we quantify the predictions for a depth of 5 km. Varying  $f_{\text{O}_2}$  from NNO-1 to NNO+2 increases  $\bar{S}$  from  $0.020 \text{ kgm}^{-3}$  to  $0.077 \text{ kgm}^{-3}$  (Figure 2.5c). However,  $V_g$  decreases from 1.6 vol% to 1.5 vol%, which corresponds to a decrease in  $\beta_m$  from  $2.6 \times 10^{-10} \text{ Pa}^{-1}$  to  $2.5 \times 10^{-10} \text{ Pa}^{-1}$  (Figure 2.5f). As a result,  $\bar{V}$  and  $\bar{z}$  increases from 0.58 to 0.59 and  $5.5 \text{ m km}^{-3}$  to  $5.6 \text{ m km}^{-3}$ , respectively (Figure 2.5g-h). The model thus predicts that while oxidised basalts have greater  $\bar{S}$  than reduced basalts, variations in oxygen fugacity of basalts has minimal impact on co-eruptive deformation.

## CHAPTER 2. CONTRASTING VOLCANIC DEFORMATION IN ARC AND OCEAN ISLAND SETTINGS DUE TO EXSOLUTION OF MAGMATIC WATER

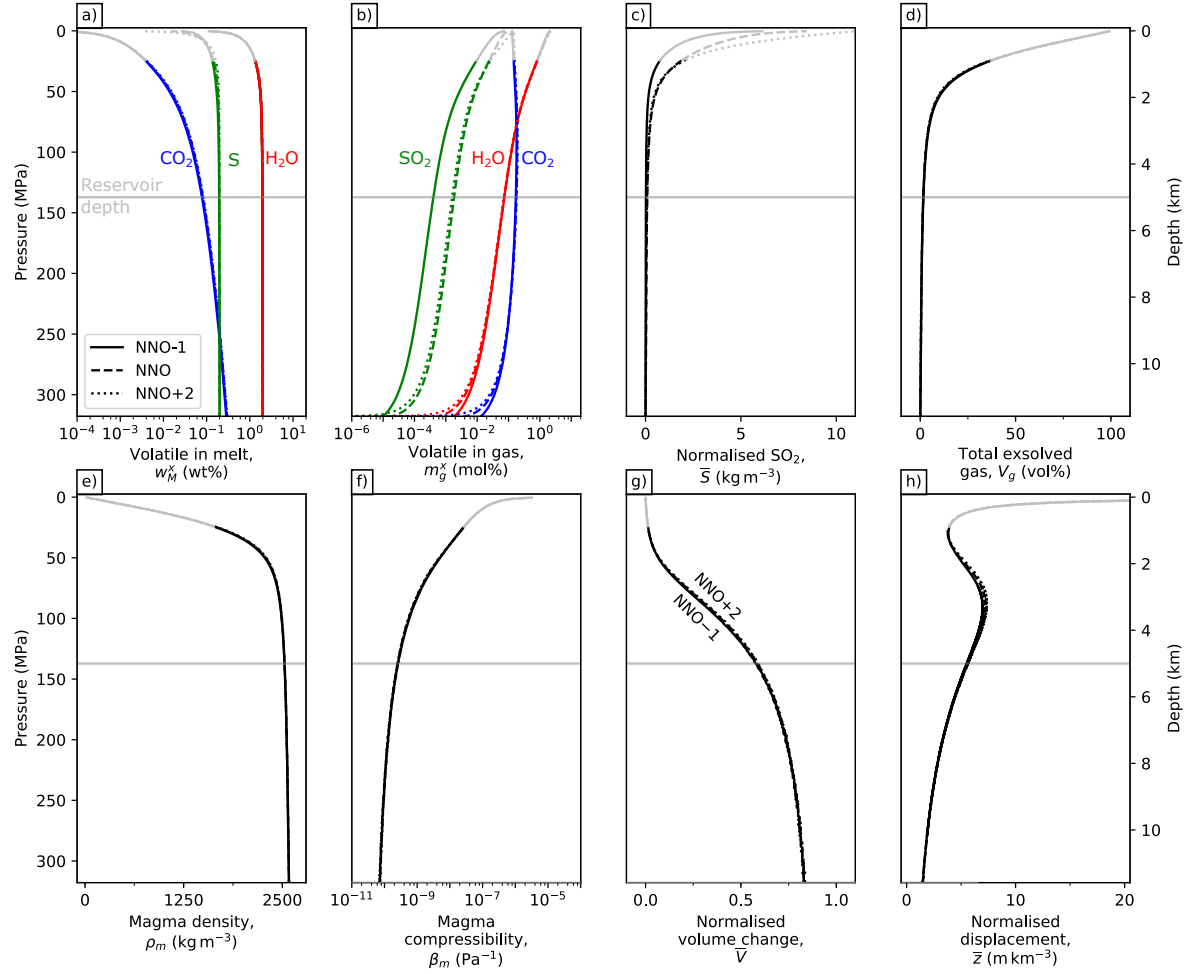


FIGURE 2.5. Physicochemical properties of basalts when varying  $f_{\text{O}_2}$  of magma storage from NNO-1 to NNO+2. Same general format as for Figure 2.2. Fixed parameters:  $w^{\text{H}_2\text{O}} = 2.0$  wt%,  $w^{\text{CO}_2} = 3000$  ppm,  $w^{\text{S}} = 2000$  ppm and  $\mu = 2.1$  GPa.

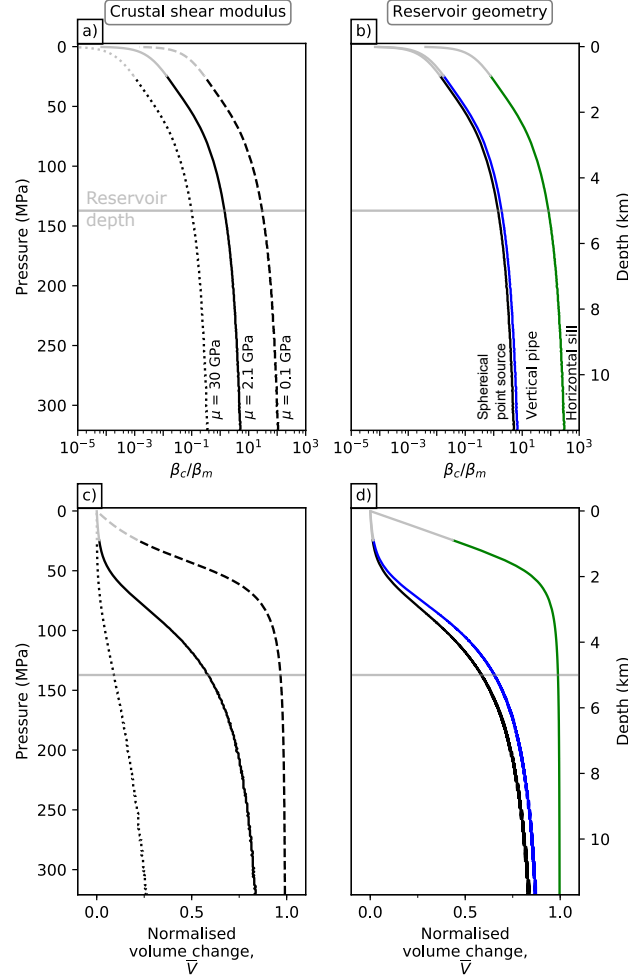


FIGURE 2.6. Physical properties of basalts when varying the crustal shear modulus ( $\mu$ ) and chamber geometry. (a) The ratio of  $\beta_c/\beta_m$  to illustrate the effects of crustal shear modulus and chamber geometry. The  $\mu$  used are 0.1 GPa, 2.1 GPa and 30 GPa (Heap et al., 2020), and the chamber geometry considered is of a spherical point source. (b) The ratio of  $\beta_c/\beta_m$  for a spherical point source, a vertical pipe-like chamber and a horizontal sill with  $\mu = 2.1$  GPa. The major to minor semiaxis of the horizontal sill,  $\frac{a}{c}$ , is 100. (c)  $\bar{V}$  for a spherical point source with varying  $\mu$ . (d)  $\bar{V}$  for a spherical point source, a vertical pipe-like chamber and a horizontal sill with  $\mu = 2.1$  GPa. Fixed parameters:  $w^{\text{H}_2\text{O}} = 2.0$  wt%,  $w^{\text{CO}_2} = 3000$  ppm,  $f_{\text{O}_2} = \text{NNO}$ , and  $w^{\text{S}} = 2000$  ppm. The grey lines represent magma properties when percolation threshold exceeds  $\phi_c = 37$  vol%.



### 2.4.5 Effects of chamber compressibility

Crustal properties and chamber geometry are known to have a major role in determining surface deformation (e.g., Gudmundsson, 2008; Amoruso and Crescentini, 2009; Anderson and Segall, 2011; Heap et al., 2020). Here we investigate the two parameters that directly affect our simplified model using the same sensitivity analysis as for the other parameters.  $\bar{V}$  is a function of  $\beta_m$  and  $\beta_c$ , and the two parameters we explore in this section are crustal shear modulus and chamber geometry that control  $\beta_c$  (Equation 2.4). We use a range of crustal shear modulus ( $\mu$ ) from 0.1 GPa (compliant crust) to 30 GPa (non-compliant crust), which is typical in volcanic areas (Gudmundsson, 2005; Rivalta and Segall, 2008). It is noted that  $\mu$  depends primarily on porosity and hence degree of fracturing of the host rock (Heap et al., 2020), which does not vary systematically with tectonic setting.  $\mu$  changes with depth but for simplicity, we assume a constant  $\mu$  at all depths. We considered three representative chamber geometries, which are a spherical point source, a vertical prolate ellipsoid (pipe-like chamber) and a horizontal oblate ellipsoid (sill), and use  $\frac{a}{c} = 100$  for the horizontal sill (Equation 2.5) (Amoruso and Crescentini, 2009; Anderson and Segall, 2011). We use a Poisson's ratio  $\nu$  of 0.30 based on the average value for volcanic rock with average porosity and fracture density (Heap et al., 2020). The sensitivity test uses fixed parameters of  $w^{\text{H}_2\text{O}} = 2.0$  wt%,  $w^{\text{CO}_2} = 3000$  ppm,  $f_{\text{O}_2} = \text{NNO}$ , and  $w^{\text{H}_2\text{O}} = 2000$  ppm.

To understand how crustal properties affect volcanic deformation, we first discuss the effects of  $\mu$  and chamber geometry on the ratio of  $\beta_c/\beta_m$ . Since  $\beta_c$  is inversely proportional to  $\mu$ , a crust with  $\mu = 0.1$  GPa results in  $\beta_c/\beta_m = 30$  for a chamber at 5 km depth, while  $\beta_c/\beta_m = 0.099$  for a crust with  $\mu = 30$  GPa (Figure 2.6a). From Equation 2.5, the crustal compressibility  $\beta_c$  for chambers with a vertical pipe-like shape is 33% higher than a spherical point source and thus increases the  $\beta_c/\beta_m$  of a vertical pipe-like chamber by 33% when compared to that of a spherical point source (Figure 2.6b). An ellipsoid with  $\frac{a}{c} = 100$  has the highest  $\beta_c$  among the three chamber geometries (i.e., 60 times greater than a spherical point source) and therefore has the highest  $\beta_c/\beta_m$ , consistent with analytical results from Anderson and Segall (2011).

Here we quantify the effects of varying  $\mu$  and the chamber geometry on  $\bar{V}$  (Figure 2.6c-d). The  $\bar{V}$  for crustal rocks with  $\mu = 0.1$  GPa is up to a maximum of  $\sim 360\%$  greater than that with  $\mu = 2.1$  GPa at 2.5 km depth. In contrast,  $\bar{V}$  is reduced up to a maximum of  $\sim 73\%$  at 9.1 km depth for a crust with  $\mu = 30$  GPa when compared to  $\mu = 2.1$  GPa. At 5 km

depth, the  $\bar{V}$  for  $\mu = 0.1$  GPa, 2.1 GPa and 30 GPa are 0.97, 0.59 and 0.090, respectively (Figure 2.6c). The effects of different chamber geometries on  $\bar{V}$  are shown in Figure 2.6d, with  $\mu = 2.1$  GPa and Poisson's ratio  $\nu$  of 0.30 (Heap et al., 2020). The normalised volume change  $\bar{V}$  is greatest for horizontal sills and smallest for spherical point source, such that  $\bar{V} = 0.99$  and 0.58, respectively, for a chamber at 5 km depth. Based on the effects of  $\mu$  and chamber geometry on  $\beta_c/\beta_m$ , we find that a volcano with low  $\beta_c/\beta_m$  (i.e., spherical, high shear modulus) has low  $\bar{V}$  which indicates muted volcanic deformation. In contrast, a volcano with high  $\beta_c/\beta_m$  (i.e., horizontal sill, low shear modulus) has high  $\bar{V}$ . For example, at 5 km depth,  $\bar{V} = 0.090$  for a spherical point source with  $\mu = 30$  GPa, but  $\bar{V} = 1.0$  for a sill with  $\mu = 0.1$  GPa.

The main takeaways from the sensitivity analysis of chamber compressibility is that 1) spherical point sources and vertical pipe-like chambers have similar  $\beta_c/\beta_m$  and  $\bar{V}$ , whereas sills have higher  $\beta_c/\beta_m$  and thus high  $\bar{V}$  (Figure 2.6b,d) and 2) crustal properties, specifically shear modulus, have a significant influence on  $\bar{V}$ , with lower crustal shear modulus contributing to larger volume changes (Figure 2.6a,c) (Heap et al., 2020; Hautmann et al., 2010).

### 2.4.6 Summary of sensitivity analyses

Here we summarise the results from each sensitivity test. A summary of the greatest percentage change of  $\bar{S}$ ,  $\bar{V}$  and  $\bar{z}$  over the depth range of each parameter is shown in Table 2.2. Our simplified model predicts that explosive eruptions of water-rich basaltic magmas have high  $\text{SO}_2$  emissions and little deformation for a particular volume of magma erupted. While initial magmatic  $\text{CO}_2$  causes insignificant changes to the total amount of  $\text{SO}_2$  degassing during eruptions, it has significant impact on the observed co-eruptive deformation, i.e.,  $\text{CO}_2$ -rich magmas are more compressible than  $\text{CO}_2$ -poor magmas with the same amount of  $\text{H}_2\text{O}$ . Additionally, we find that varying magmatic  $\text{CO}_2$  content from 1000 to 5000 ppm affects the observed co-eruptive deformation at a magnitude similar to that of varying initial magmatic  $\text{H}_2\text{O}$  content from 1.0 to 3.0 wt%, which implies that initial magmatic  $\text{CO}_2$  content also plays an important role in magma compressibility and thus co-eruptive deformation. Initial magmatic  $S$  and oxygen fugacity have a strong influence on the magnitude of  $\text{SO}_2$  degassing but have a minimal impact on the magnitude of the co-eruptive deformation. Magmas with a high oxygen fugacity yield high  $\text{SO}_2$  emissions during an eruption, but this does not impact co-eruptive deformation significantly. Magmatic reservoirs with strong surrounding crustal rocks (i.e., high  $\mu$ )

and spherical geometry may display muted co-eruptive deformation when compared to compliant host rocks (i.e., low  $\mu$ ) and horizontal sills.

## 2.5 Comparison Between Arc Basalts and Ocean Island Basalts

### 2.5.1 Thermodynamic modelling of magma properties

We now examine how tectonic setting influences the physicochemical properties of basaltic magma and consequently its impact on observed volcanic deformation and  $\text{SO}_2$  degassing. Here we compare arc basalts and ocean island basalts by considering realistic parameter combinations and the co-dependence of parameters. Basaltic magma in arc settings tend to have higher water contents than basaltic magma from ocean island settings (e.g., Wallace, 2005; Zimmer et al., 2010; Plank et al., 2013). Melt inclusion data suggest that, on average, arc basalts contain  $3.9 \pm 0.4$  wt%  $\text{H}_2\text{O}$ ,  $4000 \pm 1000$  ppm  $\text{CO}_2$ , and  $3000 \pm 1000$  ppm S, and ocean island basalts contain  $1.0 \pm 0.2$  wt%  $\text{H}_2\text{O}$ ,  $6500 \pm 3500$  ppm  $\text{CO}_2$  and  $1600 \pm 1000$  ppm S (e.g., Wallace, 2005; Ruscitto et al., 2012; Plank et al., 2013; Rasmussen et al., 2022). We note that the  $\text{CO}_2$  content for ocean island basalts is at the high end of previous estimates and has high uncertainty, and this is because it was chosen to include  $\text{CO}_2$ -rich ocean island eruptions like Kilauea (e.g., Dixon and Clague, 2001; Gerlach et al., 2002). These values represent the dissolved volatile abundances at shallow crustal levels, in which the volatiles recorded in the melt inclusions are primarily controlled by solubility. We take typical values of  $f_{\text{O}_2}$  of arc basalts and ocean island basalts at  $\text{NNO} + 1.4 \pm 1$  and  $\text{NNO} + 0.7 \pm 0.9$ , respectively (e.g., Matjuschkin et al., 2016; Brounce et al., 2017; Konecke et al., 2019). Crustal compressibility also influences the magnitude of volcanic deformation (Section 2.4.5), and thus we use  $\mu = 2.1$  GPa, which is typical in volcanic areas, and assume a Mogi deformation source for simplicity (Mogi, 1958; Gudmundsson, 2005; Heap et al., 2020). The range of parameter values used for the analyses described below are based on the magma composition typical for arc basalt and ocean island basalt (Table 2.1).

Monte-Carlo simulation allows repeated random sampling over a given input parameter space and hence allows us to estimate the possible range of model outputs. Here we use the range of magma compositions in typical arc and ocean island basalts to estimate the ranges of volume change, ground deformation and  $\text{SO}_2$  flux expected for eruptions

## 2.5. COMPARISON BETWEEN ARC BASALTS AND OCEAN ISLAND BASALTS

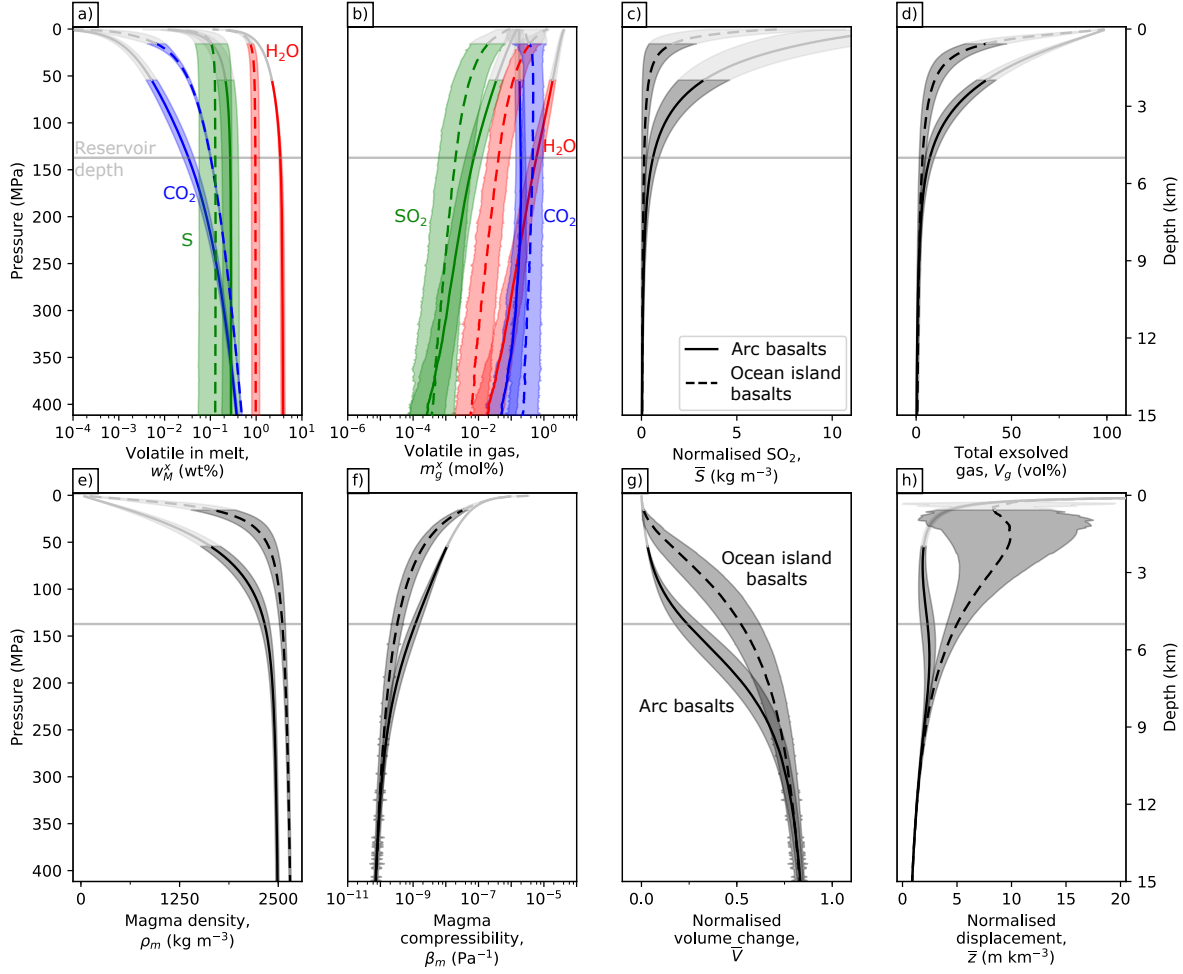


FIGURE 2.7. Comparison of magma properties between typical arc basalts (full line) and typical ocean island basalts (dashed line). The input parameters for the thermodynamic model ( $w^{H_2O}$ ,  $w^{CO_2}$ ,  $w^S$  and  $f_{O_2}$ ) and crustal shear modulus  $\mu$  are initialised using a Monte-Carlo approach (Table 2.1). 1000 simulations are performed and the magma properties are calculated using the thermodynamic framework. (a) Weight fraction of dissolved volatile contents and (b) mol fraction of exsolved volatile contents. (c) Normalised  $SO_2$   $\tilde{S}$ . (d) Volume fraction of exsolved gases in magma ( $V_g$ ). (e) Magma density ( $\rho_m$ ) and (f) Magma compressibility ( $\beta_m$ ). (g) Normalised volume change ( $\tilde{V}$ ). (h) Normalised vertical displacement ( $\tilde{z}$ ). The grey lines represent magma properties after exceeding percolation threshold  $\phi_c = 37$  vol% and the shaded region represent  $1\sigma$  uncertainty. The range of parameter values for arc basalts and ocean island basalts are listed in Table 2.1.

in different tectonic settings. We performed 1000 simulations for each type using the distribution of each variable ( $w^{\text{H}_2\text{O}}$ ,  $w^{\text{CO}_2}$ ,  $w^{\text{S}}$ ,  $f_{\text{O}_2}$ ) provided in Table 2.1 as input parameters for the thermodynamic model. Parameters that are distributed below the detection limit are readjusted accordingly (i.e.,  $w^{\text{H}_2\text{O}} < 100$  ppm,  $w^{\text{CO}_2} < 25$  ppm and  $w^{\text{S}} < 50$  ppm are changed to  $w^{\text{H}_2\text{O}} = 100$  ppm,  $w^{\text{CO}_2} = 25$  ppm and  $w^{\text{S}} = 50$  ppm, respectively). The thermodynamic model has a starting temperature of 1200 °C, a Poisson’s ratio  $\nu$  of 0.30, and we find the starting pressure/depth using the saturation point of each melt composition. After 1000 Monte-Carlo simulations, we calculate the mean and the standard deviation for each model output, such as normalised  $\text{SO}_2$ , magma compressibility and normalised volume change. Since we started each simulation at the saturation point for that composition (see Section 2.3.1), we apply a filter to discard the values for any pressure/depth with less than 100 successful simulations.

In Figure 2.7 we present the model predictions for arc basalts and ocean island basalts to illustrate the effects of tectonic settings on magma properties and co-eruptive observations. The high  $f_{\text{O}_2}$  environment of arc basalts will tend to produce more exsolved  $\text{SO}_2$  at the expense of  $\text{H}_2\text{S}$  and  $\text{S}_2$ , whereas ocean island basalts, which have a lower  $f_{\text{O}_2}$ , have less exsolved  $\text{SO}_2$  in the gas phase (Figure 2.7b). With a higher mole fraction of exsolved  $\text{SO}_2$  gas, the predicted  $\bar{S}$  (i.e.,  $\text{SO}_2$  gas in the reservoir) of arc basalts is higher than that of ocean island basalts (Figure 2.7c). In contrast, for basaltic eruptions that undergo co-eruptive degassing, such that additional sulfur is loss from melt during the final ascent to the surface, the difference in  $\bar{S}$  would be expected to result from differences in initial magmatic sulfur content and  $f_{\text{O}_2}$ . The higher magmatic volatile content of arc basalts translates to a higher  $V_g$  (Figure 2.7d), suggesting that in general, arc basalts are more compressible than ocean island basalts (Figure 2.7f). We note that while our study uses a higher  $\text{CO}_2$  content for ocean island basalts than arc basalts (Table 2.1), water-rich arc basalts remain more compressible than ocean island basalts, which highlights that the range of  $\text{H}_2\text{O}$  content in basalts plays a more important role in determining magma compressibility than  $\text{CO}_2$  content. The increased magma compressibility indicates that arc basalts have a lower  $\bar{V}$  and  $\bar{z}$  than ocean island basalts (Figure 2.7g-h).

Here we give specific values for arc basalts and ocean island basalts assuming a magma chamber at 5 km depth (Figure 2.7). If an explosive eruption should occur from a chamber at 5 km depth (where we assume that volatiles are in both exsolved and dissolved form in the magma chamber and that no co-eruptive degassing occurs during

magma ascent), the predicted  $\bar{S}$  of arc basalts is  $0.60 \text{ kgm}^{-3}$ , greater than that of ocean island basalts at  $0.14 \text{ kgm}^{-3}$  (Figure 2.7c). For a chamber at 5 km depth, arc basalts are more compressible than ocean island basalts at  $\beta_m = 12 \times 10^{-10} \text{ Pa}^{-1}$  and  $3.3 \times 10^{-10} \text{ Pa}^{-1}$ , respectively (Figure 2.7f), and thus arc basalts have  $\bar{V} = 0.24$  and  $\bar{z} = 2.3 \text{ mkm}^{-3}$  as compared to ocean island basalts that have  $\bar{V} = 0.52$  and  $\bar{z} = 5.0 \text{ mkm}^{-3}$ . It is noted that ocean island basalts eruptions are usually effusive in nature (i.e., they will exhibit extensive co-eruptive degassing; see Section 2.2), and thus we expect  $\bar{S}$  to be dominated by decompressional degassing and hence much higher than predicted the gas content in the chamber.

## 2.5.2 Comparison to Satellite Observations

In this section, we compare the magma properties predicted by the thermodynamic framework with observations of eruptions to understand published catalogues of volcanic deformation and degassing.

### 2.5.2.1 Data Compilation

Here we compiled deformation and  $\text{SO}_2$  degassing data for 94 basaltic eruptions during the satellite era (2005-2020) to understand how theoretical estimates from thermodynamic modelling compare with observed eruptions (Supplementary Table A.1). The primary magma composition and the dates for past eruptions are drawn from the Global Volcanism Program (2013). The compilation only considers volcanoes of basaltic composition. For eruptions with poorly constrained starting or ending dates, particularly for long-lived eruptions, we select the dates at which significant eruptions occur such as the the 2018 eruptions of Kilauea, Ambrym and Fuego (e.g., Neal et al., 2019; Hamling et al., 2019; Naismith et al., 2019).

We compile 23 episodes of pre- and co-eruptive deformation detected with InSAR from the published catalogues of Biggs and Pritchard (2017) and Ebmeier et al. (2018) and 58 satellite observations of  $\text{SO}_2$  degassing from individual studies (Supplementary Table A.1), published catalogues (Carn et al., 2016, 2017) and Global Volcanism Program (2013). For eruptions that are less well studied (e.g., Chikurachki, Pagan, Semisopchnoi), evidence for  $\text{SO}_2$  degassing are crosschecked with the Global Sulphur Dioxide Monitoring homepage (<https://so2.gsfc.nasa.gov/>). Persistently degassing volcanoes (e.g., Shishaldin, Saunders, Korovin), including those whose emissions can be detected by

## CHAPTER 2. CONTRASTING VOLCANIC DEFORMATION IN ARC AND OCEAN ISLAND SETTINGS DUE TO EXSOLUTION OF MAGMATIC WATER

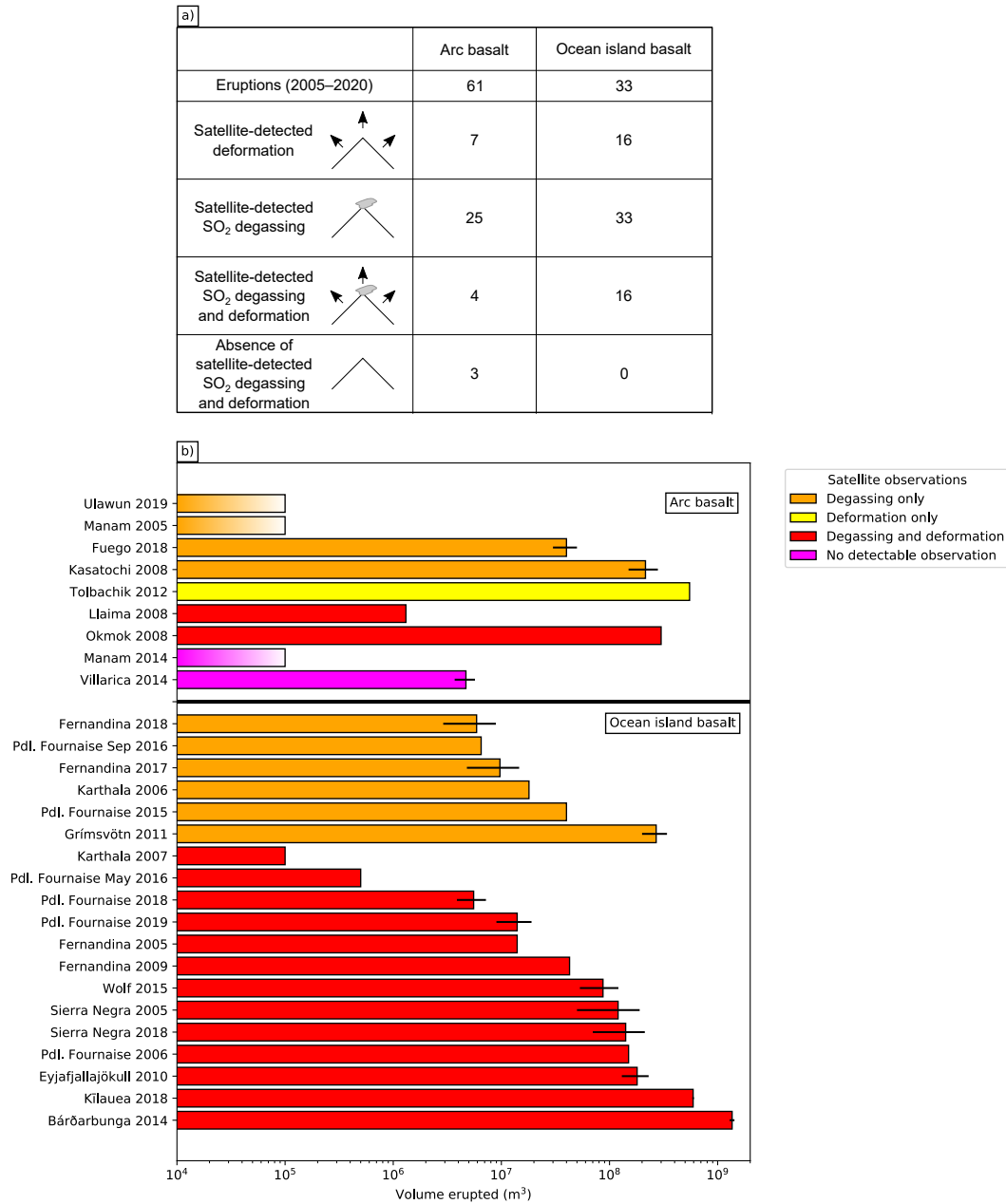


FIGURE 2.8. (a) Number of arc basalt and ocean island basalt eruptions with volcanic deformation (either uplift or subsidence) and SO<sub>2</sub> degassing measured by satellites during the satellite era (2005–2020). (b) Arc basalt and ocean island basalt eruptions with erupted volume greater than  $10^5$  m<sup>3</sup>. Columns are colour-coded for deformation and SO<sub>2</sub> degassing detectable by satellites. Uncertainties in the erupted volume, where available, are shown as horizontal error bars. Eruptions with a colour gradient use VEI index as a very rough indicator to estimate the erupted volume. We assume VEI 4 eruptions to have a volume  $> 10^5$  m<sup>3</sup>.

satellites (e.g., Masaya, Miyakejima, Telica) (Carn et al., 2017), and submarine eruptions (e.g., Mayotte, Axial Seamount, Bristol Island) are not considered in this compilation. We also do not consider volcanoes that have approximately equal passive and eruptive SO<sub>2</sub> degassing such as Rabaul (Carn et al., 2016), with the exception of VEI 4+ eruptions (e.g., the 2005 and 2014 eruption of Manam and the 2019 eruption of Ulawun). We do, however, include eruptions that are significantly explosive (e.g., 2018 eruptions of Ambrym and Kīlauea).

We find that observations of deformation and SO<sub>2</sub> degassing are not available for every eruption despite similar erupted volume or volcano (Figure 2.8b). In fact, there is no clear correlation between satellite observations and erupted volume, consistent with previous studies (Kilbride et al., 2016), largely due to the challenges in volcano monitoring such as atmospheric noise, ice cover, or limitations in satellite sensors (e.g., Ozone Monitoring Instrument (OMI) row anomaly for the 2012 eruption of Tolbachik). For example, satellite sensors could not measure the deformation associated with the 2011 eruption of Grimsvötn due to ice cover. Similarly, satellite measurement of SO<sub>2</sub> degassing is not available for the 2012-2013 eruption of Tolbachik, despite being one of the most voluminous arc basalt eruptions (Belousov et al., 2015), due to the OMI row anomaly (see [https://so2.gsfc.nasa.gov/pix/daily/1112/kamchatka\\_1112z.html](https://so2.gsfc.nasa.gov/pix/daily/1112/kamchatka_1112z.html)).

Overall, deformation was detected at 25% of eruptions (23/94) and SO<sub>2</sub> degassing at 62% of eruptions (58/94) (Supplementary Table A.1). A similar analysis conducted by Furtney et al. (2018) uses multiple satellite data spanning 1978-2016 to synthesise observations of volcanic deformation and degassing. Their study yielded similar results to ours: of the 250 volcanic eruptions between 1978-2016, 28% of eruptions have satellite observations of volcanic deformation, and SO<sub>2</sub> degassing is observed at 67% of eruptions (Furtney et al., 2018). We note that the Furtney et al. (2018) study includes a wider range of magma composition than we do here, so the slightly higher proportion of volcanoes with satellite-detected deformation and degassing analysed by Furtney et al. (2018) is likely caused by the inclusion of magma of varying compositions and also pre- and post-eruptive observations. The overall proportion of satellite observations of volcanic deformation and SO<sub>2</sub> degassing appears to be fairly consistent between studies.



### 2.5.2.2 Comparison between tectonic settings

Our compilation shows that co-eruptive deformation has been observed at 48% of eruptions involving ocean island basalts (16/33), while only 11% of arc basalt eruptions had observed deformation (7/61) (Supplementary Table A.1; Figure 2.8a). The lower frequency of detectable deformation at arc basalt eruptions can be attributed to the higher volatile contents of arc magmas, which our thermodynamic model predicts will increase magma compressibility and reduce surface deformation (Figure 2.7f-h). Systematic satellite observations of deformation spanning 1992-2010 analysed by Biggs et al. (2014) shows that the proportion of deforming volcanoes that erupted is higher for volcanoes in hotspot setting (66%; ocean island) as compared to those in subduction setting (53%; arc). For example, there are few InSAR observations from the Central American Volcanic Arc, where parental melts are water-rich (Ebmeier et al., 2013b; Wallace, 2005). Although this is an indirect comparison, the study agrees well with our results that observations of volcanic deformation are dominated by ocean island basalt eruptions. However, we note that other potential factors may also contribute to the lack of detectable deformation at volcanoes, independently or collectively (e.g., the rate of magma recharge, chamber geometry, depth of magma storage, viscoelastic crustal rheology, an open conduit, pre-eruptive degassing, atmospheric noise (Ebmeier et al., 2013a,b; Chaussard et al., 2013; Head et al., 2019; Yip et al., 2019; Mullet and Segall, 2022)) meaning that the models are very uncertain.

Volcanic SO<sub>2</sub> degassing was observed at all 33 ocean island basalt eruptions in our compilation but at only 41% of the arc basalt eruptions (25/61) (Supplementary Table A.1; Figure 2.8a). While the higher magmatic volatile content of arc basalts might be expected to produce a higher detection rate (Figure 2.7c), the high rate of detection at ocean island basalt can be attributed to co-eruptive degassing during effusive eruptions. Conversely, the explosive nature of arc basalt eruptions may mean there is no co-eruptive degassing and the only volatiles released are those in equilibrium at chamber depth. Additionally, technical difficulties in spectrometers, such as the OMI row anomaly that obscures the spectrometer's field of view (e.g., 2019 eruption of Klyuchevskoy, 2012 eruption of Tolbachik; see <https://so2.gsfc.nasa.gov/>) prevents routine volcano monitoring.

We find that satellite observations of both volcanic deformation and degassing to be higher for ocean island basalt eruptions (16/33) than arc basalt eruptions (4/61) (Figure

2.8a). We note that despite the much higher number of arc eruptions in our catalogue than ocean island eruptions, there are very much fewer observations of deformation for arc eruptions. Similarly, all ocean island basalt eruptions have been observed by at least one satellite sensor, while 3 of the 61 arc basalt eruptions were not detected by either sensors. The lack of satellite observations of arc basalt eruptions highlights the difficulties in monitoring explosive eruptions with high magmatic volatile contents and thus compressible magmas (Huppert and Woods, 2002; Rivalta and Segall, 2008; Kilbride et al., 2016), and volcanoes with deep magma storage prior to eruptions (Moran et al., 2006; Ebmeier et al., 2013b).

Finally, we further analyse 28 eruptions with erupted volume  $\geq 10^5 \text{ m}^3$  (Figure 2.8b) to ensure comparable detection thresholds (Supplementary Table A.2). We note that there is a lack of data on the erupted volume, which may result in sampling bias and therefore, we extend our search using the VEI index drawn from the Global Volcanism Program (2013) with the assumption that VEI 4 eruptions produce  $\geq 10^5 \text{ m}^3$  DRE and that they are significantly explosive. All 19 ocean island basalt eruptions with erupted volume  $\geq 10^5 \text{ m}^3$  have satellite observations of  $\text{SO}_2$  degassing of which 13 have deformation measured by satellites (Figure 2.8b). For the case of arc basalt eruptions, there are only 9 instances of eruptions with  $\geq 10^5 \text{ m}^3$  DRE, of which 3 are estimated from the VEI index (the 2005 and 2014 eruption of Manam and the 2019 eruption of Ulawun) (Figure 2.8b). We find that one arc eruption has satellite observation of co-eruptive deformation, four have satellite observations of  $\text{SO}_2$  degassing and two have observations of both deformation and degassing. The two remaining eruptions, the 2014 eruption of Manam and Villarica, were not detected by satellites, probably due to atmospheric noise (lack of co-eruptive deformation at Villarica, Delgado et al., 2017) and OMI row anomaly (see <https://so2.gsfc.nasa.gov/>). As such, we find no link between erupted volume  $\geq 10^5 \text{ m}^3$  and satellite observations of  $\text{SO}_2$  degassing and deformation (Figure 2.8b), in agreement with the wider catalogue and previous studies (Kilbride et al., 2016). This highlights the challenges for satellites to detect surface deformation, particularly for eruptions of more evolved, volatile-rich arc magmas that are more compressible.

In summary, the thermodynamic framework and satellite observations of deformation agree well with each other such that volcanic deformation of volatile-poor ocean island eruptions are more likely to be detected by satellites as compared to volatile-rich arc eruptions (Figure 2.7g-h; Figure 2.8a). This is because volatile-rich arc basalts are highly

compressible, which results in muted surface deformation. Predictions of  $\text{SO}_2$  degassing from our thermodynamic framework show that volatile-rich arc basalts have higher rates of  $\text{SO}_2$  degassing at chamber depths, yet satellite observations show that ocean island eruptions outgas more  $\text{SO}_2$  per unit of magma erupted (Figure 2.7c; Figure 2.8a), due to extensive co-eruptive degassing. We note that while the water content of arc basalts is two times greater than that of ocean island basalts, the sulfur content in basalts from both tectonic settings are similar (Table 2.1).

## 2.6 Limitations of our model

The high magmatic volatile contents of arc basalts, and their oxidised nature, lead to a substantial amount of exsolved volatiles being present in the chamber prior to eruption, which increases magma compressibility and lessens the magnitude of volcanic deformation (Figure 7). Co-eruptive deformation is less likely to be detected at arc volcanoes than at volcanoes in ocean island settings (Figure 8). However, we note that the high initial volatile content of a magma body is not the only factor that affects the magnitude of volcanic deformation. Other potential factors include 1) magma chambers with different geometries (e.g., Gudmundsson, 2008; Amoroso and Crescentini, 2009; Anderson and Segall, 2011), 2) the influence of the viscoelastic response of the crust (e.g., Hickey et al., 2013; Head et al., 2019; Gottsmann et al., 2020), and 3) the presence of a ‘transcrustal’ mush surrounding the magma body (e.g., Cashman et al., 2017; Sparks et al., 2019). It has been shown that the magnitude of the syn-eruptive surface deformation signal for a volcano overlying a transcrustal mush system would be less than that with a simple magma body in a rigid sub-solidus country rock, and this effect increases with the melt fraction of the mush (Mullet and Segall, 2022). Estimates of magma compressibility and the volume change of a magma reservoir are likely to be underestimated assuming the magma body is contained within an elastic half space rather than a mush-like system (Mullet and Segall, 2022).

Our model also predicts that explosive eruptions of arc basalts will produce a higher syn-eruptive  $\text{SO}_2$  flux than ocean island basalt eruptions. However, sulfur in basaltic magma has a high diffusivity and can continue to exsolve extensively during magma ascent, particularly during effusive eruptions (Figure 2.1c). Differences between the predicted  $\text{SO}_2$  gas per unit volume of magma in the chamber and that observed during an eruption may be modified by 1) co-eruptive degassing, 2) epistemic uncertainties in model

parameters associated with initial magmatic sulfur content and  $f_{O_2}$ , 3) pre-eruptive gas accumulation and loss (e.g., Wallace, 2005; Edmonds et al., 2014; Edmonds and Woods, 2018), 4) sulfur loss due to scrubbing or formation of sulfide globules (e.g., Sigmarsson et al., 2013; Anderson and Poland, 2016; Hurwitz and Anderson, 2019). Furthermore, we note that the solubility of sulfur species are calculated using a sulfide capacity law that is more appropriate for sulfur in reduced melt (O'Neill, 2021; Liggins et al., 2020, 2022).

The simplicity of this model is useful for considering general trends, and we note that oversimplification reduces the applicability to individual eruptions. The assumption of a typical elastic shear modulus may be appropriate for the sensitivity tests, but crustal rheology varies enormously between volcanoes (e.g., Gudmundsson, 2005; Head et al., 2019; Huber et al., 2019; Heap et al., 2020). We also consider that only depth (i.e., pressure) affects the amount of exsolved gas content in bulk magma for a given set of initial conditions, such that the magma does not undergo crystallisation nor magma recharge, which is very simplistic. Additionally, we did not consider the effects of pre-eruptive gas accumulation and loss on magma properties, which in reality could affect co-eruptive observations (e.g., Wallace, 2001; Huppert and Woods, 2002; Rivalta and Segall, 2008). While simplistic, our principal findings remains robust and we highlight the importance of exsolved magmatic  $H_2O$  in controlling magma compressibility, which helps to explain the lack of volcanic deformation that accompanies many arc eruptions.

## 2.7 Conclusion

The thermodynamic framework presented in this study provides a quantitative link between observations of volcanic deformation and degassing. The framework is used to explore the sensitivity of magma properties to several controlling parameters (magmatic  $H_2O$ , magmatic  $CO_2$ , magmatic S, oxygen fugacity  $f_{O_2}$ ), which vary systematically between tectonic setting. We demonstrated that the results from thermodynamic models can be used to calculate the volume of gas in the reservoir, which can be related to  $SO_2$  emissions and surface deformation. The conclusions of this study are as follows:

1. Magmas with a high magmatic  $H_2O$  content have high volumes of exsolved gas in the chamber, leading to high magma compressibility, which results in muted surface deformation during eruptions. While high magmatic  $CO_2$  has little effect on  $SO_2$  degassing, it increases magma compressibility and thus reduces surface deformation. Varying oxygen fugacity from NNO–1 to NNO+2 and increasing

magmatic S contents increases  $\text{SO}_2$  gas emissions but has little effect on magma compressibility.

2. The volatile content of magmas varies between tectonic settings and this influences both ground deformation and the extent of degassing during eruptions. Arc basalts, which tend to have higher magmatic volatile contents, have more muted ground deformation than ocean island basalts, which is reflected in observations over the satellite era.

With results from the thermodynamic framework, we have developed a better understanding of the effects of magmatic volatile content and degassing on the physicochemical properties of magma. Our future work will explore pre-eruptive gas segregation processes such as gas accumulation and percolative gas loss to understand their implications for observations of volcanic deformation and degassing. Future studies should refine this framework for specific circumstances to resolve additional complexities.

## Chapter 3

# The role of pre-eruptive exsolved volatile segregation on observations of volcanic deformation and degassing

Published in *Earth and Planetary Science Letters*:

**Yip, S. T. H.**, Biggs, J., Edmonds, M., & Liggins, P. (2024). The role of pre-eruptive exsolved volatile segregation on observations of volcanic deformation and degassing. <https://doi.org/10.1016/j.epsl.2023.118548>

**Author contribution and declaration:** J. Biggs and M. Edmonds provided supervision throughout this chapter. The thermodynamic model EVo was developed by P. Liggins under the guidance of O. Shorttle, who also provided advice throughout. K. Cashman, J. Gottsmann and A. Rust contributed to insightful discussions that enhanced the quality of this work.

### **Abstract**

The presence of exsolved gas bubbles influences measurements of both volcanic surface deformation and SO<sub>2</sub> emissions. In a closed-system, exsolved volatiles remain within the melt but in an open-system, the decoupled gas phase can either outgas or accumulate, leading to large variations magmatic gas fraction. Here we investigate the role of gas volume fraction and gas segregation processes on magma properties and co-eruptive monitoring data. First we use thermodynamic models of gas exsolution to model gas volume fraction and magma compressibility, and use these to calculate SO<sub>2</sub> emissions and co-eruptive volume change. We find that volume change is equally sensitive to magma compressibility and chamber compressibility over realistic parameters ranges, and both must be considered when interpreting surface deformation data. Reservoir depth and magma composition are the dominant controls on gas volume fraction, but the initial content of H<sub>2</sub>O and S have strong influences on volume change and SO<sub>2</sub> emissions, respectively. Pre-eruptive gas accumulation produces increased SO<sub>2</sub> emissions and muted co-eruptive deformation, while degassing has the opposite effect. We then compare our models to a compilation of data from 20 recent eruptions where measurements of volume change, SO<sub>2</sub> emissions and erupted volume are available. To the first order, shallow reservoirs produce smaller volume changes per volume erupted and silica-poor magmas yield greater co-eruptive volume changes than silica-rich systems, consistent with closed system degassing. Co-eruptive degassing causes high SO<sub>2</sub> emissions during effusive eruptions. Comparison between model predictions and observations suggests that all magmatic systems experience a certain degree of outgassing prior to an eruption. Our findings are consistent with current conceptual models of transcrustal magmatic systems consisting of heterogeneous mixtures of gas and melt and have important implications for the interpretation of surface deformation and SO<sub>2</sub> emission signals at all stages of the eruption cycle.

## 3.1 Introduction

Measurements of surface deformation and SO<sub>2</sub> emissions are becoming increasingly routine and can be used to study volcanic and magmatic processes and in the forecasting of eruptions (Biggs and Wright, 2020; Pritchard et al., 2022). However, most studies consider either deformation or SO<sub>2</sub> emissions in isolation (e.g., Sigmarsson et al., 2013; Hreinsdóttir et al., 2014; Hotta et al., 2019) or combine them in a qualitative manner (e.g., Sheldrake et al., 2017; Reath et al., 2020; Joseph et al., 2022). We seek to develop a robust physics-based framework that can combine measurements of deformation and SO<sub>2</sub> degassing to provide new insights into magmatic processes. The key to this framework is the exsolved volatile content of the magma which determines magma compressibility, and hence modulates observations of both surface deformation and SO<sub>2</sub> emissions (e.g., Kilbride et al., 2016; Yip et al., 2022).

Volatiles typically make up a few weight percent of magmas, yet are of significant importance in controlling the magnitude and style of volcanic eruptions (e.g., Woods and Huppert, 2003; Cashman, 2004; Cassidy et al., 2018). Volatile solubility is controlled by pressure, temperature and melt composition, and volatile exsolution can be driven by either magma ascent or isobaric crystallisation (e.g., Candela, 1997; Burgisser et al., 2015; Liggins et al., 2020). Once exsolved, the gas bubbles can decouple from the melt and whether they accumulate (e.g., Oppenheimer et al., 2015; Parmigiani et al., 2016), or escape via permeable networks (e.g., Chiodini et al., 2005; Kushnir et al., 2017; Colombier et al., 2021) has significant implications for the magnitude of co-eruptive deformation and degassing. We hypothesise that the accumulation of exsolved volatiles will 1) produce ‘excess’ SO<sub>2</sub> emissions during eruptions (e.g., Wallace and Gerlach, 1994; Wallace, 2001) and 2) reduce syn-eruptive surface deformation by increasing magma compressibility (Rivalta and Segall, 2008; Kilbride et al., 2016; Yip et al., 2022). Conversely, inter-eruptive degassing will reduce syn-eruptive SO<sub>2</sub> emissions and reduce magma compressibility such that the volume of material erupted is roughly equal to the subsurface volume change.

In this study, we use thermodynamic models to investigate the effects of exsolved gases on magma properties, deformation and SO<sub>2</sub> emissions. In Section 3.2, we explore the effects of varying magma composition and initial volatile contents and in Section 3.3, we explore the role of pre-eruptive volatile segregation processes (i.e., exsolved volatile



accumulation at the reservoir roof, or the formation of a ‘degassed plug’). Finally, in Section 3.4, we compare observations of real-world eruption data to our model predictions and discuss the implications of pre-eruptive exsolved volatile segregation on observations of volcanic deformation and SO<sub>2</sub> emissions.

## 3.2 Model Setup

### 3.2.1 Thermodynamic framework

Volatile solubility is controlled by melt chemistry, pressure and temperature conditions and fugacity. Magmas can reach volatile saturation by either decompression during ascent or isobaric crystallisation during cooling (e.g., Candela, 1997; Edmonds and Woods, 2018). Thermodynamic models (e.g., MELTS (Ghiorso and Sack, 1995; Asimow, 1998); SolEx (Witham et al., 2012); D-Compress (Burgisser et al., 2015)) use solubility laws and petrological data to predict the proportion of each species (e.g., H<sub>2</sub>O, CO<sub>2</sub>, S) that will exsolve at given pressure, temperature, melt composition and  $f_{O_2}$  and hence the gas fraction of each species. However, these models do not include sulfide and sulfate capacity laws to model sulfur behaviour (Ding et al., 2023).

Here we use the Python-based model, EVo (Liggins et al., 2020, 2022), to model the exsolution of H<sub>2</sub>O, CO<sub>2</sub> and SO<sub>2</sub> species in a C-O-H-S-Fe system during magma decompression. EVo uses the recently released thermodynamic models including the CO<sub>2</sub> solubility model of Eguchi and Dasgupta (2018), the sulfide capacity law from O’Neill (2021) and the sulfate capacity law from Nash et al. (2019) which is applicable at pressures of 300 MPa or less. We note that the sulfide capacity law used is most suitable for more reduced melts than those considered in our study (O’Neill, 2021). However, a recent study by Ding et al. (2023), which compared the different sulfide and sulfate capacity laws of Nash et al. (2019) and O’Neill and Mavrogenes (2022), shows that for a given temperature and composition the sulfur degassing pathways are similar regardless of the different laws used.

The thermodynamic model requires an estimate of initial volatile contents to begin calculations, which can be obtained using melt inclusions for basaltic magmas (Yip et al., 2022). However, for evolved magmas, where gas exsolution starts deep and a gas phase co-exists with the liquid magma during entrapment, melt inclusions often

underestimate actual volatile content (Johnson et al., 1994; Scaillet and Pichavant, 2003). Thus we consider two types of models: those using initial volatile contents estimated from global compilations of melt inclusion studies (Wallace, 2005; Ruscitto et al., 2012) and those based on the formation of rhyolitic magmas by fractional crystallisation of a primitive basaltic melt (Supplementary Material B.1). For basalts with 3 wt% water, 90% fractional crystallisation would result in rhyolites with over 30 wt% water. Such high volatile content is unlikely to be retained, therefore, we select a parameter range between the calculated values for rhyolite and the primitive basalt: 5-15 wt% H<sub>2</sub>O; 1-3 wt% CO<sub>2</sub> and 1800-4200 ppm S (Supp. Table B.1).

We chose the model starting depth by calculating the volatile saturation pressure for the specified composition and volatile content following the method of Liggins et al. (2022). We then decrease the pressure in a step-wise manner, calculating the mole fraction of exsolved volatiles for a number of species (e.g., H<sub>2</sub>O, CO<sub>2</sub>, SO<sub>2</sub>, H<sub>2</sub>S) at each step assuming closed-system degassing and thermodynamic equilibrium. From this, we can calculate the total gas fraction and magma density for a chamber at any given depth (Yip et al., 2022), and in Section 3.4, we then compare these general models to specific case studies where the chamber depth is known from geophysical or petrological constraints.

We assume the amount of exsolved SO<sub>2</sub> is equal to the co-eruptive SO<sub>2</sub> yield (Kilbride et al., 2016; Yip et al., 2022). In order to account for differences in eruption size, we define normalised SO<sub>2</sub> ( $\bar{S}$ ) as the observed SO<sub>2</sub> emitted ( $E^{\text{SO}_2}$ ), normalised by the volume of magma erupted ( $V_e$ ; assuming dense-rock equivalent, DRE):

$$\bar{S} = \frac{E^{\text{SO}_2}}{V_e} = \frac{m^{\text{SO}_2} M^{\text{SO}_2} \rho_e w_g}{M_g}, \quad (3.1)$$

where  $m^{\text{SO}_2}$  is the mole fraction of SO<sub>2</sub> in gaseous phase,  $M^{\text{SO}_2}$  is the molecular mass of SO<sub>2</sub>,  $\rho_e$  is the erupted rock density,  $w_g$  is the gas weight fraction, and  $M_g$  is the mean molecular mass of gas phase. In reality, co-eruptive exsolution and/or SO<sub>2</sub> scrubbing may modulate this value and these secondary processes are discussed further in Section 3.3.1.

We use the estimated magma density ( $\rho_m$ ) to calculate the magma compressibility using the equation  $\beta_m = \frac{1}{\rho_m} \frac{\delta \rho_m}{\delta p}$  (Rivalta and Segall, 2008). The normalised volume change

during an eruption can then be denoted as  $\bar{V}$ :

$$\bar{V} = \frac{\Delta V_c}{V_e} = \left(1 + \frac{\beta_m}{\beta_c}\right)^{-1}, \quad (3.2)$$

where  $\beta_c$  is the compressibility of the chamber, which depends on its geometry and material properties (e.g. Amoroso and Crescentini, 2009; Yip et al., 2022). For our model simulations, we use  $\beta_c = 10^{-10} \text{ Pa}^{-1}$  for our initial models and explore this further in Section 3.2.3.

### 3.2.2 Effect of Magma Composition

Our goal is to apply this framework to understand global patterns of degassing and deformation, spanning the full range of eruption types and magma compositions. Here we conduct sensitivity tests for rhyolitic magmas, building on the work of Yip et al. (2022) who conducted similar tests for basaltic magmas. We then compare our results across the full range of magma compositions.

We explore the effects of varying the weight fraction of magmatic volatile content ( $w^{\text{H}_2\text{O}}$ ,  $w^{\text{CO}_2}$ ,  $w^{\text{S}}$ ) and oxygen fugacity by performing one-at-a-time sensitivity tests, which vary a chosen parameter while keeping the other parameters constant (Figure 3.1; Supp. Table B.2). The sensitivity analysis reveals the role of each parameter on degassing and deformation, but does not consider the co-dependence of input variables, meaning some parameter combinations are not physically realistic.

The effects of varying  $w^{\text{H}_2\text{O}}$ ,  $w^{\text{CO}_2}$ ,  $w^{\text{S}}$  and  $f_{\text{O}_2}$  in rhyolitic magmas are similar to those reported by Yip et al. (2022) for basalts. Namely, 1) water-rich magmas generate higher  $\bar{S}$  than water-poor magmas and are more compressible, meaning  $\bar{V}$  is lower, 2) increasing  $S$  and  $f_{\text{O}_2}$  results in a higher  $\bar{S}$ , but these parameters have minimal impact on  $\bar{V}$ ; and 3) increasing  $\text{CO}_2$  causes a small increase in  $\bar{S}$  and a small decrease in  $\bar{V}$  (Figure 3.1; Supp. Table B.2). For comparison, we also show the model results using melt inclusions to determine the initial volatile content (red lines; Figure 3.1). These are only applicable at depths 5 km and show a lower  $\bar{S}$  and higher  $\bar{V}$  due to the much lower volatile contents.

Next we compare our model results for 1) water-poor rhyolite ( $w^{\text{H}_2\text{O}} = 5.0 \text{ wt\%}$ ) and 2) water-rich rhyolite ( $w^{\text{H}_2\text{O}} = 15 \text{ wt\%}$ ) with the model results of Yip et al. (2022) for 3) water-poor basalts from ocean island settings ( $w^{\text{H}_2\text{O}} = 1.0 \text{ wt\%}$ ) and 4) water-rich

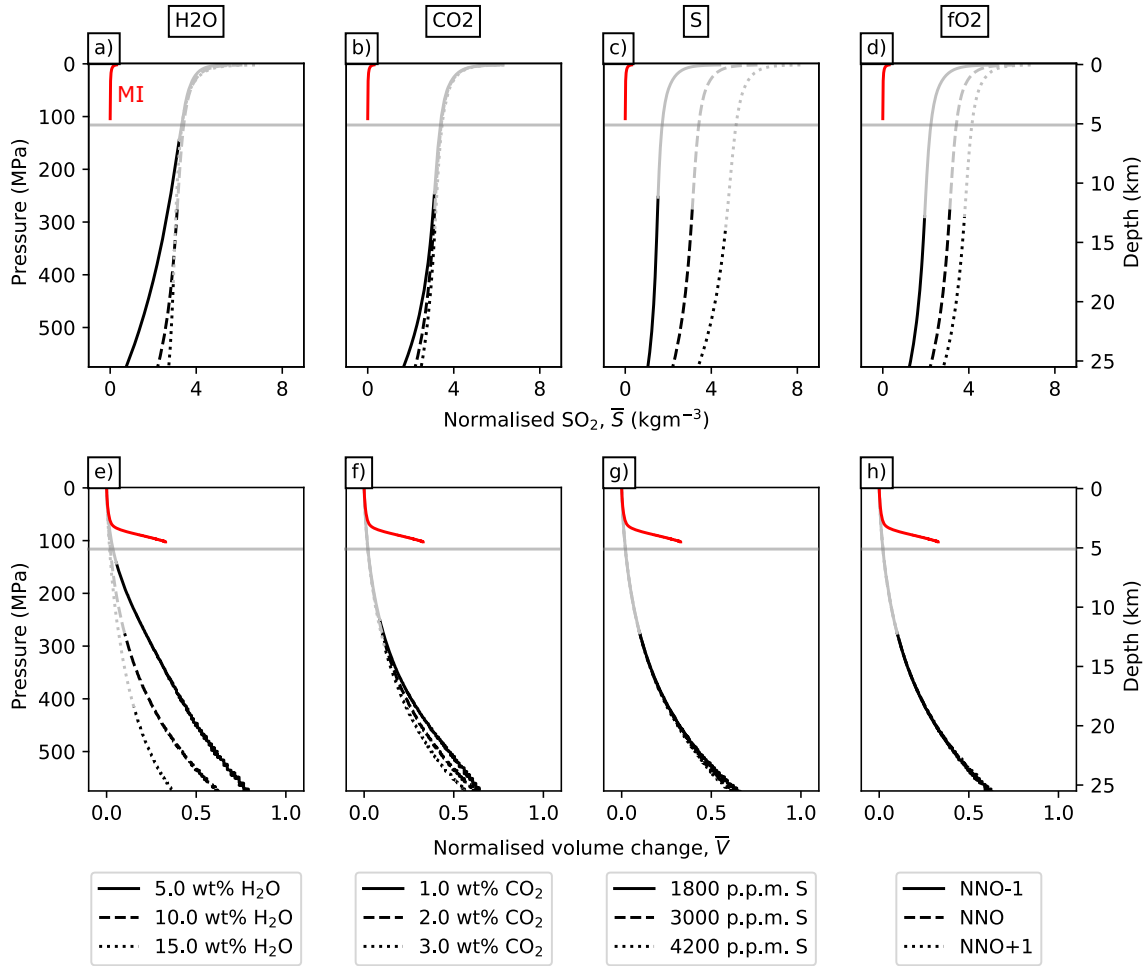


FIGURE 3.1. Sensitivity tests showing the physicochemical properties of rhyolite when varying magmatic volatile content and oxygen fugacity. The observable parameters, namely (a-d) normalised  $\text{SO}_2$  ( $\bar{S}$ ) and (e-h) normalised volume change ( $\bar{V}$ ), are shown when varying  $\text{H}_2\text{O}$ ,  $\text{CO}_2$ , S and oxygen fugacity, while the rest of the parameters are kept constant.  $\bar{S}$  and  $\bar{V}$  calculated using melt inclusion data (MI) are shown as red lines. The grey lines in each panel represent magma properties after exceeding the percolation threshold,  $\phi_c = 17$  vol%. Initial volatile contents are  $w^{\text{H}_2\text{O}} = 10.0 \pm 5.0$  wt%,  $w^{\text{CO}_2} = 2.0 \pm 1.0$  wt%,  $f_{\text{O}_2} = \text{NNO} \pm 1$  and  $w^{\text{S}} = 3000 \pm 1200$  ppm (Supp. Table B.1).

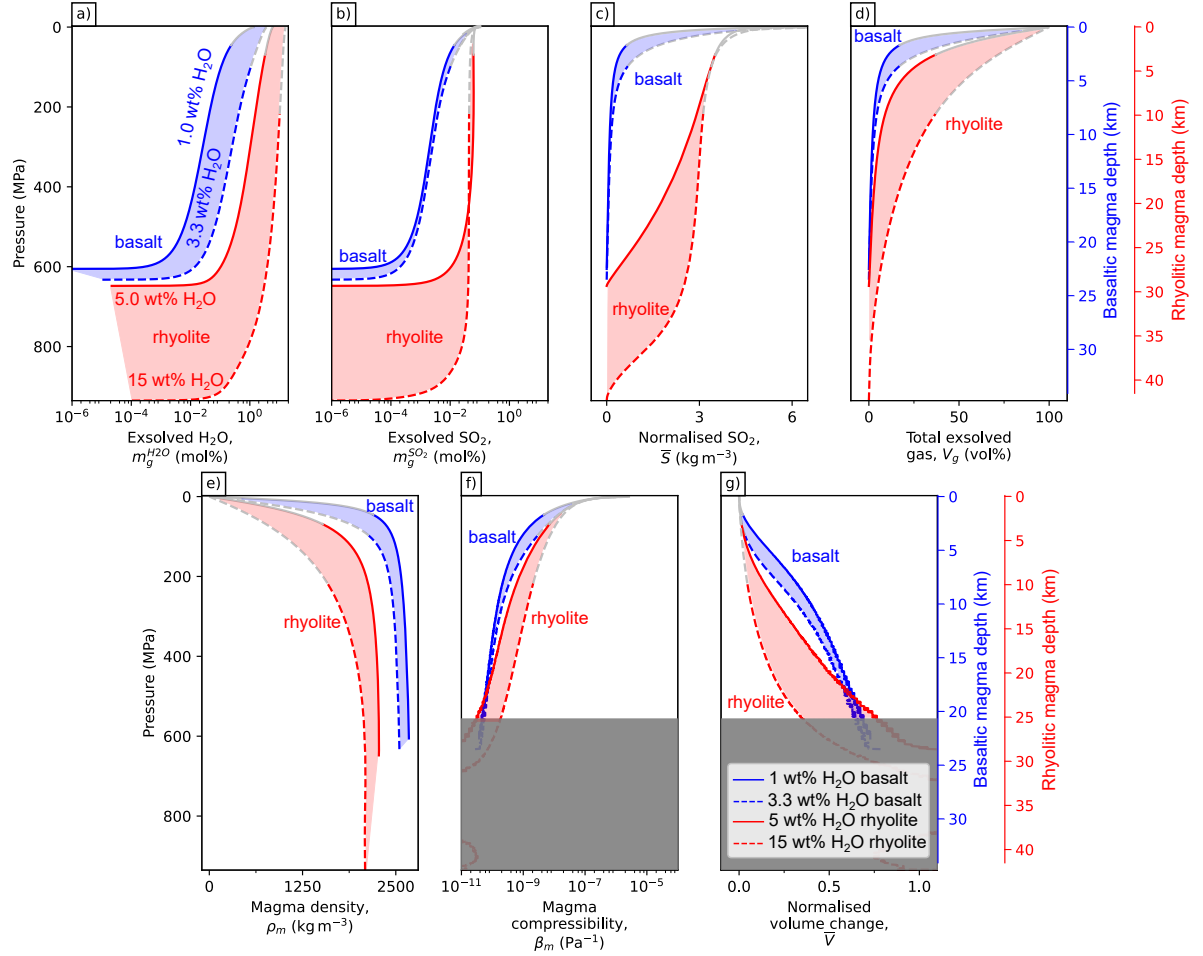


FIGURE 3.2. Comparison of model predictions for basaltic eruptions (blue) and rhyolitic eruptions (red), and water-poor (full line) and water-rich (dashed line) compositions. Initial volatile contents are listed in Supplementary Table B.1. Mole fraction of exsolved (a)  $\text{H}_2\text{O}$  and (b)  $\text{SO}_2$  in gas phase. (c) Mass of  $\text{SO}_2$  gas per unit volume of magma, also defined as normalised  $\text{SO}_2$  ( $\bar{S}$ ). (d) Volume fraction of exsolved gases in magma ( $V_g$ ). (e) Magma density ( $\rho_m$ ). (f) Magma compressibility ( $\beta_m$ ). (g) Model predicted volume change normalised by unit volume of magma ( $\bar{V}$ ). Depths below 580 MPa for panels f-h are shaded due to fluctuations in magma density at high pressures. The grey lines represent magma properties after exceeding the percolation threshold:  $\phi_c = 17$  vol% for rhyolites and  $\phi_c = 37$  vol% for basalts. The grey shaded area in panel f-g are to mask out erroneous results caused by the fluctuations in density gradient at high pressure due to numerical artefacts during modelling. Additionally, the modelling results for magma compressibility and normalised volume change at such depths (20 and 25 km for basalt and rhyolite respectively) would not be very reliable.

basalts from arc settings ( $w^{\text{H}_2\text{O}} = 3.3 \text{ wt\%}$ ) (Figure 3.2). Full details of the initial volatile contents are given in Supplementary Table B.1. As expected, we find that both water-rich and water-poor rhyolites exsolve more  $\text{H}_2\text{O}$  and  $\text{SO}_2$  gas than even the most water-rich basalts and hence produce greater  $\bar{S}$  (Figure 3.2a-c). Not only do the rhyolitic magmas have a higher initial sulfur content, the sulfur also preferentially partitions into the  $\text{H}_2\text{O}$  gas phase which forms at higher pressures in rhyolitic magmas (Figure 3.2c). Since water content is the primary control on magma compressibility, rhyolitic magma, which contains more exsolved  $\text{H}_2\text{O}$  gas than basaltic magma (Figure 3.2a), is more compressible and has lower  $\bar{V}$  (Figure 3.2f-h).

### 3.2.3 Effect of chamber compressibility

Chamber compressibility can vary over orders of magnitude depending on crustal material properties and chamber geometry (Rivalta and Segall, 2008; Anderson and Segall, 2011) and may also change over time due to fracturing and alteration (Carrier et al., 2015; Heap et al., 2020). Here we use our model to compare the relative effects of magma compressibility and chamber compressibility on volume change. We use the model of Heap et al. (2020) to estimate realistic elastic moduli for intact and fractured host rocks at depths of 2-10 km (Fig 3a). Assuming a spherical or prolate reservoir, this gives chamber compressibilities in the range  $6.0 \times 10^{-11} \text{Pa}^{-1} < \beta_c < 3.3 \times 10^{-10} \text{Pa}^{-1}$ , but oblate reservoirs are less compressible with values as high as  $\beta_c = 1.6 \times 10^{-8} \text{Pa}^{-1}$  (Fig 3b). This range is similar to the range of magma compressibilities at similar depths ( $1.5 \times 10^{-10} \text{Pa}^{-1} < \beta_m < 2.0 \times 10^{-8} \text{Pa}^{-1}$ ). We then use these values to calculate the ratio  $\frac{\beta_c}{\beta_m}$  and  $\bar{V}$  for the range of magma compositions and volatile contents considered in Section 3.3.2 (water-rich rhyolites, water-rich basalts, water-poor rhyolites and water-poor basalts). The results show that the normalised volume change is equally sensitive to variations in magma compressibility and chamber compressibility over realistic ranges, and both must be considered when analysing individual case studies (Fig 3c,d).

## 3.3 Pre-eruptive gas segregation

### 3.3.1 Conceptual Model

The terms ‘open’ and ‘closed’ are often used to describe simple conceptual models of volcanic behaviour, but are used by different communities in different ways (e.g., Newhall, 2007; Chaussard et al., 2013; Burgisser et al., 2015). When applied to degassing processes,

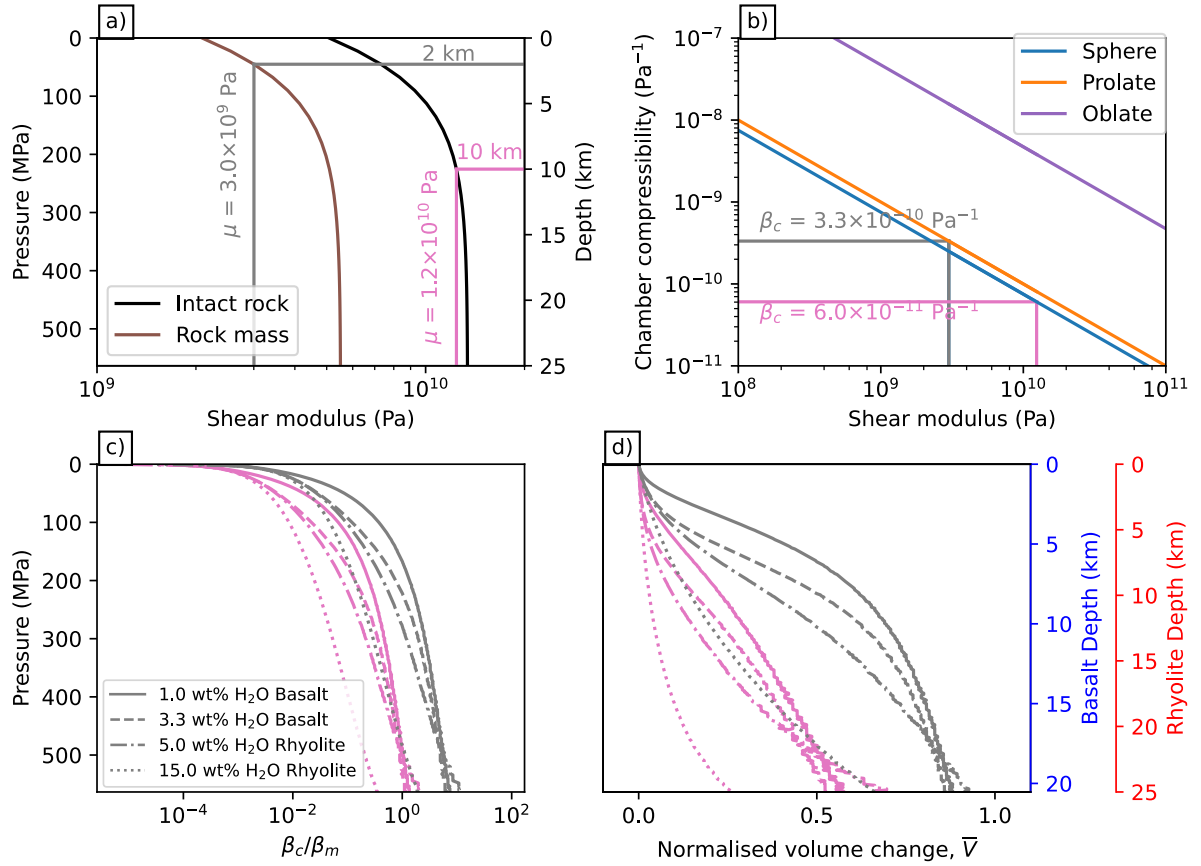


FIGURE 3.3. Sensitivity tests showing the effects of chamber compressibility on deformation. (a) Crustal shear modulus as a function of depth calculated using the model of Heap et al. (2020) for intact rocks and the rock mass. (b) The chamber compressibility as a function of shear modulus for different geometries calculated using the equations from Anderson and Segall (2011). (c) The ratio of chamber to magma compressibility ( $\frac{\beta_c}{\beta_m}$ ) and (d)  $\bar{V}$  for the range of magma compositions and volatile contents, which are listed in Supplementary Table B.1.

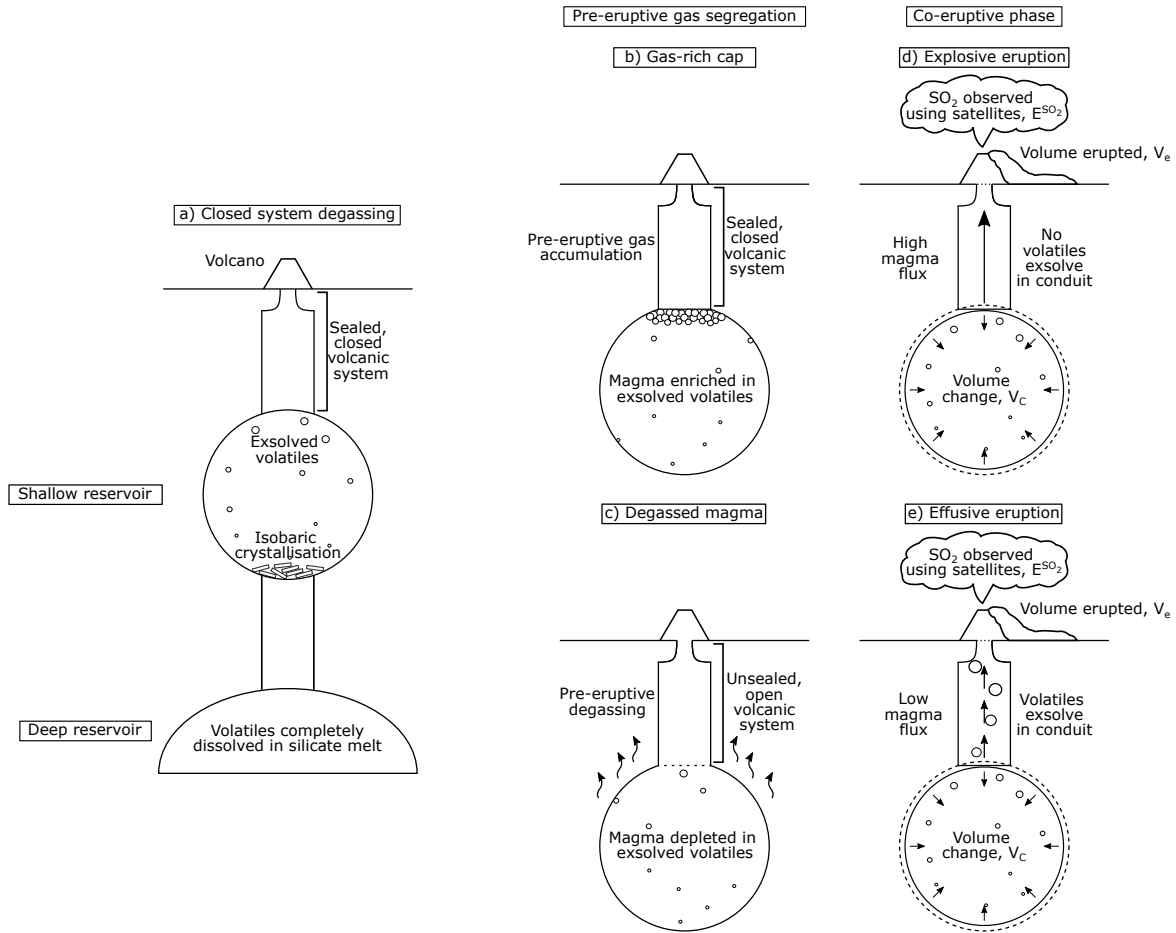


FIGURE 3.4. Conceptual model of gas segregation within magmatic system. (a) Volcano with chambers at different depths. Magmatic volatiles are highly soluble in deep magmatic chambers and thus remain dissolved in the silicate melt. In the shallow chamber, volatiles exsolve during closed system degassing and/ or isobaric crystallisation. (b) A closed volcanic system in which the exsolved gas phase segregated from the melt rises buoyantly and accumulates in the roof zone of a magma reservoir. (c) An open volcanic system with interconnected permeable pathways that allows magma outgassing, removing exsolved volatiles from the reservoir. (d) Explosive eruptions with rapid magma removal and decompression, which results in little volatile exsolution during magma ascent. (e) Effusive eruptions have a low magma ascent rate between the chamber and the surface, allowing volatile exsolution in the conduit, i.e., co-eruptive degassing.



the terms ‘open’ and ‘closed’ describe whether the exsolved volatiles remain in contact and in equilibrium with melt or not (e.g., Burgisser et al., 2015). For closed degassing, exsolved volatiles remain in physical contact with the melt and propagate at the same speed, while open degassing implies that exsolved volatiles are removed instantaneously (Burgisser et al., 2015). When applied to volcanic systems, the term ‘closed’ means that the system is sealed: no gas can escape from the reservoir (i.e., gas accumulates) and deformation may occur due to the build-up of pressure. Conversely, open volcanic systems may allow outgassing without observable deformation (Chaussard et al., 2013) (Figure 3.4b-c). In reality, most volcanoes show time-varying behaviour including elements of both open- and closed-systems and degassing processes (Reath et al., 2019).

Here, we use the term ‘pre-eruptive gas accumulation’ to refer to open degassing in a closed volcanic system - exsolved volatiles segregate from the melt and accumulate in shallow reaches of the reservoir, forming a gas-rich cap (Figure 3.4b). We use ‘pre-eruptive degassing’ to refer to open degassing in an open volcanic system whereby exsolved volatiles are removed entirely (also called ‘passive degassing’) (Figure 3.4c). We use the term ‘co-eruptive degassing’ to describe an effusive eruption where magma rises sufficiently slowly from the reservoir to the surface that additional exsolution and open degassing occurs during the eruption itself (Figure 3.4e). During an explosive eruption, we assume that no additional volatiles exsolve during magma ascent and that the volatiles are in equilibrium with reservoir pressure (Figure 3.4d). However, we note that volatiles can continue to exsolve to a certain extent during explosive eruptions. For instance, despite the explosive nature of the 2011 eruption of Grimsvötn, the volatile content in the groundmass is observed to be less than that in melt inclusions (Sigmarsson et al., 2013). This means that our model may underestimate the normalised  $\text{SO}_2$  of an eruption if we were to extract the calculated value at reservoir depth. This is further discussed in Section 3.4.2 as we model  $\text{SO}_2$  emissions as a function of depth. In both cases, secondary processes including high-temperatures gas-fluid, gas-magma and gas-rock interactions may reduce the observed  $\text{SO}_2$  emissions (Symonds et al., 2001; Casas et al., 2019).

The efficiency by which exsolved volatiles can outgas from magmatic systems is governed by permeability and pore connectivity (Colombier et al., 2017). To the first-order, the transition between closed- and open-system degassing occurs at a critical porosity, called the percolation threshold ( $\phi_c$ ), which depends on the pore size distribution, ground mass

crystallinity, degree of deformation and vesiculation processes amongst others (Colombier et al., 2017, 2020). The resulting wide range and natural variability in percolation thresholds prevents us incorporating these concepts directly in our numerical models. However, Colombier et al. (2020) identify two distinct regimes – at low melt viscosity or low gas overpressure, viscous bubble growth dominates and the percolation threshold,  $\phi_c > 0.37$ , whereas at high viscosity or high gas overpressure systems, fracture-driven processes dominate and the percolation threshold is much lower  $\phi_c \sim 0.17$ . Therefore, we indicate the point at which the gas volume fraction ( $V_g$ ) reaches the percolation threshold of  $\phi_c = 0.17$  using grey lines in Figures 3.1, 3.2 and 3.5.

It is worth noting that magma below the percolation threshold can still undergo pre-eruptive degassing (e.g., Rust and Cashman, 2004; Parmigiani et al., 2017; Colombier et al., 2022). This process includes bubble deformation through shearing (Oppenheimer et al., 2015; Lindoo et al., 2017), partial bubble collapse (Westrich and Eichelberger, 1994; Rust and Cashman, 2004) and fracture-driven processes (Oppenheimer et al., 2015; Parmigiani et al., 2017; Collombet et al., 2021). Additionally, crystal content in the magma increases bubble number density (Hurwitz and Navon, 1994; Burgisser et al., 2017; Cáceres et al., 2020), promotes bubble coalescence (Blower, 2001; Cáceres et al., 2022) and redistributes porosity (Laumonier et al., 2011; deGraffenried et al., 2021), which can enhance outgassing even at low porosity and deep in the conduit (Colombier et al., 2022).

### 3.3.2 Modelling Gas Segregation

To model magmatic systems where the gas segregates from the melt and either accumulates in certain areas or degases prior to eruption, we adjust the gas volume fraction ( $V_g$ ) calculated by EVo and consider the effect on magma density and compressibility. We use a proportion,  $k$ , to calculate the gas volume fraction accounting for pre-eruptive exsolved volatile accumulation or loss from magma ( $V'_g$ ):

$$V'_g = V_g + k V_g. \quad (3.3)$$

Positive  $k$  represents pre-eruptive gas accumulation, while negative  $k$  represents pre-eruptive degassing, where  $k$  is always  $-1 < k < 0$ . Magma density ( $\rho_m$ ) is the weighted average of the volatile-free magma density ( $\rho_M$ ) and the gas density ( $\rho_g$ ):

$$\rho_m = \rho_M(1 - V_g) + \rho_g V_g. \quad (3.4)$$

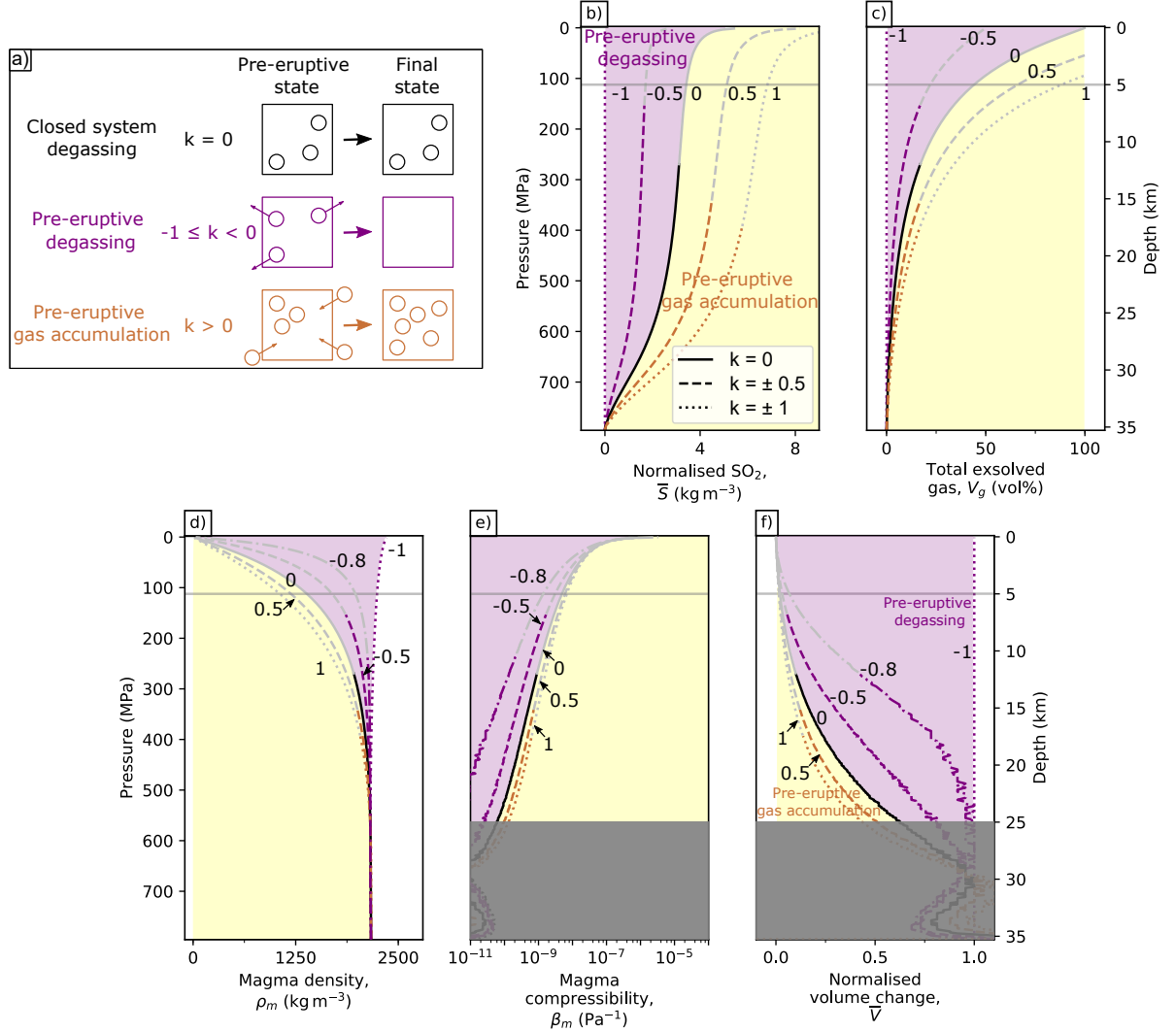


FIGURE 3.5. Model predictions considering pre-eruptive gas segregation processes. (a) Conceptual model of pre-eruptive volatile segregation, where constant  $k$  represents volatile segregation processes. Positive  $k$  represents pre-eruptive gas accumulation and negative  $k$ , such that  $-1 < k < 0$ , represents pre-eruptive degassing. (b-g) Magma properties of rhyolite with pre-eruptive volatile segregation.  $k = 0.8$  is included in panel d-g. The grey lines represent magma properties after exceeding percolation threshold  $\phi_c = 17$  vol%. Fixed parameters:  $w^{\text{H}_2\text{O}} = 10.0$  wt%,  $w^{\text{CO}_2} = 2.0$  wt%,  $w^{\text{S}} = 3000$  ppm. Explanation for grey shaded area is in Figure 3.2.

The magma density with varying gas content ( $\rho'_m$ ) can then be calculated by combining Equation 3.3 and 3.4 (see also B.2):

$$\rho'_m = \frac{\rho_M + V_g[\rho_g(1+k) - \rho_M]}{1 + k V_g}. \quad (3.5)$$

### 3.3.3 Model Results

We use this model to explore the effects of pre-eruptive gas accumulation and degassing on magma properties and co-eruptive observations of  $\bar{S}$  and  $\bar{V}$  (Figure 3.5). We vary  $k$  from  $-1$  to  $+1$  and use the default parameters of  $w^{\text{H}_2\text{O}} = 10.0$  wt%,  $w^{\text{CO}_2} = 2.0$  wt%,  $w^{\text{S}} = 3000$  ppm and  $f_{\text{O}_2} = \text{NNO}$ . For  $k = +1$ , the gas volume,  $V'_g$ , is twice that predicted by a closed system model ( $k = 0$ ) and  $\bar{S}$  is also doubled (Figure 3.5b-c). The additional volume of exsolved gas reduces the magma density (up to a maximum of 26% at 4.4 km depth) and increases compressibility (up to a maximum of 73% at 11.5 km depth) (Figure 3.5d-e) which reduces  $\bar{V}$  by up to 27% at 20.4 km depth (Figure 3.5f-g). For magmas with even higher values of  $k$ , the gas content exceeds the percolation threshold of 17 vol% (Colombier et al., 2021) and although our model predicts a highly compressible magma with very low  $\bar{V}$ , this is unlikely to be physically realistic.

For  $k = -0.5$  (partial degassing),  $\bar{S}$  and  $V_g$  are lower than for closed-system degassing. The reduced magma compressibility increases  $\bar{V}$  up to a maximum of  $\sim 30\%$  at 16.2 km (Figure 3.5f-g). A completely degassed magma ( $k = -1$ ) will have no gas content, and hence produce no emissions ( $\bar{S} = 0$ ; Figure 3.5b-c). However, because completely degassed magma is denser than the volatile-rich magma at depth (Figure 3.5d) (Stevenson and Blake, 1998), magma density ( $\rho_M$ ) actually increases with decreasing pressure ( $< 25$  km). Consequently, we cannot use this model to estimate compressibility when  $k < -0.8$  (Figure 3.5e-g) (Supp. Table B.2).

## 3.4 Comparison to Observations

In this section, we compile observations of ground deformation,  $\text{SO}_2$  emissions, volume of magma extruded and reservoir depth for eruptions with a range of magma compositions and compare them to our model results. The goal is to understand pre- and co-eruptive degassing processes and their implications for interpreting volcano monitoring data.

# CHAPTER 3. THE ROLE OF PRE-ERUPTIVE EXSOLVED VOLATILE SEGREGATION ON OBSERVATIONS OF VOLCANIC DEFORMATION AND DEGASSING

TABLE 3.1. Compilation of observations of normalised volume change,  $\bar{V}_{obs}$ , and normalised  $\text{SO}_2$ ,  $\bar{S}_{obs}$ , source depth and magma composition for 20 recent eruptions. Further details are provided in Supplementary Table B.3-B.9.

Volcano	Eruption Date	$\text{SiO}_2$ wt%	Depth km	$\bar{V}_{obs}$	$\bar{S}_{obs}$ $\text{Tg km}^{-3}$
Augustine, USA	Jan 2006	$57.5 \pm 1.5$	$4.6^{6.6}_{2.6}$		$0.64^{0.82}_{0.55}$
Bezymianny, Kamchatka	Oct 2007	$56.7 \pm 0.2$	$7.5^{9.0}_{6.0}$		$2.64^{3.38}_{1.90}$
Calbuco, Chile	Apr 2015	$54.5 \pm 0.5$	$8.2^{9.5}_{6.6}$	$0.22^{0.37}_{0.07}$	$0.66^{0.98}_{0.34}$
Chaitén, Chile	May 2008	$75.3 \pm 0.3$	$10^{12}_{8.0}$	$0.25^{0.32}_{0.18}$	$0.01^{0.02}_{0.01}$
Eyjafjallajökull, Iceland	Apr-May 2010	$47.4 \pm 1.5$	$4.4^{4.7}_{4.0}$	$0.04^{0.05}_{0.03}$	$3.73^{5.54}_{1.92}$
Fernandina, Galapagos	May 2005	$48.5 \pm 0.5$	$5.0^{6.0}_{4.0}$	$0.80^{0.94}_{0.50}$	$6.67^{8.07}_{4.07}$
Fogo, Cape Verde	Nov 2014-Feb 2015	$45.5 \pm 2.5$	16.5		$10.6^{13.0}_{8.32}$
Grimsvötn, Iceland	May 2011	$49.9 \pm 0.8$	$1.7^{1.9}_{1.5}$	$0.10^{0.13}_{0.07}$	$1.41^{1.88}_{0.94}$
Kelut, Indonesia	Feb 2014	$56.1 \pm 7.3$	$2.1^{2.5}_{1.7}$	$0.03^{0.05}_{0.02}$	$0.95^{1.32}_{0.58}$
Merapi, Indonesia	Nov 2010	$57.8 \pm 2.6$	$15^{20}_{10}$		$3.70^{5.37}_{2.03}$
Mount St. Helens, USA	2004-2008	$64.9 \pm 0.1$	$5.6^{8.3}_{2.9}$	$0.25^{0.32}_{0.18}$	$0.31^{0.37}_{0.25}$
Sierra Negra, Galapagos	Oct 2015	$49.0 \pm 0.9$	$2.1^{2.5}_{1.7}$	$0.52^{0.70}_{0.33}$	$12.4^{16.9}_{7.88}$
Okmok, USA	Jul-Aug 2008	$55.0 \pm 0.3$	$3.0^{4.5}_{1.5}$	$0.32^{0.83}_{0.20}$	$0.65^{1.73}_{0.42}$
Piton de la Fournaise, France	Mar-Apr 2007	$50.0 \pm 0.4$	$2.3^{2.7}_{1.9}$	$0.01^{0.02}_{<0.01}$	$0.99^{1.35}_{0.64}$
Puyehue-Cordón Caulle, Chile	Jun 2011	$75.4 \pm 0.7$	$6.0^{7.0}_{5.0}$	$0.11^{0.14}_{0.07}$	$0.54^{0.70}_{0.39}$
Raikoke, Kuril Islands	Jun 2019	$49.8 \pm 0.5$	$5.0^{7.5}_{2.5}$		$3.42^{5.29}_{2.15}$
Redoubt, USA	Mar-Apr 2009	$60.0 \pm 2.5$	$9.2^{15.2}_{6.9}$	$0.50^{0.74}_{0.26}$	$2.25^{2.89}_{1.61}$
Sarychev Peak, Kuril Islands	Jun 2009	$54.2 \pm 0.2$	$3.5^{5.3}_{1.8}$		$5.84^{8.99}_{2.70}$
Sinabung, Indonesia	Dec 2013-Apr 2014	$59.0 \pm 0.3$	$8.4^{9.9}_{7.4}$	$0.31^{0.43}_{0.19}$	$0.70^{0.89}_{0.51}$
Jebel al Tair, Saudi Arabia	2007-2008	$49.5 \pm 0.6$	$7.0^{15}_{7.0}$		$8.61^{13.2}_{4.41}$

## 3.4.1 Data compilation

Earth-observing satellite missions are now providing global and frequent measurements of volcanic activity, including deformation and  $\text{SO}_2$  degassing (Carn, 2016; Furtney et al., 2018; Ebmeier et al., 2018), while erupted volume can be estimated from many different methods depending on deposit type (Galetto et al., 2023). However, each measurement type has limitations in terms of spatial and temporal resolution meaning that surprisingly few eruptions have measurements of all three parameters required to estimate  $\bar{V}$  and  $\bar{S}$ , namely volume change,  $\text{SO}_2$  emissions and volume erupted. Therefore, we start with the compilation of Kilbride et al. (2016) which lists ‘sulfur yield’ which is equal to  $\bar{S}$  and the ratio,  $r = \frac{1}{\bar{V}}$ , for 11 eruptions. We then expand this dataset by conducting a literature search for additional datapoints based on the Global Volcanism Program (2013) catalogue.

We identified 20 eruptions with known erupted volume and source depth and measurements of co-eruptive  $\text{SO}_2$  degassing or deformation (Figure 3.6). Table 3.1 provides an overview with detailed descriptions provided in Supplementary Table B.3-B.9. Magma compositions are taken from published geochemical studies and divided into two categories: silica-poor eruptions ( $\text{SiO}_2 < 50\text{wt}\%$ ) and silica-rich eruptions ( $\text{SiO}_2 > 50\text{wt}\%$ )

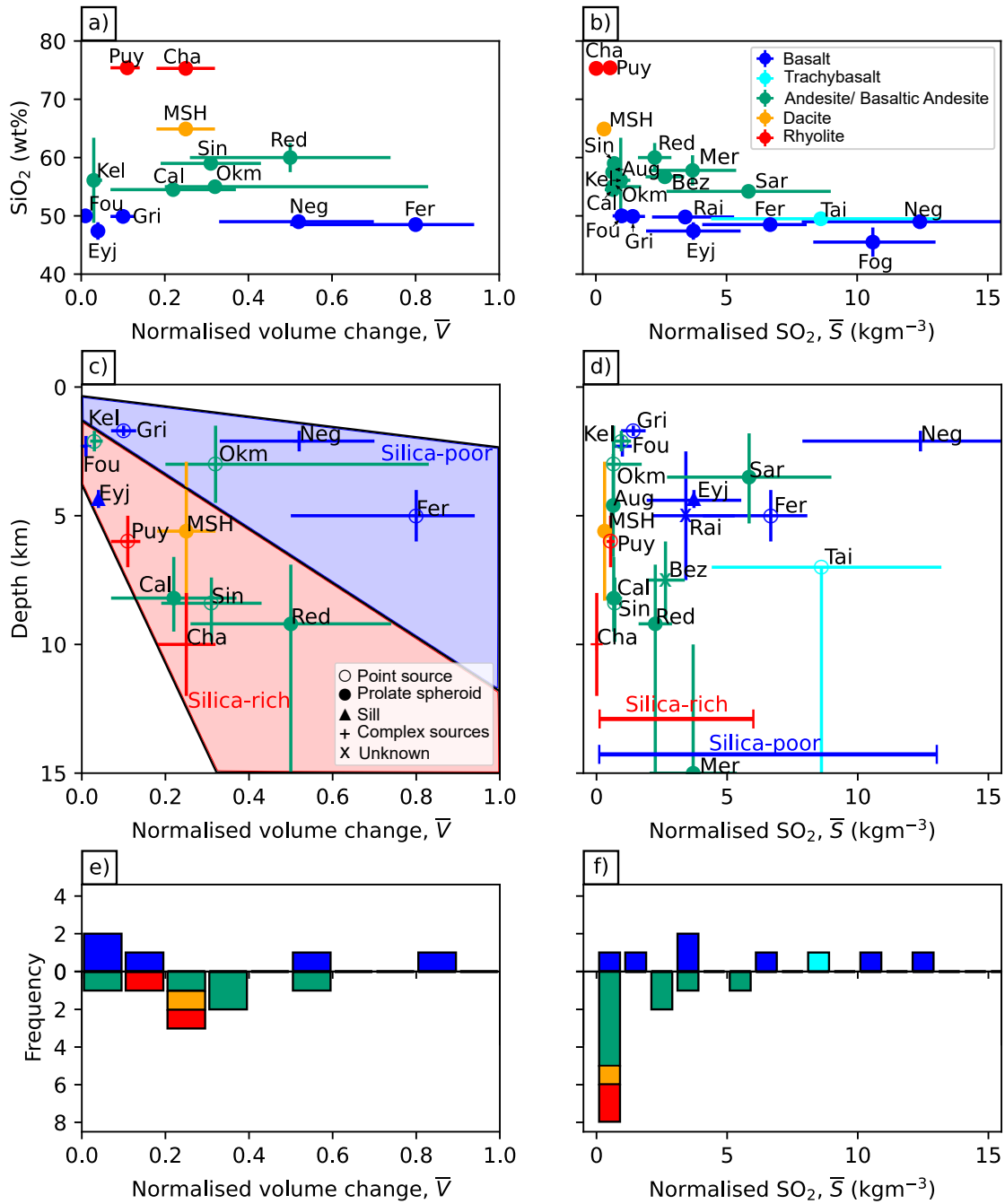


FIGURE 3.6. (page 65): Observations of deformation and SO<sub>2</sub> degassing from 20 eruptions between 2005-2021 (Supp. Table B.3-B.9). The compilation consists of co-eruptive volume change and SO<sub>2</sub> gas emissions, both normalised by the erupted volume. (a-b) Normalised volume change ( $\bar{V}_{obs}$ ) and normalised SO<sub>2</sub> ( $\bar{S}_{obs}$ ) as a function of SiO<sub>2</sub> content. The colours are defined using the GVP classifications and correspond to the following ranges of SiO<sub>2</sub> content: basalt 45-52 wt%; basaltic andesite-andesite 52-63 wt%; dacite 63-70 wt%; rhyolite >70wt%. (c-d) Normalised volume change ( $\bar{V}_{obs}$ ) and normalised SO<sub>2</sub> ( $\bar{S}_{obs}$ ) as a function of reservoir depth. Shaded regions represent the range of observations. (e-f) Frequency plot for  $\bar{V}_{obs}$  and  $\bar{S}_{obs}$ . All data points are colour-coded for magma composition, and the different symbols represent the different reservoir geometry. Data are shown for the following eruptions: (Aug) Augustine, 2006; (Bez) Bezymianny, 2007; (Cal) Calbuco, 2015; (Cha) Chaitén, 2008; (Eyj) Eyjafjallajökull, 2010; (Fer) Fernandina, 2005; (Fog) Fogo, 2014; (Fou) Piton de la Fournaise, 2007; (Gri) Grímsvötn, 2011; (Kel) Kelut, 2014; (Mer) Merapi, 2010; (MSH) Mount St. Helens 2004; (Neg) Sierra Negra, 2005; (Okm) Okmok, 2008; (Puy) Puyehue-Cordón Caulle, 2011; (Rai) Raikoke, 2019; (Red) Redoubt, 2009; (Sar) Sarychev Peak, 2009; (Sin) Sinabung, 2013; (Tai) Jebel at Tair, 2007.

(Figure 3.6). Eruption volumes range from  $10^7$ - $10^9$  m<sup>3</sup> and are collated from published studies using a range of techniques including photogrammetry, digital elevation models and analyses of tephra fall deposits (e.g., Romero et al., 2016; McKee et al., 2021; Galetto et al., 2023). SO<sub>2</sub> measurements are available for all the eruptions using space-borne spectrometers (e.g., Carn, 2016; Ge et al., 2016), except for the 2004 eruption of Mount St. Helens, USA. Volume change estimates are available for 13 eruptions, of which 8 are from InSAR and 5 from GPS (e.g., Hreinsdóttir et al., 2014; Hotta et al., 2019). Reservoir depths are primarily based on geodetic and seismic data, but petrological estimates are used where no geophysical measurements were available (Supp. Table B.7). All depths are equivalent to pressures of less than 300 MPa, compatible with the sulfide and sulfate capacity laws used in our thermodynamic model, EVo (Liggins et al., 2020) with the exception of the 2010 eruption of Merapi.

Ideally, our compilation would also include estimates of chamber compressibility on a case-by-case basis. Of the 20 examples in our compilation, 12 have point or prolate sources, 7 are unknown or complex geometries and only 1 is sill-like (Figure 3.7). However, insufficient information is available on aspect ratios or material properties to calculate individual chamber compressibilities so we consider end member values of

chamber compressibility of  $6 \times 10^{-11} \text{ Pa}^{-1}$  and  $3.3 \times 10^{-10} \text{ Pa}^{-1}$  based on Figure 3.3. These assumptions affect the interpretation of individual systems, but should not affect our overall conclusions (Figure 3.8).

### 3.4.2 Sulfur Dioxide, $\bar{S}$

Observations of  $\bar{S}_{obs}$  from silica-poor eruptions ( $\text{SiO}_2 < 50\text{wt}\%$ ) range from  $<1 \text{ kgm}^{-3}$  for the 2007 eruption of Piton de la Fournaise, France, to  $9 \text{ kgm}^{-3}$  at the 2019 eruption of Raikoke, Japan (Figure 3.6b,d,f). The total mass of  $\text{SO}_2$  emitted is consistent with model predictions for source depths of  $<2 \text{ km}$  even though the reservoirs are at depths of more than  $4 \text{ km}$  (Figure 3.7a). We attribute this to co-eruptive degassing between the reservoir and the surface, consistent with the low sulfur contents of basaltic lava flows (e.g., Sigmarsson et al., 2013; Donovan et al., 2018). In contrast, there is little evidence for co-eruptive degassing in silica-rich eruptions ( $\text{SiO}_2 > 50\text{wt}\%$ ), which have  $\bar{S}_{obs} < 5 \text{ kgm}^{-3}$  and do not cluster around the  $0\text{-}2 \text{ km}$  interval of the model predictions (Figure 3.7b). Co-eruptive degassing preferentially occurs in mafic magmas due to 1) the high temperature, which causes high volatile diffusivity (Baker et al., 2005), and 2) the slow ascent rate of effusive eruptions (Gonnermann and Manga, 2006).

In Figure 3.7c,d we compare the observations of silica-rich eruptions ( $\text{SiO}_2 > 50\text{wt}\%$ ) to the model predictions. We estimate initial  $\text{H}_2\text{O}$  and  $\text{CO}_2$  content using the model of fractional crystallisation and a broad range of initial sulfur contents to represent natural variability (1800-4200 ppm). Six of the silica-rich eruptions have  $\bar{S}_{obs}$  in the range predicted by the closed-system model (Figure 3.7c) but the other six lie close to the  $k = -1$  line, consistent with almost complete pre-eruptive outgassing (Figure 3.7d). However, all the observed eruptions have  $\bar{S}_{obs}$  greater than the model predictions when initial volatile contents are estimated from melt inclusions (Figure 3.7b-c), consistent with the presence of a gas phase (e.g., Wallace and Gerlach, 1994; Wallace et al., 1995).

### 3.4.3 Volume Change, $\bar{V}$

Measurements of normalised volume change,  $\bar{V}_{obs}$ , range from 0.03 to 0.74 with generally lower values for silica-rich eruptions at comparable depths, consistent with higher initial volatile contents (Figure 3.6a,c,e). Both silica-rich and silica-poor categories show a broad trend with larger  $\bar{V}_{obs}$  for deeper reservoirs and smaller  $\bar{V}_{obs}$  for shallower reservoirs. This is consistent with closed-system behaviour: shallower reservoirs are more gas-rich



# CHAPTER 3. THE ROLE OF PRE-ERUPTIVE EXSOLVED VOLATILE SEGREGATION ON OBSERVATIONS OF VOLCANIC DEFORMATION AND DEGASSING

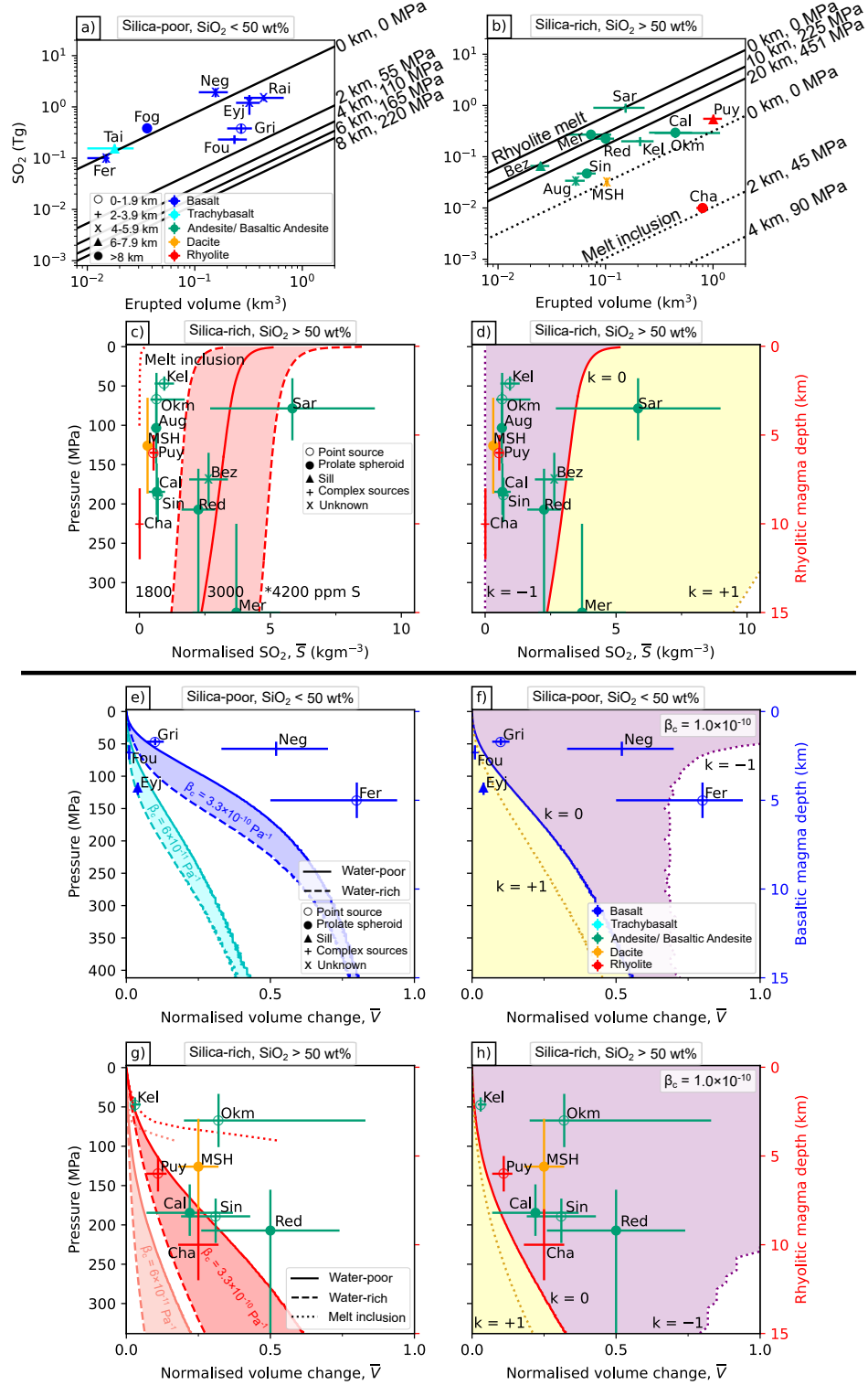


FIGURE 3.7. (page 68): Comparison between model predictions and observations of (a-d) SO<sub>2</sub> degassing and (e-h) co-eruptive volume change (Supp. Table B.3-B.9). The magma composition used for the models are that of a generic basalt and rhyolite, which are presets in EVo, and the volatile content used in the models has been listed in Supplementary Table B.1. (a) Relationship between the erupted volume (dense-rock equivalent, DRE) and the total mass of SO<sub>2</sub> released for eruptions with SiO<sub>2</sub> < 50wt%. The diagonal lines are modelled using an ocean island basalt composition ( $w^{\text{H}_2\text{O}} = 1.0 \text{ wt\%}$ ,  $w^{\text{CO}_2} = 1.0 \text{ wt\%}$ ,  $f_{\text{O}_2} = \text{NNO}$  and  $w^{\text{S}} = 1600 \text{ ppm}$ ; Supp. Table B.1) assuming a closed degassing system. (b) Same as panel a but for eruptions with SiO<sub>2</sub> > 50wt%. The diagonal lines are modelled using magma composition of rhyolite formed by fractional crystallisation (5.0 wt% H<sub>2</sub>O; full line) and melt inclusion data from typical rhyolitic magma (dotted line). (c) Normalised SO<sub>2</sub>,  $\bar{S}_{obs}$  for eruptions with SiO<sub>2</sub> > 50wt% compared to model predictions using different sulfur content (full and dashed lines) and melt inclusions (dotted line) as a function of depth. (d)  $\bar{S}_{obs}$  for eruptions with SiO<sub>2</sub> > 50wt% compared to model predictions for 5 wt% H<sub>2</sub>O rhyolite (full line), with dotted lines representing pre-eruptive exsolved volatile segregation, such that  $k = +1$  represents pre-eruptive gas accumulation and  $k = -1$  represents pre-eruptive degassing. (e) Normalised volume change  $\bar{V}_{obs}$  of eruptions with SiO<sub>2</sub> < 50wt% compared to model predictions for water-rich (dashed line) and water-poor basalts (full line) with chamber compressibilities of  $6 \times 10^{-11} \text{ Pa}^{-1}$  and  $3.3 \times 10^{-10} \text{ Pa}^{-1}$ . (f)  $\bar{V}_{obs}$  of eruptions with SiO<sub>2</sub> < 50wt% compared to model predictions for water-poor basalts (full line), with dotted lines representing pre-eruptive exsolved volatile segregation, such that  $k = +1$  represents pre-eruptive gas accumulation and  $k = -1$  represents pre-eruptive degassing. (g)  $\bar{V}_{obs}$  of eruptions with SiO<sub>2</sub> > 50wt% compared to model predictions for water-rich (15 wt% H<sub>2</sub>O; dashed line), water-poor rhyolites (5.0 wt% H<sub>2</sub>O; full line) and melt inclusions (dotted line) and chamber compressibilities of  $6 \times 10^{-11} \text{ Pa}^{-1}$  and  $3.3 \times 10^{-10} \text{ Pa}^{-1}$ . (h)  $\bar{V}_{obs}$  of eruptions with SiO<sub>2</sub> > 50wt% compared to model predictions for water-poor rhyolites that underwent closed-system degassing (full line) and pre-eruptive gas accumulation and degassing (dotted lines). See Figure 3.5 for additional information on pre-eruptive exsolved volatile segregation. \*In c, the water content is 5wt% for the model run with a sulfur content of 1800 and 3000 ppm and 10 wt% for the model run with a sulfur content of 4200 ppm. All data points are listed in Table 3.1 and colour-coded for magma composition. The different symbols represent the different (a-b) reservoir depths and (c-h) reservoir geometry. Abbreviations are shown in Figure 3.6.

and compressible and hence produce less deformation per unit volume erupted (Kilbride et al., 2016; Yip et al., 2022). However, the scatter suggests that other factors modulate the relationship, such as magmatic volatile content, pre-eruptive gas segregation and chamber compressibility.

In Figure 3.7e, we compare observations of silica-poor eruptions  $\text{SiO}_2 < 50\text{wt}\%$  to the model predictions for basaltic magmas with a range of water contents (1-3.3 wt%  $\text{H}_2\text{O}$ ) and chamber compressibilities ( $6 \times 10^{-11} \text{ Pa}^{-1}$ ;  $3.3 \times 10^{-10} \text{ Pa}^{-1}$ ). Three of the eruptions have a higher  $\bar{V}_{obs}$  than expected, even for water-poor basalts and high chamber compressibilities, indicating the magma is less compressible than can be explained using a closed-system model (Figure 3.7e). Figure 3.7f shows that these eruptions lie in the  $-1 < k < 0$  domain indicating that the magma was partially depleted by outgassing prior to eruption, consistent with observations of passive degassing at mafic volcanoes (e.g., Barry et al., 2014; Carn et al., 2016). The other two eruptions have lower  $\bar{V}_{obs}$  and can either be explained by a low chamber compressibility or pre-eruptive gas accumulation. In the case of the 2010 eruption of Eyjafjallajökull, Iceland, previous studies have suggested that some magma was sourced from a deeper reservoir and hence the co-eruptive volume change is an underestimate (Sigmundsson et al., 2010).

In Figure 3.7g, we compare the observations of silica-rich eruptions ( $\text{SiO}_2 > 50 \text{ wt}\%$ ) to the model predictions using initial  $\text{H}_2\text{O}$  contents of 5 and 15 wt%  $\text{H}_2\text{O}$  from the model of fractional crystallisation (Table 1) and chamber compressibilities of  $6 \times 10^{-11} \text{ Pa}^{-1}$  and  $3.3 \times 10^{-10} \text{ Pa}^{-1}$  (Figure 3.3). For roughly half of the eruptions,  $\bar{V}_{obs}$  lies within the range predicted for closed-system degassing of a chamber with high compressibility (Figure 3.7g), while the others have  $\bar{V}_{obs}$  greater than the predictions for even water-poor rhyolite and high chamber compressibility and lie in the pre-eruptive outgassing regime (Figure 3.7h). However, all but one of the observations can be explained by closed-system degassing, if we use a lower initial water content of 3.3 wt% based on melt inclusion studies (Figure 3.7g).

### 3.4.4 Combining $\bar{V}_{obs}$ and $\bar{S}_{obs}$

Interestingly, although our compilations of  $\bar{V}_{obs}$  and  $\bar{S}_{obs}$  both indicate that many volcanoes experience pre-eruptive outgassing, the measurements are not consistent for individual volcanoes (e.g.,  $\bar{V}_{obs}$  may be in the pre-eruptive outgassing regime but  $\bar{S}_{obs}$  is in the pre-eruptive gas accumulation regime or vice versa). This apparent discrepancy

can be explained by the heterogeneity in sulfur concentration in the melt and uncertainties in  $\text{SO}_2$  detection. For example, the 2008 eruption of Chaitén, Chile lies in the predicted range for  $\bar{V}$ , but not  $\bar{S}$ , and the anomalously low  $\text{SO}_2$  emissions have previously been explained by  $\text{SO}_2$  scrubbing (Carn et al., 2016; Casas et al., 2019).

## 3.5 Discussion

This study provides new insights into the influence of pre-eruptive magma storage conditions and co-eruptive processes on observations of volcanic deformation and degassing. We use numerical models to investigate the role of reservoir depth, water content, sulfur content, chamber compressibility and pre-eruptive gas segregation on observations of volcanic deformation and  $\text{SO}_2$  emissions. The models predict that reservoir depth, chamber compressibility and magma composition will have first-order controls, but that gas segregation processes will also have a significant impact.

Our compilation of eruption data confirms the first-order trend between normalised volume change and reservoir depth, such that shallow reservoirs produce small volume changes. While this is qualitatively consistent with a model of closed-system degassing in which shallow reservoirs contain gas-rich, compressible magma, the scatter suggests that other factors modulate the volume changes of the reservoir, namely magmatic water content and pre-eruptive gas segregation.

Comparison to model predictions suggests that all magmatic systems undergo a certain degree of outgassing prior to an eruption. For evolved magmas, the amount of degassing is similar to or lower than expected if we assume closed system fractional crystallisation, but greater than expected if we only consider the dissolved volatile content preserved in melt inclusions. This is consistent with the model of a transcrustal magmatic system, in which exsolved gas separates from the melt and rises buoyantly to accumulate in different parts of the system. Thus, the gas content of the reservoir from which the magma erupted may be gas-rich compared to predictions based on melt-inclusion data and also partially depleted in gas compared to predictions based on fractional crystallisation. We also find that mafic eruptions typically experience co-eruptive degassing, producing relatively large amounts of  $\text{SO}_2$  per volume erupted despite their low magmatic sulfur content. However, considering the input parameters represents that of a generic basalt and rhyolite, it is also important to acknowledge that the normalised  $\text{SO}_2$  and normalised

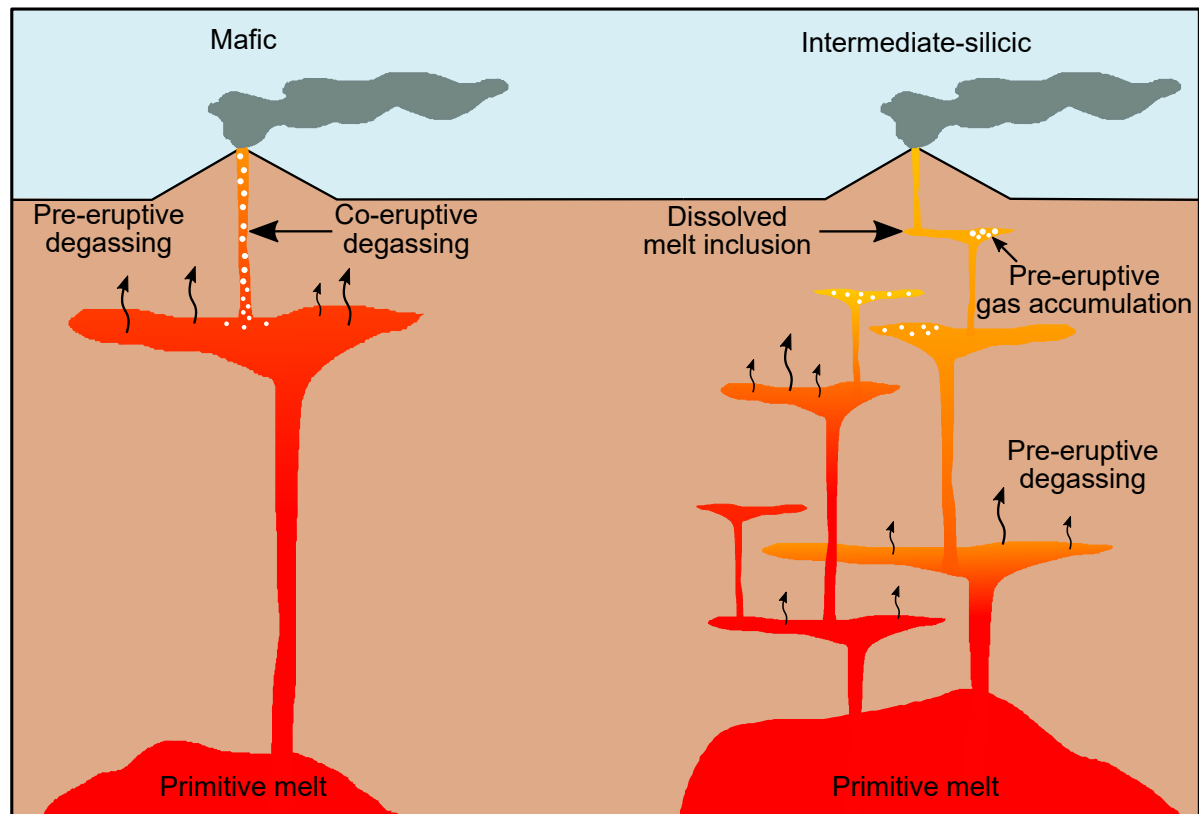


FIGURE 3.8. Conceptual model comparing the magmatic systems feeding silica-rich and silica-poor eruptions. The colour gradient represents magma composition, with red representing primitive melt (i.e., least evolved) and yellow representing evolved, silicic magma. Silica-poor systems (left) have high volatile diffusivity due to high temperature, which allows co-eruptive degassing during magma ascent to the surface. Silica-rich systems (right) have complex transcrustal magmatic systems. Volatile enrichment occurs during the fractional crystallisation of the primitive melt. The volatiles exsolved may accumulate as gas-rich caps or be lost due to outgassing at different parts of the system. The reservoir from which an eruption occurs may therefore be gas-rich or gas-poor relative to the initial magmatic conditions and thus modify observations of co-eruptive volume change and degassing. A fraction of volatiles that is already exsolved may not be recorded in melt inclusion data, thereby underestimating the pre-eruptive gas content in the reservoir and total  $\text{SO}_2$  emissions.

volume changes predicted by the model might exhibit discrepancies when compared to the actual data from specific eruptions.

However, these models are clearly oversimplified and our analysis is limited by a lack of suitable data. We were only able to identify 20 eruptions for which data was available on erupted volume, volume change and SO<sub>2</sub> emissions. Although satellite data now provides compilations of SO<sub>2</sub> emissions and surface deformation (Carn et al., 2016; Ebmeier et al., 2018), these are not provided on an operational basis and not all eruptions are included. To illustrate the challenge, we compared the three best currently-available catalogues: Galetto et al. (2023) for erupted volume, Ebmeier et al. (2018) for volcanic deformation and Carn (2016) for SO<sub>2</sub> emissions (Figure 3.9). Ebmeier et al. (2018) compiled 308 deformation episodes between 1990-2015, of which 78 were related to an eruption. However, source depths were only provided for 45 of these eruptions and there is no information on volume change. Galetto et al. (2023) compiled 682 estimates of mass erupted between 1961-2020, which relates to 209 individual eruptions. Carn (2016) compiled estimates of SO<sub>2</sub> loading for 47 eruptions between 1979-2014. If we restrict these to the overlapping date range of 2005-2014, we are left with 48 eruptions from the Ebmeier et al. (2018) catalogue, 79 eruptions from the Galetto et al. (2023) catalogue and 29 eruptions from Carn (2016). However, of these, there are only 9 eruptions for which all three measurements are available: Chaitén, Chile 2008; Puyehue-Cordón Caulle, Chile, 2011; Sierra Negra, Galapagos, 2005; Tolbachik, Russia, 2012; Jebel at Tair, Saudi Arabia, 2007; Eyjafjallajökull, Iceland, 2010; Piton de la Fournaise, France, 2007 and Merapi, Indonesia, 2010.

Even less information is available about crustal shear modulus ( $\mu$ ). Seismic tomography can be used to estimate material properties, but is only available at a small number of well-studied volcanoes. For example, the compilation of Paulatto et al. (2022) only includes one of the volcanoes in our list: Merapi. Heap et al. (2020) provide a method of estimating depth-dependent rock mass Young's moduli for volcanic rocks; their empirical data is from room pressure or shallow tunnels and it is not yet clear whether the relationships are applicable to rock masses at depths greater than a few hundred metres.

## 3.6 Conclusions

This study provides new insights into the influence of pre-eruptive magma storage conditions and co-eruptive processes on observations of volcanic deformation and degassing. We use numerical models to investigate the role of reservoir depth, water content, sulfur content, chamber compressibility and pre-eruptive gas segregation on observations of

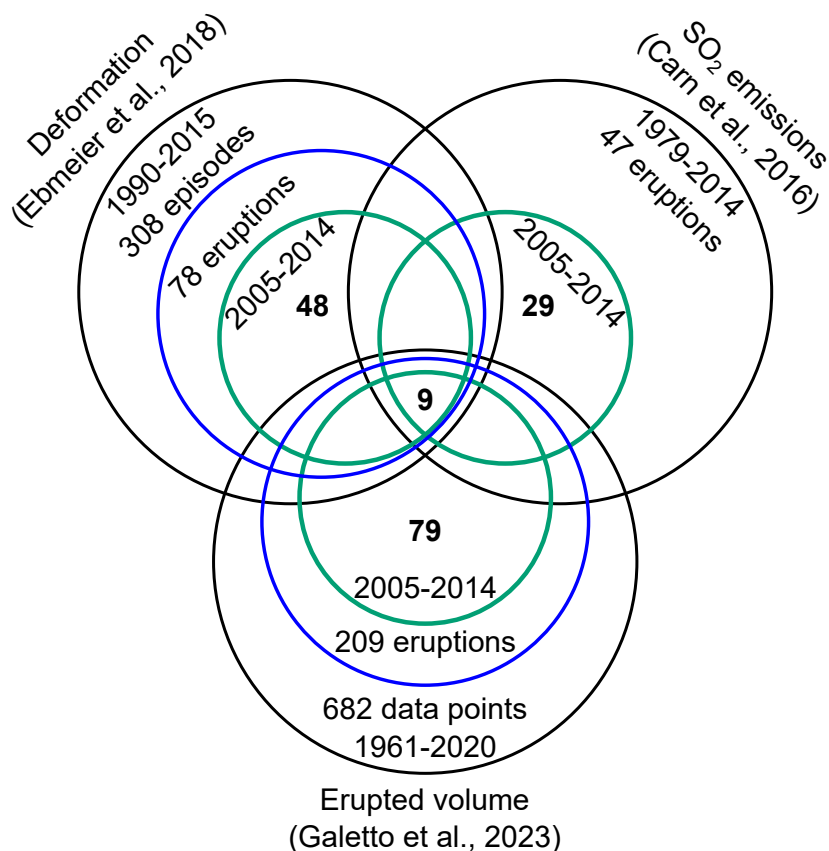


FIGURE 3.9. Illustration of the three best currently-available catalogues for volcano monitoring: Galetto et al. (2023) for erupted volume, Ebmeier et al. (2018) for volcanic deformation and Carn (2016) for SO<sub>2</sub> emissions (Figure 3.9). Each catalogue has a different observation period. With an overlapping date range of 2005-2014, there are only 9 eruptions for which all three measurements are available.

volcanic deformation and SO<sub>2</sub> emissions. The models predict that reservoir depth, chamber compressibility and magma composition will have first-order controls, but that gas segregation processes will also have a significant impact.

Our analysis of silica-poor eruptions is consistent with a simple conceptual model of a single short-lived reservoir that undergoes some minor degassing prior to eruption, followed by an effusive eruption with significant degassing taking place between the reservoir and the vent (Figure 3.8a). SO<sub>2</sub> emissions from mafic systems are dominated by co-eruptive degassing, meaning that mafic systems are big SO<sub>2</sub> gas emitters despite the fact that our analysis of volume change measurements shows that the reservoirs

have undergone some pre-eruptive degassing.

In contrast, our analysis of eruptions involving silica-rich compositions is more consistent with current models of transcrustal magmatic systems (e.g., Cashman et al., 2017), in which the exsolved volatile phase may undergo pre-eruptive degassing or gas accumulation at various depths prior to an eruption (Figure 3.8b). In this conceptual model, a fraction of the volatile content inherited from the primitive basalt is outgassed prior to the formation of melt inclusions, but subsequently, exsolved gas may accumulate as gas-rich caps. The complexity of the magma storage in silica-rich systems ultimately complicates the interpretation of volcanic deformation and SO<sub>2</sub> degassing (Figure 3.8). Indeed, many andesitic eruptions alternate between explosive and extrusive phases suggesting that the gas content in the erupting magma varies during an eruption (e.g., Jaupart and Allègre, 1991; Cassidy et al., 2018).

Our results emphasise the need to reconcile multiparameter observations from different disciplines of volcanology (e.g., geophysics, geochemistry, petrology) when interpreting monitoring data. However, our analysis is limited by a lack of a systematic approach to collecting monitoring data (gas, deformation, volume) and basic characteristics (magma composition, crustal properties). Analyses that focus on a single data type are unable to obtain a full picture of the system and may be biased by assumptions. Thus further integration of multiparameter datasets with physical models is critical for understanding magmatic plumbing systems, as well as improve our understanding of monitoring data.





## Chapter 4

# Understanding the temporal evolution of magma gas content and compressibility using observations of volcanic deformation and degassing

In preparation for submission to *Journal of Geophysical Research: Solid Earth*:

**Yip, S. T. H.**, Biggs, J., & Edmonds, M. (in preparation). Understanding the temporal evolution of magma gas content and compressibility using observations of volcanic deformation and degassing.

**Author contribution and declaration:** J. Biggs and M. Edmonds provided supervision and guidance for the work in this chapter. P. Liggins developed the thermodynamic model EVo and provided support under the supervision of O. Shorttle. The insightful discussions with J. Gottsmann and A. Rust improved the quality of this work. This chapter is in preparation for submission.

### **Abstract**

Magma reservoirs are heterogeneous meaning magma properties, including gas content, vary during volcanic eruptions. Here we investigate the effect these variations have on monitoring data, specifically surface deformation and  $\text{SO}_2$  emission measurements. We simulate an eruption from a two-layered magma reservoir model and track the gas content in the reservoir, bulk magma compressibility and volume change. When the upper layer is gas-poor (a degassed plug), its gradual removal increases the gas content and bulk compressibility of the magma in the reservoir, thus suppressing the volume change but increasing  $\text{SO}_2$  emissions. The converse is true when the upper layer is a gas-rich cap. We compare these predictions to the 2004-2005 eruption of Mount St Helens which involved a degassed plug and the 2011-2012 eruption of Cordon Caulle which involved a gas-rich cap. We show that magma compressibility increased during the eruption of Mount St Helens, but for Cordon Caulle, there was no change during the effusive phase of the eruption. The two-layer model provides a reasonable fit to the Mount St Helens data assuming the upper layer is 99.9% degassed and the lower layer is 40% degassed, but oversimplifies the observed variations in compressibility. These models emphasise the importance of integrating multi-parameter monitoring data to constrain the change in magma properties during an eruption.

## 4.1 Introduction

Monitoring changes in volcanic activity using multiparameter data is crucial for understanding magmatic properties and processes (e.g., Reath et al., 2019; Wong and Segall, 2020; Wasser et al., 2021) and as a basis for forecasting eruptions (e.g., Biggs and Wright, 2020; Pritchard et al., 2022; Christophersen et al., 2022). However, most studies focus on isolated aspects of volcanic behavior, such as deformation or SO<sub>2</sub> degassing (e.g., Sigmarsson et al., 2013; Hreinsdóttir et al., 2014; Hotta et al., 2019; Primulyana et al., 2019), combine them in a qualitative manner (e.g., Reath et al., 2020; Joseph et al., 2022) or treat an eruption as a single discrete event (Kilbride et al., 2016; Wong and Segall, 2020; Yip et al., 2022). Here, we explore how temporal variations in exsolved volatile content during eruptions affect magma compressibility and subsequently observations of ground deformation, and SO<sub>2</sub> emissions.

Exsolved volatiles, such as water and carbon dioxide, play an important role in determining the explosiveness (e.g., Gardner, 2009; Burgisser and Degruyter, 2015; La Spina et al., 2022) and eruptive behaviour of volcanoes (e.g., Gonnermann and Manga, 2006; Métrich and Wallace, 2008; Kilbride et al., 2016; Edmonds and Wallace, 2017; Wasser et al., 2021). Reservoir gas content cannot be directly measured during an eruption, but it controls magma compressibility and hence modulates surface deformation which is commonly measured. (Huppert and Woods, 2002; Woods and Huppert, 2003; Kilbride et al., 2016; Wasser et al., 2021; Yip et al., 2024). Exsolved gases can escape via permeable networks (e.g., Mount St. Helens, 2004; Chiodini et al., 2005; Gerlach et al., 2008; Dzurisin et al., 2015; Colombier et al., 2021) or accumulate within the roof zone of a magma reservoir (e.g., Cordón Caulle, 2011; Jay et al., 2014; Oppenheimer et al., 2015; Parmigiani et al., 2016). Previous studies have shown that magmatic systems with accumulated gas in the roof zone will 1) generate explosive eruption (Cashman, 2004; Gonnermann and Manga, 2006), 2) produce ‘excess’ SO<sub>2</sub> emissions (e.g., Wallace and Gerlach, 1994; Wallace, 2001) and 3) have reduced syn-eruptive surface deformation due to high magma compressibility (Yip et al., 2024). In contrast, pre-eruptive degassing promotes effusive eruptions with reduced syn-eruptive SO<sub>2</sub> emissions (assuming no co-eruptive degassing) and reduced magma compressibility such that the volume of material erupted is roughly equal to the subsurface volume change. Here we consider how the gas content in the reservoir evolves during an eruption with either a gas rich cap or a degassed plug. Assuming an interconnected reservoir, the proportion of gas in

the reservoir increases as a degassed plug is being removed, and the proportion of gas in the reservoir decreases as a gas-rich cap collapses. Here we investigate the effect the corresponding changes in magma compressibility have on observations of surface deformation. This raises two questions: 1) how does the gas content affect our ability to estimate magma volumes from deformation monitoring? and 2) can we use volcano monitoring data to estimate the gas content of a magma reservoir?

We use a simple two-layer model to explore the temporal evolution of bulk magma properties during an eruption, and the impact on observations of deformation and degassing. In our model, the lower layer consists of undegassed magma while the upper layer can be either a gas-rich cap or a degassed plug. We gradually remove material from the upper layer and explore how the changing gas content affects bulk compressibility and hence surface deformation. We apply our model to the 2004 eruption of Mount St. Helens, which involved a degassed plug (Gerlach et al., 2008; Lisowski et al., 2008; Anderson and Segall, 2013). We also consider the application to explosive eruptions, using the 2011 eruption of Cordón Caulle as an example of an eruption involving a gas-rich cap (Carboni et al., 2012; Jay et al., 2014). Our results emphasise the importance of considering gas content when interpreting observations of surface deformation and integrating multiparameter monitoring data to accurately forecast volcanic behavior and mitigate potential hazards.

## 4.2 Two-layer Model

In this section, we describe a simple two-layer model designed to investigate how the gas content in the upper layer of the reservoir affects time series of  $\text{SO}_2$  emissions and surface deformation. We consider three different factors: 1) the gas content of the upper layer (gas-rich cap or degassed plug), 2) connectivity between upper and lower layers, and 3) eruptions with varying extrusion rate. For each scenario, we calculate time series of bulk magma properties (gas volume fraction,  $V_g$ , and magma compressibility  $\beta_m$ ) and observations (normalised  $\text{SO}_2$  emissions,  $\tilde{S}$  and volume change,  $\tilde{V}$ ). A complete list of symbols is provided in Table 4.1.

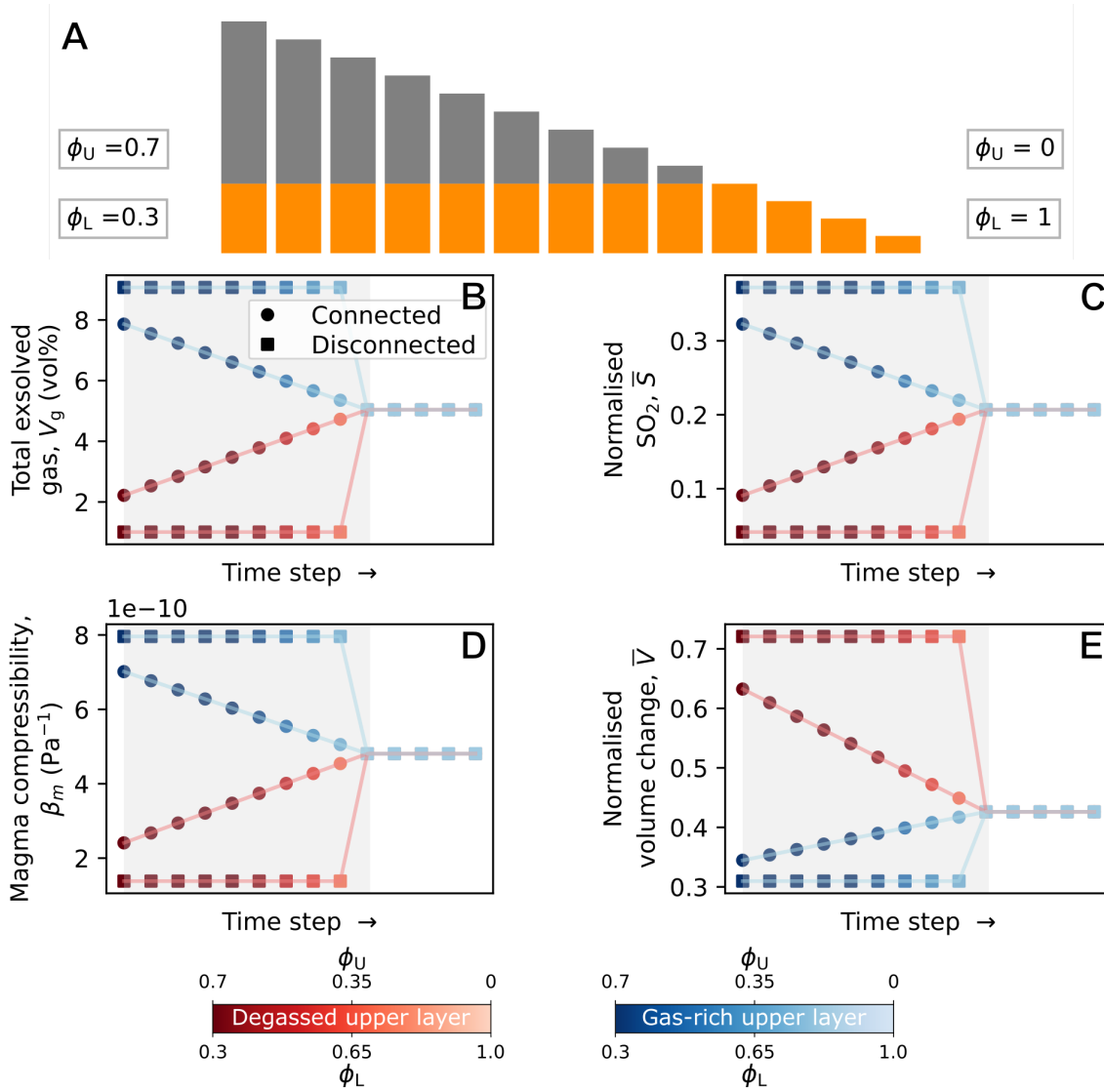


FIGURE 4.1. (a) Simple box plot of a two-layered magma plumbing system. The upper layer (grey) consists of a degassed or a gas-rich magma, underlain by a closed system degassing magma (orange). The model is initialised using an upper layer fraction ( $\phi_U$ ) = 0.7 and lower layer fraction ( $\phi_L = 1 - \phi_U$ ) = 0.3. When the upper layer has been depleted,  $\phi_U = 0$  and thus  $\phi_L = 1$ , such that the properties of the magma remaining in the reservoir is that of the magma at the lower layer. Temporal changes in the weighted average of (b) gas volume fraction, (c)  $\text{SO}_2$  gas per unit volume, (d) magma compressibility and (d) volume change per unit volume during the removal of a (red) degassed plug or a (blue) gas-rich cap. Dotted data points represent a well-connected magma plumbing system, while squares represent disconnected magma plumbing system, i.e., poor connectivity between reservoirs.

### 4.2.1 Model Setup

To calculate the gas content of each layer, we follow the method of Yip et al. (2022, in submission). First, we use the thermodynamic model, EVo (Liggins et al., 2020, 2022), to determine the gas volume fraction of an ocean island basalt ( $\text{H}_2\text{O} = 1.0 \text{ wt\%}$ ,  $\text{CO}_2 = 1 \text{ wt\%}$ ,  $\text{S} = 1600 \text{ ppm}$  and  $f_{\text{O}_2} = \text{NNO}$ ,  $1200^\circ\text{C}$ ,  $48 \text{ wt\% SiO}_2$ ) at the chosen depth (5 km) by assuming closed system degassing of a magma with a starting depth calculated using the volatile saturation pressure (Liggins et al., 2022). We then account for pre-eruptive gas segregation by modifying the gas volume fraction ( $V_g$ ) using a proportion  $k$ , where  $-1 < k < 0$  corresponds to pre-eruptive degassing and  $k > 0$  represents pre-eruptive gas accumulation. For the lower layer, we use  $k = 0$  to represent the underlying undegassed magma and for the upper layer we use either  $k = -0.8$  for a degassed plug, or  $k = 1$  for a gas-rich cap. We calculate the compressibility of each layer based on the magma density ( $\rho_m$ ), which is a function of melt and gas volume fraction ( $V_g$ ),

$$\beta_m = \frac{1}{\rho_m} \frac{\delta \rho_m}{\delta p}. \quad (4.1)$$

where  $p$  is pressure.

We simulate an eruption by progressively removing magma from the upper layer,  $U$ , first and then from the lower layer,  $L$ . Thus, initially the volume fraction of the upper layer ( $\phi_U$ ) decreases and the fraction of the lower layer ( $\phi_L$ ) increases (Figure 4.1). For simplicity, we initially model eruptions using a constant eruption rate, before considering more realistic scenarios: 1) a magma reservoir with a gas-rich cap and a decreasing eruption rate, and 2) a magma reservoir with a degassed plug and increasing eruption rate.

We then calculate the bulk properties of the two-layer reservoir during the eruption. To represent a well-connected system, we use a weighted average of the properties of the individual layers and for the disconnected system, we use the properties of the upper layer until it is completely removed and then switch to those of the lower layer. For example, the bulk magma compressibility is given by,

$$\beta_m = \begin{cases} \phi_U \beta_U + \phi_L \beta_L & \text{if connected} \\ \begin{cases} \beta_U & \text{if } \phi_U > 0 \\ \beta_L & \text{if } \phi_U = 0 \end{cases} & \text{if disconnected} \end{cases} \quad (4.2)$$

We then calculate the two observable parameters - volume change and SO<sub>2</sub> emissions, each normalised to the volume erupted in each timestep. The normalised volume change of the reservoir,  $\bar{V}$  can be calculated using

$$\bar{V} = \left(1 + \frac{\beta_m}{\beta_c}\right)^{-1}, \quad (4.3)$$

where  $\beta_c$  is the crustal compressibility (Rivalta and Segall, 2008; Kilbride et al., 2016; Yip et al., 2022). For our simple model, we assume deformation from a spherical point source ( $\beta_c = 3/4\mu$ ) with constant crustal shear modulus ( $\mu = 2.1$  GPa) (Mogi, 1958; Heap et al., 2020) but use tailored parameters for specific case studies. Measurements of surface deformation are typically calculated cumulatively as this reduces uncertainties, therefore we calculate both incremental and cumulative values of volume change and SO<sub>2</sub> emissions.

#### 4.2.2 Model Results

Figure 4.1 shows the results for models using a constant eruption flux. The initial volume of the upper layer is  $5 \times 10^9$  m<sup>3</sup> and the lower layer is  $2 \times 10^9$  m<sup>3</sup> and we remove  $0.5 \times 10^9$  m<sup>3</sup> in each timestep. For a well-connected reservoir with a gas-rich cap (blue circles), the gas volume fraction ( $V_g$ ) decreases with time leading to decreasing normalised SO<sub>2</sub> ( $\bar{S}$ ) and magma compressibility ( $\beta_m$ ), and increasing normalised volume change ( $\bar{V}$ ) (Figure 4.1b-e). Conversely, in a reservoir with a degassed plug (red circles),  $V_g$  increases resulting in increasing  $\bar{S}$  and  $\beta_m$ , and decreasing  $\bar{V}$  (Figure 1b-e). Following the complete removal of the plug or cap, the bulk magma properties match those of the underlying undegassed magma, resulting in constant values of  $V_g$ ,  $\bar{S}$ ,  $\beta_m$ , and  $\bar{V}$  (Figure 4.1b-e).

In contrast, for a disconnected system of isolated reservoirs with different exsolved volatile contents, the resulting time series show a step function (squares). The magma properties ( $\beta_m$ ,  $V_g$ ,  $\bar{S}$ ,  $\bar{V}$ ) initially match those of the upper layer, but once this is exhausted, there is a step change to the properties associated of the lower layer. This difference in behaviour highlights the influence of reservoir architecture and connectivity on magma properties and monitoring data.

Figure 4.2 shows the effect on SO<sub>2</sub> and volume change of a time-dependent eruption flux: Figure 4.2a-d shows the absolute incremental values; Figure 4.2e-h shows the absolute



CHAPTER 4. TEMPORAL EVOLUTION OF MAGMA GAS CONTENT AND  
COMPRESSIBILITY USING VOLCANIC DEFORMATION AND DEGASSING

TABLE 4.1. Symbols and their representative values. The initial parameters for the simulated eruption is included here (Section 4.2.1).

Symbol	Description	Parameter space
$V_c$	Volume change of reservoir <sup>a</sup>	-
$V_e$	Volume erupted <sup>a</sup>	-
$\bar{V}$	Normalised volume change <sup>a</sup>	-
$E^{SO_2}$	SO <sub>2</sub> emissions <sup>a</sup>	-
$\bar{S}$	Normalised SO <sub>2</sub> <sup>a</sup>	-
$\beta_m$	Magma compressibility <sup>a</sup>	-
$\beta_c$	Crustal compressibility <sup>a</sup>	-
<b>Starting parameters for simulated eruption (Section 4.2.1)</b>		
$\phi_U$	Proportion of upper layer	0.7
$\phi_L$	Proportion of lower layer	0.3
$k_U$	Proportion $k$ of upper layer	-0.8 (degassed) +1.0 (gas-rich)
$k_L$	Proportion $k$ of underlying magma	0
$w^{H_2O}$	H <sub>2</sub> O content	1.0 wt%
$w^{CO_2}$	CO <sub>2</sub> content	1.0 wt%
$w^S$	S content	1600 ppm
$w^g$	Excess gas content	0 wt%
$f_{O_2}$	Oxygen fugacity	NNO
$T$	Temperature	1200 °C
	SiO <sub>2</sub> content	48 wt%
$\mu$	Crustal shear modulus	2.1 GPa

<sup>a</sup> Symbols in the main text with superscript  $i$  and superscript  $c$  represent incremental and cumulative values, respectively. For example, incremental and cumulative volume change of the reservoir are shown as  $V_c^i$  and  $V_c^c$ , respectively.

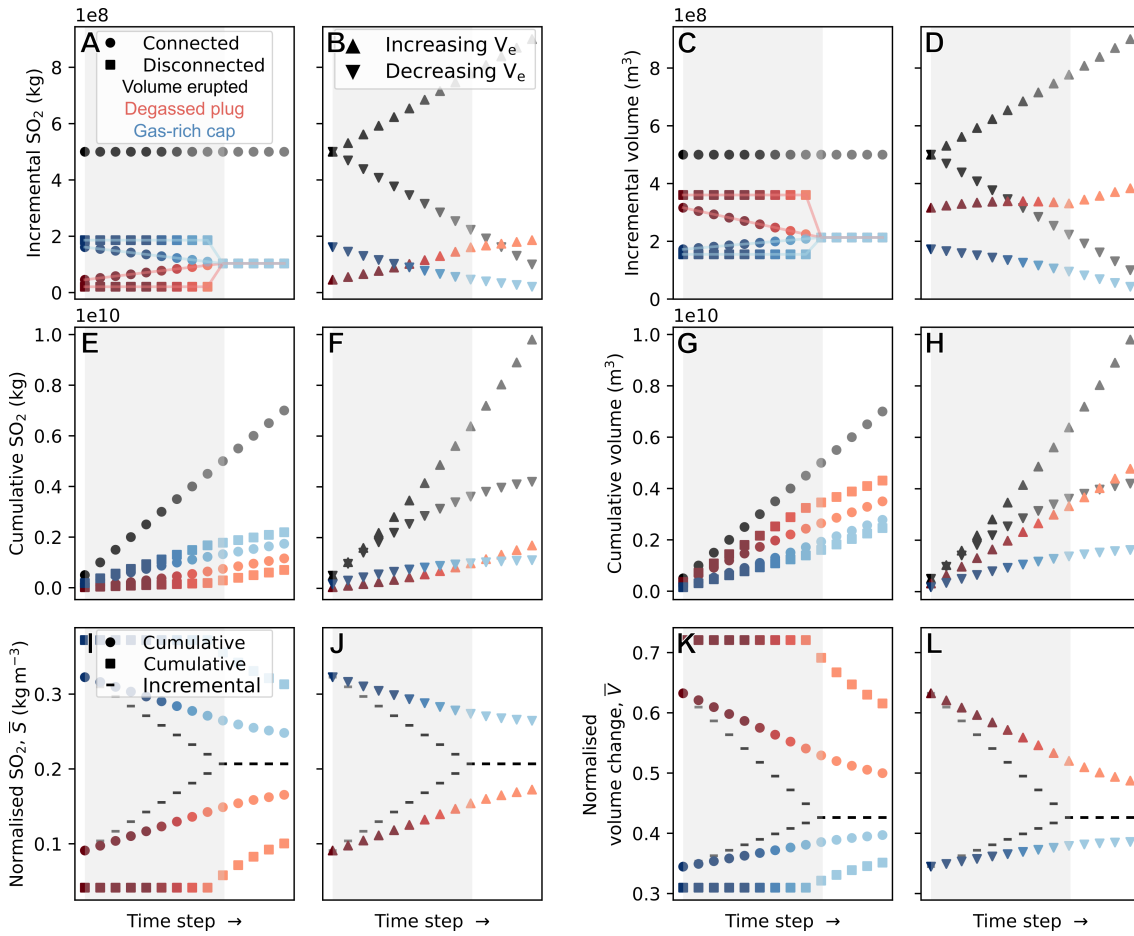


FIGURE 4.2. Temporal variation of  $\text{SO}_2$  emissions and volume changes predicted from the simulated eruption associated with a two-layered magma reservoir with a degassed plug (red) or a gas-rich cap (blue). (a) Incremental  $\text{SO}_2$  emissions assuming the volume erupted ( $V_e$ ; black) is constant throughout an eruption. Results are shown for well-connected (circles) and disconnected (squares) reservoirs. (b) Incremental  $\text{SO}_2$  emissions for eruptions with increasing  $V_e$  (triangle) and decreasing  $V_e$  (inverted triangle). Incremental volume change of a reservoir when the extrusion rate is (c) constant and (d) increasing/ decreasing. Panels e-h illustrates the cumulative values for the results shown in panels a-d. The normalised  $\text{SO}_2$   $\bar{S}$  for an eruption with (i) constant and (j) increasing/ decreasing volume erupted. The squares represent the cumulative  $\bar{S}$  for a disconnected reservoir, and the circles and bars represent the cumulative  $\bar{S}$  and incremental  $\bar{S}$  for a connected reservoir, respectively. (k-j) Normalised volume change  $\bar{V}$  for an eruption with different rate of  $V_e$ . The grey-shaded region illustrates the time step at which the plug/ cap is being removed, and the unshaded region represents the removal of the underlying undegassed magma.

cumulative values and Figure 4.2i-l shows the normalised values. For a degassed plug with an increasing eruption rate, the  $\text{SO}_2$  flux increases more rapidly than for the constant flux case (Figure 4.2b) . The increasing eruptive flux means the absolute volume change still increases with time even though the increasing gas content increases compressibility and decreases normalised volume change (Figure 4.2d). The effect of changing flux rate opposes the effect of compressibility and the balance will depend on the precise values chosen. The converse is true for eruptions involving a gas-rich cap.

In practice, time-series data are often presented as cumulative values, but these have a temporal lag relative to their incremental counterparts ( $\bar{S}^i$  and  $\bar{V}^i$ ). Although both cumulative and incremental parameters display similar trends, the incremental measurements provide more immediate insights into magma transitions and eruption styles, highlighting the importance of calculating incremental changes and normalising to eruptive volume for capturing crucial changes during eruptions (Figure 4.2i-l).

### 4.3 Case study

To understand the temporal evolution of magma properties during an eruption, we analyse and compare observations of  $\text{SO}_2$  emissions, surface deformation and extrusion flux data to our forward model as case study examples. In our case study, we have selected two distinct eruption events to serve as end members: the 2004-2005 eruption of Mount St. Helens, which has already been attributed to the removal of a degassed plug (Gerlach et al., 2008; Anderson and Segall, 2013); and the 2011-2012 eruption of Cordon Caulle, which is characterised by gas-rich pre-eruptive magma (Jay et al., 2014). The dynamics of these two eruptions can be related to Figure 4.1-4.2: a degassed plug exhibits increasing  $\bar{S}$  and decreasing  $\bar{V}$  during an eruption (red data points), while a gas-rich cap displays decreasing  $\bar{S}$  and increasing  $\bar{V}$  (blue data points). For each example, we use the observed deformation and erupted volume to constrain the evolution of magma properties, specifically gas content.

#### 4.3.1 Case Study 1: Degassed Plug

We apply our model to the 2004-2005 eruption of Mount St. Helens for which observations of  $\text{SO}_2$  emissions, surface deformation and extrusion flux are available and the presence

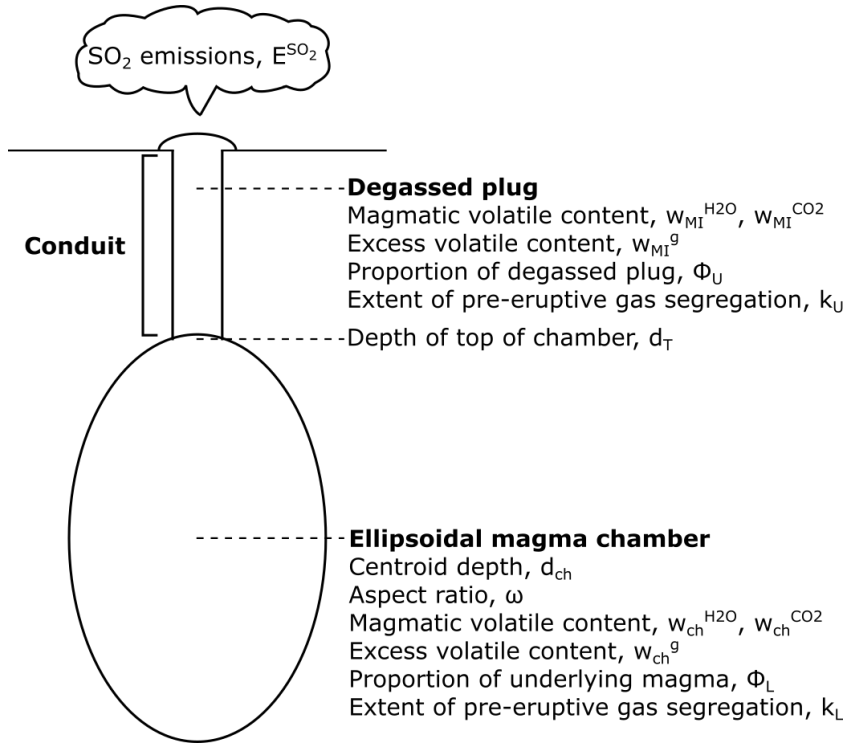


FIGURE 4.3. Conceptual model of the 2004 eruption of Mount St. Helens. The upper layer consists of degassed magma that is pushed out by the lower layer magma. The model is constrained by observations of ground deformation and volume erupted, and qualitatively compared to SO<sub>2</sub> emissions.

of a degassed plug has already been inferred (Gerlach et al., 2008; Anderson and Segall, 2013)

#### 4.3.1.1 Observations of the 2004-2005 eruption of Mount St. Helens

After nearly 20 years of quiescence, Mount St. Helens began to erupt on 27 September 2004 with the growth of a dacitic lava dome in the vent of the 1980 eruption (Vallance et al., 2008). Low volatile contents in the matrix glasses suggests that the ascending magma was depleted in exsolved volatiles due to degassing prior to its eruption (Pallister et al., 2008; Gerlach et al., 2008). The semi-solid degassed plug was forced out of the conduit along well-developed ring faults (Cashman et al., 2008) from the top of an ellipsoidal chamber ( $d_T = 5.2$  km) with a centroid depth of  $d_{ch} = 8.6$  km (Mastin et al., 2008) (Figure 4.3). The eruption continued until early 2008 with a steady decline in the extrusion rate and ground deformation (Schilling et al., 2008). We focus on the first 205 days of the eruption, for which co-eruptive deformation, SO<sub>2</sub> emissions and erupted

## CHAPTER 4. TEMPORAL EVOLUTION OF MAGMA GAS CONTENT AND COMPRESSIBILITY USING VOLCANIC DEFORMATION AND DEGASSING

volume data are available.

Co-eruptive deformation was observed through GPS measurements from a station (JRO1) located approximately 9 km north of the volcano. The deformation data showed minimal precursory deformation signals until the onset of the eruption (Anderson and Segall, 2013, Supplementary Table C.1), which coincides with the first detection of a seismic swarm on 26 September (Lisowski et al., 2008). During the first two weeks of the eruption, a rapid deflation up to 10 mm was recorded, known as the vent-clearing phase (cyan shaded area; Figure 4.4) that is characterised by increased seismicity, several phreatic explosions and lava extrusion beneath the glacier (Moran et al., 2008; Anderson and

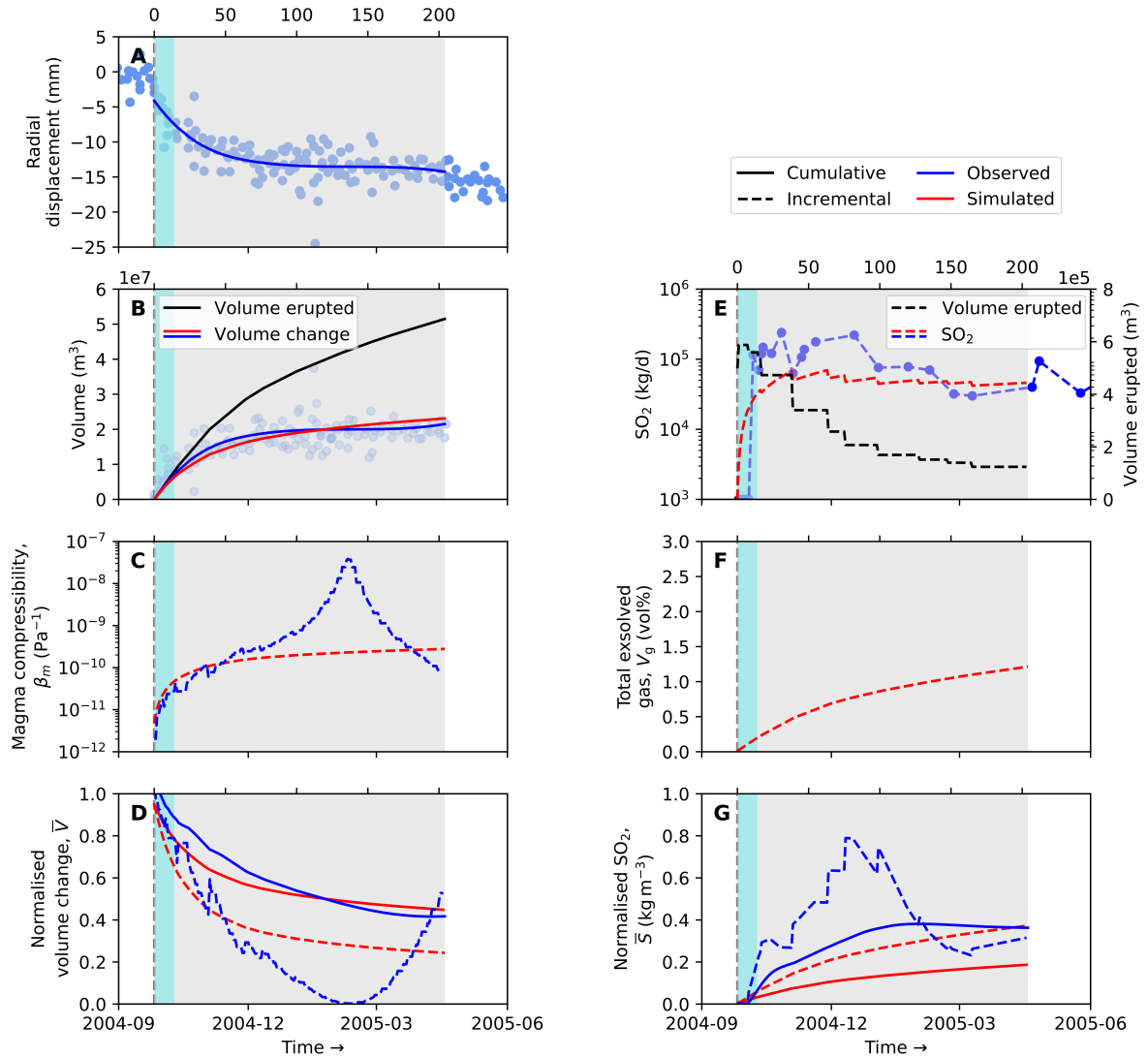


FIGURE 4.4. (page 88): Temporal evolution of eruption data for the 2004 eruption of Mount St. Helens. (a) Radial displacement from GPS measurements (Lisowski et al., 2008; Anderson and Segall, 2013). (b) Volume of extruded lava measured using digital aerophotogrammetry (Schilling et al., 2008) and volume change of reservoir estimated from the total co-eruptive volume change and ground deformation. (a-b) The raw data are shown as scatter points and they are fitted by solid lines using spline function. (c) Incremental changes of magma compressibility estimated from normalised volume change using Eq. 4.3. (d) Cumulative and incremental normalised volume change calculated by normalising the fitted volume change to the fitted volume erupted. (e) Incremental  $\text{SO}_2$  flux from airborne gas measurements (Gerlach et al., 2008) and model prediction. The incremental volume erupted is included in the plot for comparison. (f) Incremental gas volume fraction in the magma. (g) Normalised  $\text{SO}_2$  predicted from the model. The top and bottom axis of the plots show the day and date of eruption. The blue shaded area represents the vent-clearing phase which lasted for two weeks since the commence of the eruption (Anderson and Segall, 2013). The model predicted the degassed magma accounts for the whole study period assuming a constant  $k_U = -0.99$  (grey shaded area). The underlying magma that erupted after the study period has a constant  $k_L = -0.4$ , i.e., undergone certain extent of pre-eruptive degassing.

Segall, 2013). Following an explosion on 5 October, the deformation rate slowed down (Lisowski et al., 2008).

The volume of erupted lava was estimated using digital aerophotogrammetry (Schilling et al., 2008, Supplementary Table C.2), which is then converted to the dense-rock equivalent by assuming a porosity of 10% (Gerlach et al., 2008; Anderson and Segall, 2013). A zone of highly fractured ice uplifted the neighbouring crater-floor debris, referred to as the ‘welt’, with a volume of  $\sim 10 \times 10^6 \text{ m}^3$  before the lava appears on the surface (Vallance et al., 2008). The volume of this welt was added to subsequent estimates of the extruded volume to determine the total erupted volume (Anderson and Segall, 2013). The eruption exhibited a declining trend in the rate of dome growth from  $\sim 7 \times 10^5 \text{ m}^3 \text{ day}^{-1}$  until the eruption ends (black line; Figure 4.4b) (Iverson et al., 2006; Moran et al., 2008; Schilling et al., 2008).

To compare ground deformation and erupted volume, we fit a univariate spline (Python package SciPy.interpolate; B-spline basis with 2 knots) to each of the measurements (Figure 4.4a-b). We estimate the cumulative time series of volume change by assuming

the volume change of the reservoir is directly proportional to the ground deformation, such that there is just one deformation source that is stationary and has a fixed geometry (blue line; Figure 4.4b). In other words, the volume change at each time step is equal to the displacement at that time step multiplied by the ratio between the total co-eruptive volume change ( $V_c = 2.2 \times 10^7 \text{ m}^3$ ) and the total displacement ( $\sim 13 \text{ mm}$ ). We calculate the normalised volume change ( $\bar{V}$ ) using the interpolated values of both the volume change and volume erupted (Figure 4.4d). Figure 4.4d shows that cumulative  $\bar{V}$ ,  $\bar{V}^c$ , decreases with an exponential decay from 1 to  $\sim 0.4$ , and when measured incrementally,  $\bar{V}^i$  decreases from  $\sim 1$  to  $\sim 0$  after 136 days, followed by an increase to  $\sim 0.5$ . Since  $\bar{V}^i$  is a function of magma compressibility, we can use  $\bar{V}^i$  to provide insights into the gas volume fraction of magma in the reservoir (i.e., low  $\bar{V}$  corresponds to high magma compressibility and gas volume fraction) (Yip et al., 2022).

SO<sub>2</sub> emissions were measured through aircraft sampling of the plume (Gerlach et al., 2008, Supplementary Table C.3). During the initial 10 days of the eruption, SO<sub>2</sub> emissions were below the detection limit (blue; Figure 4.4e), indicating that the gas had been scrubbed or degassed before eruption (Gerlach et al., 2008). Emissions rose above the detection limit on 7 October 2004 as the eruption progressed (Figure 4.4e), peaking twice on 27 October 2004 and 17 December 2004, followed by consistent SO<sub>2</sub> emissions (Gerlach et al., 2008). We interpolate the SO<sub>2</sub> emissions using a B-spline function with 5 knots, which is then normalised by the interpolated erupted volume to calculate normalised SO<sub>2</sub> ( $\bar{S}$ ; Figure 4.4g). We find that cumulative  $\bar{S}$ ,  $\bar{S}^c$ , increases up to  $\sim 0.38 \text{ kg m}^{-3}$  after erupting for 120 days, followed by a gradual decline to  $\sim 0.36 \text{ kg m}^{-3}$ . When measuring  $\bar{S}$  incrementally,  $\bar{S}^i$  increases up to a maximum of  $0.79 \text{ kg m}^{-3}$  on 13 December 2004 before decreasing to  $\sim 0.3 \text{ kg m}^{-3}$  (Figure 4.4g).

### 4.3.1.2 Temporal changes in magma properties

During the vent-clearing phase of the eruption, which lasted for the first two weeks of the eruption, the cumulative volume change ( $V_c^c$ ) and the cumulative volume erupted ( $V_e^c$ ) are similar (Figure 4.4b). This is also illustrated by the high cumulative normalised volume change ( $\bar{V}^c = \sim 1$ ) (blue line; Figure 4.4d), which can be associated to the presence of a magma with low compressibility, analogous to a degassed magma. This interpretation is supported by the low SO<sub>2</sub> flux during this phase, which was below background level (Figure 4.4e). This is consistent with previous studies that suggested a semi-solid degassed plug that is depleted in exsolved volatiles at the top of the chamber

(e.g., Gerlach et al., 2008; Mastin et al., 2008).

Following the vent-clearing phase, the rate of volume change decreased more rapidly than the rate of extrusion (Figure 4.4b), leading to a decrease in  $\bar{V}^c$  (Figure 4.4d). By the end of the study period (205 days), the total co-eruptive volume change accounts for 40% of the total erupted volume. This suggests the existence of a relatively gas-rich, compressible magma beneath a degassed magma, consistent with previous interpretations (Gerlach et al., 2008; Mastin et al., 2009).

The existence of a relatively gas-rich magma can be evidenced by the changes in bulk magma compressibility  $\beta_m$  at different stages of an eruption. Therefore, it is best quantifying  $\beta_m$  using incremental values. First, we calculate incremental normalised volume change ( $\bar{V}^i$ ) by normalising the incremental  $V_c^i$  to the incremental  $V_e^i$  using Equation 4.3.

Considering that Mount St. Helens has a prolate ellipsoidal chamber, here we use crustal compressibility  $\beta_c = \frac{3}{\mu} \left( \frac{\omega}{2\pi} - \frac{1}{5} \right)$ , where  $\omega = 5$  is the major to minor semi-axes of the ellipsoidal chamber and crustal shear modulus  $\mu = 20$  GPa (Anderson and Segall, 2011, 2013). We test the same values ( $\omega$  and  $\mu$ ) in our forward model in Section 4.3.1.3. We find an exponential increase in  $\beta_m$  from  $2.0 \times 10^{-12} \text{ Pa}^{-1}$  that reaches its peak on 10 February 2005 (i.e., after 137 days) at  $3.8 \times 10^{-8} \text{ Pa}^{-1}$ , and later followed by a decrease in  $\beta_m$  to  $8.0 \times 10^{-11} \text{ Pa}^{-1}$  (Figure 4.4c), consistent with the changes in the fluid content in magma (Gerlach et al., 2008). The fluctuating  $\beta_m$  can be explained by the presence of pockets of relatively gas-rich magma underneath a degassed magma (Mastin et al., 2008; Iverson et al., 2006), such that  $\beta_m$  increases during the extrusion of the degassed magma and decreases when the relatively gas-rich magma is erupting. However, we note that the average  $\beta_m$  in this eruption period, including the spike, is  $2.7 \times 10^{-9} \text{ Pa}^{-1}$ , an order of magnitude greater than previous estimates (e.g.,  $0.2\text{--}5 \times 10^{-10} \text{ Pa}^{-1}$ ; Mastin et al., 2009; Wong and Segall, 2020).

#### 4.3.1.3 Numerical Model

To model these time series, we use the two-layer model described in section 2, with additional constraints from geophysical and petrological data (Figure 4.3, Table 4.2). The upper layer consists of extensively degassed magma and the lower layer representing an underlying relatively gas-rich magma and we assume the layers are well-connected. We



TABLE 4.2. Input parameters and the range of parameters explored in the forward models for Mount St. Helens, 2004. Values enclosed in curly brackets represent the extreme or end-member values.

Symbol	Description	Parameter space
<b>Upper layer</b>		
$\phi_U$	Proportion of upper layer	{0–1}
$k_U$	Proportion $k$ of upper layer	–0.99
$d_T$	Depth of top of chamber	5.2 km
$w_{MI}^{\text{H}_2\text{O}}, w_{MI}^{\text{CO}_2}$	H <sub>2</sub> O and CO <sub>2</sub> content in melt inclusion	4.4 wt%, 37 ppm
$w_{MI}^g$	Excess gas content in melt inclusion	1.2 wt%
<b>Lower layer</b>		
$\phi_L$	Proportion of lower layer	{1– $\phi_U$ }
$k_L$	Proportion $k$ of underlying magma	{–0.99–+1.0}
$d_{ch}$	Centroid depth of chamber	8.6 km
$w_{ch}^{\text{H}_2\text{O}}, w_{ch}^{\text{CO}_2}$	H <sub>2</sub> O and CO <sub>2</sub> content in melt	5.0 wt%, 350 ppm
$w_{ch}^g$	Excess gas content in melt	0.2 wt%
<b>Model parameters</b>		
	SiO <sub>2</sub> content	76 wt%
$f_{\text{O}_2}$	Oxygen fugacity	NNO
$T$	Temperature	850 °C
$\mu$	Crustal shear modulus	20 GPa
$\omega$	Chamber aspect ratio $\left(\frac{\text{height}}{\text{width}}\right)$	5
<b>Misfit analysis</b>		
$\mu$	Crustal shear modulus	{2.1–40} GPa
$\omega$	Chamber aspect ratio $\left(\frac{\text{height}}{\text{width}}\right)$	{3–10}

estimate the gas content and compressibility of the magma using the thermodynamic model EVo (Liggins et al., 2020, 2022). For the upper layer, we use  $k_U = -0.99$  to represent significant pre-eruptive gas loss and extract the gas volume fraction and magma compressibility at a depth of 5.2 km which represents the top of the chamber (Figure 4.3) (Anderson and Segall, 2011). We use initial volatile contents of  $w_{MI}^{H_2O} = 4.4$  wt%,  $w_{MI}^{CO_2} = 37$  ppm and  $w_{MI}^g = 1.2$  wt% based on melt inclusion data (Gerlach et al., 2008) which gives a gas fraction of 0.01 vol% and magma compressibility  $\beta_m = 4.5 \times 10^{-12} \text{ Pa}^{-1}$ . For the lower layer, we extract magma properties at a depth of 8.6 km which represents the centre of the chamber (Figure 4.3) (Anderson and Segall, 2011). We use initial volatile content of  $w_{ch}^{H_2O} = 5.0$  wt%,  $w_{ch}^{CO_2} = 350$  ppm and  $w_{ch}^g = 0.2$  wt% for the lower layer based on data from the 1980 eruption of Mount St. Helens, which has similar magma composition to the 2004 eruption (63 and 65 wt%  $\text{SiO}_2$ , respectively) (Gerlach et al., 2008). We use an initial starting temperature for both the upper and lower layers at 850 °C, and the  $\text{SiO}_2$  is 76 wt%, which corresponds to a generic rhyolite composition. We note that the volatile content, in particular  $\text{CO}_2$ , assigned to the lower layer is an underestimation. According to Blundy et al. (2010), phase and crystal assemblages inferred an initial  $\text{CO}_2$  content at 1.5 wt%. Nevertheless, we expect that this underestimation does not affect our modelling results because the influence of  $\text{CO}_2$  on volume changes is minimal (Yip et al., 2022), although that sensitivity test is based on lower  $\text{CO}_2$  contents. Since the eruption was primarily effusive, we calculate the mass of  $\text{SO}_2$  gas in equilibrium with the surface pressure and we also assume no  $\text{SO}_2$  was lost due to scrubbing.

This model contains two unknown parameters: the extent of pre-eruptive gas segregation,  $k_L$  and the proportion of upper ( $\phi_U$ ) and lower ( $\phi_L = 1 - \phi_U$ ) layers. We conduct a grid search consisting of 1890 forward models exploring the parameter space between  $k_L = -0.99$  (gas fraction of 0.002 vol%;  $\beta_m = 9.0 \times 10^{-12} \text{ Pa}^{-1}$ ) and  $k = 1$  (gas fraction of 4 vol%;  $\beta_m = 1.0 \times 10^{-9} \text{ Pa}^{-1}$ ) and  $\phi_U$  between 0.1 and 1 (Table 4.2). Chamber compressibility depends on crustal shear modulus,  $\mu$ , and chamber aspect ratio,  $\omega$ , both of which are poorly constrained: Anderson and Segall (2011) used  $\omega = 5$  and  $\mu = 20$  GPa, Mastin et al. (2008) used  $\mu = 40 \pm 4$  GPa based on seismic and density data and Wong and Segall (2020) used  $\omega = 3.3$ . Given this uncertainty, we also conduct a grid search for  $\omega = [3, 5, 10]$  and  $\mu = [2.1, 20, 40]$  GPa. We use the root-mean-square error (RMSE) between the model's predicted volume change and the observed interpolated volume change (Figure 4.4b) to evaluate model performance. Although we also compare the predicted and observed  $\text{SO}_2$

flux, we did not use this information to constrain the RMSE or select the best-fitting model.

Our best-fit model is an elongated ellipsoidal chamber ( $\omega = 5$  and  $\mu = 20$  GPa) that initially contains an extensively degassed magma ( $k_U = -0.99$ ) and a partially degassed magma ( $k_L = -0.4$ ). The upper layer comprises 99.9% of the initial reservoir volume ( $\phi_U = 0.999$ ). As the upper layer is gradually removed, the modelled bulk compressibility increases from  $10^{-12}$  Pa $^{-1}$  to  $10^{-10}$  Pa $^{-1}$  and the gas volume fraction increases from 0.01 to 1.2 vol% (Figure 4.4c,f). There is a strong trade-off between  $k_L$  and  $\phi_U$  as a higher  $\phi_U$  requires a greater  $k_L$  to produce an equivalent bulk magma compressibility (Figure 4.5e). Despite this the results consistently show that the lower layer is volumetrically small and relatively gas-rich but has nonetheless undergone a certain amount of pre-eruptive degassing. The values are also consistent with studies by Anderson and Segall (2011), Mastin et al. (2009) and Gerlach et al. (2008). The root-mean-square error (RMSE) between the modelled and observed volume change is  $1.4 \times 10^6$  m $^3$ , which is equivalent to 6.5% of the total volume change ( $V_c = 2.2 \times 10^7$  m $^3$ ; Figure 4.5e).

When plotted cumulatively, the modelled  $\bar{V}$  matches the observations well and the residuals are smaller than the data uncertainties (solid lines; Figure 4.4d). However, when plotted incrementally, the two-layer model predicts a simple exponential decay, but the observations reveal more complex behaviour (dashed lines; Figure 4.4d). Most noticeably the period between days 115–156 is characterised by low volume change ( $\bar{V} < 0.05$ ) and a peak in  $\beta_m$  with values up to  $3.8 \times 10^{-8}$  Pa $^{-1}$  (Figure 4.4c,d). This cannot be matched by a simple two-layer model and suggests gas fraction within the reservoir is highly variable .

The SO $_2$  emissions do not contribute to the misfit calculation, but provide a qualitative check on the results. Although the model predictions are a similar order of magnitude as the observations for the majority of the study period there is a significant discrepancy in the first two weeks (Figure 4.4e). The SO $_2$  emissions were below the detection limit, and although the model predicts a low value of  $\bar{S}$ , the erupted volume was high, giving an overall emission rate of SO $_2$  emissions  $\sim 1.5 \times 10^4$  kg/day. For the remainder of the study period, the mean SO $_2$  emission predicted by the model is  $5.0 \times 10^4$  kg/day, which is 0.6 of the observed value of  $8.5 \times 10^4$  kg/day.

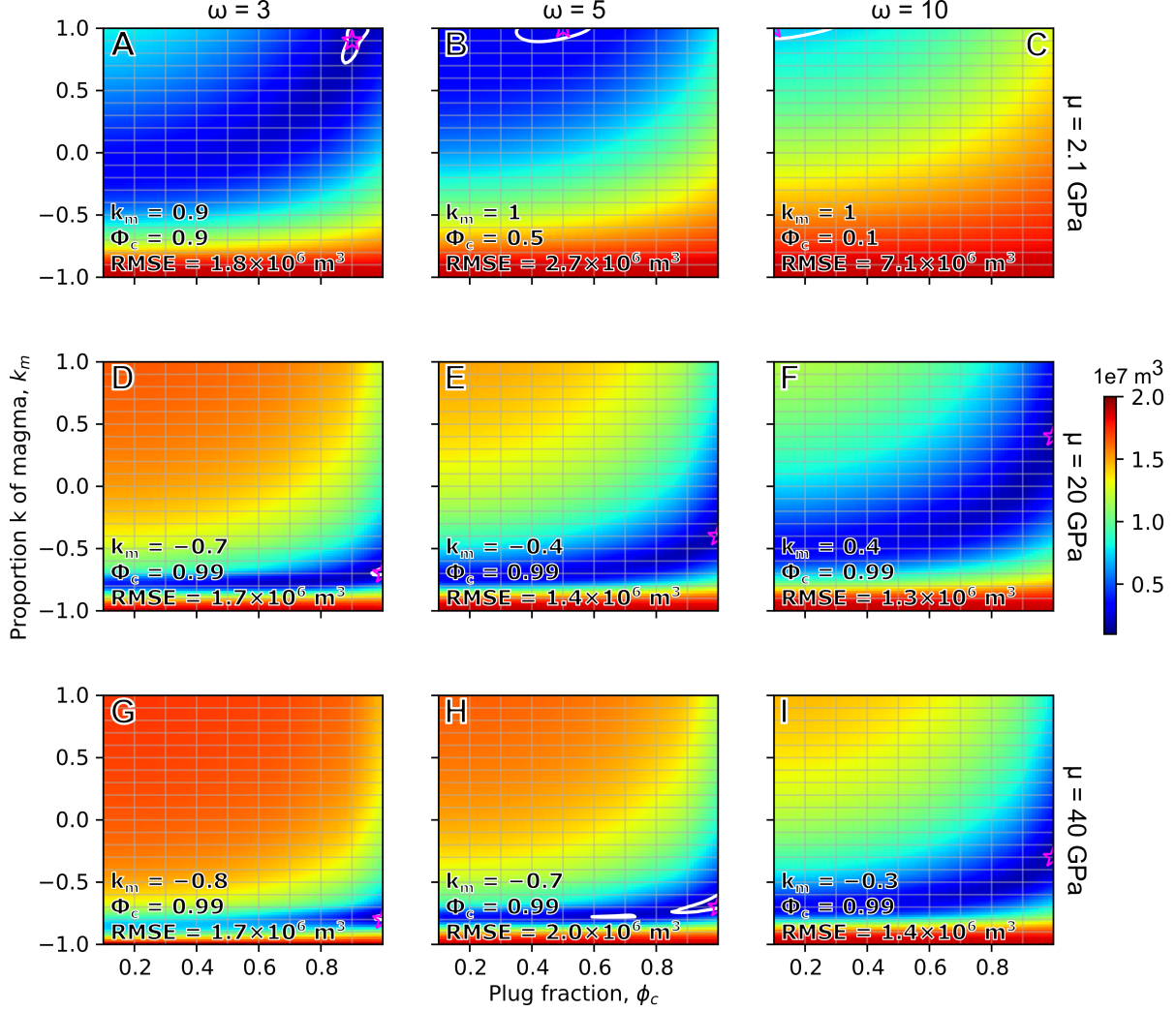


FIGURE 4.5. Misfit plot between observed and modelled volume change when varying plug fraction  $\phi_U$  and proportion  $k$  of magma  $k_L$  (grid). The default parameter combination (i.e., panel e) used are crustal shear modulus  $\mu = 20$  GPa and chamber aspect ratio  $\omega = 5$  (Anderson and Segall, 2011). Considering the different ranges of parameters reported in previous studies (Mastin et al., 2008; Wong and Segall, 2020), we also explore  $\mu = 2.1$ –40 GPa and  $\omega = 3$ –10. The values of RMSE from each grid are interpolated and illustrated using a filled contour. The star represents the best parameter combination for each model, and the white contour lines represent 5% confidence interval from the lowest RMSE.

### 4.3.2 Case Study 2: Gas-rich cap

We then apply our model to the 2011-2012 eruption of Cordon Caulle, Chile. This is the first rhyolitic eruption to be instrumentally recorded and the presence of a gas-rich cap has already been inferred (Castro et al., 2013; Jay et al., 2014; Wendt et al., 2017; Delgado et al., 2019; Lara et al., 2004). The eruption started on 4 June 2011 and can be divided into two phases: explosive (4-15th June 2011) and effusive (16th June 2011-March 2012). The eruption products from 2011-2012 had nearly identical petrology to those from the 1960 eruption, suggesting it was derived from the same reservoir (Jay et al., 2014).

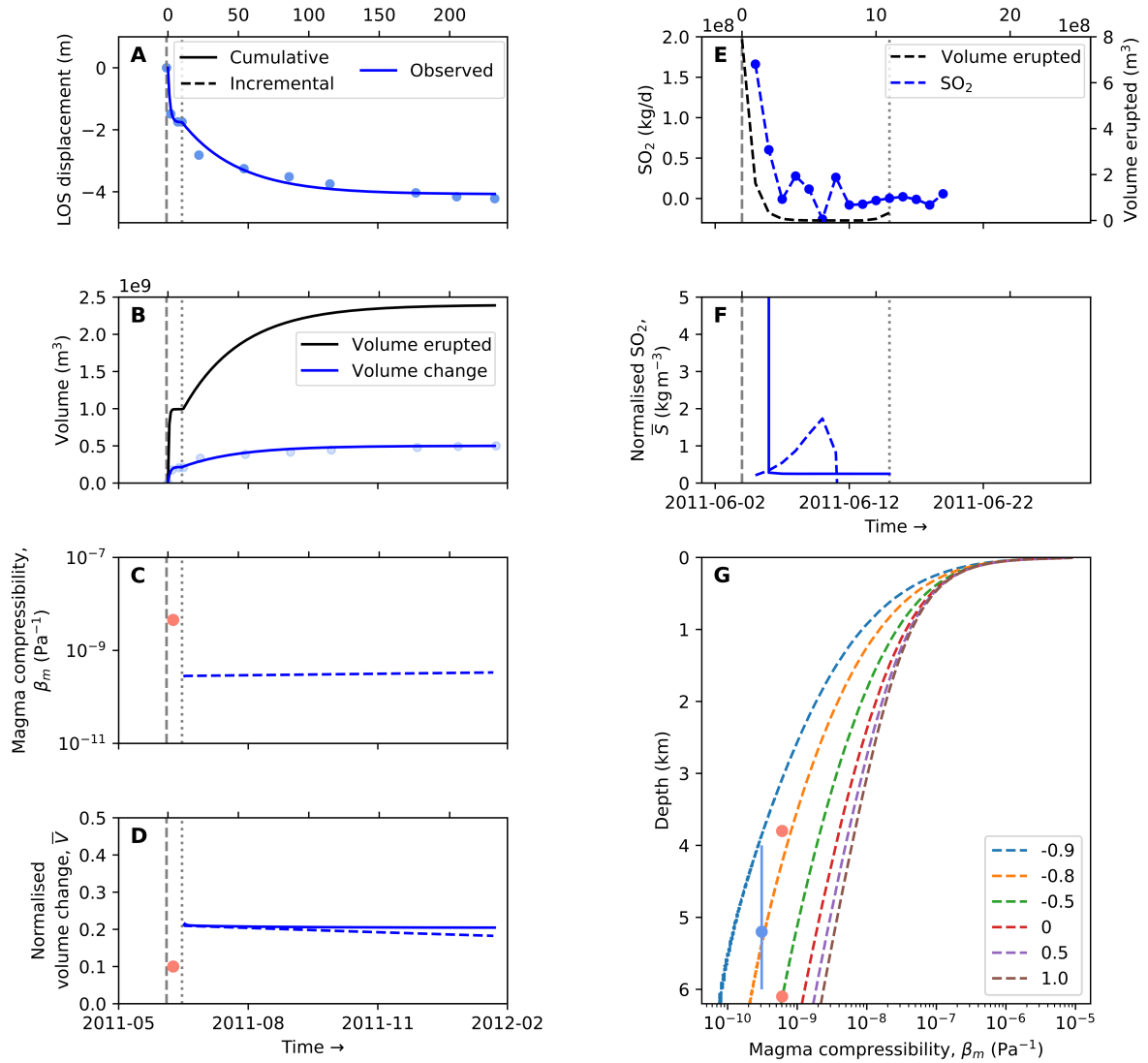


FIGURE 4.6. (page 96): Temporal evolution of eruption data for the 2011 eruption of Cordon Caulle. (a) LOS displacement from InSAR measurements (Delgado, 2021). (b) Volume of extruded lava estimated from tephra mapping and differences between pre- and post-eruptive DEM (Pistolesi et al., 2015; Delgado et al., 2019) and volume change of reservoir estimated from the total co-eruptive volume change and ground deformation. (a-b) The data (dots) are smoothed using splines (solid lines). (c) Incremental changes of magma compressibility estimated from normalised volume change using Eq. 4.3. (d) Cumulative and incremental normalised volume change calculated by normalising the fitted volume change to the fitted volume erupted. (e) Incremental  $\text{SO}_2$  flux measured with IASI (Theys et al., 2013). The incremental volume erupted is included in the plot for comparison. (f) Incremental gas volume fraction in the magma. (g) Magma compressibility with varying pre-eruptive volatile segregation. The depth of the reservoir is represented by data points, with orange indicating the depth of the two deflation sources during the explosive phase and blue indicating the depth of the reservoir during the effusive phase. In panels a-f, the vertical dashed line indicates the start of the eruption which occurred on 4 June 2011, while the dotted dashed line indicates the point at which the eruption transitioned into an effusive phase on 15 June 2011.

#### 4.3.2.1 Observations of the 2011-2012 eruption of Cordón Caulle

The explosive phase lasted for 11 days (4-15th June 2011) and produced a total volume of  $\sim 1.0 \text{ km}^3$ , the majority of which erupted within the first three days (Pistolesi et al., 2015). GNSS measurements were not available (Wendt et al., 2017), but InSAR measured subsidence of  $\sim 1 \text{ m}$  and  $0.4 \text{ m}$ , respectively, at the neighbouring volcanoes of Cordillera Nevada and Puyehue, with model depths of  $3.8$  and  $6.1 \text{ km}$  (Jay et al., 2014). These deflationary sources are  $\sim 10 \text{ km}$  away from the vent, suggesting good connectivity between distinct reservoirs within a mush system (Delgado, 2021). Jay et al. (2014) inverted the interferograms and show that the co-eruptive deflation at the eruptive vent is  $\sim 0.11 \text{ km}^3$ .

The effusive phase produced a rhyolitic lava flow with a volume of  $0.45 \text{ km}^3$ , accompanied by occasional explosive activity (Schipper et al., 2013; Coppola et al., 2017). During the effusive phase, Cordón Caulle experienced a quasi-exponential subsidence of  $2.2$ - $2.5 \text{ m}$ , which can be modelled by a horizontal prolate spheroid at a depth of  $5.2 \text{ km}$  (Figure 4.6a) (Jay et al., 2014; Delgado et al., 2019). The lava flow was accompanied by the intrusion of a shallow laccolith with a combined volume of  $\sim 1.5 \text{ km}^3$  (Delgado et al., 2019). We create

time series of surface displacement and erupted volume using the model of Delgado et al. (2019), which assumes an exponential decay of the form  $(1 - e^{-t/\tau_c})$  based on a deflating magma chamber with no magma recharge (e.g., Huppert and Woods, 2002; Woods and Huppert, 2003; Mastin et al., 2008). We fit this equation to the data and find values of  $\tau_c$  of 40 days for the displacement and 41 days for the erupted volume (Figure 4.6a-b). To convert the displacement time series to volume change, we assume that the volume change is proportional to displacement (i.e. the source geometry remains constant) and use the ratio between the total co-eruptive volume change  $\sim 0.5 \text{ km}^3$  and total displacement  $\sim 2.5 \text{ m}$  to calculate the constant of proportionality (Figure 4.6b). Finally, we normalise the estimated volume change by the erupted volume to give  $\bar{V}$  (Figure 4.6d).

SO<sub>2</sub> emissions were measured using the Infrared Atmospheric Sounding Interferometer (IASI), which is best suited to the low levels of ultraviolet radiation and strong ozone absorption during austral winter (Theys et al., 2013). The SO<sub>2</sub> flux peaked on the first day of the eruption at  $\sim 0.17 \text{ Tg}$ , followed by a sharp decrease, and fell below the detection limit on 10 June (Figure 4.6e) (Theys et al., 2013; Carbone et al., 2014). The total SO<sub>2</sub> flux during the explosive phase is  $\sim 0.25 \text{ Tg}$ . The occasional negative SO<sub>2</sub> flux in the time series are caused by uncertainties due to the large and dispersed plumes (Figure 4.6e) (Theys et al., 2013).

#### 4.3.2.2 Temporal changes in magma properties

We calculate time series of cumulative normalised volume change,  $\bar{V}$ , cumulative normalised SO<sub>2</sub> flux,  $\bar{S}$ , and magma compressibility,  $\beta_m$ , during the effusive phase, but treat the explosive phase as a single time step due to the lack of data (Figure 4.6c,d,f). To calculate chamber compressibility, we assume a horizontal prolate source with crustal compressibility  $\beta_c = \frac{3}{2\mu}$  and a shear modulus  $\mu = 20 \text{ GPa}$  (Delgado et al., 2019).

Normalising the co-eruptive volume change by the erupted volume during the explosive phase yields  $\bar{V} = 0.11$ , which corresponds to a magma compressibility of  $6.1 \times 10^{-10} \text{ Pa}^{-1}$  (Figure 4.6c-d). Neither cumulative normalised volume change ( $\bar{V}$ ) nor magma compressibility ( $\beta_m$ ) change significantly during the effusive eruption. The incremental value of  $\bar{V}$  decreases from  $\sim 0.21$  initially to  $\sim 0.18$  and magma compressibility increases from  $2.8 \times 10^{-10} \text{ Pa}^{-1}$  to  $3.6 \times 10^{-10} \text{ Pa}^{-1}$  suggesting a minor decrease in gas content (Figure 4.6c-d). The estimated compressibility is on the same order of magnitude ( $\sim 10^{-10}$

TABLE 4.3. Input parameters and the range of parameters explored in the forward models for Cordón Caulle, 2011. Values enclosed in curly brackets represent the extreme or end-member values.

Symbol	Description	Parameter space
$k_L$	Proportion $k$ of underlying magma	$\{-0.9 - +1.0\}$
$d$	Depth of chamber	5.2 km
$w^{\text{H}_2\text{O}}, w^{\text{CO}_2}$	H <sub>2</sub> O and CO <sub>2</sub> content in melt inclusion	3.9 wt%, 220 ppm
$w^g$	Excess gas content in melt inclusion	1.5 wt%
$f_{\text{O}_2}$	Oxygen fugacity	NNO-0.69
$T$	Temperature	850 °C
$\mu$	Crustal shear modulus	20 GPa
	SiO <sub>2</sub> content	76 wt%

$\text{Pa}^{-1}$ ) as the calculations by Jay et al. (2014) and Delgado et al. (2019). Comparatively, the normalised volume change during the explosive phase is lower than in the effusive phase, suggesting a decrease in gas content and magma compressibility between the two eruption phases.

We estimate the degree of degassing by comparison to model predictions for closed system degassing (Yip et al., 2022, 2024). In this case we start the model using melt inclusion data from ~5.2 km depth which gives initial volatile contents of H<sub>2</sub>O = 3.9 wt%, CO<sub>2</sub> = 220 ppm and exsolved gas phase of 1.5 wt% which is 63% H<sub>2</sub>O and 36% CO<sub>2</sub> (Jay et al., 2014) (Table 4.3). The initial starting temperature is 850 °C, and the SiO<sub>2</sub> is 76 wt%, which corresponds to a generic rhyolite composition. We use EVo to calculate compressibility for depths between 1-6 km and degree of pre-eruptive gas segregation of  $-0.9 < k < 1.0$  (Figure 4.6g). The observed values ( $\sim 3.1 \times 10^{-10} \text{ Pa}^{-1}$ ) fall within the range of  $k = -0.9$  to  $-0.8$ , consistent with the observations of Delgado et al. (2019) who noted substantial degassing of the magma following the explosive phase. This is also consistent with the the lack of SO<sub>2</sub> gas detected by satellites during the effusive phase (Theys et al., 2013; Carbone et al., 2014).



## 4.4 Discussion

Many volcanoes exhibit transitions between effusive and explosive behaviour within a single eruptive episode. We used a simple two-layer model to show that variations in gas content can cause changes in magma compressibility that are measurable using time series of deformation and eruptive volume. Thus, the framework presented here represents a new opportunity to quantify changes in magma properties during eruptions, allowing for a better understanding of magmatic systems and eruption dynamics. However, there are a number of limitations:

- Simultaneous time series of volcanic deformation,  $\text{SO}_2$  emissions and erupted volume are still relatively rare. Even for the case studies discussed here, it was necessary to interpolate the available data onto common time steps, and insufficient data was available to look for changes in compressibility during the explosive phase of the Cordón Caulle eruption.
- Minimal differences have been observed between the volatile contents of explosive and effusive eruptions (Koleszar et al., 2012). Here we have focused on the extreme differences in magma compressibility caused by gas-rich caps and degassed plugs, but many changes in eruption style may not be accompanied by significant changes in magma compressibility.
- The two-layer model is an oversimplification. For example, our analysis of the 2004-2005 Mount St Helens eruption suggests the presence of a gas-poor pocket within the reservoir. While adding additional layers or gradients is possible, a more appropriate approach may be to estimate the bulk gas fraction at each time step and reconstruct the reservoir content in reverse.
- Many eruptions involve magma from multiple sources. The effect of the connectivity between different pockets of a trans-crustal system remains to be explored (e.g., Gudmundsson, 2012; Sigurdsson, 2016; Roman and Lundgren, 2021).
- The framework would be challenging to apply to an eruption comprising multiple phases, such as the 2006 eruption of Augustine (Wasser et al., 2021).

Despite these limitations, monitoring the changes in gas emissions, deformation, and magma properties through continuous observations offer valuable insights into the

evolution of the eruptive systems (Reath et al., 2019, 2020; Manley et al., 2021), and this study presents a new conceptual framework within which they can be interpreted.

## 4.5 Conclusion

This study provides new insights into how changes in gas content during volcanic eruptions affect monitoring data, notably surface deformation and SO<sub>2</sub> emission measurements. We integrate time series of surface deformation, SO<sub>2</sub> emissions, and erupted volume to investigate the changes in gas content and their impact on magma compressibility. The models show that pre-eruptive gas segregation and gas content play a substantial role in determining eruption behaviours, surface deformation, and SO<sub>2</sub> emissions.

Our study focused on two eruption scenarios, each characterised by a two-layered magma reservoir – one featuring a gas-rich upper layer and the other a degassed upper layer. In the case of a well-connected reservoir with a gas-rich upper layer, the total gas content within the magma decreased progressively over time, which led to a reduction in SO<sub>2</sub> emissions and magma compressibility, while increasing the volume change. The opposite is true when the upper layer is a degassed plug. Once the upper layer is depleted, the bulk magma properties align with the underlying magma. Both cumulative and incremental measurements show similar trends, but the incremental data provided more immediate insights into magma properties, which emphasises the importance of calculating incremental changes during eruptions.

Analysing two distinct eruption events – 2004-2005 Mount St. Helens and 2011-2012 Cordón Caulle – revealed contrasting magma behaviors, with one involving a degassed plug and the other a gas-rich cap, respectively. Our analysis shows that magma compressibility increased during the eruption of Mount St Helens, but no change was observed during the effusive phase of the Cordón Caulle eruption. While the two-layer model captured the dynamics of the Mount St. Helens eruption, the observed variations in magma compressibility highlights the need for more sophisticated models to account for the complexity of the reservoir. We also emphasise the lack of data during explosive eruptions that limits the depth of comprehensive analysis.

Our results present a novel approach for assessing the changes in magma properties dur-

ing eruptions. However, the lack of simultaneous time-series data (surface deformation,  $\text{SO}_2$  emissions, and erupted volume) limits the analysis of changes in magma properties during explosive eruptions. Analyses involving involving complex magmatic plumbing systems and multiple eruption phases fall short in presenting a full picture of the system and may be biased by assumptions. Therefore, increasing model complexity, such as incorporating multiple layers, is crucial to capture the behaviour of magma during eruptions and improve our understanding magmatic plumbing systems and monitoring data.

# Chapter 5

## Discussion

In this chapter, I present the additional sensitivity analysis and case studies that I have investigated during my PhD research, as well as the limitations that have been identified in the development of the thermodynamic framework. Furthermore, I explore the future prospects of volcano monitoring and propose the development of a web tool based on the thermodynamic framework to facilitate collaboration among volcanologists.

### 5.1 Effects of temperature on volatile solubility

Previous chapters have established the effects of initial magmatic volatile content ( $\text{H}_2\text{O}$ ,  $\text{CO}_2$  and S), oxygen fugacity  $f_{\text{O}_2}$  and crustal compressibility (shear modulus  $\mu$  and geometry) on observations such as normalised  $\text{SO}_2$  ( $\bar{S}$ ) and normalised volume change ( $\bar{V}$ ). However, it is also important to recognise the influence of temperature on volatile exsolution, which has been briefly discussed in Chapter 2. In particular, basalts with higher temperatures have higher volatile diffusivity, which promotes degassing during shallow magma ascent (Figure 2.1). In this section, we conduct a sensitivity analysis to explore the effects of temperature on basaltic systems.

The sensitivity analysis is performed using the same method outlined in Chapter 2, with the following input parameters: a composition of generic basaltic magma (with 48 wt%  $\text{SiO}_2$ ) with an initial magmatic volatile content defined by  $w^{\text{H}_2\text{O}} = 3.3$  wt%,  $w^{\text{CO}_2} = 1.0$  wt% and  $w^{\text{S}} = 1600$  ppm, and  $f_{\text{O}_2} = \text{NNO}$  (Table B.1). The parameter under investigation is temperature, spanning the range of 1000-1200 °C, a typical temperature range for basaltic eruptions. The crustal shear modulus considered here is  $\mu = 2.1$  GPa, which is consistent with typical values found in volcanic rocks (Colombier et al., 2020), and

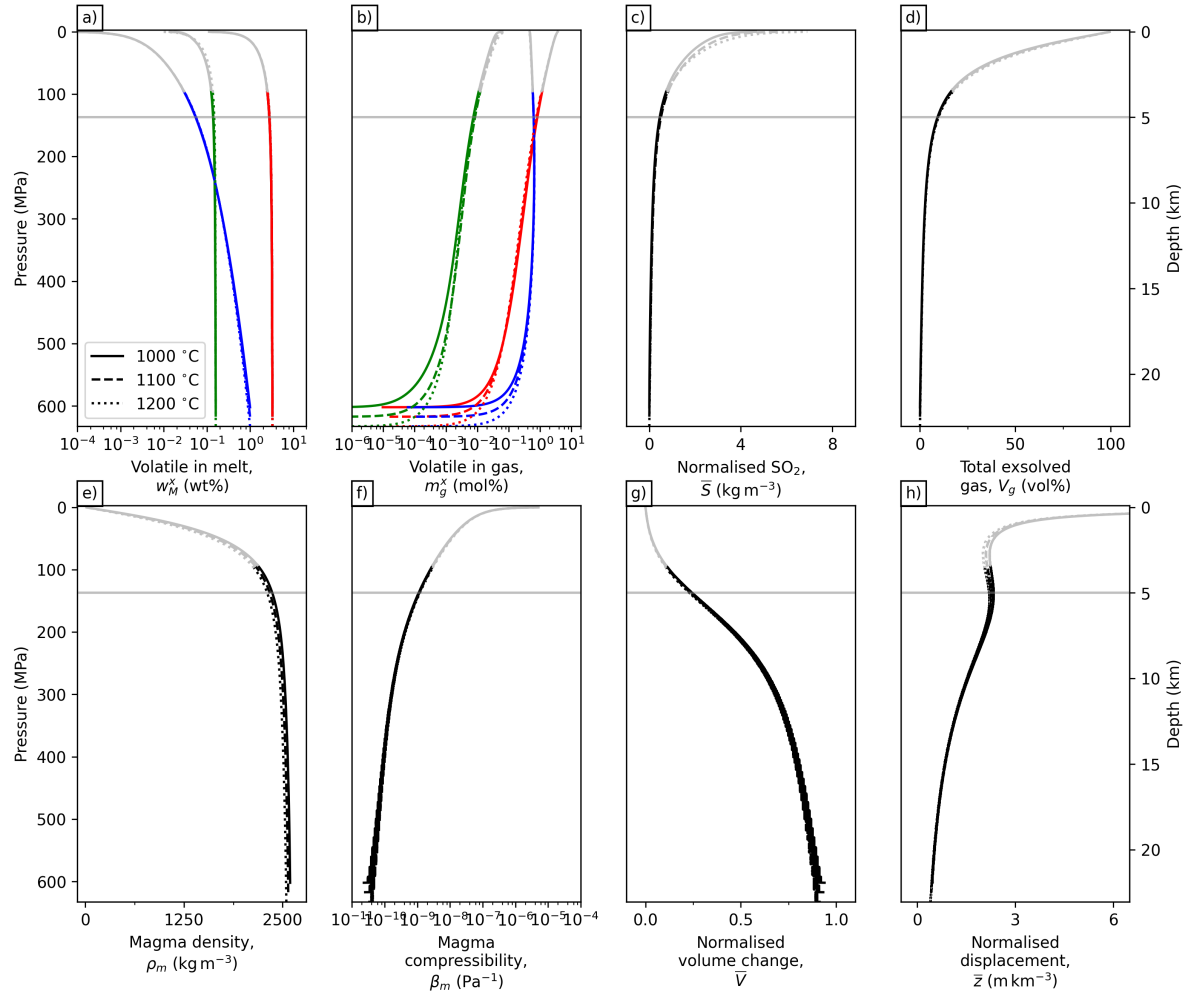


FIGURE 5.1. Physicochemical properties of basalts when varying the initial temperature from 1000-1400 °C. (a) Weight fraction of dissolved  $\text{H}_2\text{O}$ ,  $\text{CO}_2$  and S in melt ( $w_M^x$ ). (b) Mole fraction of exsolved  $\text{H}_2\text{O}$ ,  $\text{CO}_2$  and  $\text{SO}_2$  in gas ( $m_g^x$ ). (c) Mass of  $\text{SO}_2$  gas per unit volume of magma, also defined as normalised  $\text{SO}_2$  ( $\bar{S}$ ). (d) Volume fraction of exsolved gases in magma ( $V_g$ ). (e) Magma density ( $\rho_m$ ). (f) Magma compressibility ( $\beta_m$ ). (g) Model predicted volume change normalised by unit volume of magma ( $\bar{V}$ ). (h) Maximum vertical displacement normalised by unit volume of magma ( $\bar{z}$ ). Panels a, b, d and e show magma properties as a function of depth and panels c, g and h represent the model value for a unit volume of magma that instantaneously erupted from a particular depth. The grey lines represent magma properties after exceeding percolation threshold  $\phi_c = 37$  vol%. Fixed parameters:  $w^{\text{H}_2\text{O}} = 3.3$  wt%,  $w^{\text{CO}_2} = 1.0$  wt%,  $f_{\text{O}_2} = \text{NNO}$ ,  $w^{\text{S}} = 1600$  ppm and  $\mu = 2.1$  GPa.

the chamber geometry is represented as a Mogi point source within a uniform elastic half-space (Mogi, 1958). The sensitivity analysis reveals the role of each parameter on degassing and deformation, but does not consider the co-dependence of input variables, meaning some parameter combinations are not physically realistic.

Figure 5.1 shows the effects of varying temperature in basaltic magmas. Increasing the temperature of magma from 1000-1200 °C has minimal impact on H<sub>2</sub>O and CO<sub>2</sub> content, both dissolved and exsolved, while producing a slight increase in exsolved SO<sub>2</sub> gas content (Figure 5.1a-b). Consequently, hotter magmas generate higher normalised SO<sub>2</sub> ( $\bar{S}$ ) than cooler magmas, albeit minimal (Figure 5.1c). Given that H<sub>2</sub>O content is the dominant volatile that controls magma compressibility, there are minimal changes on normalised volume change ( $\bar{V}$ ) and normalised displacement ( $\bar{z}$ ) (Figure 5.1f-g). To summarise, hotter magmas generate greater SO<sub>2</sub> emissions and reduce volume changes of reservoir when compared to cooler magmas, but these effects are relatively minor when compared to the impacts of magmatic volatile content, oxygen fugacity and crustal compressibility, and thus varying temperature does not affect our main conclusions in the previous chapters.

## 5.2 Additional case studies

### 5.2.1 Applicability of thermodynamic framework

Here we demonstrate the applicability of the thermodynamic framework developed in Chapter 2 to an eruption. This analysis requires all six essential datasets to illustrate the relationship between magmatic volatile content and observations of volcanic deformation and degassing, namely: 1) co-eruptive deformation, 2) SO<sub>2</sub> budget, 3) erupted volume, 4) petrological data, 5) chamber depth and 6) chamber geometry (Table 5.1). The specific eruption chosen for this case study is the 2011 eruption of Grimsvötn in Iceland, situated beneath the Vatnajökull ice cap and thus known for its phreatomagmatic activity (Björnsson and Einarsson, 1990; Greiner and Geirsson, 2021). The 2011 eruption of Grimsvötn has a Volcanic Explosivity Index (VEI) of magnitude 4, which is the largest since 1873. This eruption prompted detailed geophysical and geochemical studies that provide the constraints required for the thermodynamic model (Table 5.1) (e.g., Reverso et al., 2014; Hreinsdóttir et al., 2014; Haddadi et al., 2017).

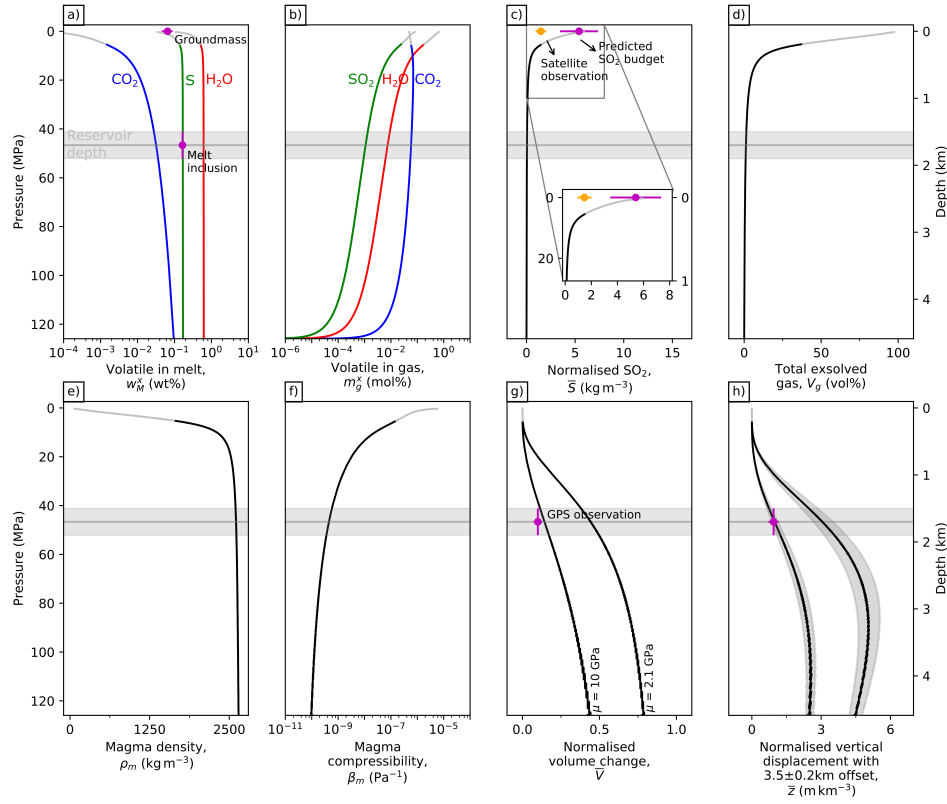


FIGURE 5.2. The magma and crustal properties of the 2011 eruption of Grims-vötn versus pressure/depth. (a) Dissolved volatile contents (in wt%) and (b) Exsolved volatile contents (in mole fraction). (c) Normalised  $\text{SO}_2$  ( $\tilde{S}$ ). Satellite observed  $\tilde{S}$  and predicted  $\tilde{S}$  when considering the  $\text{SO}_2$  budget (i.e., difference between melt inclusions and groundmass) are shown as orange and purple data points with error bars, respectively (Sigmarsson et al., 2013). The inset figure shows  $\tilde{S}$  from surface to 1 km depth. (d) Volume fraction of exsolved gases in magma ( $V_g$ ). (e) Magma density ( $\rho_m$ ) and (f) magma compressibility ( $\beta_m$ ). (g) Normalised volume change ( $\tilde{V}$ ). (h) Normalised vertical displacement ( $\tilde{z}$ ) with  $3.5 \pm 0.2$  km horizontal offset (Hreinsdóttir et al., 2014). In panel g-h, the purple data points with error bars represent observations made from the GPS station and Mogi modelling (Hreinsdóttir et al., 2014). Different crustal shear moduli are used to identify the possible value of crustal shear modulus best fitted with the observation. The horizontal line with shaded region represents the reservoir depth at  $1.7 \pm 0.2$  km. The grey lines from panels a-h represent magma properties after exceeding percolation threshold  $\phi_c = 37$  vol%. Initial conditions of basalt:  $\text{H}_2\text{O} = 0.66$  wt%,  $\text{CO}_2 = 960$  ppm,  $f_{\text{O}_2} = \text{NNO} - 0.14$ , and  $\text{S} = 1700 \pm 330$  ppm (Sigmarsson et al., 2013; Haddadi et al., 2017). Adapted from Figure 2.2.

TABLE 5.1. Model parameters for the 2011 eruption of Grimsvötn and their comparison to the model results.

Parameter	Observed	This study
<b>Model parameters</b>		
SO <sub>2</sub> budget (kg)	$3.8 \times 10^8$ <sup>a</sup>	-
Total erupted volume (m <sup>3</sup> )	$2.7 \pm 0.7 \times 10^8$	-
Total volume change (m <sup>3</sup> )	$0.27 \pm 0.3 \times 10^7$	-
Total vertical displacement <sup>b</sup> (m)	$0.25 \pm 0.01$	-
Reservoir depth <sup>c</sup> (km)	$1.7 \pm 0.2$	-
Chamber geometry	Mogi point source	-
Poisson's ratio	0.25	-
<b>Petrological data</b>		
Melt inclusion H <sub>2</sub> O (wt%)	0.66 wt%	-
Melt inclusion CO <sub>2</sub> (ppm)	960	-
Melt inclusion S (ppm)	$1700 \pm 330$	-
Groundmass S (ppm)	$650 \pm 200$	300
$f_{\text{O}_2}$	NNO-0.14	-
<b>Key results</b>		
Normalised SO <sub>2</sub> (kg m <sup>-3</sup> )	$1.4 \pm 0.3$ <sup>d</sup>	6.9
Normalised volume change	$0.10 \pm 0.03$	$0.14$ <sup>e</sup>
		$0.44$ <sup>f</sup>
Normalised displacement (m km <sup>-3</sup> )	$0.93 \pm 0.24$	$0.99 \pm 0.13$ <sup>e</sup>
		$3.1 \pm 0.43$ <sup>f</sup>

<sup>a</sup> Sigmarsson et al. (2013) predicted SO<sub>2</sub> budget of  $1.5 \pm 0.35 \times 10^9$ <sup>b</sup> GPS measurements 3.5km from source.<sup>c</sup> Reservoir depth estimated from geodesy.<sup>d</sup> Sigmarsson et al. (2013) predicted normalised SO<sub>2</sub> of  $5.4 \pm 2.0 \text{ kg m}^{-3}$ <sup>e</sup> When crustal shear modulus  $\mu$  is 10 GPa<sup>f</sup> When crustal shear modulus  $\mu$  is 2.1 GPa



Geochemical analysis of erupted products show that the melt inclusions from an average crystallisation depth of  $15 \pm 5$  km consist of  $\text{H}_2\text{O} = 0.66$  wt%,  $\text{CO}_2 = 960$  ppm and  $f_{\text{O}_2} = \text{NNO} - 0.14$  (Table 5.1) (Haddadi et al., 2017). The sulfur content measured in melt inclusions is  $1700 \pm 330$  ppm but measurements of the erupted groundmass show a sulfur content of  $650 \pm 200$  ppm (Sigmarsson et al., 2013). This discrepancy suggests that co-eruptive degassing was significant during this eruption (Sigmarsson et al., 2013). Mass balance calculations reveal that some sulfur may have been lost from the emitted gases by scrubbing, by adhering to tephra glass and some sequestered as sulfide globules (Sigmarsson et al., 2013). Satellite measurements estimated the  $\text{SO}_2$  yield to be  $3.8 \times 10^8$  kg, which is less than the  $\text{SO}_2$  output as estimated from the difference in sulfur concentration between the groundmass glass and melt inclusions at  $1.5 \pm 0.35 \times 10^9$  kg (Table 5.1) (Sigmarsson et al., 2013; Carn et al., 2016). As satellite observations of  $\text{SO}_2$  are challenging at high latitudes due to reduced ultraviolet, this sulfur ‘deficit’ suggest that the satellite observations are an underestimate.

An erupted volume of  $2.7 \pm 0.7 \times 10^8 \text{ m}^3$  dense-rock equivalent of basaltic magma is estimated based on tephra mapping, and a total vertical subsidence of  $0.25 \pm 0.01$  m is observed throughout the eruption period using a GPS site located 3.5 km from the source (Table 5.1) (Hreinsdóttir et al., 2014). The ground deformation measured by geodesy estimated a reservoir depth of  $1.7 \pm 0.2$  km and a co-eruptive volume change of  $0.27 \pm 0.3 \times 10^7 \text{ m}^3$  using a Mogi model and assuming a Poisson’s ratio of 0.25 (Hreinsdóttir et al., 2014). However, deformation signals observed over three eruptive cycles (eruptions of 1998, 2004, and 2011) suggest that Grimsvötn has two sill-shaped magma reservoirs at 3 km and 10 km depth (Reverso et al., 2014). Additionally, numerical modelling using Finite Element Method reveals that Grimsvötn has a complex heterogeneous crust, such that the caldera is filled by weak crustal rocks in addition to being surrounded by stiff crustal rocks (Greiner and Geirsson, 2021). According to numerical modelling by Greiner and Geirsson (2021), the crustal shear modulus  $\mu$  for Grimsvötn varies from surface to 3 km below summit, in which the weak crustal rocks filling the caldera have  $\mu = 0.6\text{-}9.8$  GPa while the stiff surrounding crustal rocks have  $\mu = 1.6\text{-}18$  GPa.

Here we use petrological data obtained from melt inclusions ( $\text{H}_2\text{O} = 0.66$  wt%,  $\text{CO}_2 = 960$  ppm and  $\text{S} = 1700$  ppm). The oxygen fugacity ( $f_{\text{O}_2}$ ) is set at  $\text{NNO} - 0.14$ , and the initial temperature is set to  $1200^\circ\text{C}$ . These values serve as input parameters for the thermodynamic model (Table 5.1). Magmatic processes from the shallow reservoir have

greater contributions to co-eruptive signals than a deep reservoir and thus, for simplicity, we apply the thermodynamic framework for a single shallow magma source using a Mogi model.

The thermodynamic model EVo (Liggins et al., 2020, 2022) predicts that the sulfur content of the erupted lava is 300 ppm, which is less than the observed value of  $650 \pm 200$  ppm in the matrix glass (Figure 5.2a) (Sigmarsson et al., 2013). The greater sulfur concentration observed in the matrix glass as compared to the model suggests that at least some fraction of the sulfur in the matrix glass is not in equilibrium with the atmosphere (i.e., sulfur degassing is incomplete).

The normalised  $\text{SO}_2$  estimated using measurements from satellite and erupted volume is  $1.4 \pm 0.3 \text{ kg m}^{-3}$  (Table 5.1; Figure 5.2c). However, it has been reported that sulfur scrubbing occurs during magma ascent (Sigmarsson et al., 2013), which results in the underestimation of  $\text{SO}_2$  detected by satellites and thus normalised  $\text{SO}_2$ . Using melt inclusion data, the framework predicts a normalised  $\text{SO}_2$  value of  $6.9 \text{ kg m}^{-3}$  with the assumption that the magma have undergone co-eruptive degassing, where volatiles continue to exsolve during magma ascent. This is consistent with the previous prediction of the  $\text{SO}_2$  budget ( $5.4 \pm 2.0 \text{ kg m}^{-3}$ ; Sigmarsson et al., 2013).

Using the model outlined in chapter 2, we compute normalised volume change ( $\bar{V}$ ) and normalised displacement ( $\bar{z}$ ) using  $\mu = 10 \text{ GPa}$  and assume a homogeneous crust. The model predicted  $\bar{V} = 0.14$  and  $\bar{z} = 0.99 \pm 0.13 \text{ m km}^{-3}$  at 1.7 km depth, which is comparable to the GPS measurements of  $\bar{V} = 0.10 \pm 0.03$  and  $\bar{z} = 0.93 \pm 0.24 \text{ m km}^{-3}$  (Hreinsdóttir et al., 2014) (Table 5.1; Figure 5.2g). For a homogeneous crust with  $\mu = 2.1 \text{ GPa}$ , that of typical volcanic rocks (Heap et al., 2020), the model predicts that at 1.7 km depth  $\bar{V} = 0.44$  and  $\bar{z} = 3.1 \pm 0.43 \text{ m km}^{-3}$  (Table 5.1; Figure 5.2g). This overprediction of  $\bar{V}$  suggests that the host rock at Grimsvötn is stronger than typical volcanic rocks. While the model demonstrated a quantitative link between volcanic deformation and degassing using simple model assumptions (e.g., homogeneous crust, Mogi source), the complexity of the surrounding crust has significant implications on volcanic deformation, which highlights the importance of considering crustal heterogeneity and crustal compressibility for specific volcanoes.

## 5.2.2 Time series analysis

In this section, we evaluate the framework presented in Chapter 4 and highlight its limitations using three additional examples of co-eruptive time series, namely the 2011 eruption of Grimsvötn, the 2010 eruption of Eyjafjallajökull and the 2006 eruption of Augustine (Figure 5.3). Here we analyse the change in normalised radial displacement ( $\bar{z}_R$ ) to investigate the variations in magma properties throughout an eruption.  $\bar{z}_R$  is calculated by normalising ground deformation data (specifically, the radial component of GPS measurements) to the corresponding erupted volume, which is obtained from various measurements such as aerophotogrammetry, ground-based cameras and satellite images. Given the varying frequency and timing of these measurements, the sparser datasets are interpolated to match the denser datasets. The  $\bar{z}_R$  values serve as an indicator to the changes in magma compressibility relative to the onset of eruption, where high  $\bar{z}_R$  suggests low magma compressibility and low  $\bar{z}_R$  indicates more compressible magma. Comparing the normalised radial displacement to  $\text{SO}_2$  emissions provides a qualitative check on the results and helps further our understanding of the magma plumbing system.

Many volcanoes exhibit changes in observation data within a single eruptive episode. The variations in gas content can cause changes in magma compressibility that are measurable using time series of deformation and eruptive volume. Here we analyse the temporal changes of normalised radial displacement for the three volcanic eruptions and compare them to  $\text{SO}_2$  gas emissions to showcase the limitations of the framework:

- **Grimsvötn, 2011:** A rapid deflation and an upsurge in erupted volume were evident within the initial 1.5 days of the eruption (Figure 5.3b-c) (Hreinsdóttir et al., 2014). This results in a decrease in  $\bar{z}_R$ , which suggests increased magma compressibility during this period (Figure 5.3d). These observations imply the presence of a degassed plug in the reservoir before the eruption. As this plug was removed, the total gas content in the reservoir surged, as evidenced from the rise in  $\text{SO}_2$  emissions, though we note the presence of sulfide globules associated to sulfur scrubbing (Figure 5.3a) (Sigmarsson et al., 2013; Prata et al., 2017). Notably, the observation period was only 1.5 days, indicating the rapid changes in gas content within the reservoir.
- **Eyjafjallajökull, 2010:** The volcano experienced rapid deflation that lasted for a week, followed by minimal deformation for the rest of the eruption (Figure 5.3f) (Sigmundsson et al., 2010). Conversely, there were multiple step increases in erup-

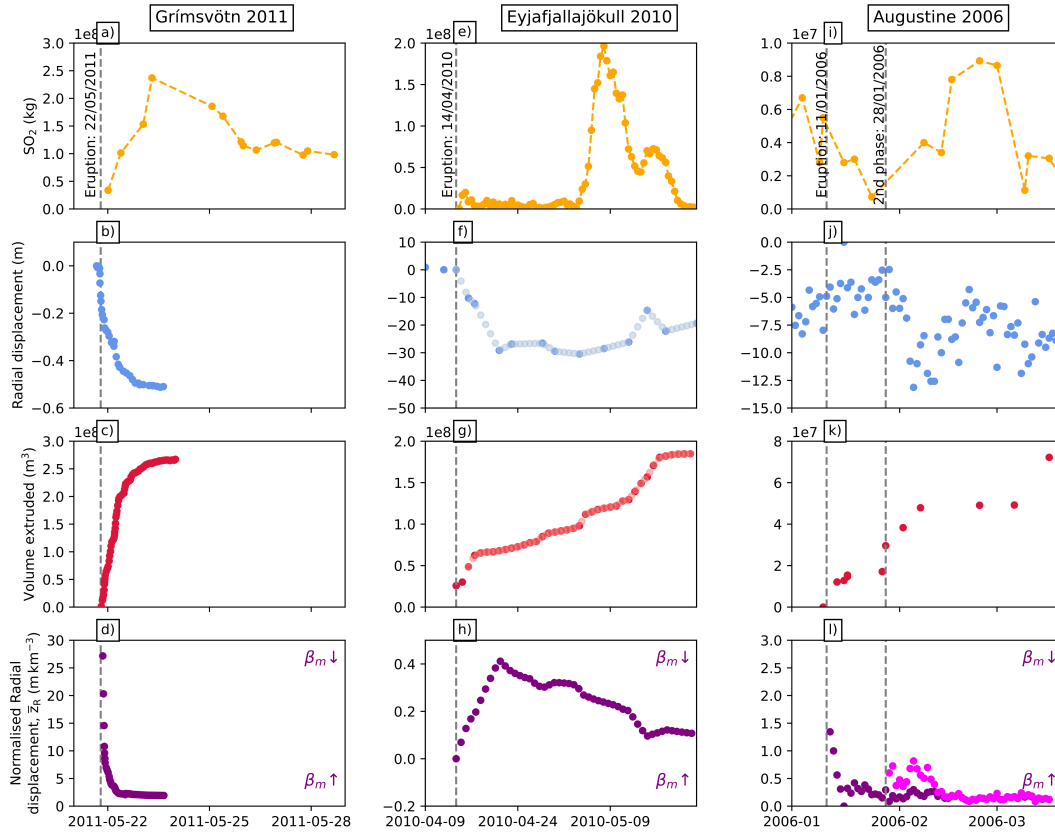


FIGURE 5.3. Temporal evolution of magma properties during the eruptions of Grímsvötn 2011 (left), Eyjafjallajökull 2010 (middle), and Augustine 2006 (right). Each row represents a different parameter (top to bottom):  $\text{SO}_2$  emission, ground deformation, erupted volume and the normalised radial displacement. The normalised radial displacement is obtained by dividing ground deformation by the erupted volume.

ted volume (Figure 5.3g). This resulted in an initial increase in  $\bar{z}_R$  for a week, followed by a gradual decline for the remaining duration of the eruption (Figure 5.3h). This preliminary analysis suggests that the magma initially showed characteristics similar to that of a gas-rich cap with high compressibility, then became less compressible for a week before again increasing compressibility. However,  $\text{SO}_2$  emissions remained consistently low during the initial three weeks, followed by a rapid increase for four days before returning to background levels for the rest of the eruption (Figure 5.3e) (Carboni et al., 2016). The low  $\text{SO}_2$  emissions could be due to the sub-glacial nature of the eruption that involves the scrubbing of magmatic  $\text{SO}_2$  gas in the glacier-filled summit and the high water vapour content of the atmosphere (Prata and Grant, 2001; Thomas and Prata, 2011; Delmelle

et al., 2021). The rapid increase in SO<sub>2</sub> emissions after three weeks of the eruption was regarded as an indicator of a magmatic eruption (Thomas and Prata, 2011). Due to scrubbing, using SO<sub>2</sub> emissions for a qualitative check on observations of volcanic deformation does not apply in this specific eruption.

- **Augustine, 2006:** The 2006 eruption occurred in multiple phases, each exhibiting distinct behaviour (Power et al., 2006; Wasser et al., 2021). The initial phase saw an increase in erupted material, with minimal changes in ground deformation (Figure 5.3j-k) (Cervelli et al., 2010; Coombs et al., 2010). Measurements of SO<sub>2</sub> emissions were elevated prior to the eruption but halved by the end of the initial phase (Figure 5.3i) (McGee et al., 2010). In the second phase, the increase in SO<sub>2</sub> emissions and the rapid deflation were accompanied by a stepped increase in the volume of erupted material. To analyse the magma compressibility during these phases, we calculated the  $\bar{z}_R$  relative to the onset of each phase (colour coded as purple and pink in Figure 5.3l). Both phases showed a decrease in  $\bar{z}_R$ , suggesting an increase in magma compressibility relative to the beginning of each phase. Notably, the initial phase (purple) showed higher  $\bar{z}_R$  compared to the second phase (pink), indicating less compressibility in the initial phase than during the second phase. This is consistent with the qualitative comparison to SO<sub>2</sub> emissions, where SO<sub>2</sub> emissions were initially low due to outgassing prior to the eruption that results in the depletion of SO<sub>2</sub> in the magma (McGee et al., 2010). However, the increase in SO<sub>2</sub> emissions in the second phase is influenced by co-eruptive degassing attributed to the effusive nature of this eruption phase (Coombs et al., 2010; McGee et al., 2010). Therefore, we note that in this specific scenario, using SO<sub>2</sub> emissions for a qualitative check may lead to misleading interpretations.

The examples presented here show that the time-dependent thermodynamic framework is a useful tool for monitoring the changes in magma properties, such as compressibility. However, they also highlight the limitations within the framework. The lack of total SO<sub>2</sub> budget during the early stages of the 2010 Eyjafjallajökull eruption due to sulfur scrubbing results in the underestimation of SO<sub>2</sub> emissions, which is essential for providing a qualitative check for interpreting normalised displacement data. Additionally, the model has difficulties in comparing SO<sub>2</sub> emissions and normalised displacement data during the second phase of the 2006 Augustine eruption due to co-eruptive degassing, which may result in overestimating the gas content in the magma and thus magma

compressibility. These examples highlight the framework's limitations in interpreting deformation data in the absence of reliable measurements of SO<sub>2</sub> emissions.

Despite these limitations, monitoring the changes in gas emissions and deformation through continuous observations provide valuable insights into the evolution magma properties and the magma plumbing systems (Reath et al., 2019, 2020; Manley et al., 2021), and this study introduces a new conceptual framework for interpreting these data.

## **5.3 Limitations of data and model assumptions**

### **5.3.1 Limitations of thermodynamic model**

The thermodynamic model EVo operates on the assumption of the ideal gas law (Liggins et al., 2020, 2022). However, this assumption is not valid when the volatile phase is considered a supercritical fluid in magma reservoirs, which is typically subjected to high pressures and temperatures. As a result, the model overestimates volatile density and compressibility, leading to an underestimation of volume changes compared to scenarios where the volatile phase exists as a supercritical fluid. Nevertheless, Wasser et al. (2021) indicate that this overestimation does not yield any significant difference in the total volume of the exsolved volatile phase when compared with other equation of state models (Redlich and Kwong, 1949; Duan and Zhang, 2006), which suggests that the model can still approximate the volume of exsolved volatile phase reasonably.

### **5.3.2 Limitations of monitoring data**

While ground-based monitoring methods are well established, syn-eruptive data, such as deformation and erupted volume, are poorly constrained due to the limited spatial coverage and the destruction of instruments near explosive eruptions. Moreover, the risks associated with the eruption prevents timely data acquisition, which introduces uncertainties in the data, including underestimation of tephra volume due to erosion (e.g., the 2011 eruption of Cordón Caulle Pistolesi et al., 2015). The inability to quantify erupted volume in a timely manner during explosive eruptions meant estimations such as extrusion flux, which is a key parameter for our model, is limited.

An alternative approach to address the limitations in ground-based monitoring is the use of satellite data. With the increasing number of satellites in space and monitoring

techniques (Taylor et al., 2018; Morishita et al., 2020; Dualeh et al., 2023; Galetto et al., 2023; Esse et al., 2024), satellite data can fill in the gaps in ground coverage and that lack of ground monitoring. However, the sheer volume of data generated by satellites can be excessive for manual analysis. Recent advancements in automated algorithms can not only detect volcanic unrest (Anantrasirichai et al., 2018, 2019) but also quantify these measurements (Lazecky et al., 2020; Morishita et al., 2020). While the use of multiparameter satellite data has notably improved the detection of volcanic unrest (Furtney et al., 2018) and provide insights into the magma plumbing system of volcanoes (Reath et al., 2019, 2020), there are a number of limitations:

- **Deformation:** The different spatial resolutions and viewing geometries between different satellite systems make it challenging to directly compare synthetic aperture radar (SAR) images from various sources, and with the delays between data acquisition and the delivery of SAR images, it can prevent rapid responses to volcanic crisis. Additionally, it remains challenging to distinguish deformation signals from various noises such as atmospheric noise (Yu et al., 2018; Yip et al., 2019; Albino et al., 2022).
- **Erupted volume:** Access to SAR data is often restricted, and the limited amount of data available for scientific use is only available after obtaining permission from relevant authorities, such as TanDEM-X and Pléiades data (Kubanek et al., 2021; Grémion et al., 2023). In fact, only a handful of studies have used Pléiades data (Moussallam et al., 2019; Walter et al., 2022; Grémion et al., 2023), which reinforces the need for improved data accessibility and availability.
- **SO<sub>2</sub> emissions:** Most sensors operate in the ultraviolet spectrum and thus can only detect SO<sub>2</sub> emissions during daytime. Moreover, the sensitivity to SO<sub>2</sub> emissions is limited by low ultraviolet radiation levels during austral winter and when there is a high presence of water vapour in the atmosphere and clouds (Prata and Grant, 2001; Prata and Kerkmann, 2007; Theys et al., 2013).

Despite these limitations, the future prospects for improvement in volcano monitoring is promising. Upcoming missions (e.g., NISAR and Harmony) and contributions from commercial companies (e.g., ICEYE and Capella) can improve the global database on volcanic activity. Collaborative efforts between space agencies can address gaps in temporal resolution between different international satellite assets to ensure optimal

data are collected for volcano monitoring (e.g., CEOS project, Pritchard et al., 2018). Additionally, when data are processed in a timely manner and presented in a user-friendly format, it can facilitate easy access for personnel responding to volcanic crises (e.g., COMET volcano deformation database, NASA Global Sulfur Dioxide Monitoring database). With adequate temporal resolution and rapid data processing, models such as the time-dependent thermodynamic framework developed in this study can be applied to volcanic eruptions, and thus enable near-real-time quantification of parameters such as magma compressibility.

### 5.3.3 Limitations of crustal data

Crustal properties, such as crustal shear modulus ( $\mu$ ), and the geometry of a magma reservoir play a role in volcanic deformation (see Section 2.4.5 and Section 3.2.3). However, crustal shear modulus  $\mu$  varies with depth and does not vary systematically with tectonic setting (Gudmundsson, 2005; Colombier et al., 2020). Thus, inappropriate values of  $\mu$  used in models may lead to inaccurate predictions of volume changes of the reservoir and misinform our understanding of magmatic processes. To improve the models developed in this study future studies should consider crustal heterogeneity and thus appropriate values of  $\mu$  with depth.

## 5.4 Outlook

Many studies highlight the significance of incorporating magma compressibility in monitoring volcanic deformation (e.g., Rivalta and Segall, 2008; Delgado et al., 2019; Wong and Segall, 2019). Quantifying magma compressibility accurately is thus crucial for understanding the behaviour of magmatic systems as compressible magmas can accommodate volume changes of the reservoir and thereby suppressing ground deformation (Johnson et al., 2000; Rivalta and Segall, 2008). Given the widespread use of ground deformation in volcano monitoring, obtaining precise constraints on magma compressibility should be a priority.

The thermodynamic framework developed in this thesis uses thermodynamic models and petrological data to determine the gas content in the reservoir, which are used to estimate magma compressibility and subsequently, volume changes and SO<sub>2</sub> gas emissions. The model results can be used to evaluate observations of volcanic deformation and degassing



Flowchart for webtool

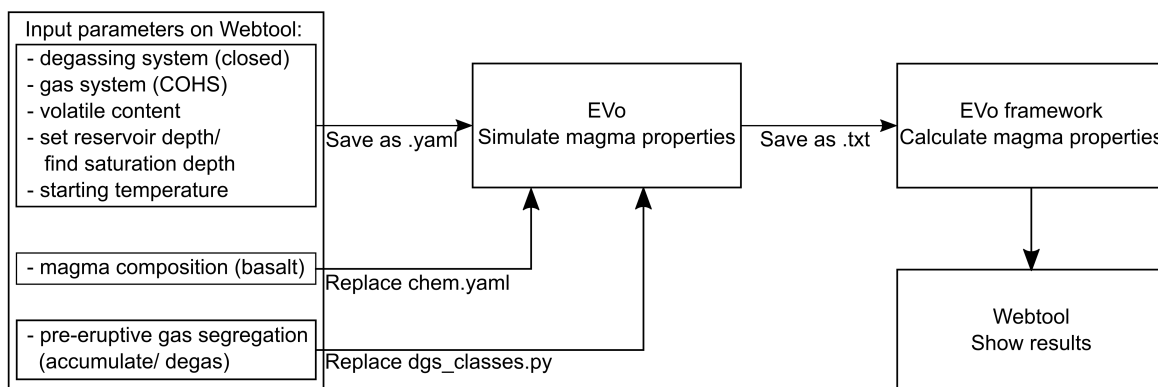


FIGURE 5.4. The flowchart depicts the process of using the thermodynamic framework webtool. This tool reads data from three separate files that provide information on 1) the magma storage conditions and volatile content, 2) magma composition and 3) gas segregation prior to eruption. These datasets are used by the thermodynamic model EVo to simulate the magma's properties, including its gas content and density. The resulting output from EVo is then used as an input for the thermodynamic framework, which calculates magma properties such as compressibility. The webtool presents and illustrates the results from the thermodynamic framework to the user.

with natural eruption data. This has been demonstrated in Chapter 2, which is the first quantitative study that shows water-rich arc eruptions exhibit less deformation than ocean island settings. Additionally, this thesis quantifies the temporal changes in magma properties such as gas content and compressibility using a combination of deformation and erupted volume data, and shows that changes in gas content during an eruption changes magma compressibility (Chapter 4). This demonstrates the importance of volcano monitoring using multiparameter observations.

To foster interdisciplinary collaboration and facilitate calculations linking volcanic deformation and degassing, the crucial next step involves developing a webtool version of the thermodynamic framework. This tool is designed to enable diverse users, including geophysicists, geochemists, and petrologists, to perform simulations and gain insights into the relationship between volcano monitoring signals and magma properties such as compressibility. The flowchart in Figure 5.4 outlines the process. First, the webtool requires data from three files that provide information on 1) magma storage conditions

and volatile content, 2) magma composition, and 3) pre-eruption gas segregation. Next, the webtool uses the thermodynamic model EVo (Liggins et al., 2020, 2022) to calculate magma properties, including the gas content of each species and magma density. The output data from EVo is further processed using a Python script to determine the magma compressibility and subsequently, volume changes. Lastly, the webtool presents these results in the form of Figure 2.2. By providing a user-friendly interface, the webtool encourages widespread application of petrology and thermodynamics to interpret monitoring signals and support volcanologists in understanding magma compressibility and gas content.



# Chapter 6

## Concluding remarks

This thesis investigates how magmatic volatile content and pre-eruptive gas segregation affect observations of volcanic deformation and degassing. However, this thesis only provides an incremental step in fully understanding the evolution of magma properties during an eruption. Exploiting the increasing number of models and data for volcano monitoring and research will facilitate further development of multi-parameter physics-based models capable of interpreting monitoring data as well as gaining further insights into the complexities of the magma plumbing system.

Volcanic deformation and outgassing are two widely observed parameters during an eruption, yet they are often treated as independent observations. While qualitative comparison between volcanic deformation and outgassing have provided insights into the underlying magma plumbing systems (Reath et al., 2019), quantitative measurements are required to better constrain magma properties that modulate magma processes. In Chapter 2, we develop a quantitative model to reconcile observations of volcanic deformation and degassing. The model investigates the impact of magmatic volatile content ( $\text{H}_2\text{O}$ ,  $\text{CO}_2$ , S), oxygen fugacity  $f_{\text{O}_2}$  and crustal compressibility on volcanic deformation and degassing. The results indicate that magma with high magmatic water content results in a highly compressible magma, which suppresses volume changes in the reservoir. While simplistic, this study remains robust and is the first to link volcanic deformation and degassing quantitatively, and reveals that water-rich arc eruptions exhibit less deformation than ocean island eruptions, which highlights the importance of exsolved magmatic  $\text{H}_2\text{O}$  for monitoring volcanic deformation, especially in arc settings.

The transition from the traditional concept of a magma chamber to a transcrustal

mush system has provided explanations for diverse observations unaccounted for by conventional models (Cashman et al., 2017; Head et al., 2019; Mullet and Segall, 2022). In Chapter 3, we extend the thermodynamic framework from the previous chapter to include pre-eruptive gas segregation processes, such as gas accumulation or loss. Our results show that pre-eruptive gas accumulation leads to increased  $\text{SO}_2$  emissions and reduced co-eruptive deformation, consistent with our current understanding of the magma plumbing system (Kilbride et al., 2016; Edmonds and Wallace, 2017). In contrast, pre-eruptive outgassing results in decreased  $\text{SO}_2$  emissions and co-eruptive deformation that is similar to the erupted volume. The global synthesis of volcanic systems reveals distinct behaviours between mafic magmatic systems ( $\text{SiO}_2 < 50\%$ ) and intermediate-silicic systems ( $\text{SiO}_2 > 50\%$ ): Mafic systems generally exhibit higher co-eruptive volume changes and wider ranges of  $\text{SO}_2$  emissions than intermediate-silicic systems due to the high volatile diffusivity and tendency for co-eruptive degassing that is characteristic of mafic systems. Our results emphasise the need to reconcile multi-parameter observations across various disciplines of volcanology (e.g., geophysics, geochemistry, petrology) when interpreting monitoring data. However, our current framework is limited by the lack of systematic approach to collecting monitoring data (gas, deformation, volume) and fundamental characteristics (magma composition, crustal properties).

The physicochemical properties of magma evolve throughout an eruption cycle. In Chapter 4, we demonstrate how changes in gas volume fraction and magma compressibility in a well-connected two-layered magma reservoir affect  $\text{SO}_2$  emissions and volume change during an eruption that is associated with a degassed plug or a gas-rich cap. Our results shows that the removal of a degassed plug increases the bulk magma compressibility and suppresses volume change of the reservoir, while the collapse of a gas-rich cap reduces the bulk magma compressibility.

Mount St. Helens is one of the most well monitored volcano, providing rich data for analysis (e.g., Gerlach et al., 2008; Lisowski et al., 2008; Anderson and Segall, 2011; Dzurisin et al., 2015). Using the observed deformation and erupted volume during the 2004 eruption, we calculated the incremental magma compressibility and tracked changes in magma compressibility over the 205-day study period. Our analysis revealed that the magma that erupted during the first 205 days had undergone extensive outgassing prior to the eruption, and subsequent magma that erupted had also undergone a certain extent of pre-eruptive outgassing. While the model is able to fit the modelled volume change

---

to the observed volume change, the analysis revealed the limitations of the two-layered magma model. The current model configuration is not able to capture the complexities of a magma plumbing system, and we suggest introducing additional layers to improve the model accuracy.

There are several examples of effusive eruptions with good data for analysing the temporal evolution of magma properties, but not many has gas-rich caps. One of the best studied eruption is the 2011 eruption of Cordón Caulle, where measurements of volcanic deformation, SO<sub>2</sub> emissions and erupted volume are available. However, the temporal resolution of the deformation and erupted volume is insufficient for rigorous analysis; only three sets of erupted volume and deformation data are available during the explosive phase that lasted for 10 days. The erupted volume were estimated from tephra that deposited during the first three days of the explosive eruption (Pistolesi et al., 2015), while the deformation data were acquired by satellites at different dates (Delgado, 2021), such that the two measurements could not be directly compared and thus restricts the analysis of this phase. As such, we focus on calculating the magma compressibility during the effusive phase of the eruption, and we find that there is no change in magma compressibility throughout the effusive phase, indicating that the magma in the reservoir was homogeneous following the explosive phase. This raises two questions: 1) how does highly heterogeneous conditions in a magma reservoir affect our ability to estimate magma volumes from deformation monitoring? and 2) can volcano monitoring data be used to estimate the gas content of a magma reservoir?

The valuable insights gained from the various case studies presented in Chapter 5 highlighted the limitations of the framework. External factors, such as sulfur scrubbing by glaciers and co-eruptive degassing during an effusive phase, influence the total SO<sub>2</sub> budget, which is essential for performing a qualitative check on deformation data. The absence of reliable measurements of SO<sub>2</sub> emission restricts the framework's capacity to interpret deformation data. Nevertheless, continuous observations of changes in gas emissions and deformation offer important insights into understanding magma properties and the plumbing systems, and this study represents a step forward in developing a framework for interpreting these data.

The success of this thesis in using thermodynamic models to model and quantify magma properties is an incremental step towards integrating multi-parameter observations to

reconcile observations of volcanic deformation and degassing. As routinely processed satellite data and upcoming satellite missions continue to evolve, we will increasingly be able to investigate the evolution of magma properties, quantify pre-eruptive magma storage conditions, and gain a better understanding of the magma plumbing system.

# **Appendix A**

## **Supplementary Material for Chapter 2**



## **Introduction**

This appendix includes the databases used in the statistical analysis of satellite-detected deformation and SO<sub>2</sub> emissions during basaltic eruptions in arc and ocean island settings, as presented in Chapter 2.

## A.1 Supplementary Tables

Table A.1: Volcanic eruptions and satellite detection of deformation and SO<sub>2</sub> emissions for 94 basaltic eruptions during the satellite era (2005-2020).

Eruption	Tectonic setting <sup>a</sup>	Degas <sup>b</sup>	Ref.	Deform <sup>b</sup>	Ref.
Alaid, 2012	ARC	No	-	No	-
Alaid, 2015	ARC	No	-	No	-
Alaid, 2018	ARC	No	-	No	-
Ambae, 2005	ARC	Yes	4	No	-
Ambae, 2011	ARC	Yes	<sup>c</sup>	No	-
Ambae, 2017	ARC	Yes	41, 54	No	-
Ambrym, 2018	ARC	Yes	9	Yes	29
Chikurachki, 2005	ARC	Yes	<sup>c</sup>	No	-
Chikurachki, 2007	ARC	Yes	<sup>c</sup>	No	-
Chikurachki, 2007	ARC	Yes	<sup>c</sup>	No	-
Chikurachki, 2008	ARC	Yes	<sup>c</sup>	No	-
Chikurachki, 2015	ARC	Yes	<sup>c</sup>	No	-
Chikurachki, 2016	ARC	Yes	<sup>c</sup>	No	-
Chikurachki, 2016	ARC	Yes	<sup>c</sup>	No	-
Fuego, 2018	ARC	Yes	<sup>c</sup>	No	-
Gorely, 2010	ARC	Yes	<sup>c</sup>	No	-
Hudson, Cerro, 2011	ARC	Yes	<sup>d</sup>	Yes	15
Iliwerung, 2013	ARC	No	-	No	-
Izu-Torishima, 2013	ARC	No	-	No	-
Kambalny, 2017	ARC	Yes	<sup>c</sup>	No	-
Kasatochi, 2008	ARC	Yes	<sup>c</sup>	No	-
Klyuchevskoy, 2005	ARC	No	-	No	-
Klyuchevskoy, 2007	ARC	Yes	23	No	-
Klyuchevskoy, 2008	ARC	No	-	No	-
Klyuchevskoy, 2009	ARC	No	-	No	-
Klyuchevskoy, 2011	ARC	No	-	No	-
Klyuchevskoy, 2011	ARC	Yes	<sup>c</sup>	No	-
Klyuchevskoy, 2012	ARC	No	-	No	-

APPENDIX A. SUPPLEMENTARY MATERIAL FOR CHAPTER 2

---

Klyuchevskoy, 2013	ARC	Yes	23	No	-
Klyuchevskoy, 2015	ARC	No	-	No	-
Klyuchevskoy, 2015	ARC	No	-	No	-
Klyuchevskoy, 2019	ARC	No	-	No	-
Klyuchevskoy, 2019	ARC	No	-	No	-
Llaima, 2007	ARC	No	-	No	-
Llaima, 2008	ARC	Yes	<sup>c</sup>	Yes	14
Manam, 2004	ARC	Yes	<sup>c</sup>	No	-
Manam, 2014	ARC	No	-	No	-
Momotombo, 2015	ARC	Yes	<sup>d</sup>	No	48
Montagu Island, 2001	ARC	No	-	No	-
Okmok, 2008	ARC	Yes	22, 46	Yes	36
Pagan, 2006	ARC	No	-	No	31
Pagan, 2009	ARC	No	-	No	31
Pagan, 2010	ARC	No	-	No	31
Pagan, 2011	ARC	No	-	No	31
Pagan, 2012	ARC	Yes	<sup>c</sup>	No	31
Raikoike, 2019	ARC	Yes	13	No	-
Semisopochnoi, 2018	ARC	No	-	No	-
Semisopochnoi, 2019	ARC	No	-	No	-
Semisopochnoi, 2019	ARC	No	-	No	-
Slamet, 2009	ARC	No	-	Yes	12
Slamet, 2014	ARC	No	-	No	-
Tolbachik, 2012	ARC	No	-	Yes	38
Ulawun, 2019	ARC	Yes	39	No	39
Villarrica, 2004	ARC	No	-	No	21, 24
Villarrica, 2008	ARC	No	-	No	-
Villarrica, 2009	ARC	No	-	No	-
Villarrica, 2009	ARC	No	-	No	-
Villarrica, 2012	ARC	No	-	No	-
Villarrica, 2013	ARC	No	-	No	-
Villarrica, 2014	ARC	No	-	No	14
Zavodovski, 2016	ARC	No	-	No	-
Cerro Azul, 2008	OIB	Yes	<sup>d</sup>	Yes	25
Bardarbunga, 2014	OIB	Yes	27, 56	Yes	18

## A.1. SUPPLEMENTARY TABLES

Eyjafjallajokull, 2010	OIB	Yes	<i>d</i>	Yes	51
Fernandina, 2005	OIB	Yes	<i>c</i>	Yes	10
Fernandina, 2009	OIB	Yes	<i>c</i>	Yes	2
Fernandina, 2017	OIB	Yes	59	No	59
Fernandina, 2018	OIB	Yes	59	No	59
Fernandina, 2020	OIB	Yes	<i>c</i>	Yes	11
Piton de la Fournaise, 2005	OIB	Yes	<i>c</i>	No	-
Piton de la Fournaise, 2005	OIB	Yes	<i>c</i>	No	-
Piton de la Fournaise, 2006	OIB	Yes	17, 57	Yes	16, 17
Piton de la Fournaise, 2008	OIB	Yes	<i>c</i>	No	-
Piton de la Fournaise, 2009	OIB	Yes	<i>c</i>	No	-
Piton de la Fournaise, 2010	OIB	Yes	<i>c</i>	No	-
Piton de la Fournaise, 2014	OIB	Yes	<i>c</i>	Yes	43
Piton de la Fournaise, 2015	OIB	Yes	30	No	-
Piton de la Fournaise, 2016	OIB	Yes	55	No	-
Piton de la Fournaise, 2016	OIB	Yes	<i>c</i>	Yes	52
Piton de la Fournaise, 2017	OIB	Yes	<i>c</i>	No	-
Piton de la Fournaise, 2017	OIB	Yes	<i>c</i>	No	-
Piton de la Fournaise, 2018	OIB	Yes	<i>c</i>	Yes	47
Piton de la Fournaise, 2019	OIB	Yes	<i>c</i>	No	-
Piton de la Fournaise, 2019	OIB	Yes	58	Yes	58
Piton de la Fournaise, 2020	OIB	Yes	<i>c</i>	No	-
Grimsvotn, 2011	OIB	Yes	50	No	32
Karthala, 2005	OIB	Yes	45	No	8
Karthala, 2005	OIB	Yes	<i>c</i>	No	8
Karthala, 2006	OIB	Yes	<i>c</i>	No	8
Karthala, 2007	OIB	Yes	<i>c</i>	Yes	8
Kilauea, 2018	OIB	Yes	33, 34	Yes	37
Sierra Negra, 2005	OIB	Yes	59	Yes	26
Sierra Negra, 2018	OIB	Yes	59	Yes	59
Wolf, 2015	OIB	Yes	<i>c</i>	Yes	53, 61

<sup>a</sup> ARC: arc; OIB: ocean island basalts.

<sup>b</sup> Satellite detection of deformation and SO<sub>2</sub> emission.

<sup>c</sup> SO<sub>2</sub> emissions detected and shown by NASA's Global Sulfur Dioxide Monitoring Home Page (<https://so2.gsfc.nasa.gov/>).

<sup>d</sup> References from Global Volcanism Program, 2013.

Table A.2: Satellite detectability of deformation and SO<sub>2</sub> degassing for 28 volcanic eruptions with erupted volume equal or greater than 10<sup>5</sup> m<sup>3</sup>.

Eruption	Tectonic setting <sup>a</sup>	Erupted volume (m <sup>3</sup> )	Uncertainty (m <sup>3</sup> )	Degas <sup>b</sup>	Deform <sup>b</sup>	Ref.
Fuego, 2018	ARC	4.00×10 <sup>7</sup>	1.00×10 <sup>7</sup>	Yes	No	43
Kasatochi, 2008	ARC	2.15×10 <sup>8</sup>	6.50×10 <sup>7</sup>	Yes	No	60
Llaima, 2008	ARC	1.31×10 <sup>6</sup>	-	Yes	Yes	49
Okmok, 2008	ARC	3.00×10 <sup>8</sup>	-	Yes	Yes	35
Tolbachik, 2012	ARC	5.50×10 <sup>8</sup>	-	No	Yes	5, 19
Manam, 2005	ARC	1.00×10 <sup>5</sup>	-	Yes	No	<sup>c</sup>
Manam, 2014	ARC	1.00×10 <sup>5</sup>	-	No	No	<sup>c</sup>
Villarica, 2014	ARC	4.70×10 <sup>6</sup>	1.00×10 <sup>6</sup>	No	No	7
Ulawun, 2019	ARC	1.00×10 <sup>5</sup>	-	Yes	No	<sup>c</sup>
Bárðarbunga, 2014	OIB	1.36×10 <sup>9</sup>	7.00×10 <sup>7</sup>	Yes	Yes	18
Eyjafjallajökull, 2010	OIB	1.80×10 <sup>8</sup>	5.00×10 <sup>7</sup>	Yes	Yes	28
Fernandina, 2005	OIB	1.40×10 <sup>7</sup>	-	Yes	Yes	10
Fernandina, 2009	OIB	4.27×10 <sup>7</sup>	-	Yes	Yes	59
Fernandina, 2017	OIB	9.70×10 <sup>6</sup>	4.90×10 <sup>6</sup>	Yes	No	59
Fernandina, 2018	OIB	5.90×10 <sup>6</sup>	3.00×10 <sup>6</sup>	Yes	No	59
Pdl. Fournaise, 2006	OIB	1.50×10 <sup>8</sup>	-	Yes	Yes	17
Pdl. Fournaise, 2015	OIB	4.00×10 <sup>7</sup>	-	Yes	No	30
Pdl. Fournaise, Sep 2016	OIB	6.50×10 <sup>6</sup>	-	Yes	No	44, 55
Pdl. Fournaise, May 2016	OIB	5.00×10 <sup>5</sup>	-	Yes	Yes	52
Pdl. Fournaise, 2018	OIB	5.54×10 <sup>6</sup>	1.66×10 <sup>6</sup>	Yes	Yes	58

Pdl. Fournaise, 2019	OIB	$1.40 \times 10^7$	$5.00 \times 10^6$	Yes	Yes	58
Grímsvötn, 2011	OIB	$2.70 \times 10^8$	$7.00 \times 10^7$	Yes	No	32
Karthala, 2006	OIB	$1.80 \times 10^7$	-	Yes	No	1
Karthala, 2007	OIB	$1.00 \times 10^5$	-	Yes	Yes	1
Kīlauea, 2018	OIB	$5.93 \times 10^8$	$1.10 \times 10^7$	Yes	Yes	37
Sierra Negra, 2005	OIB	$1.20 \times 10^8$	$7.00 \times 10^7$	Yes	Yes	59
Sierra Negra, 2018	OIB	$1.41 \times 10^8$	$7.10 \times 10^7$	Yes	Yes	59
Wolf, 2015	OIB	$8.70 \times 10^7$	$3.38 \times 10^7$	Yes	Yes	6

<sup>a</sup> ARC: arc basalts; OIB: ocean island basalts.

<sup>b</sup> Satellite detection of deformation and SO<sub>2</sub> emission.

<sup>c</sup> VEI 4+ eruptions are assumed to produce  $\geq 10^5$  m<sup>3</sup> DRE.

## A.2 Supplementary References

1. Bachèlery, P., Morin, J., Villeneuve, N., Soulé, H., Nassor, H., & Ali, A. R. (2016). Structure and eruptive history of Karthala volcano. In *Active Volcanoes of the Southwest Indian Ocean* (pp. 345-366). Springer, Berlin, Heidelberg.
2. Bagnardi, M., Amelung, F., & Poland, M. P. (2013). A new model for the growth of basaltic shields based on deformation of Fernandina volcano, Galápagos Islands. *Earth and Planetary Science Letters*, 377, 358-366.
3. Bani, P., Oppenheimer, C., Allard, P., Shinohara, H., Tsanev, V., Carn, S., ... & Garaebiti, E. (2012). First estimate of volcanic SO<sub>2</sub> budget for Vanuatu island arc. *Journal of Volcanology and Geothermal Research*, 211, 36-46.
4. Bani, P., Oppenheimer, C., Varekamp, J. C., Quinou, T., Lardy, M., & Carn, S. (2009). Remarkable geochemical changes and degassing at Vouï crater lake, Ambae volcano, Vanuatu. *Journal of Volcanology and Geothermal Research*, 188(4), 347-357.
5. Belousov, A., Belousova, M., Edwards, B., Volynets, A., & Melnikov, D. (2015). Overview of the precursors and dynamics of the 2012–13 basaltic fissure eruption of Tolbachik Volcano, Kamchatka, Russia. *Journal of Volcanology and Geothermal Research*, 307, 22-37.
6. Bernard, B., Stock, M. J., Coppola, D., Hidalgo, S., Bagnardi, M., Gibson, S., ... & Gleeson, M. (2019). Chronology and phenomenology of the 1982 and 2015 Wolf volcano eruptions, Galápagos Archipelago. *Journal of Volcanology and Geothermal Research*, 374, 26-38.
7. Bertin, D., Amigo, A., & Bertin, L. (2015). Erupción del volcán Villarrica 2015: Productos emitidos y volumen involucrado. In *Proceedings of the XIV Congreso Geológico Chileno*, La Serena, Chile (pp. 4-8).
8. Biggs, J., Rust, A., & Owens, C. (2014, December). Deformation at Lava Lake Volcanoes: Lessons from Karthala. In *AGU Fall Meeting Abstracts* (Vol. 2014, pp. V41B-4807).
9. Carn, S. A., Clarisse, L., & Prata, A. J. (2016). Multi-decadal satellite measurements of global volcanic degassing. *Journal of Volcanology and Geothermal Research*, 311, 99-134.



10. Chadwick, W.W., Jónsson, S., Geist, D.J. et al. The May 2005 eruption of Fernandina volcano, Galápagos: The first circumferential dike intrusion observed by GPS and InSAR. *Bull Volcanol* 73, 679–697 (2011). <https://doi.org/10.1007/s00445-010-0433-0>
11. Chandni, C. K., & Kumar, S. (2020, December). DInSAR based Analysis of January 2020 Eruption of Fernandina Volcano, Galapagos. In *2020 IEEE India Geoscience and Remote Sensing Symposium (InGARSS)* (pp. 250-253). IEEE.
12. Chaussard, E., Amelung, F., & Aoki, Y. (2013). Characterization of open and closed volcanic systems in Indonesia and Mexico using InSAR time series. *Journal of Geophysical Research: Solid Earth*, 118(8), 3957-3969.
13. De Leeuw, J., Schmidt, A., Witham, C. S., Theys, N., Taylor, I. A., Grainger, R. G., ... & Kristiansen, N. I. (2021). The 2019 Raikoke volcanic eruption–Part 1: Dispersion model simulations and satellite retrievals of volcanic sulfur dioxide. *Atmospheric Chemistry and Physics*, 21(14), 10851-10879.
14. Delgado, F., Pritchard, M. E., Ebmeier, S., González, P., & Lara, L. (2017). Recent unrest (2002–2015) imaged by space geodesy at the highest risk Chilean volcanoes: Villarrica, Llaima, and Calbuco (Southern Andes). *Journal of Volcanology and Geothermal Research*, 344, 270-288.
15. Delgado, F., Pritchard, M., Lohman, R. et al. The 2011 Hudson volcano eruption (Southern Andes, Chile): Pre-eruptive inflation and hotspots observed with InSAR and thermal imagery. *Bull Volcanol* 76, 815 (2014). <https://doi.org/10.1007/s00445-014-0815-9>
16. Derrien, A., Peltier, A., Villeneuve, N., & Staudacher, T. (2020). The 2007 caldera collapse at Piton de la Fournaise: new insights from multi-temporal structure-from-motion. *Volcanica*, 3(1), 55-65.
17. Di Muro, A., Métrich, N., Vergani, D., Rosi, M., Armienti, P., Fougereux, T., ... & Civetta, L. (2014). The shallow plumbing system of Piton de la Fournaise Volcano (La Reunion Island, Indian Ocean) revealed by the major 2007 caldera-forming eruption. *Journal of Petrology*, 55(7), 1287-1315.
18. Dirscherl, M., & Rossi, C. (2018). Geomorphometric analysis of the 2014–2015 Bárðarbunga volcanic eruption, Iceland. *Remote Sensing of Environment*, 204, 244-259.

19. Dvigalo, V. N., Svirid, I. Y., & Shevchenko, A. V. (2013). The first quantitative estimates of parameters for the Tolbachik Fissure Eruption of 2012–2013 from aerophotogrammetric observations. *Journal of Volcanology and Seismology*, 8(5), 261-268.
20. Dzurisin, D., Lu, Z., Poland, M. P., & Wicks Jr, C. W. (2019). Space-based imaging radar studies of US volcanoes. *Frontiers in Earth Science*, 6, 249.
21. Ebmeier, S. K., Biggs, J., Mather, T. A., & Amelung, F. (2013). On the lack of InSAR observations of magmatic deformation at Central American volcanoes. *Journal of Geophysical Research: Solid Earth*, 118(5), 2571-2585.
22. Fee, D., Steffke, A., & Garces, M. (2010). Characterization of the 2008 Kasatochi and Okmok eruptions using remote infrasound arrays. *Journal of Geophysical Research: Atmospheres*, 115(D2).
23. Flower, V. J., & Kahn, R. A. (2020). Interpreting the volcanological processes of Kamchatka, based on multi-sensor satellite observations. *Remote Sensing of Environment*, 237, 111585.
24. Fournier, T. J., Pritchard, M. E., & Riddick, S. N. (2010). Duration, magnitude, and frequency of subaerial volcano deformation events: New results from Latin America using InSAR and a global synthesis. *Geochemistry, Geophysics, Geosystems*, 11(1).
25. Galetto, F., Hooper, A., Bagnardi, M., & Acocella, V. (2020). The 2008 eruptive unrest at Cerro Azul volcano (Galápagos) revealed by InSAR data and a novel method for geodetic modelling. *Journal of Geophysical Research: Solid Earth*, 125(2), e2019JB018521.
26. Geist, D. J., Harpp, K. S., Naumann, T. R., Poland, M., Chadwick, W. W., Hall, M., & Rader, E. (2008). The 2005 eruption of Sierra Negra volcano, Galápagos, Ecuador. *Bulletin of Volcanology*, 70(6), 655-673.
27. Gíslason, S. R., Stefánsdóttir, G., Pfeffer, M. A., Barsotti, S., Jóhannsson Th, G. I., Bali, E., ... & Thordarson Th, R. M. Högnadóttir Th, Dürig T, Pedersen GBM, Höskuldsson Ám Gudmundsson MT (2015) Environmental pressure from the 2014–14 eruption of Bárðarbunga volcano, Iceland. *Geochem Persp Lett*, 1, 84-93.
28. Gurioli, L., Di Muro, A., Vlastélic, I., Moune, S., Thivet, S., Valer, M., ... & Hénot, J. M. (2018). Integrating field, textural, and geochemical monitoring to track eruption

- triggers and dynamics: a case study from Piton de la Fournaise. *Solid Earth*, 9(2), 431-455.
29. Hamling, I. J., Cevuard, S., & Garaebiti, E. (2019). Large-Scale Drainage of a Complex Magmatic System: Observations From the 2018 Eruption of Ambrym Volcano, Vanuatu. *Geophysical Research Letters*, 46(9), 4609-4617.
  30. Harris, A.J.L., Villeneuve, N., Di Muro, A. et al. Effusive crises at Piton de la Fournaise 2014–2015: a review of a multi-national response model. *J Appl. Volcanol.* 6, 11 (2017). <https://doi.org/10.1186/s13617-017-0062-9>
  31. Henderson, S. T., Pritchard, M. E., Cooper, J. R., & Aoki, Y. (2019). Remotely sensed deformation and thermal anomalies at Mount Pagan, Mariana Islands. *Frontiers in Earth Science*, 7, 238.
  32. Hreinsdóttir, S., Sigmundsson, F., Roberts, M. J., Björnsson, H., Grapenthin, R., Arason, P., ... & Óladóttir, B. A. (2014). Volcanic plume height correlated with magma-pressure change at Grímsvötn Volcano, Iceland. *Nature geoscience*, 7(3), 214-218.
  33. Johnson, M. S., Schwandner, F. M., Potter, C. S., Nguyen, H. M., Bell, E., Nelson, R. R., ... & O'Dell, C. W. (2020). Carbon dioxide emissions during the 2018 Kilauea volcano eruption estimated using OCO-2 satellite retrievals. *Geophysical Research Letters*, 47(24), e2020GL090507.
  34. Kern, C., Lerner, A.H., Elias, T. et al. Quantifying gas emissions associated with the 2018 rift eruption of Kilauea Volcano using ground-based DOAS measurements. *Bull Volcanol* 82, 55 (2020). <https://doi.org/10.1007/s00445-020-01390-8>
  35. Larsen, J., Neal, C., Webley, P., Freymueller, J., Haney, M., McNutt, S., ... & Wessels, R. (2009). Eruption of Alaska volcano breaks historic pattern. *Eos, Transactions American Geophysical Union*, 90(20), 173-174.
  36. Lu, Z., & Dzurisin, D. (2010). Ground surface deformation patterns, magma supply, and magma storage at Okmok volcano, Alaska, from InSAR analysis: 2. Coeruptive deflation, July–August 2008. *Journal of Geophysical Research: Solid Earth*, 115(B5).

37. Lundgren, P. R., Bagnardi, M., & Dietterich, H. (2019). Topographic changes during the 2018 Kīlauea eruption from single-pass airborne InSAR. *Geophysical Research Letters*, 46(16), 9554-9562.
38. Lundgren, P., Kiryukhin, A., Milillo, P., & Samsonov, S. (2015). Dike model for the 2012–2013 Tolbachik eruption constrained by satellite radar interferometry observations. *Journal of Volcanology and Geothermal Research*, 307, 79-88.
39. McKee, K., Smith, C. M., Reath, K., Snee, E., Maher, S., Matoza, R. S., ... & Perttu, A. (2021). Evaluating the state-of-the-art in remote volcanic eruption characterization Part II: Ulawun volcano, Papua New Guinea. *Journal of Volcanology and Geothermal Research*, 420, 107381.
40. Morgan, H. A., Harris, A. J., & Gurioli, L. (2013). Lava discharge rate estimates from thermal infrared satellite data for Pacaya Volcano during 2004–2010. *Journal of volcanology and geothermal research*, 264, 1-11.
41. Morin, J., Lavigne, F., Bachèlery, P., Finizola, A., & Villeneuve, N. (2009). Institutional and social responses to hazards related to Karthala volcano, Comoros: Part I: Analysis of the May 2006 eruptive crisis. *Shima: The International Journal of Research into Island Cultures.*, 3(1), 33-53.
42. Moussallam, Y., Rose-Koga, E.F., Koga, K.T. et al. Fast ascent rate during the 2017–2018 Plinian eruption of Ambae (Aoba) volcano: a petrological investigation. *Contrib Mineral Petrol* 174, 90 (2019). <https://doi.org/10.1007/s00410-019-1625-z>
43. Pardini, F., Queiße, M., Naismith, A., Watson, I. M., Clarisse, L., & Burton, M. R. (2019). Initial constraints on triggering mechanisms of the eruption of Fuego volcano (Guatemala) from 3 June 2018 using IASI satellite data. *Journal of Volcanology and Geothermal Research*, 376, 54-61.
44. Peltier, A., Beauducel, F., Villeneuve, N., Ferrazzini, V., Di Muro, A., Aiuppa, A., ... & Taisne, B. (2016). Deep fluid transfer evidenced by surface deformation during the 2014–2015 unrest at Piton de la Fournaise volcano. *Journal of Volcanology and Geothermal Research*, 321, 140-148.
45. Peltier, A., Villeneuve, N., Ferrazzini, V., Testud, S., Hassen Ali, T., Boissier, P., & Catherine, P. (2018). Changes in the long-term geophysical eruptive precursors at Piton de la Fournaise: implications for the response management. *Frontiers in Earth Science*, 104.

46. Prata, A. J., & Kerkmann, J. (2007). Simultaneous retrieval of volcanic ash and SO<sub>2</sub> using MSG-SEVIRI measurements. *Geophysical Research Letters*, 34(5).
47. Prata, A. J., Gangale, G., Clarisse, L., & Karagulian, F. (2010). Ash and sulfur dioxide in the 2008 eruptions of Okmok and Kasatochi: Insights from high spectral resolution satellite measurements. *Journal of Geophysical Research: Atmospheres*, 115(D2).
48. Richter, N., & Froger, J. L. (2020). The role of Interferometric Synthetic Aperture Radar in detecting, mapping, monitoring, and modelling the volcanic activity of Piton de la Fournaise, La Réunion: A review. *Remote Sensing*, 12(6), 1019.
49. Roman, D. C., La Femina, P. C., Connor, C., Connor, L., Dixon, T. H., Feineman, M. D., ... & Wnuk, K. (2016, December). Multidisciplinary Studies of the 2015-2016 Eruption of Momotombo Volcano, Nicaragua. In *AGU Fall Meeting Abstracts* (Vol. 2016, pp. V43A-3131).
50. Ruth, D. C., & Calder, E. S. (2014). Plate tephra: Preserved bubble walls from large slug bursts during violent Strombolian eruptions. *Geology*, 42(1), 11-14.
51. Sigmarsson, O., Haddadi, B., Carn, S., Moune, S., Gudnason, J., Yang, K., & Clarisse, L. (2013). The sulfur budget of the 2011 Grímsvötn eruption, Iceland. *Geophysical Research Letters*, 40(23), 6095-6100.
52. Sigmundsson, F., Hreinsdóttir, S., Hooper, A., Arnadóttir, T., Pedersen, R., Roberts, M. J., ... & Feigl, K. L. (2010). Intrusion triggering of the 2010 Eyjafjallajökull explosive eruption. *Nature*, 468(7322), 426-430.
53. Smittarello, D., Cayol, V., Pinel, V., Peltier, A., Froger, J. L., & Ferrazzini, V. (2019). Magma propagation at Piton de la Fournaise from joint inversion of InSAR and GNSS. *Journal of Geophysical Research: Solid Earth*, 124(2), 1361-1387.
54. Stock, M. J., Bagnardi, M., Neave, D. A., MacLennan, J., Bernard, B., Buisman, I., ... & Geist, D. (2018). Integrated petrological and geophysical constraints on magma system architecture in the western Galápagos Archipelago: insights from Wolf volcano. *Geochemistry, Geophysics, Geosystems*, 19(12), 4722-4743.
55. Theys, N., Hedelt, P., De Smedt, I. et al. Global monitoring of volcanic SO<sub>2</sub> degassing with unprecedented resolution from TROPOMI onboard Sentinel-5 Precursor. *Sci Rep* 9, 2643 (2019). <https://doi.org/10.1038/s41598-019-39279-y>

56. Thivet, S., Gurioli, L., Di Muro, A., Derrien, A., Ferrazzini, V., Gouhier, M., ... & Arelano, S. (2020). Evidences of plug pressurization enhancing magma fragmentation during the September 2016 basaltic eruption at Piton de la Fournaise (La Réunion Island, France). *Geochemistry, Geophysics, Geosystems*, 21(2), e2019GC008611.
57. Thordarson, T., & Hartley, M. (2015). Atmospheric sulfur loading by the ongoing Nornahraun eruption, North Iceland. *Geophys. Res.*
58. Tulet, P. and Villeneuve, N.: Large scale modeling of the transport, chemical transformation and mass budget of the sulfur emitted during the April 2007 eruption of Piton de la Fournaise, *Atmos. Chem. Phys.*, 11, 4533–4546, <https://doi.org/10.5194/acp-11-4533-2011>, 2011.
59. Valade, S., Ley, A., Massimetti, F., D'Hondt, O., Laiolo, M., Coppola, D., ... & Walter, T. R. (2019). Towards global volcano monitoring using multisensor sentinel missions and artificial intelligence: The MOUNTS monitoring system. *Remote Sensing*, 11(13), 1528.
60. Vasconez, F. J., Ramón, P., Hernandez, S., Hidalgo, S., Bernard, B., Ruiz, M., Alvarado, A., La Femina, P. and Ruiz, G. (2018) “The different characteristics of the recent eruptions of Fernandina and Sierra Negra volcanoes (Galápagos, Ecuador)”, *Volcanica*, 1(2), pp. 127–133. doi: 10.30909/vol.01.02.127133.
61. Waythomas, C. F., Scott, W. E., Prejean, S. G., Schneider, D. J., Izbekov, P., & Nye, C. J. (2010). The 7–8 August 2008 eruption of Kasatochi Volcano, central Aleutian Islands, Alaska. *Journal of Geophysical Research: Solid Earth*, 115(B12).
62. Xu, W., Jónsson, S., Ruch, J., & Aoki, Y. (2016). The 2015 Wolf volcano (Galápagos) eruption studied using Sentinel-1 and ALOS-2 data. *Geophysical Research Letters*, 43(18), 9573-9580. & Day, S. (2002). InSAR observations of the 1995 Fogo, Cape Verde, eruption: Implications for the effects of collapse events upon island volcanoes. *Geophysical research letters*, 29(12), 47-1.



## **Appendix B**

### **Supplementary Material for Chapter 3**



## Introduction

This appendix contains additional information about the calculation of volatile content in evolved magmas using fractional crystallisation. It also provides a detailed methodology for determining magma density associated to gas segregation. Additionally, the appendix presents a comprehensive database including volume changes, SO<sub>2</sub> emissions, erupted volume and reservoir depth, which is required for calculating normalised volume change and normalised SO<sub>2</sub> for volcanic eruptions.

### B.1 Fractional Crystallisation

Evolved magmas (i.e., andesite, dacite and rhyolite) are likely to be more volatile-rich than less-evolved mafic magmas (i.e., basalt) due to fractional crystallisation from primitive basaltic magmas (Marty and Zimmermann, 1999; Wallace, 2005). This is because volatile enrichment occurs during fractional crystallisation, in which magma differentiates and the crystals formed during cooling are removed from the gradually solidifying melt (Rogers, 2015).

The equation for crystallisation is given as:

$$C_L/C_0 = F^{D-1} \quad (\text{B.1})$$

Here,  $C_0$  is the original concentration of an element or species in the melt (e.g., water concentration in basaltic melt as a mass fraction), and  $C_L$  represents the final concentration after crystallisation (e.g., water concentration in the rhyolite melt).  $D$  denotes the partition coefficient of water, which is the ratio between the concentration in crystals and the melt.  $F$  represents the ‘melt fraction remaining’.

For simplicity, we assume that water is completely ‘incompatible’ by setting  $D$  to zero:

$$C_L = C_0/F \quad (\text{B.2})$$

Assuming 90% crystallisation of rhyolite,  $F$  is equal to 0.1. For example, if the basalt has 1 wt% H<sub>2</sub>O, then after 90% crystallisation the rhyolite melt will have  $C_L = \frac{0.01}{0.1} = 0.1$ , meaning the rhyolite will have a water content of 10 wt%.

These calculations form the basis for determining the bulk water content of rhyolitic

melt. However, it is important to note that during prolonged crystallisation in a magma storage region, some exsolved fluids may be lost, which means that this method provides an upper bound estimation. For basalts with 3 wt% water, rhyolites would result with over 30 wt% water. Similarly, for basalts with 1 wt% carbon dioxide and 1500 ppm sulfur, the rhyolite would have 10 wt% carbon dioxide and 15000 ppm sulfur, respectively. Such high magmatic volatile content is unlikely to be retained by the magma, as at these weight fractions, the magmatic volatiles are more likely to escape, particularly carbon dioxide that has less solubility. Therefore, for our modelling, a reasonable range of values for rhyolite would be 5-15 wt% water, 1-3 wt% carbon dioxide and 1800-4200 ppm sulfur.

## B.2 Magma Density

Magma density is the weighted sum of melt density and gas density:

$$\rho_m = \rho_M V_m + \rho_g V_g \quad (\text{B.3})$$

The melt volume fraction  $V_M$  and gas volume fraction  $V_g$  is the volume of the melt  $v_M$  and the volume of the gas  $v_g$  per unit volume of magma that consists of melt and gas respectively:

$$\rho_m = \rho_M \frac{v_M}{v_M + v_g} + \rho_g \frac{v_g}{v_M + v_g} \quad (\text{B.4})$$

Here we introduce gas segregation  $v_e$  into Equation B.4:

$$\rho'_m = \rho_M \frac{v_M}{v_M + v_g + v_e} + \rho_g \frac{v_g + v_e}{v_M + v_g + v_e} \quad (\text{B.5})$$

$$\rho'_m = \frac{\rho_M v_M + \rho_g (v_g + v_e)}{v_M + v_g + v_e} \quad (\text{B.6})$$

where  $\rho'_m$  represents magma density with additional or reduced gas content due to gas segregation. By letting  $v_e = k v_g$ ,

$$\rho'_m = \frac{\rho_M v_M + \rho_g (v_g + k v_g)}{v_M + v_g + k v_g} \quad (\text{B.7})$$

$$\rho'_m = \frac{\rho_M v_M + \rho_g v_g (1 + k)}{v_M + v_g (1 + k)} \quad (\text{B.8})$$

where  $k > 0$  represents pre-eruptive gas accumulation and  $-1 < k < 0$ , represents pre-eruptive degassing. We divide  $v_M + v_g$  at both sides of the fraction:

$$\rho'_m = \frac{\rho_M v_M + \rho_g v_g (1 + k)}{v_M + v_g (1 + k)} \div \frac{v_M + v_g}{v_M + v_g} \quad (\text{B.9})$$

Since  $V_M = \frac{v_M}{v_M + v_g}$  and  $V_g = \frac{v_g}{v_M + v_g}$ ,

$$\rho'_m = \frac{\rho_M V_M + \rho_g V_g (1 + k)}{1 + k V_g} \quad (\text{B.10})$$

The volume fraction of melt can also be written as  $V_M = 1 - V_g$  and thus:

$$\rho'_m = \frac{\rho_M (1 - V_g) + \rho_g V_g (1 + k)}{1 + k V_g} \quad (\text{B.11})$$

which is simplified as:

$$\rho'_m = \frac{\rho_M + V_g [\rho_g (1 + k) - \rho_M]}{1 + k V_g}. \quad (\text{B.12})$$

## B.3 Supplementary Tables

Table B.1: Initial volatile contents used in EVo models based on melt inclusion data (Wallace, 2005; Ruscitto et al., 2012) and our calculations of fractional crystallisation (Supplementary Material B.1). Rhyolite and basalt have  $\text{SiO}_2$  composition of 76% and 48%, and were initialised at a starting temperature of 850°C and 1200°C. For the sensitivity analysis, a chosen parameter is varied, while the rest of the parameters are held constant. Oxygen fugacity,  $f_{\text{O}_2}$ , is defined relative to the nickel-nickel oxide oxygen buffer, NNO. The abbreviations for FC and MI are fractional crystallisation and melt inclusions.

Parameters	Weight fraction of $\text{H}_2\text{O}$ , $w^{\text{H}_2\text{O}}$ (wt%)	Weight fraction of $\text{CO}_2$ , $w^{\text{CO}_2}$ (wt%)	Oxygen fugacity, $f_{\text{O}_2}$	Weight fraction of S, $w^{\text{S}}$ (ppm)	Source
Rhyolite sensitivity test	10.0±5.0	2.0±1.0	NNO±1	3000±1200	FC
Water-poor rhyolite	5.0	2.0	NNO	3000	FC
Water-rich rhyolite	15.0	2.0	NNO	3000	FC
Rhyolite	3.3	0.0015	NNO	75	MI
Ocean island basalt	1.0	1.0	NNO	1600	MI
Arc basalt	3.3	1.0	NNO	1600	MI

Table B.2: Supplementary table summarising the maximum percentage change of rhyolitic magma for each observation over the depth range when varying the values of each parameter (shown in brackets; e.g., increasing  $w^{\text{H}_2\text{O}}$  from 5.0 wt% to 15.0 wt%) while other parameters are held constant. For details regarding the sensitivity analyses for basaltic magma, the reader is referred to Yip et al. (2022).

Parameters	% Change in normalised $\text{SO}_2$ , $\bar{S}$	Depth (km)	% Change in normalised volume change, $\bar{V}$	Depth (km)
Magmatic $\text{H}_2\text{O}$ , $w^{\text{H}_2\text{O}}$ (5.0-15.0 wt%)	+260%	25 km	−54%	15 km
Magmatic $\text{CO}_2$ , $w^{\text{CO}_2}$ (1.0-3.0 wt%)	+49%	25 km	−8.5%	10 km
Magmatic S, $w^{\text{S}}$ (1800-4200 ppm)	+83%	surface	< −1.0%	10 km
Oxygen fugacity, $f_{\text{O}_2}$ (NNO−1-NNO+1)	+79%	2.9 km	+ < 1.0%	9.4 km
Pre-eruptive gas accumulation (0-+1)	+100%	surface	−27%	20 km
Pre-eruptive degassing (0-−0.5)	−50%	surface	+30%	16 km

Table B.3: General characteristics of eruptions and volcanoes, and satellite detection of deformation and SO<sub>2</sub> degassing during corresponding eruption.

Volcano name	Start date (dd/mm/yy)	End date (dd/mm/yy)	Eruption duration (days)	Dominant magma Composition <sup>a</sup>	Tectonic setting <sup>b</sup>	Deformation <sup>c</sup>	SO <sub>2</sub> emission <sup>c</sup>	Footnote	References
Augustine	13/1/06	28/1/06	16	A	ARC	no	yes	1	11, 41
Bezymianny	15/10/07	16/10/07	2	A	ARC	no	yes	2	34
Calbuco	22/4/15	23/4/15	2	A	ARC	yes	yes	3	45, 49
Chaiten	1/5/08	6/5/08	6	R	ARC	yes	yes	4	8, 72
Eyjafjalla- jökull	14/4/10	22/5/10	39	B	OIB	yes	yes	5	6, 55, 63
Fernandina	13/5/05	29/5/05	18	B	OIB	yes	yes	6	12, 19
Fogo	23/11/14	8/2/15	78	B	OIB	no	yes	7	23, 24
Piton de la Fournaise	30/3/07	29/4/07	30	B	OIB	yes	yes	8	17, 67
Grimsvötn	21/5/11	23/5/11	3	B	OIB	no	yes	9	28, 62
Kelut	13/2/14	13/2/14	1	A	ARC	yes	yes	10	9, 79

Merapi	1/11/10	4/11/10	4	A	ARC	yes	yes	11	47, 58, 65
Okmok	12/7/08	19/08/08	39	A	ARC	yes	yes	12	35, 36
Puyehue-Cordon Caulle	4/6/11	7/6/11	4	R	ARC	yes	yes	13	3, 29
Raikoke	21/6/19	21/6/19	1	B	ARC	no	Yes	14	42
Redoubt	23/3/09	4/4/09	13	A	ARC	yes	yes	15	4
Sarychev Peak	11/6/09	19/6/09	9	A	ARC	no	yes	16	7
Sierra Negra	22/10/05	30/10/05	9	B	OIB	yes	yes	17	21
Sinabung	18/12/13	13/4/14	117	A	ARC	no	yes	18	27
St. Helens	23/9/04	11/1/08	1206	D	ARC	yes	no	19	16, 22, 32, 52
Jebel at Tair	30/9/07	16/6/08	261	T	RIFT	no	yes	20	13, 76

<sup>a</sup> B: Basalt / Picro-Basalt; T: Trachybasalt / Tephrite Basanite; A: Andesite / Basaltic Andesite;

D: Dacite; R: Rhyolite.

<sup>b</sup> ARC: arc; OIB: ocean island basalts; RIFT: rift.

<sup>c</sup> Satellite detection of deformation and SO<sub>2</sub> emission.

### Footnotes

1. Augustine, 2006: Volume change during explosive phase suppressed by gas-rich magma; Large amount of SO<sub>2</sub> released during precursory phase.
2. Bezymianny, 2007: No information on deformation; Persistently degassing volcano.

3. Calbuco, 2015: Deformation detected by InSAR; SO<sub>2</sub> measured using GOME-2 satellite is underestimated.
4. Chaiten, 2008: SO<sub>2</sub> measurements from OMI; Deformation measured using InSAR.
5. Eyjafjallajökull, 2010: SO<sub>2</sub> gas detected by various space-borne spectrometers; SO<sub>2</sub> gas peaks after two weeks of eruption; Deformation detected by GPS and InSAR.
6. Fernandina, 2005: SO<sub>2</sub> gas detected using OMI; Deformation detected by both GPS and InSAR.
7. Fogo, 2014: Effusive eruption; SO<sub>2</sub> gas detected by OMI; Co-eruptive deformation measured using InSAR is associated to the dyke intrusion; No significant deformation from shallow reservoirs.
8. Piton de la Fournaise, 2007: SO<sub>2</sub> gas detected by OMI; Topographic changes of the caldera collapse recorded by InSAR.
9. Grimsvötn, 2011: SO<sub>2</sub> gas measured using OMI; Deformation recorded using GPS.
10. Kelut, 2014: SO<sub>2</sub> detected by OMI; Pre-eruptive deformation not detected by InSAR; Co-eruptive deformation measured using InSAR.
11. Merapi, 2010: Deformation detected using InSAR; SO<sub>2</sub> detected throughout eruption (initial phase, magmatic phase, waning phase).
12. Okmok, 2008: Deformation detected using InSAR; Modelled source depth increases through the 2008 eruption.
13. Puyehue-Cordon Caulle, 2011: SO<sub>2</sub> gas retrievals using MODIS; Deformation measurements using InSAR reveals two deflating sources during co-eruptive phase.
14. Raikoke, 2019: SO<sub>2</sub> gas detected by TROPOMI soon after the eruption, but the peak SO<sub>2</sub> emission is only detected after 3 days of the eruption; Deformation not detected due to the short duration of the eruption.
15. Redoubt, 2009: Destruction of early domes during explosive phase.

16. Sarychev Peak, 2009: SO<sub>2</sub> measured using IASI only for a day.
17. Sierra Negra, 2005: SO<sub>2</sub> measured using OMI; Deformation of caldera collapse detected by InSAR.
18. Sinabung, 2013: Deformation measured using GPS; SO<sub>2</sub> detected using OMI.
19. St. Helens, 2004: Deformation measured using GPS and InSAR; SO<sub>2</sub> gas emissions measured by direct sampling and spectrometers on helicopter and fixed-wing aircraft.
20. Jebel at Tair, 2007: SO<sub>2</sub> gas measured using OMI; Only co-eruptive deformation caused by the dike intrusion has been detected by InSAR, i.e., no co-eruptive deflation detected.



Table B.4: Co-eruptive volume change of eruptions.

Volcano name	Start date (dd/mm/yy)	End date (dd/mm/yy)	Eruption duration (days)	Deformation source <sup>a</sup>	Volume change (km <sup>-3</sup> )	Min. volume change (km <sup>-3</sup> )	Max. volume change (km <sup>-3</sup> )	Footnote	References
Augustine	13/1/06	28/1/06	16	-	-	-	-	1	11
Bezymianny	15/10/07	16/10/07	2	-	-	-	-	-	-
Calbuco	22/4/15	23/4/15	2	PS	0.099	0.050 <sup>b</sup>	0.149 <sup>b</sup>	2	45
Chaiten	1/5/08	6/5/08	6	com.	0.200	0.150	0.250	3	72
Eyjafjallajok- ull	14/4/10	22/5/10	39	Sill	0.014	0.013	0.015	4	63
Fernandina	13/5/05	29/5/05	18	Mogi	0.012	0.010 <sup>c</sup>	0.014 <sup>c</sup>	5	12
Fogo	23/11/14	8/2/15	78	-	-	-	-	-	-
Piton de la Fournaise	30/3/07	29/4/07	30	com.	0.002	0.001	0.003	6	50
Grimsvötn	21/5/11	23/5/11	3	Mogi	0.027	0.024	0.030	7	28
Kelut	13/2/14	13/2/14	1	Mogi	0.007	0.006 <sup>c</sup>	0.008 <sup>c</sup>	8	9
Merapi	1/11/10	4/11/10	4	-	-	-	-	9	-
Okmok	12/7/08	19/08/08	39	Mogi	0.140	0.130	0.150	10	35, 36

Puyehue-Cordon Caulle	4/6/11	7/6/11	4	Mogi	0.110	0.088 <sup>c</sup>	0.132 <sup>c</sup>	11	29
Raikoke	21/6/19	21/6/19	1	-	-	-	-	-	-
Redoubt	23/3/09	4/4/09	13	PS	0.050	0.028	0.100	12	25
Sarychev Peak	11/6/09	19/6/09	9	-	-	-	-	-	-
Sierra Negra	22/10/05	30/10/05	9	com.	0.080	0.064 <sup>c</sup>	0.096 <sup>c</sup>	13	21
Sinabung	22/12/13	20/4/14	120	Mogi	0.021	0.014	0.027	14	27
St. Helens	23/9/04	11/1/08	1206	PS	0.026	0.019	0.032	15	32, 38
Jebel at Tair	30/9/07	16/6/08	261	-	-	-	-	16	76

<sup>a</sup> PS: Prolate spheroid; com.: Complex deformation sources.

<sup>b</sup> Volume change is estimated from the potency calculated using the compound dislocation model.

To account for uncertainties and inaccuracies, an error margin of 50% is applied here.

<sup>c</sup> For error not reported in literature, we attributed an automatic error of 20%.

### Footnotes

1. Augustine, 2006: No deformation is evident prior to explosive eruption – below noise level; Slow extension throughout explosive eruption; Volume change during explosive phase suppressed by gas-rich magma.
2. Calbuco, 2015: Deformation measured using InSAR; Volume change is estimated using the compound dislocation model; An error margin of 50% is applied here.
3. Chaiten, 2008: Volume change represented by the three separate deforming bodies: a deep dipping reservoir, a dyke and a narrow lath-like conduit; Modelled using InSAR images between 13 Feb 2008 and 21 May 2010, and 1 Dec 2007 and 8 Mar 2008.

4. Eyjafjallajökull, 2010: Combined InSAR and GPS data shows a deflating horizontal sill; Volume change may be underestimated as the erupted magma is sourced from a deeper reservoir.
5. Fernandina, 2005: Co-eruption deformation measured using GPS and InSAR data; Volume change from deep deflating point source ( $0.006 \text{ km}^3$ ) is smaller than the combined volume of dyke intrusions and sill expansion ( $0.012 \text{ km}^3$ ); Interferograms used in the modelling are 2-4 months after the eruption, which may have included post-eruptive reinflation.
6. Piton de la Fournaise, 2007: Two stages of summit deflation measured using GPS:  $0.001 \pm 0.0001 \text{ km}^3$  deflation of a prolate spheroid between 2-5 Apr and  $0.001 \pm 0.0005 \text{ km}^3$  deflation of an oblate spheroid between 5-6 Apr.
7. Grimsvötn, 2011: Deformation measurements from GPS with an offset of  $\sim 6 \text{ km}$ .
8. Kelut, 2014: Volume change inverted from InSAR measurement.
9. Merapi, 2010: Deformation has been detected using InSAR, but no modelling of volume change has been done.
10. Okmok, 2008: Volume change of magma reservoir as a function of time is derived from the co-eruptive interferograms; Deflation rate of reservoir decreases exponentially with time.
11. Puyehue-Cordon Caulle, 2011: Volume change modelled using InSAR images between 8 May and 7 Jun, and 8 May and 7 July); Two deflating point sources: one beneath Cordillera Nevada at  $3.8 \text{ km}$  depth and one beneath Puyehue at  $6.1 \text{ km}$  depth.
12. Redoubt, 2009: Deformation source during explosive phase is offset by  $0.5 \text{ km}$  east of dome.
13. Sierra Negra, 2005: Cumulative volume loss of a sill and a point source measured using GPS and InSAR.
14. Sinabung, 2013: Deformation source is  $\sim 7 \text{ km}$  offset from vent; Note that the dates for volume changes from GPS station are different to the dates of volume erupted.

15. St. Helens, 2004: Volume change estimated from GPS data for the entire eruption.
16. Jebel at Tair, 2007: No co-eruptive deflation detected using InSAR

Table B.5: SO<sub>2</sub> emissions of eruptions.

Volcano name	Start date (dd/mm/yy)	End date (dd/mm/yy)	Eruption duration (days)	Co-eruptive degassing?	SO <sub>2</sub> emission (Tg)	Min. SO <sub>2</sub> emission (Tg)	Max. SO <sub>2</sub> emission (Tg)	Footnote	References
Augustine	13/1/06	28/1/06	16	no	0.034	0.027 <sup>a</sup>	0.041 <sup>a</sup>	1	41
Bezymianny	15/10/07	16/10/07	2	yes	0.066	0.053 <sup>a</sup>	0.079 <sup>a</sup>	2	34
Calbuco	22/4/15	23/4/15	2	no	0.295	0.231	0.359	3	49
Chaiten	2/5/08	6/5/08	5	no	0.010	0.010	0.012 <sup>a</sup>	4	8
Eyjafjallajökull	14/4/10	22/5/10	39	yes	1.20	0.70	1.70	5	55
Fernandina	13/5/05	17/5/05	5	yes	0.100	0.080 <sup>a</sup>	0.120 <sup>a</sup>	6	19
Fogo	23/11/14	8/2/15	78	yes	0.382	0.306 <sup>a</sup>	0.458 <sup>a</sup>	7	23
Piton de la Fournaise	4/4/07	9/4/07	6	yes	0.231	0.189 <sup>a</sup>	0.277 <sup>a</sup>	8	67
Grimsvötn	22/5/11	23/5/11	2	yes	0.38	0.30 <sup>a</sup>	0.46 <sup>a</sup>	9	62
Kelut	13/2/14	13/2/14	1	no	0.200	0.160 <sup>a</sup>	0.240 <sup>a</sup>	10	79
Merapi	1/11/10	4/11/10	4	no	0.270	0.220	0.320	11	65
Okmok	12/7/08	16/7/08	5	No	0.290	0.280	0.300	12	53

Puyehue-Cordon Caulle	4/6/11	7/6/11	4	no	0.550	0.440 <sup>a</sup>	0.660 <sup>a</sup>	13	3
Raikoke	21/6/19	21/6/19	1	no	1.50	1.30	1.70	14	15
Redoubt	23/3/09	4/4/09	13	no	0.225	0.180 <sup>a</sup>	0.270 <sup>a</sup>	15	33
Sarychev Peak	11/6/09	11/6/09	1	no	0.900	0.720 <sup>a</sup>	1.08 <sup>a</sup>	16	19
Sierra Negra	23/10/05	29/10/05	7	yes	1.93	1.54 <sup>a</sup>	2.32 <sup>a</sup>	17	19
Sinabung <sup>b</sup>	18/12/13	13/4/14	116	no	0.047	0.038 <sup>a</sup>	0.056 <sup>a</sup>	18	54
St. Helens	27/9/04	23/1/08	1214	no	0.032	0.026	0.039	19	16, 22
Jebel at Tair	30/9/07	4/10/07	5	yes	0.155	0.124 <sup>a</sup>	0.186 <sup>a</sup>	20	13, 76

<sup>a</sup> For error not reported in literature, we attributed an automatic error of 20%.

<sup>b</sup> Campaign measurements of SO<sub>2</sub> at Sinabung is available for 46 of the 117 days of eruption.

### Footnotes

1. Augustine, 2006: Assuming 0.003 Tg day<sup>-1</sup> for the first 10 days and 0.0007 Tg day<sup>-1</sup> for the last 5 days; Large amount of SO<sub>2</sub> released during precursory phase, so the total SO<sub>2</sub> gas in the reservoir is already underestimated.
2. Bezymianny, 2007: Persistently degassing volcano; gas emission is an underestimation.
3. Calbuco, 2015: 0.14±0.033 Tg produced by the first eruption and 0.155±0.031 Tg by the second eruption; Possible underestimation of SO<sub>2</sub> loading due to high SO<sub>2</sub> column and presence of volcanic ash (signal saturation).
4. Chaiten, 2008: 'Strikingly' low SO<sub>2</sub> emission measured by OMI on 2, 6, and 8 May; Assuming 0.01 Tg is the minimum estimate.

5. Eyjafjallajökull, 2010: SO<sub>2</sub> emissions measured using GOME-2; SO<sub>2</sub> gas peaks after two weeks of eruption.
6. Fernandina, 2005: SO<sub>2</sub> emissions using OMI from compilation by Ge et al. (2016); Note the shorter measurement duration compared to the erupted volume, i.e., SO<sub>2</sub> emissions may be underestimated.
7. Fogo, 2014: SO<sub>2</sub> measurements using OMI.
8. Piton de la Fournaise, 2007: SO<sub>2</sub> gas estimated using OMI and CALIOP; Note the shorter measurement duration compared to the erupted volume, i.e., SO<sub>2</sub> emissions may be underestimated.
9. Grimsvötn, 2011: Satellite observations of SO<sub>2</sub> less than total SO<sub>2</sub> budget due to leaching and formation of sulfide globules; Measurement provided here is the total SO<sub>2</sub> recalculated from melt inclusions.
10. Kelut, 2014: Based on comparing simulations with the OMI data.
11. Merapi, 2010: Estimated from the total SO<sub>2</sub> released (0.44 Tg) during eruption period 26/10-4/11.
12. Okmok, 2008: SO<sub>2</sub> emissions from Kasatochi and Okmok were transported together in the first 3 days of the eruption; Measurements become challenging after several days; Note the different duration of measurement compared to erupted volume.
13. Puyehue-Cordon Caulle, 2011: SO<sub>2</sub> gas retrievals from MODIS.
14. Raikoke, 2019: Peak SO<sub>2</sub> emission only detected after 3 days of the eruption; Total SO<sub>2</sub> emission estimated using the Met Office's Numerical Atmospheric-dispersion Modelling Environment (NAME).
15. Redoubt, 2009: Airborne measurements not collected during explosive phase; OMI measurements shown here is only during explosive phase; SO<sub>2</sub> emission is lower on periods of dome growth and absence of explosive eruptions.
16. Sarychev Peak, 2009: 1.2 Tg SO<sub>2</sub> emission measured using IASI; An updated SO<sub>2</sub> algorithm (Clarisse et al., 2012) found a maximum SO<sub>2</sub> emission of ~0.9 Tg, consistent with algorithm of Carn et al., 2016.

17. Sierra Negra, 2005: Cumulative daily SO<sub>2</sub> emissions from OMI.
18. Sinabung, 2013: SO<sub>2</sub> emissions measured during campaign.; Days at which no SO<sub>2</sub> measurements are reported is below the detection threshold.
19. St. Helens, 2004: SO<sub>2</sub> emissions below detection threshold from 27 Sep 2004 to 4 Oct 2004 and after 21 Sep 2007.
20. Jebel at Tair, 2007: SO<sub>2</sub> emissions measured using OMI; Fissure eruption only lasted for first several hours of eruption.



Table B.6: Volume erupted of eruptions.

Volcano name	Start date (dd/mm/yy)	End date (dd/mm/yy)	Eruption duration (days)	Volume erupted (km <sup>3</sup> )	Min. volume erupted (km <sup>3</sup> )	Max. volume erupted (km <sup>3</sup> )	Footnote	References
Augustine	13/1/06	28/1/06	16	0.053	0.042 <sup>a</sup>	0.064 <sup>a</sup>	1 <sup>b</sup>	18
Bezymianny	15/10/07	16/10/07	2	0.025	0.020 <sup>a</sup>	0.030 <sup>a</sup>	2	34, 78
Calbuco	22/4/15	23/4/15	2	0.446	0.254	0.638	3 <sup>b</sup>	10, 18, 56, 69
Chaiten	1/5/08	6/5/08	6	0.800	0.700	0.900	4	72
Eyjafjallajökull	14/4/10	22/5/10	39	0.322	0.242	0.403	5 <sup>b</sup>	18, 26
Fernandina	13/5/05	29/5/05	18	0.015	0.010	0.016	6 <sup>b</sup>	18
Fogo	23/11/14	8/2/15	78	0.036	0.033	0.039	7 <sup>b</sup>	18
Piton de la Fournaise	30/3/07	29/4/07	30	0.234	0.164	0.305	8 <sup>b</sup>	18
Grimsvötn	21/5/11	23/5/11	3	0.270	0.200	0.340	9	28
Kelut	13/2/14	13/2/14	1	0.210	0.140	0.280	10	37

Merapi	1/11/10	4/11/10	4	0.073	0.043	0.113	11 <sup>b</sup>	18, 47, 65
Okmok	12/7/08	19/08/08	39	0.442	0.286	1.163	12 <sup>b</sup>	18, 30
Puyehue-Cordon Caulle	4/6/11	7/6/11	4	1.01 <sup>c</sup>	0.81	1.21	13	51
Raikoke	21/6/19	21/6/19	1	0.439	0.287	0.672	14	42
Redoubt	23/3/09	4/4/09	13	0.100	0.080	0.120	15	4
Sarychev Peak	11/6/09	19/6/09	9	0.154	0.077	0.231	16	57
Sierra Negra	22/10/05	30/10/05	9	0.156	0.109	0.203	17	21
Sinabung	18/12/13	13/4/14	116	0.067	0.054 <sup>a</sup>	0.081 <sup>a</sup>	18	48
St. Helens	23/9/04	11/1/08	1206	0.103	0.099	0.107	19	38, 60, 68
Jebel at Tair	30/9/07	16/6/08	261	0.018	0.010	0.027	20 <sup>b</sup>	18

<sup>a</sup> For error not reported in literature, we attributed an automatic error of 20%.

<sup>b</sup> Volume erupted estimated from the compilation by Galetto et al. (2023). Mass is converted to volume assuming ash density = 1000 kgm<sup>-3</sup>, PDC density = 1700 kgm<sup>-3</sup> and lava density = 2600 kgm<sup>-3</sup>, unless otherwise specified.

<sup>c</sup> The estimated erupted volume for Puyehue-Cordon Caulle is the cumulative volume measured between 4-7 June, 2011.

### Footnotes

1. Augustine, 2006: Volume estimates from Galetto et al. (2023).

2. Bezymianny, 2007: Eruptive mass of  $66 \times 10^9$  kg from the October 2007 eruption deposits is obtained from Zharinov and Demyanchuk (2011) and converted to dense rock equivalent (DRE) volume of  $0.025 \text{ km}^3$  (López et al., 2013).
3. Calbuco, 2015: Volume estimates from Galetto et al. (2023). Estimated assuming ash density =  $900 \text{ kgm}^{-3}$ , as noted from IVESPA; Total erupted volumes estimates from previous studies are  $0.27 \pm 0.007$  (Romero et al., 2016),  $0.56 \pm 0.28$  (Van Eaton et al., 2016), and  $0.38 \text{ km}^3$  (Castruccio et al., 2016).
4. Chaiten, 2008: Estimated erupted volume during the Plinian eruption and a new dome.
5. Eyjafjallajökull, 2010: Volume estimates from Galetto et al. (2023); Volume estimated from mass erupted assuming tephra density =  $1400 \text{ kgm}^{-3}$  and lava density =  $2400 \text{ kgm}^{-3}$  (Gudmundsson et al., 2012).
6. Fernandina, 2005: Volume estimates from Galetto et al. (2023).
7. Fogo, 2014: Volume estimates from Galetto et al. (2023).
8. Piton de la Fournaise, 2007: Volume estimates from Galetto et al. (2023).
9. Grimsvötn, 2011: Volume estimated from tephra discharge rate and plume height.
10. Kelut, 2014: DRE estimated from tephra fallout and PDC deposits.
11. Merapi, 2010: Erupted volume only available during magmatic phase; Initial phase (26/10-31/10) removed  $0.006 \text{ km}^3$  of non-juvenile material from summit.
12. Okmok, 2008: Volume estimates from Galetto et al. (2023).
13. Puyehue-Cordon Caulle, 2011: Erupted volume in the first phase (4–5 June) is  $\sim 0.75 \text{ km}^3$ ; Erupted volume in the second phase (5–6 June) is  $\sim 0.21 \text{ km}^3$ ; Erupted volume in the third phase (7 June) is  $\sim 0.05 \text{ km}^3$ .
14. Raikoke, 2019: Volume estimated from mass of plume assuming density  $1000 \text{ kgm}^{-3}$ .

15. Redoubt, 2009: Erupted volume considers DRE for four domes and fall deposits.
16. Sarychev Peak, 2009: Bulk volume  $0.4\text{km}^3$  is converted to DRE assuming tephra density  $1000\text{ kgm}^{-3}$  and magma density  $2600\text{ kgm}^{-3}$ ; Estimated with an error of 50
17. Sierra Negra, 2005: Volume estimated from volume flux.
18. Sinabung, 2013: Derived from satellite measurements of extrusion rate.
19. St. Helens, 2004: Photogrammetry recorded a volume of  $0.093\pm0.004\text{ km}^3$ ;  $0.010\text{ km}^3$  of welt was pushed out before the lava extrudes.
20. Jebel at Tair, 2007: Volume estimates from Galetto et al. (2023).

Table B.7: Reservoir depth of volcanic eruption.

Volcano name	Start date (dd/mm/yy)	End date (dd/mm/yy)	Eruption duration (days)	Chamber geometry <sup>a</sup>	Depth (km)	Min. depth (km)	Max. depth (km)	Footnote	References
Augustine	13/1/06	28/1/06	16	PS	4.6	2.6	6.6	1	11, 41
Bezymianny	15/10/07	16/10/07	2	<i>see</i>	7.5	6.0	9.0	2	34, 66
				<i>notes</i>					
Calbuco	22/4/15	23/4/15	2	PS	8.2	6.6	9.5	3	45
Chaiten	1/5/08	6/5/08	6	com.	10	8	12	4	72
Eyjafjallajökull	14/4/10	22/5/10	39	Sill	4.4	4.0	4.7	5	63
Fernandina	13/5/05	29/5/05	18	Mogi	5.0	4.0 <sup>b</sup>	6.0 <sup>b</sup>	6	12
Fogo	23/11/14	8/2/15	78	<i>see</i>	16.5	-	-	7	1, 39
				<i>notes</i>					
Fournaise, Piton de la	30/3/07	29/4/07	30	com.	2.3	1.9	2.7	8	50
Grimsvötn	21/5/11	23/5/11	3	Mogi	1.7	1.5	1.9	9	28
Kelut	13/2/14	13/2/14	1	Mogi	2.1	1.7 <sup>b</sup>	2.5 <sup>b</sup>	10	9
Merapi	1/11/10	4/11/10	4	PS	15	10	20	11	73

Okmok	12/7/08	19/08/08	39	Mogi	3.0	1.5	4.5	12	35, 36
Puyehue-Cordon Caulle	4/6/11	7/6/11	4	Mogi	6.0	5.0	7.0	13	29
Raikoke	21/6/19	21/6/19	1	<i>see notes</i>	5.0	2.5	7.5	14	64
Redoubt	23/3/09	4/4/09	13	PS	9.2	6.9	15.2	15	25
Sarychev Peak	11/6/09	19/6/09	9	<i>see notes</i>	3.5	1.8	5.3	16	57
Sierra Negra	22/10/05	30/10/05	9	com.	2.1	1.7	2.5	17	22
Sinabung	22/12/13	20/4/14	119	Mogi	8.4	7.4	9.9	18	27
St. Helens	23/9/04	11/1/08	1206	PS	5.6	2.9	8.3	19	2, 32
Jebel at Tair	30/9/07	16/6/08	261	Mogi	7	7	15	20	76

<sup>a</sup> PS: Prolate spheroid; com.: Complex deformation sources.

<sup>b</sup> For error not reported in literature, we attributed an automatic error of 20%.

### Footnotes

1. Augustine, 2006: 2 models exist: closed pipe with depth ranging 4.5-10.5 km and open pipe with depth ranging 2.6-6.6 km; Open pipe is chosen considering SO<sub>2</sub> emissions prior to eruption.
2. Bezymianny, 2007: Depth of magma storage from 6 to > 9 km is estimated from seismic data and are supported by estimated melt inclusion entrapment depths.
3. Calbuco, 2015: Depth calculated using compound dislocation model.

4. Chaiten, 2008: Multiple deformation sources, including a deep reservoir at 20 km depth, a dyke, and the reservoir; Reservoir steeply dipping between 31° and 57°.
5. Eyjafjallajökull, 2010: Horizontal deflating sill; Deflating source is spatially offset from the pre-eruptive complex.
6. Fernandina, 2005: Magma from a deflating point source contributed to three dyke intrusions and sill expansion.
7. Fogo, 2014: Minimum depth of 16.5 km based on InSAR measurements of the 1995 eruption (Amelung and Day, 2002); Petrological estimates of the 2014 eruption indicated greater depths, with suggestions that the eruption was fed from a deep mantle source (Mata et al., 2017).
8. Piton de la Fournaise, 2007: Two deflation sources measured using GPS: a prolate spheroid at  $1.2\text{--}2.3\pm0.4$  km depth between 2-5 Apr and an oblate spheroid at  $2.3\pm0.4$  km depth between 5-6 Apr.
9. Grimsvötn, 2011: Mogi Point source modelled using GPS measurements.
10. Kelut, 2014: Best but not uniquely fitting point source model; Consistent with petrological data.
11. Merapi, 2010: Seismic tomography reveals fluid rich zone at <4 km depth and a main reservoir at ~10–20 km depth, in agreement with petrological studies (4-15 km).
12. Okmok, 2008: Average Mogi source depth from InSAR before the 2008 eruption; Estimated with an error of 50%; Mogi depth of the first 13 hours of the 2008 eruption is  $1.9\pm0.3$  km.
13. Puyehue-Cordon Caulle, 2011: Two deflating point sources: hydrothermal system beneath Cordillera Nevada and shallow magma reservoir beneath Puyehue.
14. Raikoke, 2019: Petrological studies show plagioclase joining the crystallization of olivine, suggesting fractionation occurred at shallow reservoirs; The parental magma responsible for the eruption had a basaltic composition, with

the deepest level of fractionation at ~26 km depth; Petrological data of the eruption pyroclastics reveals that magma evolution occurred at different depths.

15. Redoubt, 2009: Magma evacuated from a prolate spheroid with semimajor axis 4.5 and semiminor axis 0.475.
16. Sarychev Peak, 2009: Preliminary petrological observations suggest influx of basalt into a shallow magma reservoir located at a depth of ~3-4 km; Added an error of 50%.
17. Sierra Negra, 2005: The best-fitting model has a sill and a point source, both located at 2.1 km depth.
18. Sinabung, 2013: Deformation source is ~7km offset from vent; Calculated dates of volume changes from GPS station different to dates of volume erupted.
19. St. Helens, 2004: - The chamber geometry of the 2004 eruption is a prolate spheroid chamber with a centroid depth of  $9 \pm 0.5$  km; The eruption is sourced from the top of the magma reservoir that is estimated to be between 2.9-8.3 km depth.
20. Jebel at Tair, 2007: Co-eruptive deflation would have been detected for a Mogi reservoir shallower than 7 km; The lack of a shallow magma reservoir at slow-spreading centers is not uncommon.



Table B.8: Normalised volume change and normalised SO<sub>2</sub> of eruptions.

Volcano name	Start date (dd/mm/yy)	End date (dd/mm/yy)	Eruption duration (days)	Normalised volume change	Min. Normalised volume change	Max. Normalised volume change	Normalised SO <sub>2</sub> (Tg km <sup>-3</sup> )	Min. Normalised SO <sub>2</sub> (Tg km <sup>-3</sup> )	Max. Normalised SO <sub>2</sub> (Tg km <sup>-3</sup> )
Augustine	13/1/06	28/1/06	16	-	-	-	0.64	0.45	0.82
Bezymianny	15/10/07	16/10/07	2	-	-	-	2.64	1.90	3.38
Calbuco	22/4/15	23/4/15	2	0.22	0.07	0.37	0.66	0.34	0.98
Chaiten	1/5/08	6/5/08	6	0.25	0.18	0.32	0.01	0.01	0.02
Eyjafjalla- jökull	14/4/10	22/5/10	39	0.04	0.03	0.05	3.73	1.92	5.54
Fernandina	13/5/05	29/5/05	18	0.80	0.50	0.94	6.67	4.07	8.07
Fogo	23/11/14	8/2/15	78	-	-	-	10.6	8.32	13.0
Piton de la Fournaise	30/3/07	29/4/07	30	0.01	0.00	0.01	0.99	0.64	1.35
Grimsvötn	21/5/11	23/5/11	3	0.10	0.07	0.13	1.41	0.94	1.88
Kelut	13/2/14	13/2/14	1	0.03	0.02	0.05	0.95	0.58	1.32
Merapi	1/11/10	4/11/10	4	-	-	-	3.70	2.03	5.37

Okmok <sup>a</sup>	12/7/08	19/08/08	39	0.32	0.20	0.83	0.65	0.42	1.73
Puyehue- Cordon Caulle	4/6/11	7/6/11	4	0.11	0.07	0.14	0.54	0.39	0.70
Raikoke	21/6/19	21/6/19	1	-	-	-	3.42	2.15	5.29
Redoubt	23/3/09	4/4/09	13	0.50	0.26	0.74	2.25	1.61	2.89
Sarychev Peak <sup>a</sup>	11/6/09	19/6/09	9	-	-	-	5.84	2.70	8.99
Sierra Negra	22/10/05	30/10/05	9	0.52	0.33	0.70	12.4	7.88	16.9
Sinabung	22/12/13	20/4/14	119	0.31	0.19	0.43	0.70	0.51	0.89
St. Helens <sup>a</sup>	23/9/04	11/1/08	1206	0.25	0.18	0.32	0.31	0.25	0.37
Jebel at Tair <sup>a</sup>	30/9/07	16/6/08	261	-	-	-	8.61	4.41	13.2

<sup>a</sup> Different duration of measurements for SO<sub>2</sub> and erupted volume.

Table B.9: Reservoir depth of volcanic eruption.

Volcano name	Start date (dd/mm/yy)	End date (dd/mm/yy)	Eruption duration (days)	SiO <sub>2</sub> (wt%)	References
Augustine	13/1/06	28/1/06	16	57.5±1.5	14
Bezymianny	15/10/07	16/10/07	2	56.7±0.2	61
Calbuco	22/4/15	23/4/15	2	54.5±0.5	10
Chaiten	1/5/08	6/5/08	6	75.3±0.3	47
Eyjafjallajokull	14/4/10	22/5/10	39	47.4±1.5	43
Fernandina	13/5/05	29/5/05	18	48.5±0.5	20
Fogo	23/11/14	8/2/15	78	45.5±2.5	39
Fournaise, Piton de la	30/3/07	29/4/07	30	50.0±0.4	70
Grimsvötn	21/5/11	23/5/11	3	49.9±0.8	62
Kelut	13/2/14	13/2/14	1	56.1±7.3	71
Merapi	1/11/10	4/11/10	4	57.8±2.6	75
Okmok	12/7/08	19/08/08	39	55.0±0.3	30
Puyehue-Cordon	4/6/11	7/6/11	4	75.4±0.7	74
Caulle					
Raikoke	21/6/19	21/6/19	1	49.8±0.5	64

Redoubt	23/3/09	4/4/09	13	60.0±2.5	59
Sarychev Peak	11/6/09	19/6/09	9	54.2±0.2	57
Sierra Negra	22/10/05	30/10/05	9	49.0±0.9	51
Sinabung	22/12/13	20/4/14	119	59.0±0.3	44
St. Helens	23/9/04	11/1/08	1206	64.9±0.1	46
Jebel at Tair	30/9/07	16/6/08	261	49.5±0.6	40

### Footnotes

1. Augustine, 2006: Pyroclastic flows initially rich in a low-silica andesite (57 wt% SiO<sub>2</sub>) that become progressively more silica rich and voluminous.
2. Bezymianny, 2007: Bulk rock composition of erupted products.
3. Calbuco, 2015: Bulk rock composition of erupted products.
4. Chaiten, 2008: Phenocryst-poor obsidian and microcrystalline rhyolite.
5. Eyjafjallajökull, 2010: Whole-rock composition of basaltic eruption from volcano's flank.
6. Fernandina, 2005: Wholerock composition of erupted products.
7. Fogo, 2014: SiO<sub>2</sub> composition of glass data.
8. Piton de la Fournaise, 2007: SiO<sub>2</sub> analysis from matrix glass scoria.
9. Grimsvötn, 2011: SiO<sub>2</sub> analysis from melt inclusions.
10. Kelut, 2014: Analysis from ash samples.

11. Merapi, 2010: Wholerock compositions from fresh interior slabs cut.
12. Okmok, 2008: Wholerock compositions cluster tightly ( $54.97 \pm 0.25$  wt%  $\text{SiO}_2$ ).
13. Puyehue-Cordon Caulle, 2011:  $\text{SiO}_2$  analysis of glass data.
14. Raikoke, 2019: Glass compositions of shards from air fall ash.
15. Redoubt, 2009:  $\text{SiO}_2$  composition of tephra and dome lavas.
16. Sarychev Peak, 2009: Wholerock compositions from fragments of volcanic bombs.
17. Sierra Negra, 2005:  $\text{SiO}_2$  analysis of tephra.
18. Sinabung, 2013: Wholerock chemical compositions of lava samples.
19. St. Helens, 2004: Bulk rock composition from 2004–2006 Mount St. Helens lava dome.
20. Jebel at Tair, 2007:  $\text{SiO}_2$  composition of lava.

## B.4 Supplementary References

1. Amelung, F., & Day, S. (2002). InSAR observations of the 1995 Fogo, Cape Verde, eruption: Implications for the effects of collapse events upon island volcanoes. *Geophysical research letters*, 29(12), 47-1.
2. Anderson, K., & Segall, P. (2013). Bayesian inversion of data from effusive volcanic eruptions using physics-based models: Application to Mount St. Helens 2004–2008. *Journal of Geophysical Research: Solid Earth*, 118(5), 2017-2037.
3. Bignami, C., Corradini, S., Merucci, L., de Michele, M., Raucoules, D., De Astis, G., ... & Piedra, J. (2014). Multisensor satellite monitoring of the 2011 Puyehue-Cordon Caulle eruption. *IEEE journal of selected topics in applied earth observations and remote sensing*, 7(7), 2786-2796.
4. Bull, K. F., & Buurman, H. (2013). An overview of the 2009 eruption of Redoubt Volcano, Alaska. *Journal of Volcanology and Geothermal Research*, 259, 2-15.
5. Champion, R., & Coppola, D. (2023). Classification of lava lakes based on their heat and SO<sub>2</sub> emission: Implications for their formation and feeding processes. *Frontiers in Earth Science*, 11, 1040199.
6. Carboni, E., Grainger, R., Walker, J., Dudhia, A., & Siddans, R. (2012). A new scheme for sulphur dioxide retrieval from IASI measurements: application to the Eyjafjallajökull eruption of April and May 2010. *Atmospheric Chemistry and Physics*, 12(23), 11417-11434.
7. Carn, S. A., & Lopez, T. M. (2011). Opportunistic validation of sulfur dioxide in the Sarychev Peak volcanic eruption cloud. *Atmospheric Measurement Techniques*, 4(9), 1705-1712.
8. Carn, S. A., Pallister, J. S., Lara, L., Ewert, J. W., Watt, S., Prata, A. J., ... & Villarosa, G. (2009). The unexpected awakening of Chaitén volcano, Chile. *Eos, Transactions American Geophysical Union*, 90(24), 205-206.
9. Cassidy, M., Ebmeier, S. K., Helo, C., Watt, S. F. L., Caudron, C., Odell, A., ... & Castro, J. M. (2019). Explosive eruptions with little warning: Experimental petrology and volcano monitoring observations from the 2014 eruption of Kelud, Indonesia. *Geochemistry, Geophysics, Geosystems*, 20(8), 4218-4247.

10. Castruccio, A., Clavero, J., Segura, A., Samaniego, P., Roche, O., Le Pennec, J. L., & Droguett, B. (2016). Eruptive parameters and dynamics of the April 2015 sub-Plinian eruptions of Calbuco volcano (southern Chile). *Bulletin of Volcanology*, 78, 1-19.
11. Cervelli, P.F., Fournier, T.J., Freymueller, J.T., Power, J.A., Lisowski, Michael, and Pauk, B.A., 2010, Geodetic constraints on magma movement and withdrawal during the 2006 eruption of Augustine Volcano, chapter 17 of Power, J.A., Coombs, M.L., and Freymueller, J.T., eds., *The 2006 eruption of Augustine Volcano, Alaska: U.S. Geological Survey Professional Paper 1769*, p. 427–452 [[https://pubs.usgs.gov/pp/1769/chapters/p1769\\_chapter17](https://pubs.usgs.gov/pp/1769/chapters/p1769_chapter17)].
12. Chadwick Jr, W. W., Nooner, S. L., Butterfield, D. A., & Lilley, M. D. (2012). Seafloor deformation and forecasts of the April 2011 eruption at Axial Seamount. *Nature Geoscience*, 5(7), 474-477.
13. Clarisse, L., Coheur, P. F., Prata, A. J., Hurtmans, D., Razavi, A., Phulpin, T., ... & Clerbaux, C. (2008). Tracking and quantifying volcanic SO<sub>2</sub> with IASI, the September 2007 eruption at Jebel at Tair. *Atmospheric Chemistry and Physics*, 8(24), 7723-7734.
14. Coombs, M.L., Bull, K.F., Vallance, J.W., Schneider, D.J., Thoms, E.E., Wessels, R.L., and McGimsey, R.G., 2010, Timing, distribution, and volume of proximal products of the 2006 eruption of Augustine Volcano, chapter 8 of Power, J.A., Coombs, M.L., and Freymueller, J.T., eds., *The 2006 eruption of Augustine Volcano, Alaska: U.S. Geological Survey Professional Paper 1769*, p. 145–185, 1 plate, scale 1:20,000, and GIS data [[https://pubs.usgs.gov/pp/1769/chapters/p1769\\_chapter08](https://pubs.usgs.gov/pp/1769/chapters/p1769_chapter08)].
15. de Leeuw, J., Schmidt, A., Witham, C. S., Theys, N., Taylor, I. A., Grainger, R. G., ... & Kristiansen, N. I. (2021). The 2019 Raikoke volcanic eruption–Part 1: Dispersion model simulations and satellite retrievals of volcanic sulfur dioxide. *Atmospheric Chemistry and Physics*, 21(14), 10851-10879.
16. Dzurisin, D., Moran, S. C., Lisowski, M., Schilling, S. P., Anderson, K. R., & Werner, C. (2015). The 2004–2008 dome-building eruption at Mount St. Helens, Washington: epilogue. *Bulletin of Volcanology*, 77, 1-17.
17. Froger, J. L., Famin, V., Cayol, V., Augier, A., Michon, L., & Lénat, J. F. (2015). Time-dependent displacements during and after the April 2007 eruption of Piton

- de la Fournaise, revealed by interferometric data. *Journal of Volcanology and Geothermal Research*, 296, 55-68.
18. Galetto, F., Pritchard, M. E., Hornby, A. J., Gazel, E., & Mahowald, N. M. (2023). Spatial and Temporal Quantification of Subaerial Volcanism From 1980 to 2019: Solid Products, Masses, and Average Eruptive Rates. *Reviews of Geophysics*, 61(1), e2022RG000783.
  19. Ge, C., Wang, J., Carn, S., Yang, K., Ginoux, P., & Krotkov, N. (2016). Satellite-based global volcanic SO<sub>2</sub> emissions and sulfate direct radiative forcing during 2005–2012. *Journal of Geophysical Research: Atmospheres*, 121(7), 3446-3464.
  20. Geist, D., Chadwick, W., & Johnson, D. (2006). Results from new GPS and gravity monitoring networks at Fernandina and Sierra Negra Volcanoes, Galápagos, 2000–2002. *Journal of Volcanology and Geothermal Research*, 150(1-3), 79-97.
  21. Geist, D. J., Harpp, K. S., Naumann, T. R., Poland, M., Chadwick, W. W., Hall, M., & Rader, E. (2008). The 2005 eruption of Sierra Negra volcano, Galápagos, Ecuador. *Bulletin of Volcanology*, 70, 655-673.
  22. Gerlach, T. M., McGee, K. A., & Doukas, M. P. (2008). Emission rates of CO<sub>2</sub>, SO<sub>2</sub>, and H<sub>2</sub>S, scrubbing, and preeruption excess volatiles at Mount St. Helens, 2004-2005 (No. 1750-26, pp. 543-571). US Geological Survey.
  23. Global Volcanism Program, 2023. Fogo (384010) Volcanoes of the World (v. 5.1.0; 9 Jun 2023). Distributed by Smithsonian Institution, compiled by Venzke, E. <https://doi.org/10.5479/si.GVP.VOTW5-2023.5.1>
  24. González, P. J., Bagnardi, M., Hooper, A. J., Larsen, Y., Marinkovic, P., Samsonov, S. V., & Wright, T. J. (2015). The 2014–2015 eruption of Fogo volcano: Geodetic modeling of Sentinel-1 TOPS interferometry. *Geophysical research letters*, 42(21), 9239-9246.
  25. Grapenthin, R., Freymueller, J. T., & Kaufman, A. M. (2013). Geodetic observations during the 2009 eruption of Redoubt Volcano, Alaska. *Journal of Volcanology and Geothermal Research*, 259, 115-132.
  26. Gudmundsson, M. T., Thordarson, T., Höskuldsson, Á., Larsen, G., Björnsson, H., Prata, F. J., ... & Jónsdóttir, I. (2012). Ash generation and distribution from the April-May 2010 eruption of Eyjafjallajökull, Iceland. *Scientific reports*, 2(1), 572.



27. Hotta, K., Iguchi, M., Ohkura, T., Hendrasto, M., Gunawan, H., Rosadi, U., & Kriswati, E. (2019). Magma intrusion and effusion at Sinabung volcano, Indonesia, from 2013 to 2016, as revealed by continuous GPS observation. *Journal of Volcanology and Geothermal Research*, 382, 173-183.
28. Hreinsdóttir, S., Sigmundsson, F., Roberts, M. J., Björnsson, H., Grapenthin, R., Arason, P., ... & Óladóttir, B. A. (2014). Volcanic plume height correlated with magma-pressure change at Grímsvötn Volcano, Iceland. *Nature geoscience*, 7(3), 214-218.
29. Jay, J., Costa, F., Pritchard, M., Lara, L., Singer, B., & Herrin, J. (2014). Locating magma reservoirs using InSAR and petrology before and during the 2011–2012 Cordón Caulle silicic eruption. *Earth and Planetary Science Letters*, 395, 254-266.
30. Larsen, J. F., Śliwiński, M. G., Nye, C., Cameron, C., & Schaefer, J. R. (2013). The 2008 eruption of Okmok Volcano, Alaska: Petrological and geochemical constraints on the subsurface magma plumbing system. *Journal of Volcanology and Geothermal Research*, 264, 85-106.
31. Larsen, J., Neal, C. A., Schaefer, J. R., Kaufman, M., & Lu, Z. (2015). The 2008 phreatomagmatic eruption of Okmok Volcano, Aleutian Islands, Alaska: chronology, deposits, and landform changes (No. RI 2015-2). Alaska Division of Geological & Geophysical Surveys.
32. Lisowski, M., Dzurisin, D., Denlinger, R. P., & Iwatsubo, E. Y. (2008). Analysis of GPS-measured deformation associated with the 2004-2006 dome-building eruption of Mount St. Helens, Washington (No. 1750-15, pp. 301-333). US Geological Survey.
33. Lopez, T., Carn, S., Werner, C., Fee, D., Kelly, P., Doukas, M., ... & Schneider, D. (2013). Evaluation of Redoubt Volcano's sulfur dioxide emissions by the Ozone Monitoring Instrument. *Journal of Volcanology and Geothermal Research*, 259, 290-307.
34. López, T., Ushakov, S., Izbekov, P., Tassi, F., Cahill, C., Neill, O., & Werner, C. (2013). Constraints on magma processes, subsurface conditions, and total volatile flux at Bezymianny Volcano in 2007–2010 from direct and remote volcanic gas measurements. *Journal of Volcanology and Geothermal Research*, 263, 92-107.

35. Lu, Z., & Dzurisin, D. (2010). Ground surface deformation patterns, magma supply, and magma storage at Okmok volcano, Alaska, from InSAR analysis: 2. Coeruptive deflation, July–August 2008. *Journal of Geophysical Research: Solid Earth*, 115(B5).
36. Lu, Z., Dzurisin, D., Biggs, J., Wicks Jr, C., & McNutt, S. (2010). Ground surface deformation patterns, magma supply, and magma storage at Okmok volcano, Alaska, from InSAR analysis: 1. Intereruption deformation, 1997–2008. *Journal of Geophysical Research: Solid Earth*, 115(B5).
37. Maeno, F., Nakada, S., Yoshimoto, M., Shimano, T., Hokanishi, N., Zaennudin, A., & Iguchi, M. (2019). A sequence of a plinian eruption preceded by dome destruction at Kelud volcano, Indonesia, on February 13, 2014, revealed from tephra fallout and pyroclastic density current deposits. *Journal of Volcanology and Geothermal Research*, 382, 24-41.
38. Mastin, L. G., Lisowski, M., Roeloffs, E., & Beeler, N. (2009). Improved constraints on the estimated size and volatile content of the Mount St. Helens magma system from the 2004–2008 history of dome growth and deformation. *Geophysical Research Letters*, 36(20).
39. Mata, J., Martins, S., Mattielli, N., Madeira, J., Faria, B., Ramalho, R. S., ... & Martins, L. (2017). The 2014–15 eruption and the short-term geochemical evolution of the Fogo volcano (Cape Verde): Evidence for small-scale mantle heterogeneity. *Lithos*, 288, 91-107.
40. Mattash, M. A., Pinarelli, L., Vaselli, O., Minissale, A., Jaimes-Viera, M. C., Al-Kadasi, M., ... & Tassi, F. (2014). Geochemical evolution of southern Red Sea and Yemen flood volcanism: evidence for mantle heterogeneity. *Arabian Journal of Geosciences*, 7, 4831-4850.
41. McGee, K.A., Doukas, M.P., McGimsey, R.G., Neal, C.A., and Wessels, R.L., 2010, Emission of SO<sub>2</sub>, CO<sub>2</sub>, and H<sub>2</sub>S from Augustine Volcano, 2002–2008, chapter 26 of Power, J.A., Coombs, M.L., and Freymueller, J.T., eds., *The 2006 eruption of Augustine Volcano, Alaska: U.S. Geological Survey Professional Paper 1769*, p. 609–627 [[https://pubs.usgs.gov/pp/1769/chapters/p1769\\_chapter26.pdf](https://pubs.usgs.gov/pp/1769/chapters/p1769_chapter26.pdf)].
42. McKee, K., Smith, C. M., Reath, K., Snee, E., Maher, S., Matoza, R. S., ... & Perttu, A. (2021). Evaluating the state-of-the-art in remote volcanic eruption characterization

- Part I: Raikoke volcano, Kuril Islands. *Journal of Volcanology and Geothermal Research*, 419, 107354.
43. Moune, S., Sigmarsson, O., Schiano, P., Thordarson, T., & Keiding, J. K. (2012). Melt inclusion constraints on the magma source of Eyjafjallajökull 2010 flank eruption. *Journal of Geophysical Research: Solid Earth*, 117(B9).
44. Nakada, S., Zaennudin, A., Yoshimoto, M., Maeno, F., Suzuki, Y., Hokanishi, N., ... & Triastuty, H. (2019). Growth process of the lava dome/flow complex at Sinabung Volcano during 2013–2016. *Journal of Volcanology and Geothermal Research*, 382, 120-136.
45. Nikkhoo, M., Walter, T. R., Lundgren, P. R., & Prats-Iraola, P. (2016). Compound dislocation models (CDMs) for volcano deformation analyses. *Geophysical Journal International*, ggw427.
46. Pallister, J. S., Thornber, C. R., Cashman, K. V., Clynne, M. A., Lowers, H. A., Mandeville, C. W., ... & Stauffer, P. H. (2008). Petrology of the 2004–2006 Mount St. Helens lava dome—implications for magmatic plumbing and eruption triggering. In *A Volcano Rekindled: The Renewed Eruption of Mount St. Helens, 2004–2006* (Vol. 1750, pp. 647-702). Reston, Va: US Geol. Surv.
47. Pallister, J. S., Schneider, D. J., Griswold, J. P., Keeler, R. H., Burton, W. C., Noyles, C., ... & Ratdomopurbo, A. (2013). Merapi 2010 eruption—Chronology and extrusion rates monitored with satellite radar and used in eruption forecasting. *Journal of Volcanology and Geothermal Research*, 261, 144-152.
48. Pallister, J., Wessels, R., Griswold, J., McCausland, W., Kartadinata, N., Gunawan, H., ... & Primulyana, S. (2019). Monitoring, forecasting collapse events, and mapping pyroclastic deposits at Sinabung volcano with satellite imagery. *Journal of Volcanology and Geothermal Research*, 382, 149-163.
49. Pardini, F., Burton, M., Arzilli, F., La Spina, G., & Polacci, M. (2018). SO<sub>2</sub> emissions, plume heights and magmatic processes inferred from satellite data: The 2015 Calbuco eruptions. *Journal of Volcanology and Geothermal Research*, 361, 12-24.
50. Peltier, A., Bachèlery, P., & Staudacher, T. (2009). Magma transport and storage at Piton de La Fournaise (La Réunion) between 1972 and 2007: A review of geophysical and geochemical data. *Journal of Volcanology and Geothermal Research*, 184(1-2), 93-108.

51. Pistolesi, M., Cioni, R., Bonadonna, C., Elissondo, M., Baumann, V., Bertagnini, A., ... & Francalanci, L. (2015). Complex dynamics of small-moderate volcanic events: the example of the 2011 rhyolitic Cordón Caulle eruption, Chile. *Bulletin of Volcanology*, 77, 1-24.
52. Poland, M. P., & Lu, Z. (2008). Radar interferometry observations of surface displacements during pre-and coeruptive periods at Mount St. Helens, Washington, 1992–2005. *US geological survey professional paper*, 1750, 361-382.
53. Prata, A. J., Gangale, G., Clarisse, L., & Karagulian, F. (2010). Ash and sulfur dioxide in the 2008 eruptions of Okmok and Kasatochi: Insights from high spectral resolution satellite measurements. *Journal of Geophysical Research: Atmospheres*, 115(D2).
54. Primulyana, S., Kern, C., Lerner, A. H., Saing, U. B., Kunrat, S. L., Alfianti, H., & Marlia, M. (2019). Gas and ash emissions associated with the 2010–present activity of Sinabung Volcano, Indonesia. *Journal of Volcanology and Geothermal Research*, 382, 184-196.
55. Rix, Meike, et al. "Volcanic SO<sub>2</sub>, BrO and plume height estimations using GOME-2 satellite measurements during the eruption of Eyjafjallajökull in May 2010." *Journal of Geophysical Research: Atmospheres* 117.D20 (2012).
56. Romero, J. E., Morgavi, D., Arzilli, F., Daga, R., Caselli, A., Reckziegel, F., ... & Perugini, D. (2016). Eruption dynamics of the 22–23 April 2015 Calbuco Volcano (Southern Chile): Analyses of tephra fall deposits. *Journal of Volcanology and Geothermal Research*, 317, 15-29.
57. Rybin, A., Chibisova, M., Webley, P., Steensen, T., Izbekov, P., Neal, C., & Realmuto, V. (2011). Satellite and ground observations of the June 2009 eruption of Sarychev Peak volcano, Matua Island, Central Kuriles. *Bulletin of Volcanology*, 73, 1377-1392.
58. Saepuloh, A., Urai, M., Aisyah, N., Widiwijayanti, C., & Jousset, P. (2013). Interpretation of ground surface changes prior to the 2010 large eruption of Merapi volcano using ALOS/PALSAR, ASTER TIR and gas emission data. *Journal of Volcanology and Geothermal Research*, 261, 130-143.
59. Schaefer, J. R. (2011). The 2009 eruption of Redoubt Volcano, Alaska. *Report of Investigations*, 5, 45.

60. Schilling, S. P., Thompson, R. A., Messerich, J. A., & Iwatsubo, E. Y. (2008). Use of digital aerophotogrammetry to determine rates of lava dome growth, Mount St. Helens, Washington, 2004-2005 (No. 1750-8, pp. 145-167). US Geological Survey.
61. Shcherbakov, V. D., Plechov, P. Y., Izbekov, P. E., & Shipman, J. S. (2011). Plagioclase zoning as an indicator of magma processes at Bezymianny Volcano, Kamchatka. *Contributions to Mineralogy and Petrology*, 162, 83-99.
62. Sigmarsson, O., Haddadi, B., Carn, S., Moune, S., Gudnason, J., Yang, K., & Clarisse, L. (2013). The sulfur budget of the 2011 Grímsvötn eruption, Iceland. *Geophysical Research Letters*, 40(23), 6095-6100.
63. Sigmundsson, F., Hreinsdóttir, S., Hooper, A., Arnadóttir, T., Pedersen, R., Roberts, M. J., ... & Feigl, K. L. (2010). Intrusion triggering of the 2010 Eyjafjallajökull explosive eruption. *Nature*, 468(7322), 426-430.
64. Smirnov, S. Z., Nizametdinov, I. R., Timina, T. Y., Kotov, A. A., Sekisova, V. S., Kuzmin, D. V., ... & Abersteiner, A. (2021). High explosivity of the June 21, 2019 eruption of Raikoke volcano (Central Kuril Islands); mineralogical and petrological constraints on the pyroclastic materials. *Journal of Volcanology and Geothermal Research*, 418, 107346.
65. Surono, Jousset, P., Pallister, J., Boichu, M., Buongiorno, M. F., Budisantoso, A., Costa, F., ... & Lavigne, F. (2012). The 2010 explosive eruption of Java's Merapi volcano—a '100-year' event. *Journal of volcanology and geothermal research*, 241, 121-135.
66. Thelen, W., West, M., & Senyukov, S. (2010). Seismic characterization of the fall 2007 eruptive sequence at Bezymianny Volcano, Russia. *Journal of Volcanology and Geothermal Research*, 194(4), 201-213.
67. Tulet, P., & Villeneuve, N. (2011). Large scale modeling of the transport, chemical transformation and mass budget of the sulfur emitted during the April 2007 eruption of Piton de la Fournaise. *Atmospheric Chemistry and Physics*, 11(9), 4533-4546.
68. Vallance, J. W., Schneider, D. J., & Schilling, S. P. (2008). Growth of the 2004-2006 lava-dome complex at Mount St. Helens, Washington (No. 1750-9, pp. 169-208). US Geological Survey.

69. Van Eaton, A. R., Amigo, Á., Bertin, D., Mastin, L. G., Giacosa, R. E., González, J., ... & Behnke, S. A. (2016). Volcanic lightning and plume behavior reveal evolving hazards during the April 2015 eruption of Calbuco volcano, Chile. *Geophysical Research Letters*, 43(7), 3563-3571.
70. Villemant, B., Salaün, A., & Staudacher, T. (2009). Evidence for a homogeneous primary magma at Piton de la Fournaise (La Réunion): A geochemical study of matrix glass, melt inclusions and Pélé's hairs of the 1998–2008 eruptive activity. *Journal of volcanology and geothermal research*, 184(1-2), 79-92.
71. Vogel, A., Diplas, S., Durant, A. J., Azar, A. S., Sunding, M. F., Rose, W. I., ... & Stohl, A. (2017). Reference data set of volcanic ash physicochemical and optical properties. *Journal of Geophysical Research: Atmospheres*, 122(17), 9485-9514.
72. Wicks, C., de La Llera, J. C., Lara, L. E., & Lowenstern, J. (2011). The role of dyking and fault control in the rapid onset of eruption at Chaitén volcano, Chile. *Nature*, 478(7369), 374-377.
73. Widiyantoro, S., Ramdhan, M., Métaixian, J. P., Cummins, P. R., Martel, C., Erdmann, S., ... & Fahmi, A. A. (2018). Seismic imaging and petrology explain highly explosive eruptions of Merapi Volcano, Indonesia. *Scientific Reports*, 8(1), 13656.
74. Winslow, H., Ruprecht, P., Gonnermann, H. M., Phelps, P. R., Muñoz-Saez, C., Delgado, F., ... & Amigo, A. (2022). Insights for crystal mush storage utilizing mafic enclaves from the 2011–12 Cordón Caulle eruption. *Scientific Reports*, 12(1), 9734.
75. Wulaningsih, T., Humaida, H., Harijoko, A., & Watanabe, K. (2013). Major element and rare earth elements investigation of Merapi Volcano, Central Java, Indonesia. *Procedia Earth and Planetary Science*, 6, 202-211.
76. Xu, W., & Jónsson, S. (2014). The 2007–8 volcanic eruption on Jebel at Tair island (Red Sea) observed by satellite radar and optical images. *Bulletin of Volcanology*, 76, 1-14.
77. Yip, S. T. H., Biggs, J., Edmonds, M., Liggins, P., & Shorttle, O. (2022). Contrasting volcanic deformation in arc and ocean island settings due to exsolution of magmatic water. *Geochemistry, Geophysics, Geosystems*, 23(7), e2022GC010387.

78. Zharinov, N. A., & Demyanchuk, Y. V. (2011). Assessing the volumes of material discharged by Bezmyannyi Volcano during the 1955–2009 period. *Journal of Volcanology and Seismology*, 5(2), 100-113.
79. Zhu, Y., Toon, O. B., Jensen, E. J., Bardeen, C. G., Mills, M. J., Tolbert, M. A., ... & Woods, S. (2020). Persisting volcanic ash particles impact stratospheric SO<sub>2</sub> lifetime and aerosol optical properties. *Nature communications*, 11(1), 4526.

## **Appendix C**

### **Supplementary Material for Chapter 4**



## **Introduction**

This appendix includes supplementary tables for Chapter 4.

---

Table C.1: GPS measurements for the 2004 eruption of St. Helens spanning 2004-2005 (Anderson and Segall, 2013).

Day	Date	Displacement (mm)
-117	31/05/2004	-0.26
-116	01/06/2004	-0.69
-114	03/06/2004	-3.44
-111	06/06/2004	0.90
-107	10/06/2004	1.75
-105	12/06/2004	-0.90
-104	13/06/2004	0.26
-101	16/06/2004	-2.70
-100	17/06/2004	1.32
-97	20/06/2004	-1.29
-96	21/06/2004	-0.53
-93	24/06/2004	-0.02
-92	25/06/2004	-1.96
-88	29/06/2004	-0.19
-87	30/06/2004	-0.87
-84	03/07/2004	0.83
-82	05/07/2004	-2.17
-81	06/07/2004	-0.78
-80	07/07/2004	1.33
-76	11/07/2004	0.23
-75	12/07/2004	2.27
-72	15/07/2004	-1.46
-71	16/07/2004	-0.44
-70	17/07/2004	0.66
-68	19/07/2004	1.76
-64	23/07/2004	-0.44
-62	25/07/2004	1.08
-57	30/07/2004	0.15
-56	31/07/2004	-0.78
-53	03/08/2004	0.91
-50	06/08/2004	1.67
-49	07/08/2004	-0.10

-48	08/08/2004	-1.80
-44	12/08/2004	2.10
-43	13/08/2004	-0.27
-42	14/08/2004	0.74
-39	17/08/2004	-0.36
-39	17/08/2004	-1.63
-38	18/08/2004	0.57
-37	19/08/2004	1.50
-33	23/08/2004	-2.14
-32	24/08/2004	-1.04
-28	28/08/2004	0.74
-27	29/08/2004	1.33
-26	30/08/2004	-0.19
-25	31/08/2004	0.57
-22	03/09/2004	-1.12
-18	07/09/2004	-1.04
-17	08/09/2004	0.15
-16	09/09/2004	-4.34
-14	11/09/2004	-0.02
-11	14/09/2004	-0.61
-10	15/09/2004	2.52
-9	16/09/2004	-2.56
-8	17/09/2004	-1.80
-6	19/09/2004	0.15
-3	22/09/2004	0.66
-2	23/09/2004	-0.95
-1	25/09/2004	-1.04
0	26/09/2004	-2.14
1	27/09/2004	-2.98
2	28/09/2004	-3.58
3	29/09/2004	-5.52
5	01/10/2004	-3.91
6	02/10/2004	-5.18
7	03/10/2004	-10.77
8	04/10/2004	-5.69

---

9	05/10/2004	-9.08
10	06/10/2004	-6.45
11	07/10/2004	-7.39
14	10/10/2004	-7.22
15	11/10/2004	-8.74
16	12/10/2004	-9.50
23	19/10/2004	-10.86
24	20/10/2004	-7.22
25	21/10/2004	-8.99
26	22/10/2004	-9.42
27	23/10/2004	-3.49
28	24/10/2004	-13.48
29	25/10/2004	-8.40
31	27/10/2004	-10.69
34	30/10/2004	-9.42
35	31/10/2004	-14.16
36	01/11/2004	-11.62
38	03/11/2004	-10.52
40	05/11/2004	-9.67
44	09/11/2004	-11.19
46	11/11/2004	-14.24
47	12/11/2004	-10.69
48	13/11/2004	-9.84
51	16/11/2004	-11.87
52	17/11/2004	-12.21
53	18/11/2004	-14.24
55	20/11/2004	-9.76
56	21/11/2004	-11.36
58	23/11/2004	-12.13
62	27/11/2004	-10.77
64	29/11/2004	-12.38
66	01/12/2004	-10.43
67	02/12/2004	-11.70
70	05/12/2004	-13.06
71	06/12/2004	-15.77

72	07/12/2004	-16.02
73	08/12/2004	-12.55
74	09/12/2004	-13.99
76	11/12/2004	-15.09
78	13/12/2004	-12.46
81	16/12/2004	-11.70
82	17/12/2004	-13.06
83	18/12/2004	-11.87
84	19/12/2004	-14.41
86	21/12/2004	-13.48
89	24/12/2004	-15.51
90	25/12/2004	-11.11
91	26/12/2004	-13.23
92	27/12/2004	-11.36
94	29/12/2004	-10.69
95	30/12/2004	-14.16
97	02/01/2005	-13.23
98	03/01/2005	-13.65
99	04/01/2005	-11.36
101	06/01/2005	-12.46
101	06/01/2005	-16.98
102	07/01/2005	-17.51
105	10/01/2005	-12.89
106	11/01/2005	-11.62
109	14/01/2005	-9.59
110	15/01/2005	-10.60
111	16/01/2005	-15.82
112	17/01/2005	-24.50
113	18/01/2005	-18.47
114	19/01/2005	-15.08
115	20/01/2005	-11.28
116	21/01/2005	-12.97
117	22/01/2005	-12.97
118	23/01/2005	-13.57
119	24/01/2005	-9.59

---

120	25/01/2005	-10.35
121	26/01/2005	-14.33
124	29/01/2005	-12.46
125	30/01/2005	-12.63
128	02/02/2005	-14.76
129	03/02/2005	-13.99
130	04/02/2005	-11.45
133	07/02/2005	-14.76
135	09/02/2005	-10.86
136	10/02/2005	-13.23
137	11/02/2005	-15.77
138	12/02/2005	-13.81
140	14/02/2005	-15.60
143	17/02/2005	-12.89
148	22/02/2005	-13.23
149	23/02/2005	-14.02
151	25/02/2005	-9.26
152	26/02/2005	-17.20
153	27/02/2005	-10.11
154	28/02/2005	-12.75
155	01/03/2005	-13.82
159	05/03/2005	-13.65
160	06/03/2005	-14.87
166	12/03/2005	-14.13
167	13/03/2005	-12.65
168	14/03/2005	-16.24
171	17/03/2005	-13.81
175	21/03/2005	-14.02
178	24/03/2005	-12.54
179	25/03/2005	-14.87
182	28/03/2005	-13.39
183	29/03/2005	-15.19
184	30/03/2005	-14.23
186	01/04/2005	-12.43
188	03/04/2005	-12.54

192	07/04/2005	-13.81
194	09/04/2005	-13.60
195	10/04/2005	-15.29
199	14/04/2005	-13.92
200	15/04/2005	-13.39
201	16/04/2005	-15.61
204	19/04/2005	-12.65
205	20/04/2005	-14.97
206	21/04/2005	-16.35
207	22/04/2005	-12.54
209	24/04/2005	-17.94
210	25/04/2005	-15.19
211	26/04/2005	-13.92
214	29/04/2005	-15.71
216	01/05/2005	-17.09
219	04/05/2005	-15.29
221	06/05/2005	-15.71
224	09/05/2005	-14.76
227	12/05/2005	-15.50
229	14/05/2005	-17.83
230	15/05/2005	-17.20
231	16/05/2005	-13.49
232	17/05/2005	-15.82
233	18/05/2005	-18.36
234	19/05/2005	-15.29
239	24/05/2005	-15.71
242	27/05/2005	-16.88
244	29/05/2005	-17.94

---

---

Table C.2: Volume erupted for the 2004 eruption of St. Helens spanning 2004-2005 (Gerlach et al., 2008).

Day	Date	Volume extruded ( $\times 10^6 \text{ m}^3$ )
0	26/09/2004	0.00
8	04/10/2004	4.24
15	11/10/2004	9.02
17	13/10/2004	9.56
39	04/11/2004	19.73
64	29/11/2004	28.26
76	11/12/2004	32.03
99	04/01/2005	36.59
128	02/02/2005	40.69
148	22/02/2005	44.44
165	11/03/2005	46.83
205	20/04/2005	51.59



Table C.3: SO<sub>2</sub> measurements for the 2004 eruption of St. Helens spanning 2004-2005 (Gerlach et al., 2008).

Day	Date	SO2 (t/d)	SO2 (t)
1	27/09/2004	1	nan
3	29/09/2004	1	nan
4	30/09/2004	1	nan
5	01/10/2004	1	nan
7	03/10/2004	1	nan
8	04/10/2004	1	nan
11	07/10/2004	115	115
15	11/10/2004	70	370
17	13/10/2004	120	560
18	14/10/2004	148	694
24	20/10/2004	121	1501
31	27/10/2004	240	2764
39	04/11/2004	63	3976
45	10/11/2004	107	4486
47	12/11/2004	138	4732
55	20/11/2004	177	5993
82	17/12/2004	221	11370
99	03/01/2005	76	13893
120	24/01/2005	78	15509
135	08/02/2005	70	16619
152	25/02/2005	32	17485
165	10/03/2005	30	17888
207	21/04/2005	40	19347
212	26/04/2005	94	19681
241	25/05/2005	33	21522
256	09/06/2005	50	22145
290	13/07/2005	40	23675
304	27/07/2005	51	24312
320	12/08/2005	14	24832
339	31/08/2005	22	25174
367	28/09/2005	45	26112
387	18/10/2005	53	27092

409	09/11/2005	88	28643
422	22/11/2005	75	29702

---

## C.1 Supplementary References

1. Anderson, K., & Segall, P. (2013). Bayesian inversion of data from effusive volcanic eruptions using physics-based models: Application to Mount St. Helens 2004–2008. *Journal of Geophysical Research: Solid Earth*, 118(5), 2017-2037.
2. Gerlach, T. M., McGee, K. A., & Doukas, M. P. (2008). Emission rates of CO<sub>2</sub>, SO<sub>2</sub>, and H<sub>2</sub>S, scrubbing, and preeruption excess volatiles at Mount St. Helens, 2004-2005 (No. 1750-26, pp. 543-571). US Geological Survey.



# References

- Agee, C. B. (2008). Compressibility of water in magma and the prediction of density crossovers in mantle differentiation. *Philosophical Transactions of the Royal Society A: Mathematical, Physical and Engineering Sciences*, 366(1883):4239–4252.
- Aiuppa, A., Federico, C., Giudice, G., Giuffrida, G., Guida, R., Gurrieri, S., Liuzzo, M., Moretti, R., and Papale, P. (2009). The 2007 eruption of Stromboli volcano: Insights from real-time measurement of the volcanic gas plume CO<sub>2</sub>/SO<sub>2</sub> ratio. *Journal of Volcanology and Geothermal Research*, 182(3-4).
- Albino, F., Biggs, J., Lazecký, M., and Maghsoudi, Y. (2022). Routine Processing and Automatic Detection of Volcanic Ground Deformation Using Sentinel-1 InSAR Data: Insights from African Volcanoes. *Remote Sensing*, 14(22):5703.
- Albino, F., Biggs, J., and Syahbana, D. K. (2019). Dyke intrusion between neighbouring arc volcanoes re- sponsible for 2017 pre-eruptive seismic swarm at Agung, Bali. *Nature Communications*, 10(1):748.
- Alfano, F., Bonadonna, C., Volentik, A. C., Connor, C. B., Watt, S. F., Pyle, D. M., and Connor, L. J. (2011). Tephra stratigraphy and eruptive volume of the May, 2008, Chaitén eruption, Chile. *Bulletin of Volcanology*, 73(5):613–630.
- Allison, C. M., Roggensack, K., and Clarke, A. B. (2022). MafiCH: a general model for H<sub>2</sub>O–CO<sub>2</sub> solubility in mafic magmas. *Contributions to Mineralogy and Petrology*, 177(3):1–22.
- Amoruso, A. and Crescentini, L. (2009). Shape and volume change of pressurized ellipsoidal cavities from deformation and seismic data. *Journal of Geophysical Research*, 114(B2):B02210.

## REFERENCES

---

- Anantrasirichai, N., Biggs, J., Albino, F., and Bull, D. (2019). The Application of Convolutional Neural Networks to Detect Slow, Sustained Deformation in InSAR Time Series. *Geophysical Research Letters*, page 2019GL084993.
- Anantrasirichai, N., Biggs, J., Albino, F., Hill, P., and Bull, D. (2018). Application of Machine Learning to Classification of Volcanic Deformation in Routinely Generated InSAR Data. *Journal of Geophysical Research: Solid Earth*, 123(8):6592–6606.
- Anderson, A. T. (1995). CO<sub>2</sub> and the eruptibility of picrite and komatiite. *Lithos*, 34(1-3):19–25.
- Anderson, K. and Poland, M. P. (2016). Bayesian estimation of magma supply, storage, and eruption rates using a multiphysical volcano model: Kīlauea Volcano, 2000–2012. *Earth and Planetary Science Letters*, 447:161–171.
- Anderson, K. and Segall, P. (2011). Physics-based models of ground deformation and extrusion rate at effusively erupting volcanoes. *Journal of Geophysical Research: Solid Earth*, 116(7):1–20.
- Anderson, K. and Segall, P. (2013). Bayesian inversion of data from effusive volcanic eruptions using physics-based models: Application to Mount St. Helens 2004–2008. *Journal of Geophysical Research: Solid Earth*, 118(5):2017–2037.
- Asimow, P. D. (1998). Algorithmic modifications extending MELTS to calculate subsolidus phase relations. *American Mineralogist*, 83(9-10):1127–1132.
- Bachmann, O. and Bergantz, G. W. (2006). Gas percolation in upper-crustal silicic crystal mushes as a mechanism for upward heat advection and rejuvenation of near-solidus magma bodies. *Journal of Volcanology and Geothermal Research*, 149(1-2):85–102.
- Bagnardi, M. and Hooper, A. (2018). Inversion of Surface Deformation Data for Rapid Estimates of Source Parameters and Uncertainties: A Bayesian Approach. *Geochemistry, Geophysics, Geosystems*, 19(7):2194–2211.
- Baker, D. R., Freda, C., Brooker, R. A., and Scarlato, P. (2005). Volatile diffusion in silicate melts and its effects on melt inclusions. *Annals of Geophysics*, 48(4-5).
- Barry, P. H., Hilton, D. R., Füre, E., Halldórsson, S. A., and Grönvold, K. (2014). Carbon isotope and abundance systematics of Icelandic geothermal gases, fluids and subglacial basalts with implications for mantle plume-related CO<sub>2</sub> fluxes. *Geochimica et Cosmochimica Acta*, 134:74–99.

- Bato, M. G., Lundgren, P., Pinel, V., Solidum, R., Daag, A., and Cahulogan, M. (2021). The 2020 Eruption and Large Lateral Dike Emplacement at Taal Volcano, Philippines: Insights From Satellite Radar Data. *Geophysical Research Letters*, 48(7):e2021GL092803.
- Belousov, A., Belousova, M., Edwards, B., Volynets, A., and Melnikov, D. (2015). Overview of the precursors and dynamics of the 2012-13 basaltic fissure eruption of Tolbachik Volcano, Kamchatka, Russia. *Journal of Volcanology and Geothermal Research*, 307:22–37.
- Bemelmans, M. J., de Zeeuw-van Dalfsen, E., Poland, M. P., and Johanson, I. A. (2021). Insight into the May 2015 summit inflation event at Kīlauea Volcano, Hawai‘i. *Journal of Volcanology and Geothermal Research*, 415:107250.
- Biggs, J., Ebmeier, S. K., Aspinall, W. P., Lu, Z., Pritchard, M. E., Sparks, R. S., and Mather, T. A. (2014). Global link between deformation and volcanic eruption quantified by satellite imagery. *Nature Communications*, 5.
- Biggs, J. and Pritchard, M. E. (2017). Global volcano monitoring: What does it mean when volcanoes deform? *Elements*, 13(1):17–22.
- Biggs, J. and Wright, T. J. (2020). How satellite InSAR has grown from opportunistic science to routine monitoring over the last decade.
- Björnsson, H. and Einarsson, P. (1990). Volcanoes beneath Vatnajökull, Iceland: Evidence from radio echo-sounding, earthquakes and jökulhlaups. *Jökull*, 40:147–168.
- Blower, J. (2001). Factors controlling permeability-porosity relationships in magma. *Bulletin of Volcanology*, 63(7):497–504.
- Blundy, J., Cashman, K. V., Rust, A., and Witham, F. (2010). A case for CO<sub>2</sub>-rich arc magmas. *Earth and Planetary Science Letters*, 290(3-4):289–301.
- Boudreau, A. (2016). Bubble migration in a compacting crystal-liquid mush. *Contributions to Mineralogy and Petrology* 2016 171:4, 171(4):1–17.
- Brounce, M., Stolper, E., and Eiler, J. (2017). Redox variations in Mauna Kea lavas, the oxygen fugacity of the Hawaiian plume, and the role of volcanic gases in Earth’s oxygenation. *Proceedings of the National Academy of Sciences of the United States of America*, 114(34):8997–9002.

## REFERENCES

---

- Burgisser, A., Alletti, M., and Scaillet, B. (2015). Simulating the behavior of volatiles belonging to the C-O-H-S system in silicate melts under magmatic conditions with the software D-Compress. *Computers and Geosciences*.
- Burgisser, A., Chevalier, L., Gardner, J. E., and Castro, J. M. (2017). The percolation threshold and permeability evolution of ascending magmas. *Earth and Planetary Science Letters*, 470:37–47.
- Burgisser, A. and Degruyter, W. (2015). Magma Ascent and Degassing at Shallow Levels. *The Encyclopedia of Volcanoes*, pages 225–236.
- Cáceres, F., Scheu, B., Colombier, M., Hess, K. U., Feisel, Y., Ruthensteiner, B., and Dingwell, D. B. (2022). The roles of microlites and phenocrysts during degassing of silicic magma. *Earth and Planetary Science Letters*, 577:117264.
- Cáceres, F., Wadsworth, F. B., Scheu, B., Colombier, M., Madonna, C., Cimarelli, C., Hess, K. U., Kaliwoda, M., Ruthensteiner, B., and Dingwell, D. B. (2020). Can nanolites enhance eruption explosivity? *Geology*, 48(10):997–1001.
- Calder, E. S., Cole, P. D., Dade, W. B., Druitt, T. H., Hoblitt, R. P., Huppert, H. E., Ritchie, L., Sparks, R. S., and Young, S. R. (1999). Mobility of pyroclastic flows and surges at the Soufriere Hills Volcano, Montserrat. *Geophysical Research Letters*, 26(5):537–540.
- Cameron, C. E., Prejean, S. G., Coombs, M. L., Wallace, K. L., Power, J. A., and Roman, D. C. (2018). Alaska Volcano Observatory Alert and Forecasting Timeliness: 1989–2017. *Frontiers in Earth Science*, 0:86.
- Candela, P. (1997). A Review of Shallow, Ore-related Granites: Textures, Volatiles, and Ore Metals. *Journal of Petrology*, 38(12):1619–1633.
- Candela, P. and Piccoli, P. (1998). Magmatic Contributions to Hydrothermal Ore Deposits: An Algorithm (MVPart) for Calculating the Composition of the Magmatic Volatile Phase. *Techniques in Hydrothermal Ore Deposits Geology*.
- Carbone, D., Aloisi, M., Vinciguerra, S., and Puglisi, G. (2014). Stress, strain and mass changes at Mt. Etna during the period between the 1991-93 and 2001 flank eruptions.
- Carboni, E., Grainger, R., Walker, J., Dudhia, A., and Siddans, R. (2012). A new scheme for sulphur dioxide retrieval from IASI measurements: application to the Eyjafjallajökull eruption of April and May 2010. *Atmospheric Chemistry and Physics*, 12(23):11417–11434.

- Carboni, E., Grainger, R. G., Mather, T. A., Pyle, D. M., Thomas, G. E., Siddans, R., Smith, A. J., Dudhia, A., Koukouli, M. E., and Balis, D. (2016). The vertical distribution of volcanic SO<sub>2</sub> plumes measured by IASI. *Atmospheric Chemistry and Physics*, 16(7):4343–4367.
- Carn, S. A. (2016). On the detection and monitoring of effusive eruptions using satellite SO<sub>2</sub> measurements. *Geological Society Special Publication*, 426(1):277–292.
- Carn, S. A., Clarisse, L., and Prata, A. J. (2016). Multi-decadal satellite measurements of global volcanic degassing.
- Carn, S. A., Fioletov, V. E., McLinden, C. A., Li, C., and Krotkov, N. A. (2017). A decade of global volcanic SO<sub>2</sub> emissions measured from space. *Scientific Reports*, 7(1):1–12.
- Carrier, A., Got, J. L., Peltier, A., Ferrazzini, V., Staudacher, T., Kowalski, P., and Boissier, P. (2015). A damage model for volcanic edifices: Implications for edifice strength, magma pressure, and eruptive processes. *Journal of Geophysical Research: Solid Earth*, 120(1):567–583.
- Casas, A. S., Wadsworth, F. B., Ayris, P. M., Delmelle, P., Vasseur, J., Cimarelli, C., and Dingwell, D. B. (2019). SO<sub>2</sub> scrubbing during percolation through rhyolitic volcanic domes. *Geochimica et Cosmochimica Acta*, 257:150–162.
- Cashman, K. V. (2004). Volatile Controls on Magma Ascent and Eruption. *Geophysical Monograph Series*, 150:109–124.
- Cashman, K. V., Sparks, R. S. J., and Blundy, J. D. (2017). Vertically extensive and unstable magmatic systems: A unified view of igneous processes. *Science*, 355(6331).
- Cashman, K. V., Stephen, R., and Sparks, J. (2013). How volcanoes work: A 25 year perspective. *Bulletin of the Geological Society of America*, 125(5-6):664–690.
- Cashman, K. V., Thornber, C. R., and Pallister, J. S. (2008). From dome to dust: shallow crystallization and fragmentation of conduit magma during the 2004-2006 dome extrusion of Mount St. Helens, Washington. *US Geological Survey*, 1750(19):387–413.
- Cassidy, M., Manga, M., Cashman, K., and Bachmann, O. (2018). Controls on explosive-effusive volcanic eruption styles. *Nature Communications*, 9(1):2839.



## REFERENCES

---

- Castro, J. M., Schipper, C. I., Mueller, S. P., Militzer, A. S., Amigo, A., Parejas, C. S., and Jacob, D. (2013). Storage and eruption of near-liquidus rhyolite magma at Cordón Caulle, Chile. *Bulletin of Volcanology*, 75(4):1–17.
- Cervelli, P. F., Fournier, T. J., Freymueller, J. T., Power, J. A., Lisowski, M., and Pauk, B. A. (2010). Geodetic constraints on magma movement and withdrawal during the 2006 eruption of Augustine Volcano. *Professional Paper*, pages 427–452.
- Chaussard, E. and Amelung, F. (2014). Regional controls on magma ascent and storage in volcanic arcs. *Geochemistry, Geophysics, Geosystems*, 15(4):1407–1418.
- Chaussard, E., Amelung, F., and Aoki, Y. (2013). Characterization of open and closed volcanic systems in Indonesia and Mexico using InSAR time series. *Journal of Geophysical Research: Solid Earth*.
- Chiodini, G., Granieri, D., Avino, R., Caliro, S., Costa, A., and Werner, C. (2005). Carbon dioxide diffuse degassing and estimation of heat release from volcanic and hydro-thermal systems. *Journal of Geophysical Research: Solid Earth*, 110(B8):1–17.
- Christophersen, A., Behr, Y., and Miller, C. (2022). Automated Eruption Forecasting at Frequently Active Volcanoes Using Bayesian Networks Learned From Monitoring Data and Expert Elicitation: Application to Mt Ruapehu, Aotearoa, New Zealand. *Frontiers in Earth Science*, 10:1127.
- Collins, S. J., Pyle, D. M., and MacLennan, J. (2009). Melt inclusions track pre-eruption storage and dehydration of magmas at Etna. *Geology*, 37(6):571–574.
- Collombet, M., Burgisser, A., Colombier, M., and Gaunt, E. (2021). Evidence for deep gas loss in open volcanic systems. *Bulletin of Volcanology*, 83(2):1–16.
- Colombier, M., Bernard, B., Wright, H., Le Pennec, J. L., Cáceres, F., Cimorelli, C., Heap, M. J., Samaniego, P., Vasseur, J., and Dingwell, D. B. (2022). Conduit processes in crystal-rich dacitic magma and implications for eruptive cycles at Guagua Pichincha volcano, Ecuador. *Bulletin of Volcanology*, 84(12):1–23.
- Colombier, M., Vasseur, J., Houghton, B. F., Cáceres, F., Scheu, B., Kueppers, U., Thivet, S., Gurioli, L., Montanaro, C., Soldati, A., Di Muro, A., and Dingwell, D. B. (2021). Degassing and gas percolation in basaltic magmas. *Earth and Planetary Science Letters*, 573:117134.

- Colombier, M., Wadsworth, F. B., Gurioli, L., Scheu, B., Kueppers, U., Di Muro, A., and Dingwell, D. B. (2017). The evolution of pore connectivity in volcanic rocks. *Earth and Planetary Science Letters*, 462:99–109.
- Colombier, M., Wadsworth, F. B., Scheu, B., Vasseur, J., Dobson, K. J., Cáceres, F., Allabar, A., Marone, F., Schlepütz, C. M., and Dingwell, D. B. (2020). In situ observation of the percolation threshold in multiphase magma analogues. *Bulletin of Volcanology*, 82(4):1–15.
- Coltelli, M., d’Aranno, P. J., de Bonis, R., Tello, J. F., Marsella, M., Nardinocchi, C., Pecora, E., Proietti, C., Scifoni, S., Scutti, M., and Wahbeh, W. (2017). The Use of Surveillance Cameras for the Rapid Mapping of Lava Flows: An Application to Mount Etna Volcano. *Remote Sensing 2017, Vol. 9, Page 192*, 9(3):192.
- Coombs, M., Bull, K., Vallance, J., Schneider, D., Thoms, E., Wessels, R., and McGimsey, R. (2010). Timing, Distribution, and Volume of Proximal Products of the 2006 Eruption of Augustine Volcano. *The 2006 eruption of Augustine Volcano, Alaska: U.S. Geological Survey Professional Paper 1769*, pages 148–185.
- Coppola, D., Laiolo, M., Cigolini, C., Massimetti, F., Delle Donne, D., Ripepe, M., Arias, H., Barsotti, S., Parra, C. B., Centeno, R. G., Cevuard, S., Chigna, G., Chun, C., Garaebiti, E., Gonzales, D., Griswold, J., Juarez, J., Lara, L. E., López, C. M., Macedo, O., Mahinda, C., Ogburn, S., Prambada, O., Ramon, P., Ramos, D., Peltier, A., Saunders, S., de Zeeuw-van Dalfsen, E., Varley, N., and William, R. (2020). Thermal Remote Sensing for Global Volcano Monitoring: Experiences From the MIROVA System. *Frontiers in Earth Science*, 7:362.
- Coppola, D., Laiolo, M., Franchi, A., Massimetti, F., Cigolini, C., and Lara, L. E. (2017). Measuring effusion rates of obsidian lava flows by means of satellite thermal data. *Journal of Volcanology and Geothermal Research*, 347:82–90.
- Coppola, D., Macedo, O., Ramos, D., Finizola, A., Delle Donne, D., del Carpio, J., White, R., McCausland, W., Centeno, R., Rivera, M., Apaza, F., Ccallata, B., Chilo, W., Cigolini, C., Laiolo, M., Lazarte, I., Machaca, R., Masias, P., Ortega, M., Puma, N., and Taipe, E. (2015). Magma extrusion during the Ubinas 2013–2014 eruptive crisis based on satellite thermal imaging (MIROVA) and ground-based monitoring. *Journal of Volcanology and Geothermal Research*, 302:199–210.

## REFERENCES

---

- deGraffenried, R., Hammer, J., Dieterich, H., Perroy, R., Patrick, M., and Shea, T. (2021). Evaluating lava flow propagation models with a case study from the 2018 eruption of Kīlauea Volcano, Hawai'i. *Bulletin of Volcanology*, 83(11):1–19.
- Degruyter, W., Bachmann, O., Burgisser, A., and Manga, M. (2012). The effects of outgassing on the transition between effusive and explosive silicic eruptions. *Earth and Planetary Science Letters*, 349-350:161–170.
- Delgado, F. (2021). Rhyolitic volcano dynamics in the Southern Andes: Contributions from 17 years of InSAR observations at Cordón Caulle volcano from 2003 to 2020. *Journal of South American Earth Sciences*, 106:102841.
- Delgado, F., Kubanek, J., Anderson, K., Lundgren, P., and Pritchard, M. (2019). Physico-chemical models of effusive rhyolitic eruptions constrained with InSAR and DEM data: A case study of the 2011-2012 Cordón Caulle eruption. *Earth and Planetary Science Letters*, 524:115736.
- Delgado, F., Pritchard, M. E., Ebmeier, S., González, P., and Lara, L. (2017). Recent unrest (2002–2015) imaged by space geodesy at the highest risk Chilean volcanoes: Villarrica, Llaima, and Calbuco (Southern Andes). *Journal of Volcanology and Geothermal Research*, 344:270–288.
- Delmelle, P., Maters, E. C., Calkins, J. A., Gaspard, F., Opfergelt, S., and Jenkins, S. F. (2021). Eruptive style controls the formation of silicon hexafluoride salts on volcanic ash: The case of the 2010 eruption of Eyjafjallajökull volcano, Iceland. *Chemical Geology*, 579.
- Dieterich, J. H. and Decker, R. W. (1975). Finite element modeling of surface deformation associated with volcanism. *Journal of Geophysical Research*, 80(29):4094–4102.
- Ding, S., Plank, T., Wallace, P. J., and Rasmussen, D. J. (2023). Sulfur\_X: A Model of Sulfur Degassing During Magma Ascent. *Geochemistry, Geophysics, Geosystems*, 24(4):e2022GC010552.
- Dixon, J. E. and Clague, D. A. (2001). Volatiles in Basaltic Glasses from Loihi Seamount, Hawaii: Evidence for a Relatively Dry Plume Component. *Journal of Petrology*, 42(3):627–654.

- Dixon, J. E., Stolper, E. M., Holloway, J. R., and Science, A. (1995). An Experimental Study of Water and Carbon Dioxide Solubilities in Mid-Ocean Ridge Basaltic Liquids. Part II: Applications to Degassing. *Journal of Petrology*, 3.
- Donovan, A., Blundy, J., Oppenheimer, C., and Buisman, I. (2018). The 2011 eruption of Nabro volcano, Eritrea: perspectives on magmatic processes from melt inclusions. *Contributions to Mineralogy and Petrology*, 173(1):1–23.
- Dualeh, E. W., Ebmeier, S. K., Wright, T. J., Poland, M. P., Grandin, R., Stinton, A. J., Camejo-Harry, M., Esse, B., and Burton, M. (2023). Rapid pre-explosion increase in dome extrusion rate at La Soufrière, St. Vincent quantified from synthetic aperture radar backscatter. *Earth and Planetary Science Letters*, 603:117980.
- Duan, X. (2014). A general model for predicting the solubility behavior of H<sub>2</sub>O-CO<sub>2</sub> fluids in silicate melts over a wide range of pressure, temperature and compositions. *Geochimica et Cosmochimica Acta*, 125:582–609.
- Duan, Z. and Zhang, Z. (2006). Equation of state of the H<sub>2</sub>O, CO<sub>2</sub>, and H<sub>2</sub>O–CO<sub>2</sub> systems up to 10 GPa and 2573.15 K: Molecular dynamics simulations with ab initio potential surface. *Geochimica et Cosmochimica Acta*, 70(9):2311–2324.
- Dzurisin, D., Moran, S. C., Lisowski, M., Schilling, S. P., Anderson, K. R., and Werner, C. (2015). The 2004–2008 dome-building eruption at Mount St. Helens, Washington: epilogue. *Bulletin of Volcanology*, 77(10):1–17.
- Ebmeier, S. K., Andrews, B. J., Araya, M. C., Arnold, D. W. D., Biggs, J., Cooper, C., Cottrell, E., Furtney, M., Hickey, J., Jay, J., Lloyd, R., Parker, A. L., Pritchard, M. E., Robertson, E., Venzke, E., and Williamson, J. L. (2018). Synthesis of global satellite observations of magmatic and volcanic deformation: implications for volcano monitoring & the lateral extent of magmatic domains. *Journal of Applied Volcanology*, 7(1):1–26.
- Ebmeier, S. K., Biggs, J., Mather, T. A., and Amelung, F. (2013a). Applicability of InSAR to tropical volcanoes: insights from Central America. *Geological Society, London, Special Publications*.
- Ebmeier, S. K., Biggs, J., Mather, T. A., and Amelung, F. (2013b). On the lack of InSAR observations of magmatic deformation at Central American volcanoes.
- Ebmeier, S. K., Elliott, J. R., Nocquet, J. M., Biggs, J., Mothes, P., Jarrín, P., Yépez, M., Aguaiza, S., Lundgren, P., and Samsonov, S. V. (2016). Shallow earthquake inhibits

## REFERENCES

---

- unrest near Chiles–Cerro Negro volcanoes, Ecuador–Colombian border. *Earth and Planetary Science Letters*, 450:283–291.
- Edmonds, M. (2021). Geochemical monitoring of volcanoes and the mitigation of volcanic gas hazards. *Forecasting and Planning for Volcanic Hazards, Risks, and Disasters*, pages 117–151.
- Edmonds, M., Cashman, K. V., Holness, M., and Jackson, M. (2019). Architecture and dynamics of magma reservoirs. *Philosophical Transactions of the Royal Society A: Mathematical, Physical and Engineering Sciences*, 377(2139).
- Edmonds, M., Humphreys, M. C., Hauri, E. H., Herd, R. A., Wadge, G., Rawson, H., Ledden, R., Plail, M., Barclay, J., Aiuppa, A., Christopher, T. E., Giudice, G., and Guida, R. (2014). Pre-eruptive vapour and its role in controlling eruption style and longevity at Soufrière Hills Volcano. *Geological Society Memoir*, 39(1):291–315.
- Edmonds, M., Mather, T. A., and Liu, E. J. (2018). A distinct metal fingerprint in arc volcanic emissions. *Nature Geoscience*, 11(10):790–794.
- Edmonds, M. and Wallace, P. J. (2017). Volatiles and exsolved vapor in volcanic systems.
- Edmonds, M. and Woods, A. W. (2018). Exsolved volatiles in magma reservoirs. *Journal of Volcanology and Geothermal Research*, 368:13–30.
- Eguchi, J. and Dasgupta, R. (2018). A CO<sub>2</sub> solubility model for silicate melts from fluid saturation to graphite or diamond saturation. *Chemical Geology*, 487:23–38.
- Esse, B., Burton, M., Hayer, C., Contreras-Arratia, R., Christopher, T., Joseph, E. P., Varnam, M., and Johnson, C. (2024). SO<sub>2</sub> emissions during the 2021 eruption of La Soufrière, St Vincent, revealed with back-trajectory analysis of TROPOMI imagery. *Geological Society, London, Special Publications*, 539(1).
- Fialko, Y., Simons, M., and Agnew, D. (2001). The complete (3-D) surface displacement field in the epicentral area of the 1999 Mw 7.1 Hector Mine earthquake, California, from space geodetic observations. *Geophysical Research Letters*, 28(16):3063–3066.
- Fiege, A., Holtz, F., Behrens, H., Mandeville, C. W., Shimizu, N., Crede, L. S., and Göttlicher, J. (2015). Experimental investigation of the S and S-isotope distribution between H<sub>2</sub>O–S ± Cl fluids and basaltic melts during decompression. *Chemical Geology*, 393-394:36–54.

- Fournier, T. J., Pritchard, M. E., and Riddick, S. N. (2010). Duration, magnitude, and frequency of subaerial volcano deformation events: New results from Latin America using InSAR and a global synthesis. *Geochemistry, Geophysics, Geosystems*, 11(1).
- Furtney, M. A., Pritchard, M. E., Biggs, J., Carn, S. A., Ebmeier, S. K., Jay, J. A., McCormick Kilbride, B. T., and Reath, K. A. (2018). Synthesizing multi-sensor, multi-satellite, multi-decadal datasets for global volcano monitoring. *Journal of Volcanology and Geothermal Research*, 365:38–56.
- Gaillard, F. and Scaillet, B. (2014). A theoretical framework for volcanic degassing chemistry in a comparative planetology perspective and implications for planetary atmospheres. *Earth and Planetary Science Letters*, 403:307–316.
- Galetto, F., Pritchard, M. E., Hornby, A. J., Gazel, E., and Mahowald, N. M. (2023). Spatial and Temporal Quantification of Subaerial Volcanism From 1980 to 2019: Solid Products, Masses, and Average Eruptive Rates. *Reviews of Geophysics*, 61(1):e2022RG000783.
- Gardner, J. E. (2009). The impact of pre-existing gas on the ascent of explosively erupted magma. *Bulletin of Volcanology*, 71(8):835–844.
- Ge, C., Wang, J., Carn, S., Yang, K., Ginoux, P., and Krotkov, N. (2016). Satellite-based global volcanic SO<sub>2</sub> emissions and sulfate direct radiative forcing during 2005-2012. *Journal of Geophysical Research*, 121(7):3446–3464.
- Geist, D. J., Harpp, K. S., Naumann, T. R., Poland, M., Chadwick, W. W., Hall, M., and Rader, E. (2008). The 2005 eruption of Sierra Negra volcano, Galápagos, Ecuador. *Bulletin of Volcanology*, 70(6):655–673.
- Gennaro, E., Paonita, A., Iacono-Marziano, G., Moussallam, Y., Pichavant, M., Peters, N., and Martel, C. (2020). Sulphur behaviour and redox conditions in etnean magmas during magma differentiation and degassing. *Journal of Petrology*, 61(10).
- Gerlach, T. M., Delgado, H., McGee, K. A., Doukas, M. P., Venegas, J. J., and Cárdenas, L. (1997). Application of the LI-COR CO<sub>2</sub> analyzer to volcanic plumes: A case study, volcán Popocatepetl, Mexico, June 7 and 10, 1995. *Journal of Geophysical Research: Solid Earth*, 102(B4):8005–8019.
- Gerlach, T. M., McGee, K. A., and Doukas, M. P. (2008). Emission rates of CO<sub>2</sub>, SO<sub>2</sub>, and H<sub>2</sub>S, scrubbing, and preeruption excess volatiles at Mount St. Helens, 2004-2005. A

## REFERENCES

---

- volcano rekindled: the renewed eruption of Mount St. Helens, 2004-2006 (No. 1750-26)*, pages 543–571.
- Gerlach, T. M., Mcgee, K. A., Elias, T., Sutton, A. J., Doukas, M. P., Mcgee, T. A., Elias, A. J., and Sutton, M. P. (2002). Carbon dioxide emission rate of Kīlauea Volcano: Implications for primary magma and the summit reservoir. *Journal of Geophysical Research: Solid Earth*, 107(B9):3–1.
- Gerlach, T. M., Westrich, H. R., Casadevall, T. J., and Finnegan, D. L. (1994). Vapor saturation and accumulation in magmas of the 1989-1990 eruption of Redoubt Volcano, Alaska. *Journal of Volcanology and Geothermal Research*, 62(1-4):317–337.
- Ghiorso, M. S. and Sack, R. O. (1995). Chemical mass transfer in magmatic processes IV. A revised and internally consistent thermodynamic model for the interpolation and extrapolation of liquid-solid equilibria in magmatic systems at elevated temperatures and pressures. *Contributions to Mineralogy and Petrology*, 119(2-3):197–212.
- Girona, T., Costa, F., Newhall, C., and Taisne, B. (2014). On depressurization of volcanic magma reservoirs by passive degassing. *Journal of Geophysical Research: Solid Earth*, 119(12):8667–8687.
- Global Volcanism Program (2013). Volcanoes of the World.
- Gonnermann, H. M. and Manga, M. (2006). The Fluid Mechanics Inside a Volcano. <https://doi.org/10.1146/annurev.fluid.39.050905.110207>, 39:321–356.
- Gottsmann, J., Biggs, J., Lloyd, R., Biranhu, Y., and Lewi, E. (2020). Ductility and compressibility accommodate high magma flux beneath a silicic continental rift caldera: Insights from Corbetti caldera (Ethiopia). *Geochemistry, Geophysics, Geosystems*, 21(4):e2020GC008952.
- Greiner, S. H. M. and Geirsson, H. (2021). An elastic 3D Finite-Element-Model for Grímsvötn, Iceland. *EGU General Assembly 2021, online*.
- Grémion, S., Pinel, V., Shreve, T., Beauducel, F., Putra, R., Solikhin, A., Santoso, A. B., and Humaida, H. (2023). Tracking the evolution of the summit lava dome of Merapi volcano between 2018 and 2019 using DEMs derived from TanDEM-X and Pléiades data. *Journal of Volcanology and Geothermal Research*, 433:107732.

- Gualda, G. A., Ghiorso, M. S., Lemons, R. V., and Carley, T. L. (2012). Rhyolite-MELTS: a Modified Calibration of MELTS Optimized for Silica-rich, Fluid-bearing Magmatic Systems. *Journal of Petrology*, 53(5):875–890.
- Gudmundsson, A. (2005). The effects of layering and local stresses in composite volcanoes on dyke emplacement and volcanic hazards. *Comptes Rendus - Geoscience*, 337(13):1216–1222.
- Gudmundsson, A. (2008). Chapter 8 Magma-Chamber Geometry, Fluid Transport, Local Stresses and Rock Behaviour During Collapse Caldera Formation.
- Gudmundsson, A. (2012). Magma chambers: Formation, local stresses, excess pressures, and compartments. *Journal of Volcanology and Geothermal Research*, 237-238:19–41.
- Haddadi, B., Sigmarsson, O., and Larsen, G. (2017). Magma storage beneath Grímsvötn volcano, Iceland, constrained by clinopyroxene-melt thermobarometry and volatiles in melt inclusions and groundmass glass. *Journal of Geophysical Research: Solid Earth*, 122(9):6984–6997.
- Hamling, I. J., Cevuard, S., and Garaebiti, E. (2019). Large-Scale Drainage of a Complex Magmatic System: Observations From the 2018 Eruption of Ambrym Volcano, Vanuatu. *Geophysical Research Letters*, 46(9):4609–4617.
- Hautmann, S., Gottsmann, J., Sparks, R. S. J., Mattioli, G. S., Sacks, I. S., and Strutt, M. H. (2010). Effect of mechanical heterogeneity in arc crust on volcano deformation with application to Soufrière Hills Volcano, Montserrat, West Indies. *Journal of Geophysical Research: Solid Earth*, 115(B9):9203.
- Head, M., Hickey, J., Gottsmann, J., and Fournier, N. (2019). The Influence of Viscoelastic Crustal Rheologies on Volcanic Ground Deformation: Insights From Models of Pressure and Volume Change. *Journal of Geophysical Research: Solid Earth*, 124(8):8127–8146.
- Heap, M. J., Villeneuve, M., Albino, F., Farquharson, J. I., Brothelande, E., Amelung, F., Got, J. L., and Baud, P. (2020). Towards more realistic values of elastic moduli for volcano modelling. *Journal of Volcanology and Geothermal Research*, 390:106684.
- Hickey, J., Gottsmann, J., and Del Potro, R. (2013). The large-scale surface uplift in the Altiplano-Puna region of Bolivia: A parametric study of source characteristics and crustal rheology using finite element analysis. *Geochemistry, Geophysics, Geosystems*, 14(3):540–555.



## REFERENCES

---

- Holloway, J. R. and Blank, J. G. (1994). Chapter 6. APPLICATION OF EXPERIMENTAL RESULTS TO C-O-H SPECIES IN NATURAL MELTS. *Volatiles in Magmas*, pages 187–230.
- Hotta, K., Iguchi, M., Ohkura, T., Hendrasto, M., Gunawan, H., Rosadi, U., and Kriswati, E. (2019). Magma intrusion and effusion at Sinabung volcano, Indonesia, from 2013 to 2016, as revealed by continuous GPS observation. *Journal of Volcanology and Geothermal Research*, 382:173–183.
- Hreinsdóttir, S., Sigmundsson, F., Roberts, M. J., Björnsson, H., Grapenthin, R., Arason, P., Árnadóttir, T., Hólmjárn, J., Geirsson, H., Bennett, R. A., Gudmundsson, M. T., Oddsson, B., Ófeigsson, B. G., Villemin, T., Jónsson, T., Sturkell, E., Höskuldsson, A., Larsen, G., Thordarson, T., and Óladóttir, B. A. (2014). Volcanic plume height correlated with magma-pressure change at Grímsvötn Volcano, Iceland. *Nature Geoscience*, 7(3):214–218.
- Huber, C., Townsend, M., Degruyter, W., and Bachmann, O. (2019). Optimal depth of subvolcanic magma chamber growth controlled by volatiles and crust rheology. *Nature Geoscience*, 12(9):762–768.
- Hughes, E. C., Ding, S., Iacovino, K., Wieser, P. E., and Kilgour, G. (2023a). Workshop report: Modelling volatile behaviour in magmas. Technical report.
- Hughes, E. C., Saper, L. M., Liggins, P., O'Neill, H. S. C., and Stolper, E. M. (2023b). The sulfur solubility minimum and maximum in silicate melt. *Journal of the Geological Society*, 180(3).
- Huppert, H. E. and Woods, A. W. (2002). The role of volatiles in magma chamber dynamics. *Nature*, 420(6915):493–495.
- Hurwitz, S. and Anderson, K. (2019). Temporal Variations in Scrubbing of Magmatic Gases at the Summit of Kīlauea Volcano, Hawai‘i. *Geophysical Research Letters*, 46(24):14469–14476.
- Hurwitz, S. and Navon, O. (1994). Bubble nucleation in rhyolitic melts: Experiments at high pressure, temperature, and water content. *Earth and Planetary Science Letters*, 122(3-4):267–280.
- Hutchison, W., Biggs, J., Mather, T. A., Pyle, D. M., Lewi, E., Yirgu, G., Caliro, S., Chiodini, G., Clor, L. E., and Fischer, T. P. (2016). Causes of unrest at silicic calderas in the East

- African Rift: New constraints from InSAR and soil-gas chemistry at Aluto volcano, Ethiopia. *Geochemistry, Geophysics, Geosystems*, 17(8):3008–3030.
- Iverson, R. M., Dzurisin, D., Gardner, C. A., Gerlach, T. M., LaHusen, R. G., Lisowski, M., Major, J. J., Malone, S. D., Messerich, J. A., Moran, S. C., Pallister, J. S., Qamar, A. I., Schilling, S. P., and Vallance, J. W. (2006). Dynamics of seismogenic volcanic extrusion at Mount St Helens in 2004–05. *Nature* 2006 444:7118, 444(7118):439–443.
- Jaupart, C. and Allègre, C. J. (1991). Gas content, eruption rate and instabilities of eruption regime in silicic volcanoes. *Earth and Planetary Science Letters*, 102(3-4):413–429.
- Jay, J., Costa, F., Pritchard, M., Lara, L., Singer, B., and Herrin, J. (2014). Locating magma reservoirs using InSAR and petrology before and during the 2011–2012 Cordón Caulle silicic eruption. *Earth and Planetary Science Letters*, 395:254–266.
- Jiang, Y. and González, P. J. (2020). Bayesian Inversion of Wrapped Satellite Interferometric Phase to Estimate Fault and Volcano Surface Ground Deformation Models. *Journal of Geophysical Research: Solid Earth*, 125(5):e2019JB018313.
- Johnson, D. J., Sigmundsson, F., and Delaney, P. T. (2000). Comment on. *Bulletin of Volcanology* 2000 61:7, 61(7):491–493.
- Johnson, M. C., Anderson, A. T., and Rutherford, M. J. (1994). Pre-eruptive volatile contents of magmas. *Reviews in Mineralogy and Geochemistry*, 30(1):281–330.
- Joseph, E. P., Camejo-Harry, M., Christopher, T., Contreras-Arratia, R., Edwards, S., Graham, O., Johnson, M., Juman, A., Latchman, J. L., Lynch, L., Miller, V. L., Papadopoulos, I., Pascal, K., Robertson, R., Ryan, G. A., Stinton, A., Grandin, R., Hamling, I., Jo, M. J., Barclay, J., Cole, P., Davies, B. V., and Sparks, R. S. (2022). Responding to eruptive transitions during the 2020–2021 eruption of La Soufrière volcano, St. Vincent. *Nature Communications* 2022 13:1, 13(1):1–15.
- Kilbride, B. M. C., Edmonds, M., and Biggs, J. (2016). Observing eruptions of gas-rich compressible magmas from space. *Nature Communications*, 7(1):1–8.
- Koleszar, A. M., Kent, A. J., Wallace, P. J., and Scott, W. E. (2012). Controls on long-term low explosivity at andesitic arc volcanoes: Insights from Mount Hood, Oregon. *Journal of Volcanology and Geothermal Research*, 219-220:1–14.

## REFERENCES

---

- Konecke, B. A., Fiege, A., Simon, A. C., Linsler, S., and Holtz, F. (2019). An experimental calibration of a sulfur-in-apatite oxybarometer for mafic systems. *Geochimica et Cosmochimica Acta*, 265:242–258.
- Kubaneck, J., Poland, M. P., and Biggs, J. (2021). Applications of bistatic radar to volcano topography—a review of ten years of TanDEM-X. *IEEE Journal of Selected Topics in Applied Earth Observations and Remote Sensing*, 14:3282–3302.
- Kushnir, A. R., Martel, C., Champallier, R., and Arbaret, L. (2017). In situ confirmation of permeability development in shearing bubble-bearing melts and implications for volcanic outgassing. *Earth and Planetary Science Letters*, 458:315–326.
- La Spina, G., Arzilli, F., Burton, M. R., Polacci, M., and Clarke, A. B. (2022). Role of volatiles in highly explosive basaltic eruptions. *Communications Earth & Environment* 2022 3:1, 3(1):1–13.
- Lara, L. E., Naranjo, J. A., and Moreno, H. (2004). Rhyodacitic fissure eruption in Southern Andes (Cordón Caulle; 40.5°S) after the 1960 (Mw:9.5) Chilean earthquake: a structural interpretation. *Journal of Volcanology and Geothermal Research*, 138(1-2):127–138.
- Laumonier, M., Arbaret, L., Burgisser, A., and Champallier, R. (2011). Porosity redistribution enhanced by strain localization in crystal-rich magmas. *Geology*, 39(8):715–718.
- Lazecky, M., Spaans, K., González, P. J., Maghsoudi, Y., Morishita, Y., Albino, F., Elliott, J., Greenall, N., Hatton, E., Hooper, A., Juncu, D., McDougall, A., Walters, R. J., Watson, C. S., Weiss, J. R., and Wright, T. J. (2020). LiCSAR: An Automatic InSAR Tool for Measuring and Monitoring Tectonic and Volcanic Activity. *Remote Sensing* 2020, Vol. 12, Page 2430, 12(15):2430.
- Lechner, P., Tupper, A., Guffanti, M., Loughlin, S., and Casadevall, T. (2018). Volcanic Ash and Aviation—The Challenges of Real-Time, Global Communication of a Natural Hazard. *Advances in Volcanology*, pages 51–64.
- Lesage, P., Carrara, A., Pinel, V., and Arámbula-Mendoza, R. (2018). Absence of Detectable Precursory Deformation and Velocity Variation Before the Large Dome Collapse of July 2015 at Volcán de Colima, Mexico. *Frontiers in Earth Science*, 6:93.

- Liggins, P., Jordan, S., Rimmer, P. B., and Shorttle, O. (2022). Growth and Evolution of Secondary Volcanic Atmospheres: I. Identifying the Geological Character of Hot Rocky Planets. *Journal of Geophysical Research: Planets*, 127(7):e2021JE007123.
- Liggins, P., Shorttle, O., and Rimmer, P. B. (2020). Can volcanism build hydrogen-rich early atmospheres? *Earth and Planetary Science Letters*, 550:116546.
- Lindoo, A., Larsen, J. F., Cashman, K. V., and Oppenheimer, J. (2017). Crystal controls on permeability development and degassing in basaltic andesite magma. *Geology*, 45(9):831–834.
- Lisowski, M., Dzurisin, D., Denlinger, R. P., and Iwatsubo, E. Y. (2008). Analysis of GPS-measured deformation associated with the 2004-2006 dome-building eruption of Mount St. Helens, Washington. *A volcano rekindled: the renewed eruption of Mount St. Helens, 2004-2006 (No. 1750-15)*, pages 301–333.
- Liu, E. J., Aiuppa, A., Alan, A., Arellano, S., Bitetto, M., Bobrowski, N., Carn, S., Clarke, R., Corrales, E., de Moor, J. M., Diaz, J. A., Edmonds, M., Fischer, T. P., Freer, J., Fricke, G. M., Galle, B., Gerdes, G., Giudice, G., Gutmann, A., Hayer, C., Itikarai, I., Jones, J., Mason, E., McCormick Kilbride, B. T., Mulina, K., Nowicki, S., Rahilly, K., Richardson, T., Rüdiger, J., Schipper, C. I., Watson, I. M., and Wood, K. (2020). Aerial strategies advance volcanic gas measurements at inaccessible, strongly degassing volcanoes. *Science Advances*, 6(44):eabb9103.
- Loughlin, S. C., Sparks, R. S. J., Sparks, S., Brown, S. K., Jenkins, S. F., and Vye-Brown, C. (2015). *Global volcanic hazards and risk*. Cambridge University Press.
- Lowenstern, J. B. (1994). Dissolved volatile concentrations in an ore-forming magma. *Geology*, 22(10):893–896.
- Manley, G. F., Mather, T. A., Pyle, D. M., Clifton, D. A., Rodgers, M., Thompson, G., and Roman, D. C. (2021). Machine Learning Approaches to Identifying Changes in Eruptive State Using Multi-Parameter Datasets From the 2006 Eruption of Augustine Volcano, Alaska. *Journal of Geophysical Research: Solid Earth*, 126(12):e2021JB022323.
- Marty, B. and Zimmermann, L. (1999). Volatiles (He, C, N, Ar) in mid-ocean ridge basalts: assesment of shallow-level fractionation and characterization of source composition. *Geochimica et Cosmochimica Acta*, 63(21):3619–3633.

## REFERENCES

---

- Masterlark, T. (2003). Finite element model predictions of static deformation from dislocation sources in a subduction zone: Sensitivities to homogeneous, isotropic, Poisson-solid, and half-space assumptions. *Journal of Geophysical Research: Solid Earth*, 108(B11):2540.
- Mastin, L. G., Lisowski, M., Roeloffs, E., and Beeler, N. (2009). Improved constraints on the estimated size and volatile content of the Mount St. Helens magma system from the 2004–2008 history of dome growth and deformation. *Geophysical Research Letters*, 36(20).
- Mastin, L. G., Roeloffs, E., Beeler, N. M., and Quick, J. E. (2008). Constraints on the size, overpressure, and volatile content of the Mount St. Helens magma system from geodetic and dome-growth measurements during the 2004-2006+ eruption. *A volcano rekindled: the renewed eruption of Mount St. Helens, 2004-2006 (No. 1750)*, pages 461–488.
- Matjuschkin, V., Blundy, J. D., and Brooker, R. A. (2016). The effect of pressure on sulphur speciation in mid- to deep-crustal arc magmas and implications for the formation of porphyry copper deposits. *Contributions to Mineralogy and Petrology* 171:7, 171(7):1–25.
- McGee, K. A., Doukas, M. P., McGimsey, R. G., Neal, C. A., and Wessels, R. L. (2010). Emission of SO<sub>2</sub>, CO<sub>2</sub>, and H<sub>2</sub>S from Augustine Volcano, 2002-2008: Chapter 26 in The 2006 eruption of Augustine Volcano, Alaska. *The 2006 eruption of Augustine Volcano, Alaska: U.S. Geological Survey Professional Paper 1769*, pages 609–627.
- McKee, K., Smith, C. M., Reath, K., Snee, E., Maher, S., Matoza, R. S., Carn, S., Mastin, L., Anderson, K., Damby, D., Roman, D. C., Degterev, A., Rybin, A., Chibisova, M., Assink, J. D., de Negri Leiva, R., and Perttu, A. (2021). Evaluating the state-of-the-art in remote volcanic eruption characterization Part I: Raikoke volcano, Kuril Islands. *Journal of Volcanology and Geothermal Research*, 419:107354.
- Melnik, O., Barmin, A. A., and Sparks, R. S. J. (2005). Dynamics of magma flow inside volcanic conduits with bubble overpressure buildup and gas loss through permeable magma. *Journal of Volcanology and Geothermal Research*, 143(1-3):53–68.
- Melnik, O. and Sparks, R. S. (1999). Nonlinear dynamics of lava dome extrusion. *Nature* 1999 402:6757, 402(6757):37–41.

- Métrich, N. and Wallace, P. J. (2008). Volatile abundances in basaltic magmas and their degassing paths tracked by melt inclusions. *Reviews in Mineralogy and Geochemistry*, 69(1):363–402.
- Mogi, K. (1958). Relations between the eruptions of various volcanoes and the deformations of the ground surfaces around them. *Bulletin of the Earthquake Research Institute*, 36:99–134.
- Morales Rivera, A. M., Amelung, F., and Mothes, P. (2016). Volcano deformation survey over the Northern and Central Andes with ALOS InSAR time series. *Geochemistry, Geophysics, Geosystems*, 17(7):2869–2883.
- Moran, S. C., Kwoun, O., Masterlark, T., and Lu, Z. (2006). On the absence of InSAR-detected volcano deformation spanning the 1995–1996 and 1999 eruptions of Shishaldin Volcano, Alaska. *Journal of Volcanology and Geothermal Research*, 150(1-3):119–131.
- Moran, S. C., Malone, S. D., Qamar, A. I., Thelen, W. A., Wright, A. K., and Caplan-Auerbach, J. (2008). Seismicity associated with renewed dome building at Mount St. Helens, 2004-2005. *Professional Paper*, pages 27–60.
- Mori, T. and Burton, M. (2006). The SO<sub>2</sub> camera: A simple, fast and cheap method for ground-based imaging of SO<sub>2</sub> in volcanic plumes. *Geophysical Research Letters*, 33(24).
- Morishita, Y., Lazecky, M., Wright, T. J., Weiss, J. R., Elliott, J. R., and Hooper, A. (2020). LiCSBAS: An Open-Source InSAR Time Series Analysis Package Integrated with the LiCSAR Automated Sentinel-1 InSAR Processor. *Remote Sensing 2020, Vol. 12, Page 424*, 12(3):424.
- Moussallam, Y., Rose-Koga, E. F., Koga, K. T., Médard, E., Bani, P., Devidal, J. L., and Tari, D. (2019). Fast ascent rate during the 2017–2018 Plinian eruption of Ambae (Aoba) volcano: a petrological investigation. *Contributions to Mineralogy and Petrology*, 174(11):1–24.
- Mullet, B. and Segall, P. (2022). The surface deformation signature of a transcrustal, crystal mush-dominant magma system. *Journal of Geophysical Research: Solid Earth*, page e2022JB024178.
- Naismith, A. K., Matthew Watson, I., Escobar-Wolf, R., Chigna, G., Thomas, H., Coppola, D., and Chun, C. (2019). Eruption frequency patterns through time for the current

## REFERENCES

---

- (1999–2018) activity cycle at Volcán de Fuego derived from remote sensing data: Evidence for an accelerating cycle of explosive paroxysms and potential implications of eruptive activity. *Journal of Volcanology and Geothermal Research*, 371:206–219.
- Nash, W. M., Smythe, D. J., and Wood, B. J. (2019). Compositional and temperature effects on sulfur speciation and solubility in silicate melts. *Earth and Planetary Science Letters*, 507:187–198.
- Neal, C. A., Brantley, S. R., Antolik, L., Babb, J. L., and Etc (2019). The 2018 rift eruption and summit collapse of Kīlauea Volcano. *Science*, 363(January):367–374.
- Newhall, C. G. (2007). Volcanology 101 for seismologists. In Schubert, G. and Kanamori, H., editors, *Treatise on Geophysics*, pages 351–388, Amsterdam, The Netherlands. Elsevier.
- Ohmoto, H. and Kerrick, D. M. (1977). Devolatilization equilibria in graphitic systems. *American Journal of Science*, 277(8):1013–1044.
- Okada, Y. (1985). SURFACE DEFORMATION DUE TO SHEAR AND TENSILE FAULTS IN A HALF-SPACE. *Bulletin of the Seismological Society of America*, 75(4):1135–1154.
- O'Neill, H. S. (2021). The Thermodynamic Controls on Sulfide Saturation in Silicate Melts with Application to Ocean Floor Basalts. *Magma Redox Geochemistry*, pages 177–213.
- O'Neill, H. S. C. and Mavrogenes, J. A. (2022). The sulfate capacities of silicate melts. *Geochimica et Cosmochimica Acta*, 334:368–382.
- Oppenheimer, J., Rust, A. C., Cashman, K. V., and Sandnes, B. (2015). Gas migration regimes and outgassing in particle-rich suspensions. *Frontiers in Physics*, 0(AUG):60.
- Pallister, J. S., Schneider, D. J., Griswold, J. P., Keeler, R. H., Burton, W. C., Noyles, C., Newhall, C. G., and Ratdomopurbo, A. (2013). Merapi 2010 eruption—Chronology and extrusion rates monitored with satellite radar and used in eruption forecasting. *Journal of Volcanology and Geothermal Research*, 261:144–152.
- Pallister, J. S., Thornber, C. R., Cashman, K. V., Clyne, M. A., Lowers, H., Mandeville, C. W., Brownfield, I. K., and Meeker, G. P. (2008). Petrology of the 2004–2006 Mount St. Helens lava dome – implications for magmatic plumbing and eruption triggering. *US Geological Survey*, 1750(30):647–702.

- Papale, P. (1999). Modeling of the solubility of a two-component H<sub>2</sub>O + CO<sub>2</sub> fluid in silicate liquids. *American Mineralogist*, 84(4):477–492.
- Papale, P. (2005). Determination of total H<sub>2</sub>O and CO<sub>2</sub> budgets in evolving magmas from melt inclusion data. *Journal of Geophysical Research*, 110(B3):B03208.
- Papale, P., Moretti, R., and Barbato, D. (2006). The compositional dependence of the saturation surface of H<sub>2</sub>O + CO<sub>2</sub> fluids in silicate melts. *Chemical Geology*, 229(1–3):78–95.
- Parmigiani, A., Degruyter, W., Leclaire, S., Huber, C., and Bachmann, O. (2017). The mechanics of shallow magma reservoir outgassing. *Geochemistry, Geophysics, Geosystems*, 18(8):2887–2905.
- Parmigiani, A., Faroughi, S., Huber, C., Bachmann, O., and Su, Y. (2016). Bubble accumulation and its role in the evolution of magma reservoirs in the upper crust. *Nature*, 532(7600):492–495.
- Paulatto, M., Hooft, E. E., Chrapkiewicz, K., Heath, B., Toomey, D. R., and Morgan, J. V. (2022). Advances in seismic imaging of magma and crystal mush. *Frontiers in Earth Science*, 10:970131.
- Piochi, M., Bruno, P. P., De Astis, G., Piochi, M., Bruno, P. P., and De Astis, G. (2005). Relative roles of rifting tectonics and magma ascent processes: Inferences from geophysical, structural, volcanological, and geochemical data for the Neapolitan volcanic region (southern Italy). *Geochemistry, Geophysics, Geosystems*, 6(7).
- Pistolesi, M., Cioni, R., Bonadonna, C., Elissondo, M., Baumann, V., Bertagnini, A., Chiari, L., Gonzales, R., Rosi, M., and Francalanci, L. (2015). Complex dynamics of small-moderate volcanic events: the example of the 2011 rhyolitic Cordón Caulle eruption, Chile. *Bulletin of Volcanology*, 77(1):1–24.
- Plank, T., Kelley, K. A., Zimmer, M. M., Hauri, E. H., and Wallace, P. J. (2013). Why do mafic arc magmas contain ~4wt% water on average? *Earth and Planetary Science Letters*, 364:168–179.
- Popa, R. G., Bachmann, O., and Huber, C. (2021). Explosive or effusive style of volcanic eruption determined by magma storage conditions. *Nature Geoscience* 2021 14:10, 14(10):781–786.



## REFERENCES

---

- Power, J. A., Nye, C. J., Coombs, M. L., Wessels, R. L., Cervelli, P. F., Dehn, J., Wallace, K. L., Freymueller, J. T., and Doukas, M. P. (2006). The reawakening of Alaska's Augustine volcano. *Eos, Transactions American Geophysical Union*, 87(37):373–377.
- Prata, A. J. and Grant, I. F. (2001). Retrieval of microphysical and morphological properties of volcanic ash plumes from satellite data: Application to Mt Ruapehu, New Zealand. *Quarterly Journal of the Royal Meteorological Society*, 127(576):2153–2179.
- Prata, A. J. and Kerkmann, J. (2007). Simultaneous retrieval of volcanic ash and SO<sub>2</sub> using MSG-SEVIRI measurements. *Geophysical Research Letters*, 34(5).
- Prata, F., Woodhouse, M., Huppert, H. E., Prata, A., Thordarson, T., and Carn, S. (2017). Atmospheric processes affecting the separation of volcanic ash and SO<sub>2</sub> in volcanic eruptions: Inferences from the May 2011 Grímsvötn eruption. *Atmospheric Chemistry and Physics*, 17(17):10709–10732.
- Primulyana, S., Kern, C., Lerner, A. H., Saing, U. B., Kunrat, S. L., Alfianti, H., and Marlia, M. (2019). Gas and ash emissions associated with the 2010–present activity of Sinabung Volcano, Indonesia. *Journal of Volcanology and Geothermal Research*, 382:184–196.
- Pritchard, M. E., Biggs, J., Wauthier, C., Sansosti, E., Arnold, D. W., Delgado, F., Ebmeier, S. K., Henderson, S. T., Stephens, K., Cooper, C., Wnuk, K., Amelung, F., Aguilar, V., Mothes, P., Macedo, O., Lara, L. E., Poland, M. P., and Zoffoli, S. (2018). Towards coordinated regional multi-satellite InSAR volcano observations: results from the Latin America pilot project. *Journal of Applied Volcanology*, 7(1).
- Pritchard, M. E., Poland, M., Reath, K., Andrews, B., Bagnardi, M., Biggs, J., Carn, S., Coppola, D., Ebmeier, S., Furtney, M., Girona, T., Griswold, J., Lopez, T., Lundgren, P., Ogburn, S., Pavolonis, M., Rumpf, E., Vaughan, G., Wauthier, C., Wessels, R., Wright, R., Anderson, K., Bato, M., and Roman, A. (2022). Optimizing satellite resources for the global assessment and mitigation of volcanic hazards—Suggestions from the USGS Powell Center Volcano Remote Sensing Working Group. *U.S. Geological Survey Scientific Investigations Report*, 5116.
- Pyle, D. M. (1989). The thickness, volume and grainsize of tephra fall deposits. *Bulletin of Volcanology*, 51(1):1–15.
- Rasmussen, D. J., Plank, T. A., Roman, D. C., and Zimmer, M. M. (2022). Magmatic water content controls the pre-eruptive depth of arc magmas. *Science*, 375(6585):1169–1172.

- Reath, K., Pritchard, M., Biggs, J., Andrews, B., Ebmeier, S. K., Bagnardi, M., Girona, T., Lundgren, P., Lopez, T., and Poland, M. (2020). Using Conceptual Models to Relate Multiparameter Satellite Data to Subsurface Volcanic Processes in Latin America. *Geochemistry, Geophysics, Geosystems*, 21(1):1–26.
- Reath, K., Pritchard, M., Poland, M., Delgado, F., Carn, S., Coppola, D., Andrews, B., Ebmeier, S. K., Rumpf, E., Henderson, S., Baker, S., Lundgren, P., Wright, R., Biggs, J., Lopez, T., Wauthier, C., Moruzzi, S., Alcott, A., Wessels, R., Griswold, J., Ogburn, S., Loughlin, S., Meyer, F., Vaughan, G., and Bagnardi, M. (2019). Thermal, Deformation, and Degassing Remote Sensing Time Series (CE 2000–2017) at the 47 most Active Volcanoes in Latin America: Implications for Volcanic Systems. *Journal of Geophysical Research: Solid Earth*, 124(1):195–218.
- Redlich, O. and Kwong, J. N. (1949). On the thermodynamics of solutions. V. An equation of state. Fugacities of gaseous solutions. *Chemical Reviews*, 44(1):233–244.
- Remy, D., Chen, Y., Froger, J. L., Bonvalot, S., Cordoba, L., and Fustos, J. (2015). Revised interpretation of recent InSAR signals observed at Llaima volcano (Chile). *Geophysical Research Letters*.
- Reverso, T., Vandemeulebrouck, J., Jouanne, F., Pinel, V., Villemin, T., Sturkell, E., and Bascou, P. (2014). A two-magma chamber model as a source of deformation at Grímsvötn Volcano, Iceland. *Journal of Geophysical Research: Solid Earth*, 119(6):4666–4683.
- Rivalta, E. and Segall, P. (2008). Magma compressibility and the missing source for some dike intrusions. *Geophysical Research Letters*, 35(4):1–5.
- Rogers, N. (2015). The Composition and Origin of Magmas. *The Encyclopedia of Volcanoes*, pages 93–112.
- Roman, A. and Lundgren, P. (2021). Dynamics of large effusive eruptions driven by caldera collapse. *Nature* 2021 592:7854, 592(7854):392–396.
- Romero, J. E., Morgavi, D., Arzilli, F., Daga, R., Caselli, A., Reckziegel, F., Viramonte, J., Díaz-Alvarado, J., Polacci, M., Burton, M., and Perugini, D. (2016). Eruption dynamics of the 22–23 April 2015 Calbuco Volcano (Southern Chile): Analyses of tephra fall deposits. *Journal of Volcanology and Geothermal Research*, 317:15–29.

## REFERENCES

---

- Ruscitto, D. M., Wallace, P. J., Cooper, L. B., and Plank, T. (2012). Global variations in H<sub>2</sub>O/Ce: 2. Relationships to arc magma geochemistry and volatile fluxes. *Geochemistry, Geophysics, Geosystems*, 13(3).
- Rust, A. C. and Cashman, K. V. (2004). Permeability of vesicular silicic magma: inertial and hysteresis effects. *Earth and Planetary Science Letters*, 228(1-2):93–107.
- Rust, A. C. and Cashman, K. V. (2011). Permeability controls on expansion and size distributions of pyroclasts. *Journal of Geophysical Research: Solid Earth*, 116(11).
- Rutherford, M. J. (2008). Magma Ascent Rates. *Reviews in Mineralogy and Geochemistry*, 69(1):241–271.
- Ryan, G. A., Loughlin, S. C., James, M. R., Jones, L. D., Calder, E. S., Christopher, T., Strutt, M. H., and Wadge, G. (2010). Growth of the lava dome and extrusion rates at Soufrière Hills Volcano, Montserrat, West Indies: 2005–2008. *Geophysical Research Letters*, 37(19).
- Scaillet, B. and Pichavant, M. (2003). Experimental constraints on volatile abundances in arc magmas and their implications for degassing processes. *Geological Society Special Publication*, 213(1):23–52.
- Scaillet, B. and Pichavant, M. (2005). A model of sulphur solubility for hydrous mafic melts: application to the determination of magmatic fluid compositions of Italian volcanoes. *Annals of Geophysics*.
- Schilling, S. P., Thompson, R. A., Messerich, J. A., and Iwatsubo, E. Y. (2008). Use of digital aerophotogrammetry to determine rates of lava dome growth, Mount St. Helens, Washington, 2004–2005. *A volcano rekindled: the renewed eruption of Mount St. Helens, 2004–2006 (No. 1750-8)*, pages 145–167.
- Schipper, C. I., Castro, J. M., Tuffen, H., James, M. R., and How, P. (2013). Shallow vent architecture during hybrid explosive–effusive activity at Cordón Caulle (Chile, 2011–12): Evidence from direct observations and pyroclast textures. *Journal of Volcanology and Geothermal Research*, 262:25–37.
- Sheldrake, T. E., Aspinall, W. P., Odbert, H. M., Wadge, G., and Sparks, R. S. (2017). Understanding causality and uncertainty in volcanic observations: An example of forecasting eruptive activity on Soufrière Hills Volcano, Montserrat. *Journal of Volcanology and Geothermal Research*, 341:287–300.

- Shinohara, H., Kazahaya, K., Saito, G., Fukui, K., and Odai, M. (2003). Variation of CO<sub>2</sub>/SO<sub>2</sub> ratio in volcanic plumes of Miyakejima: Stable degassing deduced from heliborne measurements. *Geophysical Research Letters*, 30(5):n/a–n/a.
- Sigmarsson, O., Haddadi, B., Carn, S., Moune, S., Gudnason, J., Yang, K., and Clarisse, L. (2013). The sulfur budget of the 2011 Grímsvötn eruption, Iceland. *Geophysical Research Letters*, 40(23):6095–6100.
- Sigmundsson, F. (2016). New insights into magma plumbing along rift systems from detailed observations of eruptive behavior at Axial volcano.
- Sigmundsson, F., Hreinsdóttir, S., Hooper, A., Árnadóttir, T., Pedersen, R., Roberts, M. J., Óskarsson, N., Auriac, A., Decriem, J., Einarsson, P., Geirsson, H., Hensch, M., Ófeigsson, B. G., Sturkell, E., Sveinbjörnsson, H., and Feigl, K. L. (2010). Intrusion triggering of the 2010 Eyjafjallajökull explosive eruption. *Nature*, 468(7322):426–432.
- Sigmundsson, F., Pinel, V., Grapenthin, R., Hooper, A., Halldórsson, S. A., Einarsson, P., Ófeigsson, B. G., Heimisson, E. R., Jónsdóttir, K., Gudmundsson, M. T., Vogfjörð, K., Parks, M., Li, S., Drouin, V., Geirsson, H., Dumont, S., Fridriksdóttir, H. M., Gudmundsson, G. B., Wright, T. J., and Yamasaki, T. (2020). Unexpected large eruptions from buoyant magma bodies within viscoelastic crust. *Nature Communications*, 11(1):1–11.
- Sparks, R. S. (1978). The dynamics of bubble formation and growth in magmas: A review and analysis. *Journal of Volcanology and Geothermal Research*, 3(1-2):1–37.
- Sparks, R. S., Annen, C., Blundy, J. D., Cashman, K. V., Rust, A. C., and Jackson, M. D. (2019). Formation and dynamics of magma reservoirs. *Philosophical Transactions of the Royal Society A: Mathematical, Physical and Engineering Sciences*, 377(2139).
- Spera, F. J. (2000). Physical properties of magma. *Encyclopedia on Volcanoes*.
- Stevenson, D. S. and Blake, S. (1998). Modelling the dynamics and thermodynamics of volcanic degassing. *Bulletin of Volcanology*, 60(4):307–317.
- Stolper, E. and Walker, D. (1980). Melt density and the average composition of basalt. *Contributions to Mineralogy and Petrology* 1980 74:1, 74(1):7–12.
- Symonds, R. B., Gerlach, T. M., and Reed, M. H. (2001). Magmatic gas scrubbing: implications for volcano monitoring. *Journal of Volcanology and Geothermal Research*, 108(1-4):303–341.

## REFERENCES

---

- Tait, S., Jaupart, C., and Vergnolle, S. (1989). Pressure, gas content and eruption periodicity of a shallow, crystallising magma chamber. *Earth and Planetary Science Letters*, 92(1):107–123.
- Taylor, I. A., Preston, J., Carboni, E., Mather, T. A., Grainger, R. G., Theys, N., Hidalgo, S., and Kilbride, B. M. (2018). Exploring the Utility of IASI for Monitoring Volcanic SO<sub>2</sub> Emissions. *Journal of Geophysical Research: Atmospheres RESEARCH*, 123:5588–5606.
- Telling, J., Flower, V. J., and Carn, S. A. (2015). A multi-sensor satellite assessment of SO<sub>2</sub> emissions from the 2012–13 eruption of Plosky Tolbachik volcano, Kamchatka. *Journal of Volcanology and Geothermal Research*, 307:98–106.
- Theys, N., Champion, R., Clarisse, L., Brenot, H., van Gent, J., Dils, B., Corradini, S., Merucci, L., Coheur, P.-F., Van Roozendaal, M., Hurtmans, D., Clerbaux, C., Tait, S., and Ferrucci, F. (2013). Volcanic SO<sub>2</sub> fluxes derived from satellite data: a survey using OMI, GOME-2, IASI and MODIS. *Atmospheric Chemistry and Physics*, 13(12):5945–5968.
- Theys, N., Hedelt, P., De Smedt, I., Lerot, C., Yu, H., Vlietinck, J., Pedernana, M., Arellano, S., Galle, B., Fernandez, D., Carlito, C. J., Barrington, C., Taisne, B., Delgado-Granados, H., Loyola, D., and Van Roozendaal, M. (2019). Global monitoring of volcanic SO<sub>2</sub> degassing with unprecedented resolution from TROPOMI onboard Sentinel-5 Precursor. *Scientific Reports*, 9(1):1–10.
- Thomas, H. E. and Prata, A. J. (2011). Sulphur dioxide as a volcanic ash proxy during the April-May 2010 eruption of Eyjafjallajökull Volcano, Iceland. *Atmospheric Chemistry and Physics*, 11(14).
- Townsend, M. (2022). Linking surface deformation to thermal and mechanical magma chamber processes. *Earth and Planetary Science Letters*, 577:117272.
- Vallance, J. W., Schneider, D. J., and Schilling, S. P. (2008). Growth of the 2004-2006 lava-dome complex at Mount St. Helens, Washington. *US Geological Survey*, 1750(9):169–208.
- Voight, B., Widiwijayanti, C., Mattioli, G., Elsworth, D., Hidayat, D., and Strutt, M. (2010). Magma-sponge hypothesis and stratovolcanoes: Case for a compressible reservoir and quasi-steady deep influx at Soufrière Hills Volcano, Montserrat. *Geophysical Research Letters*, 37(19):n/a–n/a.

- Wadge, G., Saunders, S., and Itikarai, I. (2012). Pulsatory andesite lava flow at Bagana Volcano. *Geochemistry, Geophysics, Geosystems*, 13(11):11011.
- Wallace, P. J. (2001). Volcanic SO<sub>2</sub> emissions and the abundance and distribution of exsolved gas in magma bodies. *Journal of Volcanology and Geothermal Research*, 108(1-4):85–106.
- Wallace, P. J. (2003). From mantle to atmosphere: magma degassing, explosive eruptions, and volcanic volatile budgets. *Developments in Volcanology*, 5(C):105–127.
- Wallace, P. J. (2005). Volatiles in subduction zone magmas: Concentrations and fluxes based on melt inclusion and volcanic gas data. *Journal of Volcanology and Geothermal Research*, 140(1-3):217–240.
- Wallace, P. J., Anderson, A., and Davis, A. M. (1995). Quantification of pre-eruptive exsolved gas contents in silicic magmas. *Nature*, 377(6550):612–616.
- Wallace, P. J. and Gerlach, T. M. (1994). Magmatic vapor source for sulfur dioxide released during volcanic eruptions: Evidence from Mount Pinatubo. *Science*, 265(5171):497–499.
- Walter, T. R., Zorn, E. U., Harnett, C. E., Shevchenko, A. V., Belousov, A., Belousova, M., and Vassileva, M. S. (2022). Influence of conduit and topography complexity on spine extrusion at Shiveluch volcano, Kamchatka. *Communications Earth & Environment* 2022 3:1, 3(1):1–10.
- Wasser, V. K., Lopez, T. M., Anderson, K. R., Izbekov, P. E., and Freymueller, J. T. (2021). Multidisciplinary Constraints on Magma Compressibility, the Pre-Eruptive Exsolved Volatile Fraction, and the H<sub>2</sub>O/CO<sub>2</sub> Molar Ratio for the 2006 Augustine Eruption, Alaska. *Geochemistry, Geophysics, Geosystems*, 22(9):e2021GC009911.
- Wendt, A., Tassara, A., Báez, J. C., Basualto, D., Lara, L. E., and García, F. (2017). Possible structural control on the 2011 eruption of Puyehue-Cordón Caulle Volcanic Complex (southern Chile) determined by InSAR, GPS and seismicity. *Geophysical Journal International*, 208(1):134–147.
- Westrich, H. R. and Eichelberger, J. C. (1994). Gas transport and bubble collapse in rhyolitic magma: an experimental approach. *Bulletin of Volcanology*, 56(6-7):447–458.
- Wieser, P. E., Jenner, F., Edmonds, M., MacLennan, J., and Kunz, B. E. (2020). Chalcophile elements track the fate of sulfur at Kīlauea Volcano, Hawai‘i. *Geochimica et Cosmochimica Acta*, 282:245–275.

## REFERENCES

---

- Wieser, P. E., Petrelli, M., Lubbers, J., Wieser, E., Özaydın, S., Kent, A. J., and Till, C. B. (2022). Thermobar: An open-source Python3 tool for thermobarometry and hygrometry. *Volcanica*, 5(2):349–384.
- Wilkes, T. C., Pering, T. D., McGonigle, A. J. S., Tamburello, G., and Willmott, J. R. (2017). A Low-Cost Smartphone Sensor-Based UV Camera for Volcanic SO<sub>2</sub> Emission Measurements. *Remote Sensing 2017, Vol. 9, Page 27*, 9(1):27.
- Williams-Jones, G. and Rymer, H. (2015). Hazards of Volcanic Gases. *The Encyclopedia of Volcanoes*, pages 985–992.
- Witham, F., Blundy, J., Kohn, S. C., Lesne, P., Dixon, J., Churakov, S. V., and Botcharnikov, R. (2012). SolEx: A model for mixed COHSCl-volatile solubilities and exsolved gas compositions in basalt. *Computers and Geosciences*, 45:87–97.
- Wong, Y. and Segall, P. (2019). Numerical Analysis of Time-Dependent Conduit Magma Flow in Dome-Forming Eruptions With Application to Mount St. Helens 2004–2008. *Journal of Geophysical Research: Solid Earth*, 124(11):11251–11273.
- Wong, Y. and Segall, P. (2020). Joint Inversions of Ground Deformation, Extrusion Flux, and Gas Emissions Using Physics-Based Models for the Mount St. Helens 2004–2008 Eruption. *Geochemistry, Geophysics, Geosystems*, 21(12):1–24.
- Wong, Y., Segall, P., Bradley, A., and Anderson, K. (2017). Constraining the Magmatic System at Mount St. Helens (2004–2008) Using Bayesian Inversion With Physics-Based Models Including Gas Escape and Crystallization. *Journal of Geophysical Research: Solid Earth*, 122(10):7789–7812.
- Woods, A. W. (1995). The dynamics of explosive volcanic eruptions. *Reviews of Geophysics*, 33(4):495–530.
- Woods, A. W. and Huppert, H. E. (2003). On magma chamber evolution during slow effusive eruptions. *Journal of Geophysical Research*, 108(B8):1–16.
- Wu, Z., Wang, X., Liu, J., and Chen, X. (2020). Mineral fibres: basalt. *Handbook of Natural Fibres: Second Edition*, 1:433–502.
- Yamaguchi, Y., Kahle, A. B., Tsu, H., Kawakami, T., and Pniel, M. (1998). Overview of advanced spaceborne thermal emission and reflection radiometer (ASTER). *IEEE Transactions on Geoscience and Remote Sensing*, 36(4):1062–1071.

- Yang, K., Krotkov, N. A., Krueger, A. J., Carn, S. A., Bhartia, P. K., and Levelt, P. F. (2009). Improving retrieval of volcanic sulfur dioxide from backscattered UV satellite observations. *Geophysical Research Letters*, 36(3):n/a–n/a.
- Yang, X.-M., Davis, P. M., and Dieterich, J. H. (1988). Deformation from inflation of a dipping finite prolate spheroid in an elastic half-space as a model for volcanic stressing. *Journal of Geophysical Research: Solid Earth*, 93(B5):4249–4257.
- Yip, S. T. H., Biggs, J., and Albino, F. (2019). Reevaluating Volcanic Deformation Using Atmospheric Corrections: Implications for the Magmatic System of Agung Volcano, Indonesia. *Geophysical Research Letters*, 46(23):13704–13711.
- Yip, S. T. H., Biggs, J., Edmonds, M., and Liggins, P. (2024). The role of pre-eruptive gas segregation on co-eruptive deformation and SO<sub>2</sub> emissions. *Earth and Planetary Science Letters*, 626:118548.
- Yip, S. T. H., Biggs, J., Edmonds, M., Liggins, P., and Shorttle, O. (2022). Contrasting Volcanic Deformation in Arc and Ocean Island Settings Due To Exsolution of Magmatic Water. *Geochemistry, Geophysics, Geosystems*, 23(7):e2022GC010387.
- Yu, C., Li, Z., Penna, N. T., and Crippa, P. (2018). Generic atmospheric correction model for Interferometric Synthetic Aperture Radar observations. *Journal of Geophysical Research: Solid Earth*, (i).
- Zajacz, Z. (2015). The effect of melt composition on the partitioning of oxidized sulfur between silicate melts and magmatic volatiles. *Geochimica et Cosmochimica Acta*, 158:223–244.
- Zajacz, Z., Candela, P. A., Piccoli, P. M., and Sanchez-Valle, C. (2012). The partitioning of sulfur and chlorine between andesite melts and magmatic volatiles and the exchange coefficients of major cations. *Geochimica et Cosmochimica Acta*, 89:81–101.
- Zhan, Y. and Gregg, P. M. (2019). How Accurately Can We Model Magma Reservoir Failure With Uncertainties in Host Rock Rheology? *Journal of Geophysical Research: Solid Earth*, 124(8):8030–8042.
- Zhan, Y., Gregg, P. M., Le Mével, H., Miller, C. A., and Cardona, C. (2019). Integrating Reservoir Dynamics, Crustal Stress, and Geophysical Observations of the Laguna del Maule Magmatic System by FEM Models and Data Assimilation. *Journal of Geophysical Research: Solid Earth*, 124(12):13547–13562.



## REFERENCES

---

- Zhang, Y. and Stolper, E. M. (1991). Water diffusion in a basaltic melt. *Nature* 1991 351:6324, 351(6324):306–309.
- Zimmer, M. M., Plank, T., Hauri, E. H., Yogodzinski, G. M., Stelling, P., Larsen, J., Singer, B., Jicha, B., Mandeville, C., and Nye, C. J. (2010). The role of water in generating the calc-alkaline trend: New volatile data for aleutian magmas and a new tholeiitic index. *Journal of Petrology*, 51(12):2411–2444.